© Copyright 2023

Duyen Ky Tran

Studies of Charge Transport and Photovoltaic Properties of Semiconducting Polymers

Duyen Ky Tran

A dissertation
submitted in partial fulfillment of the
requirements for the degree of

Doctor of Philosophy

University of Washington
2023

Reading Committee:
Samson A. Jenekhe, Chair
David S. Bergsman
David S. Ginger
Vincent C. Holmberg

Program Authorized to Offer Degree:
Department of Chemical Engineering.

University of Washington

Abstract

Studies of Charge Transport and Photovoltaic Properties of Semiconducting Polymers

Duyen Ky Tran
Chair of the Supervisory Committee: Professor Samson A. Jenekhe
Department of Chemical Engineering

Semiconducting polymers are finding growing applications in electronics and optoelectronics, including organic light-emitting diodes (OLEDs) for displays and lighting, organic field-effect transistors for flexible/foldable electronics, organic photovoltaics to tackle climate change, organic electrochemical transistors (OECTs) for biosensing and neuron-like computing, organic thermoelectrics for harvesting waste heat, and so on. Understanding of the molecular and supramolecular factors that influence the properties of single- and multi-component semiconducting polymers is central to further advancement in these and other applications. However, knowledge of such factors that limit the photovoltaic and charge transport properties of electron-conducting (n-type) conjugated polymers remains scarce and lags behind their hole-conducting (p-type) counterparts. This dissertation aims to establish the structure–morphology–property relationships of n-type semiconducting polymers with respect to charge transport and photovoltaic properties, elucidate the underlying physics, and provide quantitative guidelines for the molecular engineering of next-generation semiconducting polymers and organic electronic devices.

The first objective of the dissertation is to tackle the question: what molecular and supramolecular factors govern the photovoltaic properties of all-polymer solar cells (all-PSCs), which are composed of binary blends of n-type and p-type semiconducting polymers? My studies of various binary polymer blend systems presented in Chapter 2 show that polymer molecular weight and surface energy of the blend constituents have profound influences on the blend photophysics, charge transport, and morphology, which in turn dictate the photovoltaic properties of all-PSCs. Highly efficient all-PSC devices with photon-to-electricity conversion efficiency > 10% are achieved by scalable strategies that control the blend component molecular weight and differences in surface energies.

A second objective focused on elucidating the mechanism of electron transport of n-type semiconducting polymers in view of polymer chain topology and polymer chain length. In these studies (Chapter 3 and 4), I combined the field-effect transistor as the electron transport probe with model semi-flexible and model rigid-rod conjugated polymers, and diverse thin-film morphological characterization tools. I found that significant structural disorder in semi-flexible polymers imposed an upper limit on the electron mobility at a modest chain length of 45-60 repeat units. In contrast, suppressed structural disorder and favorable energetic landscapes in rigid-rod polymers enable continuous growth of electron mobility with chain length.

A third objective is to probe the formation mechanism of different polaronic species in n-type semiconducting polymers upon electrochemical doping (Chapter 5). A ternary mixture of singlet polarons, singlet bipolarons, and triplet bipolarons is demonstrated for the first time to coexist in equilibrium in heavily n-doped polymers. Singlet electron-polarons are the primary charge carriers at a low to moderate doping level, and triplet electron-bipolarons are the dominating charged states at extremely high doping level.

Table of Contents

List of Figures

List of Tables

List of Schemes

Acknowledgements

I wish to express my most sincere appreciation to my dissertation advisor, Professor Samson A. Jenekhe, for his guidance and support. His insightful comments and valuable suggestions have been instrumental to the successful completion of my work. I would also like to thank Professors David S. Bergsman, David S. Ginger, Bruce J. Hinds, Vincent C. Holmberg, and Qiuming Yu for their time serving on my committee and for providing valuable comments.

During my graduate education, I have had opportunities to cross paths with several brilliant fellow students and researchers who have helped to shape my overall experiences. The time spent in the lab with the past and present members of the Jenekhe group has been an integral part of my journey to becoming a better scientist and a better person – Sarah M. West, Mary Nguyen, Dr. Xiaomei Ding, Hyunjong Lee, and Dr. Nagesh B. Kolhe. Special thanks to Sarah who has been a great colleague and collaborator to exchange ideas and share discussions as well as provide precious materials that enable a large portion of my work. Above all, you have been a good friend who is always down to go on coffee runs with me and hang out after work. Xiaomei taught me a lot of things around the labs and shared successful collaboration on multiple projects. Hyunjong, Nagesh, and Mary helped me get started at the beginning when I first joined the lab.

I thank all of my collaborators, including Dr. Daiki Kuzuhara and Dr. Tomoyuki Koganezawa at the Japan Synchrotron Radiation Facility Spring-8 who have helped to collect the GIWAXS data for the first half of my works, Dr. Amélie Robitaille and Professor Mario Leclerc at Laval University in Canada who have provided interesting materials to my studies, and Dr. Jiajie Guo and Dr. Shinya E. Chen from the Ginger group at the University of Washington who

have helped to collect the GIWAXS data for the later halves of my Ph.D. works and shared fruitful discussions.

I would like to acknowledge the Department of Chemical Engineering, the Clean Energy Institute at the University of Washington, the Office of Naval Research, the National Science Foundation, and the U.S. Department of Energy, Basic Energy Sciences for financial support.

Finally, I would like to take this opportunity to express my gratitude to my parents for providing me with a strong educational foundation from an early age and support over the years. I also want to thank my extended family – grandparents, aunts, and cousins for their support and encouragement. I especially thank my family here in the U.S. – my aunt and uncle, who have been there since day one with unwavering love and support; my beloved cousins-but-more-like-siblings, who are one of my biggest cheerleaders. I also thank my friends for their constant encouragement. Without them, this work would not have been possible.

Chapter 1. Introduction

1.1. π-Conjugated Semiconducting Polymers

The breakthrough discovery of iodine doped polyacetylene exhibiting metallic conductivity in 1977 has paved the way for rapid development of π-conjugated semiconducting polymers.[1-3] The extensive library of polymer semiconductors accumulated since then, and their unique properties have enabled the emergence of an era of low-cost thin film organic electronic devices including organic light-emitting diodes (OLEDs) for commercial displays and lighting,[4] organic field-effect transistors (OFETs) for flexible and stretchable electronics,[5-10] organic photovoltaics (OPVs) as solution to climate change and global warming threats,[11-46] organic thermoelectrics (OTEs) to convert waste heat into electricity,[47-49] and organic bioelectronics as sensors and neuromorphic computing.[50, 51] Understanding of the structure-property relationships of semiconducting polymers has been essential to the design and synthesis of new materials with enhanced properties that advance these device applications.[4-16, 47-52]

π-conjugated polymers have alternating single bonds and double bonds in the backbone[1-3] allowing electrons in the π-orbitals to delocalize across many atomic sites. The overlapping interactions between these π-orbital electrons result in continuous energy bands rather than discrete energy levels. Regardless, a finite gap between the highest occupied molecular orbital (HOMO) level and the lowest unoccupied molecular orbital (LUMO) level, which is called a bandgap (E_g), is still present (4eV < E_g < 1.0 – 1.2 eV). As a result, π-conjugated polymers behave intrinsically as insulators or semiconductors with a typical dc conductivity ranging between 10^{-12} S/cm and 10^{-9} S/cm.

Semiconducting polymers and related organic electronic devices are of fundamental and technological interests due to the unique advantages that the inorganic counterparts fail to offer.

First of all, the optical properties, electrochemical properties, and electronic structure of semiconducting polymers are highly tunable via rational molecular engineering. For instance, the donor-acceptor copolymerization motif allows tailoring of the optoelectronic properties by varying the electron-donating and the electron-accepting strength of the moieties.[53, 54] Controlling the planarity and rigidity of backbone is another effective strategy to fine-tune the optical absorption spectra and the bandgap of semiconducting polymers whereby a completely planar backbone with minimal torsional defect would enable efficient electron delocalization[55, 56] resulting in enhanced absorption in the near-infrared region and a narrower bandgap. Moreover, the solution processability that is unique to semiconducting polymers enables large area device fabrication via roll-to-roll printing or inkjet printing, both of which require minimal energy input and low capital investment as opposed to the energy- and capital-intensive manufacturing process of inorganic semiconductors. In addition, remarkable thermal stability (> 400^{o}C) and excellent mechanical durability also endow semiconducting polymers with great latitudes for a variety of device applications.

π-conjugated semiconducting polymers are fundamentally unipolar and can be classified as either *hole-conducting* (p-type) or *electron-conducting* (n-type). Although parity in hole mobility of p-type polymers with electron mobility in n-type polymers is necessary for developing high-performing organic electronic devices, the development of n-type polymers still lags behind that of p-type polymers.[47, 48] The lack of molecular diversity of electron-deficient building blocks, challenging syntheses, and poor ambient stability are pressing issues that need to be addressed in order to improve the electron transport properties and the photovoltaic properties of semiconducting polymers. Establishing fundamental understandings of the underlying mechanism that governs the aforementioned properties is equally important. Novel

molecular engineering and device engineering approaches are also of great interest in order to further advance this interdisciplinary field of organic semiconductors and related opto-electronic applications.

1.2. Properties of Semiconducting Polymers and Associated Organic Electronic Devices

1.2.1. Basic Principles and Figure-of-merits of All-Polymer Solar Cells.

Organic photovoltaics (OPVs) have been garnering much attention in recent years and received significant research efforts to push the power conversion efficiency towards the 20% commercialization benchmark. Unlike silicon-based photovoltaic technology whose manufacturing process is highly energy intensive, organic solar cells can be fabricated from solution-based processing techniques such as spin-coating, spray coating, inkjet printing, or roll-to-roll printing, all of which require minimal input energy; thereby, substantially lowering the cost. OPVs are also mechanically robust, ultrathin, and light weight making them an ideal candidate to be integrated into buildings and wearable electronic devices. Most importantly, OPVs have the lowest carbon footprint among the current photovoltaic technologies with over an order of magnitude lower amount of carbon dioxide emitted per kWh produced compared to that of silicon-based solar cells.[57-60] These remarkable merits are indicators that the future of photovoltaics is organic semiconductors based.

All-polymer solar cells (all-PSCs) is a subset of organic photovoltaics where the photoactive layer is comprised of a phase-separated blend of an electron-donating (donor) conjugated polymer and an electron-accepting (acceptor) conjugated polymer. All-PSCs combines the aforementioned properties of OPVs with additional advantages including facile tailoring of the optoelectronic properties,[11-46] superior photochemical stability,[43, 61, 62] and

excellent thermal and mechanical durability.[45, 63-68] A typical device architecture of an all-polymer solar cell is shown in Figure 1-1a whereas its basic working mechanism is illustrated in Figure 1-1b.

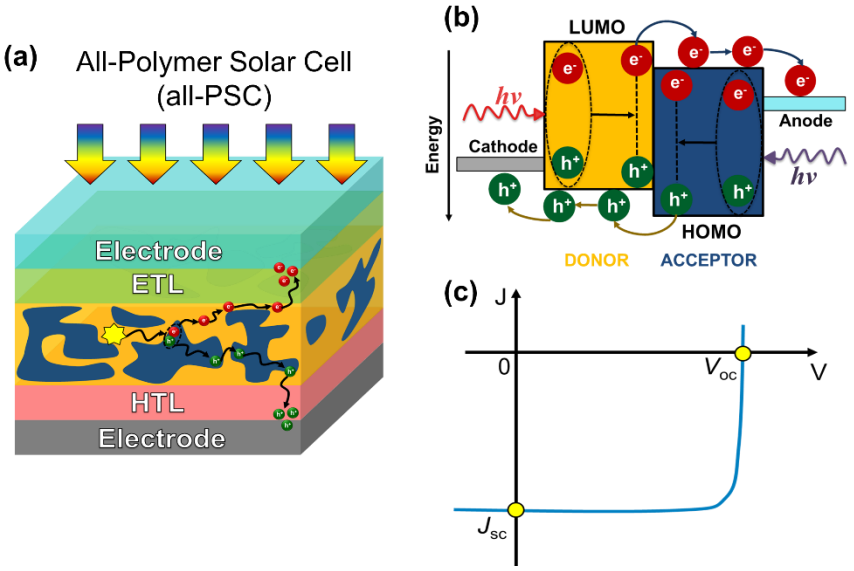

Figure 1-1. (a) Schematic of an all-polymer solar cell (all-PSC), (b) Working mechanism of all-PSCs, and (c) Current density (*J*) versus applied voltage (*V*) response curve of all-PSCs.

The photon-to-electricity conversion in all-polymer solar cells can be categorized into five major processes including (i) light absorption/exciton generation, (ii) exciton diffusion, (iii) exciton dissociation into holes/electrons, (iv) charge transport/charge recombination, and (v) charge extraction. Upon light absorption, incident photons with energy greater than or equal to the π- π* gap will excite either the donor polymer (P_D) or the acceptor polymer (P_A) to generate excitons which are electrostatically bound electron and hole pairs (Figure 1-1b). Due to the intrinsically low dielectric constant (ε ~ 3 – 4) of organic semiconductors, the exciton binding energy (E_B ~ 0.4 – 0.5 eV) is significantly larger than the thermal energy at room temperature (k_BT ~ 0.026 eV); thus, the process of exciton dissociation into free charges is not spontaneous in polymer solar cells. Within their characteristic lifetime, the excitons will then diffuse to the interface between the P_D and the P_A where they can be dissociated into charges (holes and

electrons) with the additional driving force provided by the energy level offsets between P_D and P_A. The holes will be transported within the donor phases whereas the electrons will be transported within the acceptor phases to their respective electrodes. Due to the random arrangement of the donor phase and the acceptor phase throughout the photoactive layer, holes and electrons can also encounter each other and recombine either radiatively or non-radiatively. Once the charges arrive at the electrodes, they will be extracted to generate electricity.

The performance of a polymer solar cell is characterized by measuring photocurrent response as a function of sweeping voltage bias (Figure 1-1c) whereby important photovoltaic parameters are extracted including short-circuit current density (J_{sc}), open-circuit voltage (V_{oc}), and fill factor (FF) which cosmbine to produce the power conversion efficiency (PCE):

$$PCE = \frac{J_{sc}V_{oc}FF}{P_{in}} \ (Eq. 1-1)$$

The short-circuit current density is the current density obtained without any voltage bias. The open-circuit voltage is the voltage obtained when no current is extracted. The fill factor is the ratio of the maximum efficiency to the product of J_{sc} and V_{oc}, and the incident light intensity (P_{in}) is 100mW/cm^2. Simultaneous improvement in the photovoltaic parameters (J_{sc}, V_{oc}, and FF) is required to maximize the power conversion efficiency of all-PSCs.

1.2.2. Brief Literature Review of Factors that Govern Photovoltaic Properties of Semiconducting Polymers

From a device engineering perspective, major bottlenecks hindering further advances in the photovoltaic performance of all-PSCs include the low photocurrent (J_{sc} < 20 mA/cm^2),[11, 12, 17, 18, 23, 24, 26-28, 32, 40] the poor open-circuit voltage (V_{oc} < 1V),[11, 12, 17, 32] and the modest FF (FF < 0.7).[11, 12, 17, 18, 30, 32, 40] The photocurrent is limited by the lack of broad and complementary

absorbing spectrum hindering efficient sunlight harvesting, the low thin-film absorption coefficient, inefficient exciton generation rate due to insufficient energetic offset between P_D and P_A, low charge carrier mobility of both donor and acceptor polymer component, and poor charge extraction at the electrodes because of non-Ohmic contact.[11, 12, 17, 18, 23, 24, 26-28, 32, 40] The low V_{oc} (< 1V) is mainly due to the large optical bandgap energy loss ($E_{loss} = E_g - eV_{oc} > 0.6$ eV).[11, 12, 17, 29] The small fill factor is primarily due to the suboptimal blend morphology, which in turn is influenced by several factors including polymer molecular weight,[21, 22, 25, 29, 33] polymer/polymer interchain interactions,[15, 24, 30, 37, 40] polymer blend crystallinity,[15, 24, 37, 43] molecular orientations,[22, 37, 69, 70] domain size, and domain purity.[71-73] Several device engineering strategies have been explored to tailor the blend morphology including thermal annealing,[23, 74] solvent vapor annealing,[24] room-temperature aging,[14, 75] co-solvents,[19] and solvent processing additives.[23, 29, 36, 76] Advancing all-PSCs from a materials chemistry point of view involves harvesting more of the solar spectrum,[16, 23, 29, 41, 42] increasing the charge carrier mobilities of the donor polymers and the acceptor polymers,[29, 36, 41, 42] exerting molecular control over the blend morphology[15, 24, 30, 37, 40, 72] and blend photophysics,[41, 44, 67] as well as understanding the underlying structure-property-performance relationships.

The performance of all-PSCs is also influenced by the efficacy of the electron transport layer (ETL) (e.g. LiF, PFN-Br, etc.) and hole transport layer (HTL) (e.g. PEDOT:PSS, MoO_x, WO_x, etc.). For instance, suitable energy alignment is required not only between the LUMO energy level of P_A and the work function of the ETL but also between the HOMO energy level of P_D and the work function of HTL to enable efficient charge extraction. High electrical conductivity and low contact resistance between the transport layers and the photoactive layer is also necessary to suppress shunt resistance and series resistance; thereby, maximizing the

photovoltaic parameters. For the electrodes, while the oxidative stability and suitable work function of the bottom electrode will enable long-term operation of solar cells, the top electrode requires high transparency for efficient light transmittance and excellent electrical conductivity. Thus, molecular engineering to develop novel electron and hole transporting interlayers and interface engineering to modify electrode's work function and reduce surface trap densities have been demonstrated to also improve the photovoltaic properties of all-polymer solar cells.

1.3. Charge Transport Properties of Semiconducting Polymers

1.3.1. Basic Principles and Figure-of-merits of Organic Field-Effect Transistors (OFETs).

The invention of transistors at Bell Labs in 1948, which was awarded the Nobel Prize in physics in 1956,[77] has marked a new era in digital electronics. Transistor is a switching device consisting of three terminals and a fundamental building block in nearly all modern electronic devices that require signal processing.[78] In particular, field-effect transistors (FETs) consist of three terminals (source, drain, and gate electrodes), a semiconductor layer bridging the source and the drain electrodes, and a dielectric layer insulating the gate electrode from the semiconductor (Figure 1-2). Current flowing from source to drain under the potential difference between the electrodes in induced by voltage bias at the gate. Organic field-effect transistor (OFET) is a subset of the FET family where a thin film of organic semiconductors is the active layer.

The working mechanism of organic field-effect transistors is illustrated in Figure 1-2. In the off state without any applied gate bias, no current flows across the channel due to the intrinsically low electrical conductivity of organic semiconductors and the low charge carrier concentration. For p-channel OFETs, a negative voltage is applied at the gate electrode to induce holes at the interface between the semiconductor and the dielectric layer (Figure 1-2). The

transistor is now operating in its on state with charges accumulating and moving across the channel to produce current. Similarly, for n-channel OFETs, a positive voltage bias is applied at the gate electrode to induce electrons in the semiconductor channel leading to current flowing between the source and the drain electrodes (Figure 1-2). The operational mechanism of OFETs can also be examined from an energy level point of view. Holes can be injected from the source to the highest occupied energy level (HOMO) of the semiconductor and transported to the drain electrodes in p-channel OFETs whereas electrons are injected to the lowest unoccupied energy level (LUMO) of the semiconductor in n-channel OFETs (Figure 1-2).

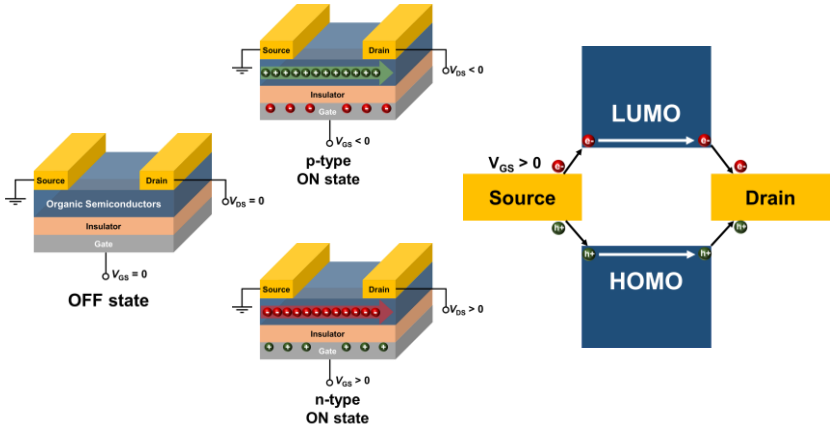

Figure 1-2. Working mechanism of organic field-effect transistors.

The performance of a polymer field-effect transistor is characterized by current flowing across the channel between the source and the drain electrodes (I_{DS}) as sweeping drain-source voltage (V_{DS}) at various gate-source voltage (V_{GS}); thereby, producing a family of output curves as shown in Figure 1-3a. Another way to examine the performance of polymer field-effect transistor is using the transfer curs as presented in Figure 1-3b. The transfer curve (Figure 1-3b) is made up from $|I_{DS}|$ and $|I_{DS}|^{1/2}$ versus modulating V_{GS} at a constant applied V_{DS}. A few important charge transport parameters can be measured using the polymer field-effect transistor platform including charge carrier mobility (μ), threshold voltage (V_T), subthreshold swing (S),

and on/off current ratio (I_{on}/I_{off}). The charge carrier mobility governs how fast the carriers (electrons or holes) move in the semiconducting polymer layer. The threshold voltage is the switching point of the transistor whereas the subthreshold swing controls how fast the switching occurs in the transistor. The on/off current ratio is the difference in magnitude of current between the off state and the on state. The channel dimensions, width (W) and length (L), as well as the areal capacitance of the dielectric (C_i) are device parameters that also govern the measured charge transport properties. The charge transport parameters are related to one another as follows:

$$I_{DS} = \frac{\mu W C_i}{L}\left(V_{GS} - V_T - \frac{V_{DS}}{2}\right)V_{DS} \quad (linear\ regime, V_{DS} \ll V_{GS} - V_T) \quad (Eq. 1-2)$$

$$I_{DS} = \frac{\mu W C_i}{2L}(V_{GS} - V_T)^2 \quad (saturation\ regime) \quad (Eq. 1-3)$$

$$S = \frac{\partial V_{GS}}{\partial \log(I_{DS})} \ (Eq. 1-4)$$

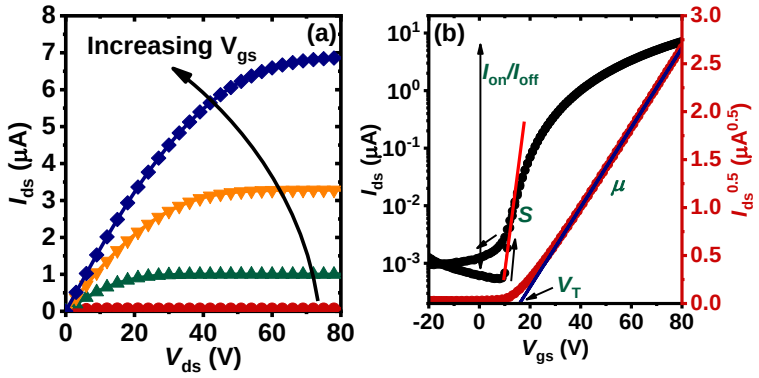

Figure 1-3. (a) Output curves of organic field-effect transistors, and (b) Transfer curve of organic field-effect transistors where electron transport parameters (μ, V_T, S, I_{on}/I_{off}) can be extracted.

1.3.2. Brief Literature Review of Charge Transport Properties of Semiconducting Polymers.

The charge transport properties of the semiconducting polymers extracted from the field-effect transistor platform are governed by numerous factors, one of which is thin film

morphology. Enhanced charge carrier mobility can be achieved by optimizing the thin film microstructure to feature tight π-π packing distance to enhance interlayer electronic coupling facilitating fast interchain charge transport, *edge-on* vs. *face-on* molecular orientations to enable efficient *in-plane* vs. *out-of-plane* charge transport, improved short-range and long-range ordering, and high polymer crystallinity.[5-10] These desirable macroscopic properties are in turn controlled at a molecular level through rational design of the polymer structures via side chain engineering, synthesizing novel conjugated building blocks to enable rigid planar polymer backbones with minimal torsional and conformational defects, tuning of polymer molecular weights, and controlling of polymer's regioregularity.[5-10] The charge transport properties are also controlled by the electronic structures of the semiconducting polymers whereby a suitable energy level alignment between either the LUMO and the HOMO with the electrodes would allow efficient charge injection and charge extraction.[5-10] Furthermore, minimizing the density of traps is also imperative to enhance the charge transport properties.[79, 80] Charge trapping sites can be present within the semiconducting polymer due to chemical defects or impurities (bulk traps) and at the interface between semiconducting polymer and the insulating dielectric layer (interface traps).[80]

1.4. Major Challenges

Recent years have seen remarkable strides in the development of organic semiconductors materials design and organic electronic devices with notable advances such as a fast-growing library of semiconducting polymers beyond the archetypal polythiophenes, some understandings of the relationships between molecular structures, film morphology, and properties of p-type semiconducting polymers, and enhanced device performance with some commercialization

efforts. Nevertheless, there remain several challenges that need to be addressed to establish new fundamental insights and bring about technological advances to the field.

Thermodynamics and kinetics governing the mixing of all-polymer blend are rather complicated; thereby, arriving at *a priori* prediction on the photovoltaic properties of all-polymer solar cells remains highly challenging. Furthermore, available studies in literature present divergent conclusions on a variety of issues. For instance, investigation to the effects of increasing the polymer molecular weights on the photovoltaic properties of all-polymer solar cells was found to enhance the PCEs due to the synergistic improvement of the short-circuit current (J_{sc}) and the fill factor (FF) in some studies[21, 22, 29, 81, 82] while other reports found simultaneous drop in both J_{sc} and FF with increasing polymer molecular weight.[25, 33] As a result, it is rather challenging to arrive at a comprehensive understanding on factors that govern the photovoltaic properties all-polymer solar cells and to provide impactful molecular design insights to develop novel semiconducting polymers with desired properties.

In addition, although parity in the hole mobility of p-type polymers with the electron mobility of n-type polymers is required in all organic electronic device applications, the synthesis and investigation of the charge transport properties of n-type semiconducting polymers have generally lagged behind those of p-type semiconducting polymers.[7, 8] Recent efforts have led to improved electron mobility in some classes of n-type semiconducting polymers (μ > 3 cm^2/Vs).[83-86] However, mechanistic studies to elucidate the underlying physics and factors that govern the electron transport properties in n-type semiconducting polymers remain scarcely explored. Thus, studies to explore the fundamental question that is “What are the factors that govern the electron transport properties of n-type semiconducting polymer?” remain to be

explored, and more quantitative guidelines to molecular engineer high-mobility n-type semiconducting polymers are also needed.

Understanding the nature of charge carriers in π-conjugated polymer is central to the development of high-performing organic electronic devices. Extensive studies have been done in p-type semiconducting polymers to understand how mobile charge carriers are formed and stabilized along the polymer backbone as well as the nature of these charge carriers (polarons vs. bipolarons).[87-93] Yet, there exists a large knowledge gap regarding collective properties of mobile charge carriers in n-type semiconducting polymers. In particular, the nature of these charge carriers (electron-polaron vs. electron-bipolaron), their formation mechanism, and factors that control their stability remain unclear. Thus, studies to investigate the nature of different polaronic species in n-type conjugated polymers and dynamically probe the transition between these polaronic states are of broad fundamental and technological interests.

1.5. Research Objectives and Significance

The primary objectives of this research are to establish the structure–morphology–property relationships of n-type semiconducting polymers with respect to charge transport and photovoltaic properties, elucidate the underlying physics, and provide quantitative guidelines for the molecular engineering of next-generation semiconducting polymers and organic electronic devices. The objectives of this research focus on addressing several current issues in the field.

(i) Understanding factors that govern the photovoltaic properties of semiconducting polymers towards high-performing all-polymer solar cells. The photovoltaic properties of all-PSCs rely on numerous factors from molecular level to macroscopic device level. Careful consideration of all parameters is required to improve the photovoltaic properties of semiconducting polymers. For this purpose, detailed case studies on the relationships

between structures, blend morphology, blend photophysics, blend charge transport properties, and photovoltaic properties of different donor polymer – acceptor polymer pairs are presented in Chapter 2. Knowledge gained from these studies provides more comprehensive understandings on different molecular and supramolecular factors that govern the photovoltaic properties of all-PSCs. New design guidelines are developed to engineer better performing semiconducting polymers with desired properties.

(ii) **Investigating mechanism of electron transport in n-type semiconducting polymers.** Fundamental understanding of electron transport physics of n-type semiconducting polymers is crucial to the development of organic electronics. Towards bridging the knowledge gap between p-type semiconducting polymers and n-type semiconducting polymers, the mechanism of electron transport in different classes of n-type semiconducting polymers is examined. The influences of polymer chain topology and polymer chain length on electron transport properties of n-type π-conjugated polymers are discussed in Chapters 3 and 4. N-type conjugated polymers with a semi-flexible chain topology are shown to exhibit a Λ-shaped chain length dependent electron mobility, and the maximum mobility is obtained at a critical chain length of 45 – 60 repeat units as a result of severe structural disorder associated with further increased chain length. In contrast, n-type conjugated ladder polymers with rigid-rod chain topology combines suppressed structural disorder and favorable electronic landscapes to enable continuous growth of electron mobility without saturation with respect to polymer chain length.

(iii) **Probing the nature of mobile charge carriers (polarons vs. bipolarons vs. polaron pairs) in n-type π-conjugated polymer.** Elucidating the nature of mobile charge carriers to determine whether they are electron-polaron, electron-bipolaron, or electron-polaron pairs is

central to bridging the knowledge gap between p-type conjugated polymers and n-type conjugated polymers. In chapter 5, the formation mechanism of polarons, bipolarons, and polaron pairs in an electrochemically doped n-type conjugated polymer is discussed. An equilibrium between polaron, bipolaron, and polaron pair is demonstrated for the first time in heavily doped n-type semiconducting polymers, whereas singlet polarons are preferentially formed in lightly doped polymers. Extremely high doping level leads to annihilation of singlet polarons and singlet bipolarons such that polaron pairs (triplet bipolarons) become the dominating charge carriers.

Chapter 2. Elucidating Factors Governing the Photovoltaic Properties of Semiconducting Polymers in All-Polymer Solar Cells

The results in this chapter are reprinted with permission from Tran, D. K.; Kolhe, N. B.; Hwang, Y.-J..; Kuzuhara, D.; Koganezama, T.; Jenekhe, S. A. Effects of a Fluorinated Donor Polymer on the Morphology, Photophysics, and Performance of All-Polymer Solar Cells Based on Naphthalene Diimide-Arylene Copolymer Acceptors. *ACS Appl. Mater. Interfaces* **2020**, *12*, 16490-1650. (Copyright 2020 American Chemical Society) and from Tran, D. K.;* Robitaille, A.;* Hai, I. J.; Ding, X.; Kuzuhara, D.; Koganezama, T.; Chiu, Y-C.; Leclerc, M.; Jenekhe, S. A. Elucidating the Impact of Molecular Weight on Morphology, Charge Transport, Photophysics, and Performance of All-Polymer Solar Cells. *J. Mater. Chem. A* **2020**, *8*, 21070-27083. (Copyright 2020 Royal Society of Chemistry).

2.1. Effects of a Fluorinated Donor Polymer on the Morphology, Photophysics, and Performance of All-Polymer Solar Cells Based on Napthalene Diimide-Arylene Copolymer Acceptors

2.1.1. Introduction

All-polymer solar cells (all-PSCs), in which the active layer is comprised of a binary blend of an electron-donating (donor) polymer and an electron-accepting (acceptor) polymer, have garnered significant research efforts over the past several years, leading to great strides in terms of device performance.[11, 17, 18, 94] Although the power conversion efficiency (PCE) of all-PSCs lags the efficiency of small molecule non-fullerene acceptors (SM-NFAs) based solar cells,[95, 96] all-PSCs have unique advantages over SM-NFA devices, including superior photo- and electro-chemical stability,[14, 97] enhanced thermal and mechanical robustness,[33, 63, 64] and enhanced

rheological properties which are ideal for large scale film coating.[33, 64] These advantages make all-PSCs promising candidates for large-scale manufacturing.[14, 29, 64, 98] The key parameters limiting the device efficiency of all-PSCs have long been identified as the generally low fill factor (FF)[11, 17, 18, 24, 94] and the modest open-circuit voltage (V_{oc}).[11, 17, 32, 94] The low V_{oc} (< 1V) is mainly due to the large optical bandgap energy loss ($E_{loss} = E_g - eV_{oc} > 0.6$ eV),[11, 17, 29, 94] while the poor FF originates primarily from non-optimal blend morphology and inefficient charge extraction at the organic/metal interfaces.[11, 17, 94] Several strategies have been explored for tailoring the blend morphology of all-PSCs, including thermal annealing,[23, 74, 99] solvent vapor annealing,[24] room-temperature aging,[14, 75] co-solvents,[19] solvent processing additives,[23, 29, 36, 76] side chain engineering,[20, 100, 101] and random copolymerization,[15, 30, 31, 37] whereby some systems could achieve near unity internal quantum efficiency (IQE).[24, 30, 37]

A potential strategy to improve the V_{oc} of all-PSCs is incorporation of fluorine atoms into the molecular structure of either the donor or the acceptor polymer. Fluorination has been demonstrated to be an effective molecular design strategy to enhance the photovoltaic properties, especially in SM-NFA solar cells.[95, 96, 102, 103] Effects of fluorination include lowering the highest occupied molecular orbital (HOMO) and the lowest unoccupied molecular orbital (LUMO) energy levels,[104] enhancing the crystallinity of the blend components and forming a favorable blend morphology due to F-F intermolecular interactions,[31, 105-107] altering the dielectric constant of the materials,[31, 102, 108, 109] suppressing charge recombination and enhancing charge photogeneration,[107, 110] and increasing charge carrier mobility.[111] Despite the impressive performance of SM-NFA solar cells based on fluorinated donor polymers, application of such fluorinated donor polymers in all-PSCs is surprisingly rare; in the few known examples, the fluorinated donor polymers, poly[(2,6-(4,8-bis(5-(2-ethylhexyl-3-fluoro)thiophen-2-yl)-

benzo[1,2-b:4,5-b']dithiophene))-alt-(5,5-(1',3'-di-2-thienyl-5',7'-bis(2-ethylhexyl)benzo[1',2'-c:4',5'-c']dithiophene-4,8-dione)], (PBDB-TF or PM6) shown in Figure 2-1a has been paired with various acceptor polymers having a ladder-type fused ring co-monomer in their repeating units.[36, 39, 46] The pairing of PM6 with such fused-ring acceptor polymers such as PZ1,[46] PFBDT-IDTIC,[36] and PN1[39] has resulted in high performance all-PSCs with PCEs of 10 – 11% and V_{oc} of 0.96 – 1.0V.[36, 39, 46] Surprisingly, effects of a fluorinated donor polymer on the performance of all-PSCs based on naphthalene diimide (NDI) copolymer acceptors have yet to be explored. NDI-arylene copolymer acceptors have been widely studied as materials for constructing highly efficient all-PSCs.[14, 29, 52, 112, 113] Indeed, our group[14, 29, 37] and others[98, 114-116] have showed that all-PSCs with PCEs as high as 8-10% can be achieved by pairing various NDI-arylene copolymers with the non-fluorinated derivative of PM6, i.e. PBDB-T. However, because numerous factors determine the compatibility, nanoscale morphology, and PCE of all-PSC devices, *a priori* prediction of how the fluorination of the donor polymer could influence the performance of all-PSCs based on NDI-arylene copolymer acceptors is not possible.

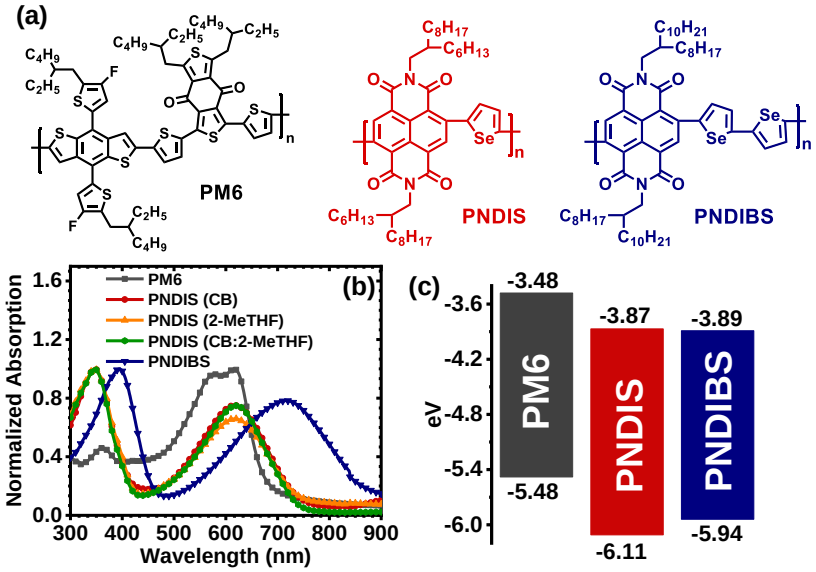

Figure 2-1. (a) Molecular structures of donor polymer, PM6, and acceptor polymers, PNDIS and PNDIBS. (b) Normalized thin-film optical absorption spectra of the donor and acceptor polymers processed from different solvents. (c) HOMO/LUMO energy levels of the donor and acceptor polymers. Reproduced with permission from Ref.[44] Copyright 2020 American Chemical Society.

In this paper, we report an investigation of the effects of fluorination of the donor polymer on the blend morphology, blend photophysics, and photovoltaic properties of all-PSCs based on NDI-arylene copolymer acceptors. We found that pairing the fluorinated donor polymer PM6 with two different related NDI-arylene copolymers – NDI-biselenophene copolymer (PNDIBS) and NDI-selenophene copolymer (PNDIS) shown in Figure 2-1a – resulted in dramatically different outcomes and very divergent observations. Contrary to expectations from the known high performance (> 9% PCE) of PBDB-T:PNDIBS all-PSCs,[29] blends of the fluorinated donor polymer PM6 with PNDIBS gave rise to substantially inferior photovoltaic properties with a maximum PCE of 3.1%. In contrast, blends of PM6 with PNDIS could be used to develop all-PSCs with a maximum PCE of over 9%. Furthermore, these efficient PM6:PNDIS blend all-PSCs were found to be relatively insensitive to device processing methods and to active layer thickness of up to 300 nm. Detailed comparative studies of the PM6:PNDIBS and PM6:PNDIS blend systems show that the divergent effects of the fluorinated donor polymer on the photovoltaic properties originate from the stark differences in blend morphology and blend photophysics. We show that the PM6:PNDIBS blend system exhibits a lateral bulk phase separation in which both *face-on* and *edge-on* molecular orientations are displayed. In contrast, the bulk thin films of the PM6:PNDIS blend system are characterized by prominent vertical phase stratification and some lateral phase segregation in conjunction with predominant *face-on* molecular orientation. The photophysics of PM6:PNDIBS blends was characterized by low charge photogeneration rate, high electron-hole pair recombination rate, and poor charge

collection probability (P(E,T) = 65.5%). In stark difference, the PM6:PNDIS blend photophysics featured enhanced charge photogeneration rate, suppressed geminate and bimolecular recombinations and near unity charge collection probability (P(E,T) = 99.1%). These results show that in addition to the generally expected enhancement of V_{oc}, fluorination of a polymer component of all-PSCs can also dramatically influence the blend morphology and blend photophysics with consequent net negative or positive impact on the photovoltaic efficiency.

2.1.2. Experimental Methods

Materials. The donor polymer, PM6, was purchased from Solarmer Energy Inc (M_n = 14.6 kDa, M_w = 38 kDa, $Đ$ = 2.60) (Irwindale, CA, United States) while PNDIS and PNDIBS were previously synthesized in our lab.[14, 29] Optical absorption spectra were obtained from a PerkinElmer Lambda 900 UV-vis/near-IR spectrophotometer. Polymer molecular weight information was obtained with gel-permeation chromatography (GPC) eluting with chloroform at room temperature (25^{o}C) for PNDIS (M_n = 22.1 kDa, M_w = 64.9 kDa, $Đ$ = 2.94) whereas the GPC characterization was done in chlorobenzene at room temperature for PNDIBS (M_n = 114.6 kDa, M_w = 218 kDa, $Đ$ = 1.90).

Cyclic Voltammetry. Cyclic voltammetry (CV) experiments were done on an EG&G Princeton Applied Research Potentiostat/Galvanostat (model 273A). A three-electrode cell was used, using platinum wire electrodes as both counter and working electrode. Ag/Ag^+ (Ag in 0.01 M $AgNO_3$ solution) was used as a reference electrode. The films of the polymer were coated onto the Pt wires by dipping the wires into polymer solutions of the polymers (PM6, PNDIS, and PNDIBS) and drying the coated films at 25 °C. All the CV measurements were carried out in 0.1 M tetrabutylammonium hexafluorophosphate (Bu_4NPF_6) electrolyte solution in acetonitrile at a scan rate of 50 mV/s. The reduction and oxidation potentials were referenced to the Fc/Fc^+

couple by using ferrocene as an internal standard. The LUMO and HOMO energy levels were estimated using a ferrocene value of −4.8 eV with respect to vacuum level. The LUMO and HOMO energy levels were determined using the equations $E_{LUMO} = -(eE_{red\text{-}onset} + 4.8)$ and $E_{HOMO} = -(eE_{ox\text{-}onset} + 4.8)$, respectively.

Fabrication and Characterization of all-PSCs. Solar cells devices were fabricated with an inverted architecture of ITO/ZnO/PEI/Blend/MoO_3/Ag. ITO-coated substrates (15 Ω/square, Shanghai B. Tree Tech, Shanghai, China) were cleaned sequentially in ultrasonic baths with acetone, deionized water, and isopropyl alcohol for 30 min, dried using nitrogen gas, and followed by 10 mins of O_2 plasma cleaning. The ZnO precursor solution was spin-coated onto the ITO and followed by thermal annealing at 250 °C for 30 min to make ~30 nm thick ZnO layer. A 0.05 wt% solution of polyethylenimine (PEI) in 2-methoxyethanol was spin-coated onto the ZnO layer and dried at 120 °C for 10 min. The PM6:PNDIS (1:0.6 wt/wt) blends were prepared in chlorobenzene (CB), mixed and stirred overnight at 85^{o}C in the glovebox. A mixture of 0.25% (v/v) of 1,8-diiodooctane (DIO) and 0.25% (v/v) of 1,8-octanedithiol (ODT) was added into the PM6:PNDIS blend solutions. Similarly, the PM6:PNDIBS (1:0.4 wt/wt) blends were prepared in chlorobenzene, mixed and stirred overnight at 85^{o}C in the glovebox. 0.5% (v/v) diphenyl ether (DPE) was added to the blend solution as a processing additive. For the sake of comparisons, the PBDB-T:PNDIS and PBDB-T:PNDIBS blends were prepared in the exact same conditions as the optimized PM6:PNDIS and PM6:PNDIBS blends, respectively. In case of device fabrication using co-solvents, the PM6:PNDIS (1:0.6 wt/wt) blends were prepared in a mixture of CB and 2-methyltetrahydrofuran (2-MeTHF) (CB:2-MeTHF) at the optimal ratio of 70:30 (v:v), mixed and stirred overnight at 65^{o}C in the glovebox. No processing additive was used when devices were processed from CB:2-MeTHF co-solvents. The blend solutions were

spin-coated at 1000 rpm for 50s, followed by thermal annealing at 110°C for 10 min in the Argon-filled glovebox. All the active layers had a thickness of 102 ± 3 nm. MoO_3 (0.5 nm) and Ag (100 nm) were thermally deposited onto the active layer. An aperture mask with area of 3.14 mm^2 was applied during measurements to define the illuminated device area. After evaporation of the electrode, the photovoltaic cells were tested under AM 1.5G solar illumination at 100 mW/cm^2 in ambient air by using a solar simulator (Model 16S, Solar Light Co., Philadelphia, PA) with a 200W Xenon Lamp Power Supply (Model XPS 200, Solar Light Co., Philadelphia, PA) calibrated by NREL certified Si photodiode (Model 1787-04, Hamamatsu Photonics K.K., Japan) and a HP4155A semiconductor parameter analyzer (Yokogawa Hewlett Packard, Japan). After the *J-V* measurements, the external quantum efficiency (EQE) spectra were measured by using a solar cell quantum efficiency measurement system (Model QEX10, PV Measurements, Inc., Boulder, CO) with a 2 mm^2 (2 mm × 1 mm) size masked incident light source and TF Mini Super measurement apparatus for multiple devices in a single substrate. The EQE system was calibrated with a Si photodiode before measurement.

Fabrication and Characterization of SCLC Devices. Current-voltage (*J-V*) characteristics of the space-charge limited current (SCLC) devices were measured by using a HP4155A semiconductor parameter analyzer (Yokogawa Hewlett-Packard, Tokyo). The carrier mobility was deduced by fitting the *J-V* curves to the Mott−Gurney equation,

$$J = \frac{9}{8}\varepsilon_0\varepsilon\mu\frac{V^2}{L^3}$$

where J is the current density, ε_0 is the permittivity of free space, ε is the relative permittivity, μ is the zero-field mobility, V is the applied voltage, L is the thickness of active layer.

The SCLC device structures for electron-only and hole-only were ITO/ZnO/PEI/Blend/LiF (1nm)/Al (100nm) and ITO/PEDOT: PSS/Blend/MoO_3 (7.5nm)/Ag (100nm), respectively. Each active layer of both neat and blend films was processed at the optimized all-PSC device conditions as described above and spin-coated at 1000 rpm for 50s and followed by thermal annealing at 110^{o}C for 10 min inside glovebox.

AFM Imaging. Atomic force microscopy (AFM) characterization of the surface morphology was done on the active layers of the actual polymer solar cells, used in the photovoltaic measurements, by using a Bruker Dimension scanning probe microscope (SPM) system.

2D-GIWAXS. Grazing incidence X-ray scattering (GIWAXS) experiments were conducted at the Japan Synchrotron Radiation Facility SPring-8 by using the beamlines BL46XU. Thin film samples of the neat donor polymer (PM6) and acceptor polymers (PNDIS and PNDIBS) were spin-coated on the top of glass substrates and annealed at 110 ℃ for 10 min. The binary blend films were prepared in the same manner as the actual all-PSC devices on ZnO/PEI-coated ITO substrates. The X-ray beam was monochromatized by a double-crystal Si(111) monochromator, and the X-ray energy in this experiment was 12.40 keV (λ = 0.1 nm). The angle of incident X-ray to sample surface was 0.12° with a Huber diffractometer. The scattered profile from the film sample was detected using an area detector (PILATUS 300K) for 1 s at room temperature, and the distance between the sample and detector was 175.0 mm. The crystal coherence length (L_c) of samples was determined by using the Scherrer equation: $L_c = 2\pi K/\Delta q$, where K is a shape factor (typically 0.89) and Δq is the full width at half-maximum (FWHM) of the diffraction peak. Here, the L_c (100) was obtained from the FWHM of the (100) diffraction peak in the-plane (q_{xy}) line cut.

2.1.3. Results and Discussion

2.1.3.1. Optical Properties and Electronic Structure.

The thin film absorption spectra of the donor polymer PM6 and the acceptor polymers PNDIS and PNDIBS are presented in Figure 2-1b. Two characteristics peaks at around 362 nm and 570 – 620 nm representing π-π* transition and intramolecular charge transfer (ICT) band, respectively, were observed in PM6 in agreement with prior reports.[46, 117] PNDIS exhibits two peaks at about 348 and 618 nm and an absorption onset (λ_{onset}) at around 740 nm corresponding to an optical bandgap ($E_g^{opt.}$) of 1.67 eV. PNDIBS has a clearly red-shifted absorption with π-π* and ICT peaks at 394 and 716 nm, respectively, and an λ_{onset} at 885 nm ($E_g^{opt.}$ = 1.40 eV). The red-shifted absorption of PNDIBS compared to PNDIS is due to the longer conjugation length as well as the effect of the stronger electron-donating nature of the biselenophene moiety on the ICT absorption band compared to the selenophene moiety in PNDIS. These thin film absorption spectra are in accord with previous reports.[13, 14, 19, 29]

The thin film and solution absorption spectra in neat 2-MeTHF and CB:2-MeTHF co-solvents are shown in Figures 2-1b and A-1b, respectively, since the CB:2-MeTHF co-solvents will also be used to fabricate all-PSC devices. We note that only the absorption profiles of PNDIS in the various co-solvents were collected and presented due to the limited solubility of PM6 and PNDIBS in 2-MeTHF. Although the thin film absorption spectra of PNDIS deposited from CB, 2-MeTHF, and CB:2-MeTHF were virtually similar (Figure 2-1b), their corresponding solution absorption spectra (Figure A-1b) showed distinct bathochromic shifts. The ICT band and the λ_{onset} of PNDIS in 2-MeTHF as well as in CB:2-MeTHF were red-shifted by about 42 nm relative to those in CB. Given that the dielectric constant (ε) of 2-MeTHF (ε = 6.97) is larger than of CB (ε = 5.62), the observed bathochromic shift of the absorption of PNDIS with increasing solvent polarity reflects the greater charge separation and ICT character in the

electronic ground state.[53, 118] Alternatively, the solution absorption spectra indicate that 2-MeTHF is a theta solvent for PNDIS, which means PNDIS chains would prefer to stay in 2-MeTHF phase and are likely to undergo conformational changes to become less coiled,[119, 120] and thereby increase the effective conjugated length. In this case, using a mixture of chlorobenzene and 2-methyltetrahydrofuran as co-solvents for device processing could enable independent tuning of the aggregation rates of PM6 and PNDIS. In particular, the PNDIS chains in the low boiling point solvent, 2-MeTHF (T_b = 80.2°C), undergo a quick film-forming kinetics to form relatively pure domains with smaller domain sizes due to the fast evaporation rate of 2-MeTHF whereas the PM6 chains in the higher boiling point solvent, CB (T_b = 132°C), slowly aggregate to form its own domains. As a result, the aggregation rates of PM6 and PNDIS can be independently tailored via their differential solubility in the CB:2-MeTHF co-solvent and the differential boiling point of the solvents. Use of such a co-solvent system thus eliminates the need for processing additives in solution-based active layer fabrication.

The LUMO and HOMO energy levels of the component polymers shown in Figure 2-1c were measured using cyclic voltammetry, and the resulting oxidation and reduction cyclic voltammograms are shown in Figure A-2. The LUMO and HOMO energy levels of the donor polymer PM6 are found to be -3.48 eV and -5.48 eV, respectively, which are consistent with previous report.[117] The LUMO energy levels of the acceptor polymers, PNDIS and PNDIBS, are essentially identical at -3.87 eV and -3.89 eV, respectively. The HOMO energy level of PNDIBS (HOMO = -5.94 eV) is higher lying than that of PNDIS (HOMO = -6.11 eV) mainly due to the stronger electron-donating nature of the biselenophene unit relative to the selenophene unit, which are also in good agreement with previous reports.[14, 29] As Figure 2-1c suggests, the driving

forces for exciton dissociation (ΔHOMO and ΔLUMO) are comparable between PM6:PNDIS blends and PM6:PNDIBS blends.

2.1.3.2. Photovoltaic Properties.

The photovoltaic properties of the binary PM6:PNDIS and PM6:PNDIBS blends were investigated by fabricating and characterizing all-PSCs with an inverted device architecture: ITO/ZnO/PEI/Blend/MoO_3/Ag, where polyethyleneimine (PEI) is used as the cathode buffer layer.[121] Thin film absorption spectra and the energy levels of the blend components (PM6, PNDIS, and PNDIBS) are shown in Figures 2-1b and 2-1c, respectively. The PM6:PNDIS and PM6:PNDIBS all-PSC devices were fully optimized by varying the donor : acceptor (D:A) ratio, choice of solvent additives, and thermal annealing at different temperatures (Tables A-2 and A-3). The optimal processing conditions for the PM6:PNDIS blends included spin-coating the chlorobenzene blend solution of 1:0.6 (wt:wt) D:A ratio with a mixture of solvent processing additives (0.25% (v/v) 1,8-octanedithiol (ODT) and 0.25% (v/v) 1,8-diiodooctane (DIO)) followed by thermal annealing at 110^{o}C for 10 min in an Argon-filled glovebox. The PM6:PNDIBS blends were optimized separately by spin-coating the chlorobenzene blend solution of 1:0.4 (wt:wt) D:A ratio with 0.5% (v/v) diphenyl ether (DPE) solvent processing additive followed by thermal annealing at 110^{o}C for 10 min in the glovebox. The *J-V* curves and the EQE spectra of optimized PM6:PNDIS, PM6:PNDIBS all-PSC devices are presented in Figure 2-2, and the corresponding photovoltaic parameters are summarized in Table 2-1. The PBDB-T:PNDIS devices and PBDB-T:PNDIBS devices were fabricated at the exact same optimal processing conditions for the PM6:PNDIS devices and PM6:PNDIBS devices, respectively. The *J-V* curves and the EQE spectra of PBDB-T:PNDIS and PBDB-T:PNDIBS all-

PSC devices are shown in Figure A-3, and the photovoltaic parameters are summarized in Table A-1.

All-PSC devices fabricated from the PM6:PNDIS binary blend at 1:0.6 (wt:wt) D:A ratio had an average PCE of 7.55% with a J_{sc} of 11.89 mA/cm^2, a V_{oc} of 0.962 V, and a FF of 0.66 (Table A-2). Through screening of processing additives, we found that addition of both 0.25% (v/v) of DIO and 0.25% (v/v) of ODT to the chlorobenzene solvent resulted in significant enhancement in the photovoltaic parameters (J_{sc}, FF, and PCE) (Table A-2). The combination of 0.25% ODT and 0.25% DIO as solvent additives was found to be more effective than using a single solvent additive mainly due to the suppressed aggregation and the optimal domain sizes as evidenced by the smoother surface of the blend films from AFM images (Figure A-4a) and the increased spatial frequency from the power spectral density (Figure A-4b). Although the V_{oc} was unaffected by the solvent additives (V_{oc} = 0.97 V), the J_{sc} improved from 11.89 mA/cm^2 to 13.45 mA/cm^2 while the FF increased from 0.66 to 0.70. As a result, the optimized PM6:PNDIS all-PSC devices exhibited a maximum PCE of 9.07% (Table 2-1). This efficiency (9.1%) seen in PM6:PNDIS blends is the highest observed so far for this acceptor polymer in all-PSC devices.[13, 14, 19]

Table 2-1. Photovoltaic Properties of Optimized PM6:PNDIS and PM6:PNDIBS. All Active Layers were Thermally Annealed at 110^{o}c for 10 min. Reproduced in part with permission from Ref.[44] Copyright 2020 American Chemical Society.

Blend	J_{sc} (mA/cm^2)	V_{oc} (V)	FF	PCE$_{ave}$[(a)] (%)	$J_{sc}^{calc.}$ (mA/cm^2)
PM6:PNDIS	13.45 (13.14±0.13)	0.967 (0.96±0. 014)	0.70 (0.68±0. 02)	9.07 (8.63±0.36)	13.25
PM6:PNDIBS	6.72 (6.32±0.18)	0.925 (0.93±0. 005)	0.50 (0.50±0. 01)	3.11 (2.93±0.08)	6.52

(a) Average of over 12 devices.

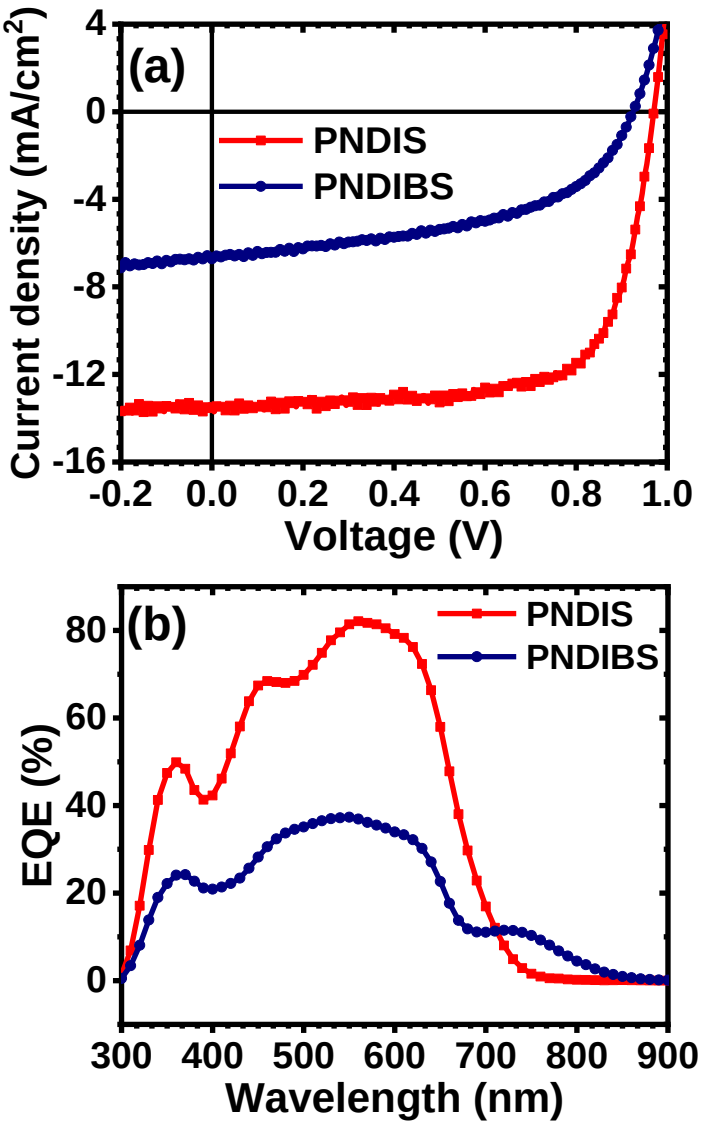

Figure 2-2. (a) *J-V* curves for the optimized PM6:PNDIS and PM6:PNDIBS devices processed from chlorobenzene. (b) EQE spectra for the optimized PM6:PNDIS and PM6:PNDIBS devices processed from chlorobenzene. Reproduced with permission from Ref.[44] Copyright 2020 American Chemical Society.

The similarly optimized PM6:PNDIBS blend devices have rather poor photovoltaic properties. The best performing PM6:PNDIBS blend devices had a PCE of 3.11% with a low J_{sc} of 6.72 mA/cm^2, a V_{oc} of 0.925V, and an FF of 0.50 (Table 2-1). While the marginal drop in V_{oc} is most likely due to the lower-lying LUMO energy level of PNDIBS compared to PNDIS (Figure 2-1c), the markedly inferior J_{sc} and FF can be attributed to the suboptimal morphology of

the PM6:PNDIBS blends, which likely exaggerated charge recombination and inhibited efficient charge transport. Unlike the PM6:PNDIS blends, the use of solvent additives in the processing of PM6:PNDIBS blends led to only a marginal improvement in the photovoltaic properties (Table A-3); for example, raising the PCE from 3.11% to 3.36-3.47% by using either 0.5% (v/v) DPE or DIO. This lack of effectiveness of processing additives suggests that the morphology of PM6:PNDIBS blends is trapped in a state inaccessible to fine-tuning by various optimization conditions.

The photovoltaic properties of the PM6:PNDIS and PM6:PNDIBS devices are staggeringly different from those of the all-PSC devices fabricated from the non-fluorinated donor polymer, PBDB-T. For the sake of comparison, the PBDB-T:PNDIS and PBDB-T:PNDIBS devices were fabricated at the exact optimized conditions of the PM6:PNDIS and PM6:PNDIBS devices, respectively. The photovoltaic parameters are summarized in Table A-1 whereas the *J*-*V* curves and the EQE spectra are shown in Figure A-3. The PBDB-T:PNDIS devices exhibited an average J_{sc} of 14.8 mA/cm^2, an average V_{oc} of 0.827 V, and an average FF of 0.61, leading to an average PCE of 7.5%. The PBDB-T:PNDIBS all-PSCs showed comparable device performance relative to the PBDB-T:PNDIS devices. In particular, the J_{sc} and V_{oc} were simultaneously enhanced (J_{sc} = 15.6 mA/cm^2, V_{oc} = 0.85 V) while the FF was slightly reduced to 0.58; thus, the best performing PBDB-T:PNDIBS had a PCE of 7.9%. We note that the photovoltaic parameters of PBDB-T:PNDIBS all-PSCs are slightly lower than our previous report[29] due to the differences in processing conditions. Nevertheless, the observed substantial difference in the photovoltaic properties of the fluorinated donor polymer PM6 compared to PBDB-T in all-PSCs is fundamentally interesting. The remaining of the manuscript will address

the underlying reasons that drive the deviations in the device performance of PM6:PNDIS and PM6:PNDIBS blends.

We also explored an alternative simpler optimization strategy to the device fabrication process by using a co-solvent system consisting of chlorobenzene and 2-methyltetrahydrofuran at various ratios (Table A-4). In addition, we used the CB:2-MeTHF solvent system to examine the effects of the active layer thickness on the photovoltaic properties of the PM6:PNDIS all-PSC devices. In terms of the overall photovoltaic performance, the CB:2-MeTHF co-solvent processed optimized PM6:PNDIS devices (Table 2-2) are quite comparable to those processed with the aid of processing additives (Table 2-1). The *J-V* curves for PM6:PNDIS devices processed from CB:2-MeTHF co-solvents at various active layer thicknesses are presented in Figure 2-3a. All-PSC devices fabricated from the optimized CB:2-MeTHF co-solvents (Table A-4) showed an average PCE of 8.41% with a high J_{sc} of 14.13 mA/cm^2, a V_{oc} of 0.963 V, and an FF of 0.62 (Table 2-2). The maximum PCE of 8.71% (J_{sc} = 14.72 mA/cm^2, V_{oc} = 0.96 V, and FF = 0.61) obtained for a 200-nm active layer is quite comparable to the 9.07% achieved with processing additives. These results were achieved by utilizing the difference in solubility of the donor and the acceptor polymer in 2-MeTHF to independently tune the aggregation rates of PM6 and PNDIS in the blend, enabling the self-organization of the polymer blends into optimal nanoscale morphology without using solvent additives. We conclude that that the PM6:PNDIS blend system is highly versatile, insensitive to processing methods, and is capable of yielding highly efficient all-PSC devices.

The dependencies of the photovoltaic parameters (J_{sc}, V_{oc}, FF, and PCE) on the active layer thicknesses are shown in Figures 2-3c – 2-3f. The V_{oc} is observed to be relatively constant at around 0.96 – 0.97V across all thicknesses whereas the FF progressively decreases from 0.63

to 0.58 as the thickness increased from 100 to 300 nm. The photocurrent density reaches a maximum value of 14.72 mA/cm^2 at 200 nm (Figure 2-3c). The maximum PCE peaks at 8.71% at 200 nm and decreases to 8.20% at 300 nm (Table 2-2 and Figure 2-3f). The minimal changes of the PCE of PM6:PNDIS all-PSC devices with the active layer thickness clearly indicate that this blend system is insensitive to both the processing methods and the film thicknesses, which are highly desirable for future commercial applications of all-PSCs.

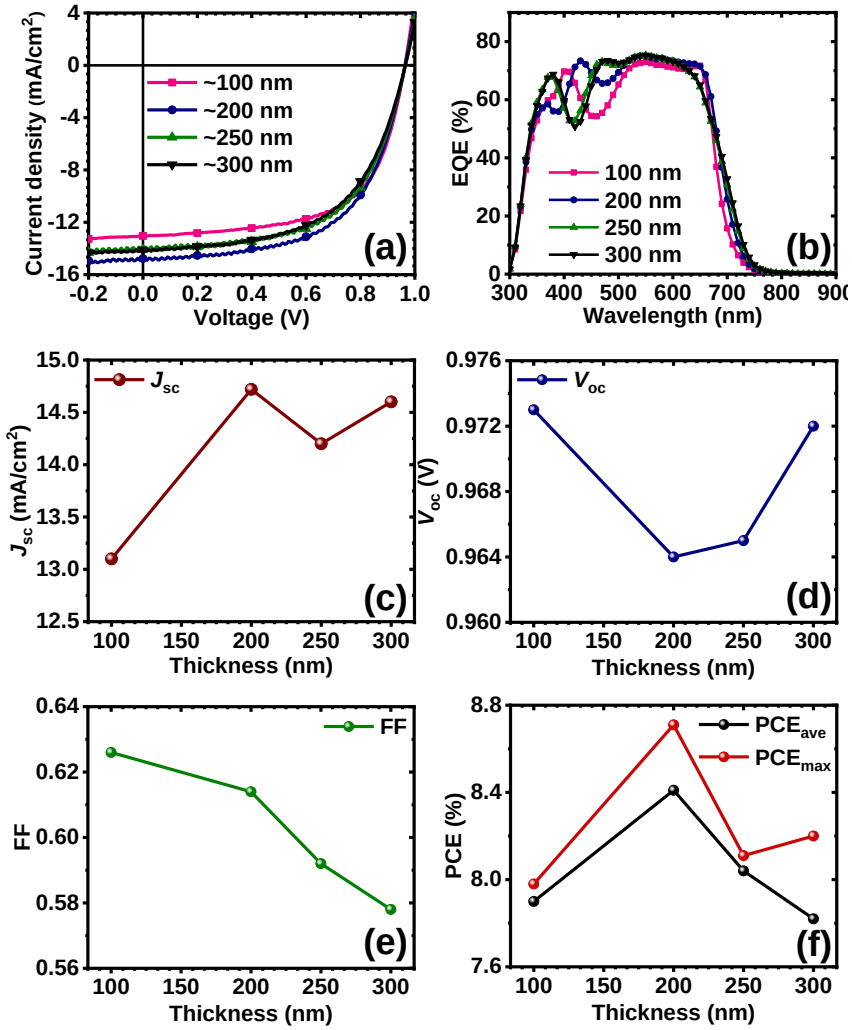

Figure 2-3. The optimized PM6:PNDIS devices processed from CB:2-MeTHF at various active layer thicknesses: (a) *J*-*V* curves; (b) EQE spectra; (c-f) J_{sc}, V_{oc}, FF, and PCE as a function of the active layer thickness. Reproduced with permission from Ref.[44] Copyright 2020 American Chemical Society.

Table 2-2. Photovoltaic Properties of Optimized PM6:PNDIS Devices Processed at the Optimized CB:2-MeTHF Co-solvents Without Using a Processing Solvent Additive at Various Active Layer Thicknesses. All Active Layers were Thermally Annealed at 110°C for 10 min. Reproduced in part with permission from Ref.[44] Copyright 2020 American Chemical Society.

Blend	J_{sc} (mA/cm^2)	V_{oc} (V)	FF	PCE$_{ave}$[(a)] (%)	$J_{sc}^{calc.}$ (mA/cm^2)
100 nm	13.10 (13.04±0.13)	0.973 (0.964±0.005)	0.626 (0.629±0.004)	7.98 (7.90±0.08)	13.05
200 nm	14.72 (14.13±0.77)	0.964 (0.963±0. 001)	0.614 (0.619±0.028)	8.71 (8.41±0.17)	14.08
250 nm	14.20 (14.09±0.25)	0.965 (0.965±0. 001)	0.592 (0.591±0.004)	8.11 (8.04±0.10)	13.96
300 nm	14.60 (14.12±0.23)	0.972 (0.965±0. 004)	0.578 (0.574±0.006)	8.20 (7.82±0.21)	14.03

[(a)] Average of 8 devices.

The effect of fluorination of the donor polymer on optical bandgap energy loss (E_{loss} = $E_g^{opt.}$ – eV_{oc}) can be examined by considering the present results on PM6:PNDIBS and PM6:PNDIS in comparison to prior results on the non-fluorinated donor polymer PBDB-T.[29] From the $E_g^{opt.}$ values for PM6:PNDIS (1.67 eV) and PM6:PNDIBS (1.40 eV) blends and the observed V_{oc} values (Table 2-2), we obtain E_{loss} values of 0.70 eV for PM6:PNDIS and 0.475 eV for PM6:PNDIBS all-PSCs. Although the fluorinated donor polymer leads to a slight reduction (0.14 eV) from the PBDB-T blend, the observed E_{loss} for PM6:PNDIS is still quite large.[122, 123] The PNDIBS all-PSCs based on the non-fluorinated PBDB-T were found to combine E_{loss} of 0.55 eV with a moderate PCE of 7.9%. Thus, although fluorination results in the expected reduction in E_{loss} and enhancement of V_{oc} in PM6:PNDIBS, there is simultaneously an unexpected dramatic reduction in the photovoltaic efficiency from 7.9% to 3.1%. The possible sources of this unexpected huge effect of fluorination of the donor polymer on the performance of all-PSCs include blend morphology, blend photophysics, and charge transport, which will be examined later.

The EQE spectra of the optimized PM6:PNDIS and PM6:PNDIBS devices processed from CB as well as those processed from CB:2-MeTHF at various thicknesses are shown in Figure 2-2b and Figure 2-3b, respectively. The photo-response of PM6:PNDIS devices spanned from 740 nm to 300 nm and rose to a maximum EQE of 82% in the 540 – 590 nm region (Figure 2-2b). Although it covers a much broader range from 300 nm to 840 nm, the EQE spectrum of the optimal PM6:PNDIBS devices showed much lower EQE values almost across the entire spectrum with a maximum of 37% in the 520 – 570 nm region (Figure 2-2b). The broad photo-response over the entire ranges 300 – 840 nm for PM6:PNDIBS and 300 – 740 nm for PM6:PNDIS blends indicates efficient photoinduced electron and hole transfer.[124] In the case of PM6:PNDIS devices processed from CB:2-MeTHF co-solvent at various active layer thicknesses (Figure 2-3b), they showed lower maximum EQE values of around 72 – 75% at 540 – 550 nm compared to those processed from CB. However, CB:2-MeTHF processed devices exhibited flatter EQE responses over a broad range from 450 nm to 650 nm (Figure 2-3b) and thus resulted in a slightly higher J_{sc} as observed in Table 2-2. The variations of the EQE spectra at certain wavelengths with increasing active layer thickness have been observed in prior reports ranging from fullerene-based devices to all-polymer solar cells and non-fullerene organic solar cells;[125-129] these variations can be rationalized by the inhomogeneous blend composition distribution in thicker films and optical interferences.[130-132] The corresponding photocurrent obtained from integration of the EQE spectra for PM6:PNDIS and PM6:PNDIBS blends were 13.25 mA/cm^2 and 6.52 mA/cm^2, respectively, which matched well with the values obtained from the *J*-*V* measurement (Table 2-1) within 2-4% error. The calculated J_{sc} from the EQE spectra of PM6:PNDIS based devices fabricated from CB:2-MeTHF co-solvents at various thicknesses were similarly in good agreement with the *J*-*V* measurements.

2.1.3.3. Charge Photogeneration and Charge Recombination.

To elucidate the striking difference between the photovoltaic performance of PM6:PNDIS and PM6:PNDBS devices, the photoinduced charge generation rate and charge collection behavior of the optimized devices were characterized by measuring the photocurrent current ($J_{ph} = J_{illuminated} - J_{dark}$) as a function of effective voltage ($V_{eff} = V_{bias} - V_{applied}$). As shown in Figure 2-4a, the optimized PM6:PNDIS devices exhibited a field-independent charge photogeneration rate beyond 0.5V, which is consistent with previously observed systems that have FF higher than 0.65.[133-135] This result suggests that nearly all generated excitons effectively diffused to the donor/acceptor interface to form exciplexes[136] and instantaneously dissociated into free charges that are collected at the two electrodes and thereby effectively suppressing geminate recombination.[133] In contrast, the PM6:PNDIBS devices exhibited increasing photocurrent with increasing electric field, suggesting significant electron-hole pair recombination. As a result, the charge photogeneration rate of PM6:PNDIS (8.58×10^{27} $m^{-3}s^{-1}$) was found to be 1.3-fold higher than that of PM6:PNDIBS (6.40×10^{27} $m^{-3}s^{-1}$). The charge collection probability (*P(E,T)*) at short-circuit condition was also calculated to be 99.1% and 65.5% for PM6:PNDIS and PM6:PNDIBS, respectively. The superior and near unity *P(E,T)* observed in PM6:PNDIS devices suggest that almost all dissociated charges were collected at the two electrodes, which is in agreement with the high J_{sc} and FF.

We also performed charge recombination analysis by characterizing the light-intensity dependence of J_{sc} and V_{oc}. The relationship between J_{sc} and the incident light intensity (P_{light}) can be generally described as $J_{sc} \propto P_{light}^{\alpha}$, where α represents the degree of bimolecular recombination.[133, 134] The value of α for the optimized PM6:PNDIBS blends ($\alpha = 0.95$) deviated slightly from unity as shown in Figure 2-4b suggesting that some degree of bimolecular

recombination can be expected in these devices. However, the optimized PM6:PNDIS devices exhibited an α value of 1.01 indicative of highly suppressed bimolecular recombination, which is in good accordance with the observed higher J_{sc} and FF. The relationship between V_{oc} and P_{light} which can be generalized as $V_{oc} \propto s \times \ln(P_{light})$. The proportional coefficient s usually varies between 1 and 2 representing either a dominating bimolecular recombination (s = 1kT/q) or a preferable trap-assisted recombination (s = 2kT/q).[133] The data in Figure 2-4c show that PM6:PNDIS devices follow a trap-assisted recombination (s = 1.48 kT/q) whereas PM6:PNDIBS devices have a s coefficient of 1.21kT/q which suggests that bimolecular recombination governs its charge recombination kinetics.

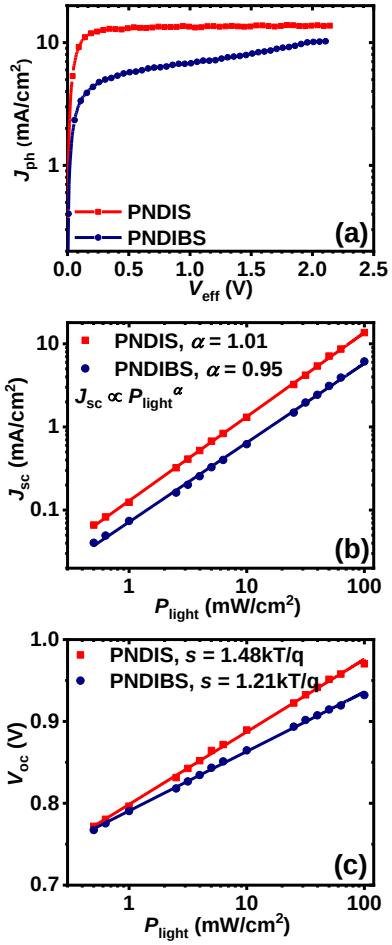

Figure 2-4. (a) J_{ph}-V_{eff} curves, (b) J_{sc} dependency on incident light intensity , and (c) V_{oc} dependency on incident light intensity for the optimized PM6:PNDIS and PM6:PNDIBS blend devices. All blends were processed under optimized conditions from chlorobenzene. Reproduced with permission from Ref.[44] Copyright 2020 American Chemical Society.

2.1.3.4. Charge Transport Properties.

We investigated the charge transport properties of PM6:PNDIS and PM6:PNDIBS blend films and neat films of the individual components by the space-charge limited current (SCLC) method. Single-carrier devices were fabricated in the following device architectures: ITO/PEDOT:PSS/Blend/MoO_3/Ag for hole-only devices and ITO/ZnO/PEI/Blend/LiF/Al for electron-only devices. The resulting *J-V* curves were fitted to the Mott-Gurney equation to extract the charge carrier mobilities. The *J-V* curves and their fit lines for neat and blend films are shown in Figures A-6 and A-7, respectively, while the carrier mobilities are summarized in Table 2-3.

The neat films of the donor polymer PM6 showed a relatively high hole mobility (μ_h) of 1.2 x 10^{-4} cm^2/Vs, which is in agreement with prior reports.[36, 39, 46] The electron mobility (μ_e) of neat films of PNDIS and PNDIBS was found to be 1.24 x 10^{-4} cm^2/Vs and 2.13 x 10^{-4} cm^2/Vs, respectively, which are also in agreement with reported values.[13, 14, 19, 29] The slightly higher electron mobility in neat PNDIBS films can be explained by its higher crystallinity compared to PNDIS as evidenced by GIWAXS and AFM results to be discussed below. In PM6:PNDIBS blend films, μ_h and μ_e were 1.98 x 10^{-4} cm^2/Vs and 7.28 x 10^{-5} cm^2/Vs, respectively. Compared to the PM6:PNDIBS blends, the hole mobility of the PM6:PNDIS blends increased by 1.6-fold to 3.25 x 10^{-4} cm^2/Vs; however, the electron mobility was lowered to 1.89 x 10^{-5} cm^2/Vs. The asymmetric charge transport observed in PM6:PNDIS indicated that further optimization to improve the device performance is feasible.

Effects of the co-solvent processing on the bulk charge carrier mobilities of PM6:PNDIS blends were also examined. The μ_h was found to increase from 3.25 x 10^{-4} cm^2/Vs when processed from CB to 4.11 x 10^{-4} cm^2/Vs when processed from the CB:2-MeTHF co-solvents. Similarly, the bulk μ_e for blends processed from CB:2-MeTHF was significantly increased by almost an order of magnitude to 1.36 x 10^{-4} cm^2/Vs. As explained earlier, the solubility differences of the blend components in the co-solvent system (CB:2-MeTHF) and the boiling point differences of the two solvents enable independent tuning of the aggregation rates and thereby, higher domain purity can be achieved as evidenced by the increased surface roughness observed in AFM images (Figure A-5). Thus, the observed higher hole and electron mobilities for blends processed from the CB:2-MeTHF co-solvent can be rationalized by the optimal blend morphology featuring higher domain purity and optimal domain sizes, which is consistent to previous study demonstrating enhanced charge carrier mobility for blends processed from 2-MeTHF.[137] Furthermore, the observed higher hole and electron mobilities for blends processed via the CB:2-MeTHF co-solvent technique are in good agreement with the efficient photovoltaic device performance even for thick film active layers.

Table 2-3. Space-Charge Limited Current Electron Mobility (μ_e) and Hole Mobility (μ_h) of Neat Films of PM6, PNDIS, and PNDIBS and Blend Films of PM6:PNDIS and PM6:PNDIBS. All Active Layers were Processed at Optimal Conditions. Reproduced with permission from Ref.[44] Copyright 2020 American Chemical Society.

Neat or Blend Films	μ_e (cm^2/Vs)	μ_h (cm^2/Vs)	μ_h/μ_e
PM6	-	1.20 x 10^{-4}	-
PNDIS	1.24 x 10^{-4}	-	-
PNDIBS	2.13 x 10^{-4}	-	-
PM6:PNDIS (CB)	1.89 x 10^{-5}	3.25 x 10^{-4}	17.2
PM6:PNDIBS (CB)	7.28 x 10^{-5}	1.98 x 10^{-4}	2.72
PM6:PNDIS (CB:2-MeTHF)	1.36 x 10^{-4}	4.11 x 10^{-4}	3.03

2.1.3.5. Vertical Phase Stratification.

Interestingly, we found that the electron mobility of PM6:PNDIS blends varied by orders of magnitude depending on the direction of bias voltage. As shown in Figure 2-5a, the PM6:PNDIS electron-only devices exhibited asymmetric *J-V* behavior under positive and negative bias, which was not observed in the PM6:PNDIBS devices (Figures 2-5b and 2-5d). Observation of such asymmetric electron injection behavior has previously been attributed to the vertical phase stratification of the active layer.[138] In the present case, vertical phase segregation in the blend means that PNDIS was buried near the ZnO/PEI interface and PM6 accumulated near the top surfaces, and thus, forming a significant energetic barrier at the Al electrode and inhibiting electron injection into the active layer (Figure 2-5c).[138]

Additional characterizations using time-of-flight secondary ion mass spectroscopy (TOF-SIMs) and contact angle measurements further confirmed a greater degree of vertical phase separation in the PM6:PNDIS blends. Figure 2-6 shows the vertical composition distribution of F^- and CN^-, which are representative of the donor polymer (PM6) and the acceptor polymers (PNDIS and PNDIBS), respectively, from the top air surface to the bottom ZnO/PEI interface. The profile of CN^- in the PM6:PNDIS blends clearly showed a gradient with increasing concentration towards the ZnO/PEI interface (Figure 2-6a), whereas the concentration of CN^- in the PM6:PNDIBS blends remained constant across the active layer thickness (Figure 2-6b). Moreover, the profile of F^- in the PM6:PNDIS blends exhibited a sharp decline as $t/t_{\text{active layer}}$ approached unity (Figure 2-6a), which indicated that the donor polymer PM6 was depleted at the cathode interface. On the other hand, as shown in Figure 2-6b, the concentration of F^- in the PM6:PNDIBS blends stayed nearly unchanged throughout the active layer thickness. These results strongly suggest that a greater degree of vertical phase separation exists in the

PM6:PNDIS blends, where the acceptor polymer concentration gradually increases and accumulates at the cathode interface. This result is in agreement with the asymmetric *J-V* behavior under different voltage bias direction.

The surface energy of the donor polymer and the acceptor polymers and the Flory-Huggins interaction parameters of the respective blends were investigated and are summarized in Table A-5 via contact angle measurements on their neat films with diiodomethane and water as the wetting liquids shown in Figure A-8. As summarized in Table A-5, the surface energy (γ) of the donor polymer PM6 was found to be 37.05 mN/m which is comparable to that of PNDIBS (γ = 37.46 mN/m), suggesting a homogenous blend distribution across the active layer thickness in very good agreement with the *J-V* behaviors and the TOF-SIMs analysis. The estimated Flory-Huggins interaction parameter was also calculated based on the empirical equation $\chi_{donor,acceptor} = K\left(\sqrt{\gamma_{donor}} - \sqrt{\gamma_{donor}}\right)^2$, where K is a constant. A small $\chi_{\text{donor, acceptor}}$ value means a highly miscible blends while a large $\chi_{\text{donor, acceptor}}$ value suggests phase separation in blend films.[30] The $\chi_{\text{donor, acceptor}}$ value for the PM6:PNDIBS blends was found to be extremely low at 0.00113K (Table A-5) suggesting excessively miscible blends, which would be detrimental to domain purity. As a result, the PM6:PNDIBS devices suffered from poor charge photogeneration and significant charge recombination. On the other hand, the higher surface energy of PNDIS (γ = 39.08 mN/m) (Table A-5) compared to PM6 indicated that the donor polymer PM6 would migrate towards the air interface while the acceptor polymer PNDIS would be preferentially buried at the bottom interface.[139] The $\chi_{\text{donor, acceptor}}$ value of the PM6:PNDIS blends increased over 20-fold compared to that of the PM6:PNDIBS blends, suggesting that optimal blend miscibility was achieved and thereby, enhancing the domain purity. The results of these characterization techniques collectively show that there is a greater degree of vertical phase

separation and better domain purity in the PM6:PNDIS blends, which is beneficial for charge extraction and suppression of bimolecular charge recombination. This result is in excellent agreement with the near unity charge collection probability and the negligible charge recombination, leading to the observed higher J_{sc} and FF in the PM6:PNDIS all-PSCs.[138, 140, 141]

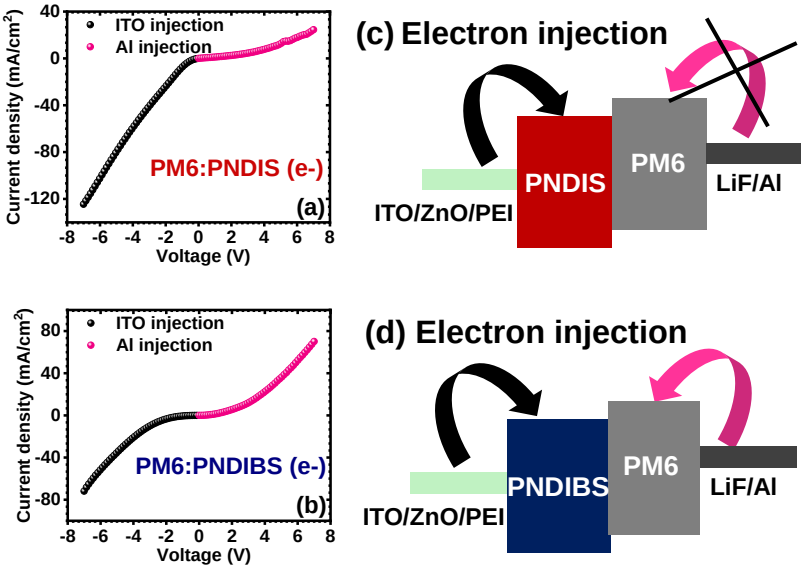

Figure 2-5. (a) *J-V* curves for electron-only SCLC PM6:PNDIS devices under positive and negative bias. (b) *J-V* curves for electron-only SCLC PM6:PNDIBS devices under positive and negative bias. (c) Schematics for electron injection in PM6:PNDIS devices under positive and negative bias. (d) Schematics for electron injection in PM6:PNDIBS devices under positive and negative bias. All blends were processed under optimized conditions from chlorobenzene. Reproduced with permission from Ref.[44] Copyright 2020 American Chemical Society.

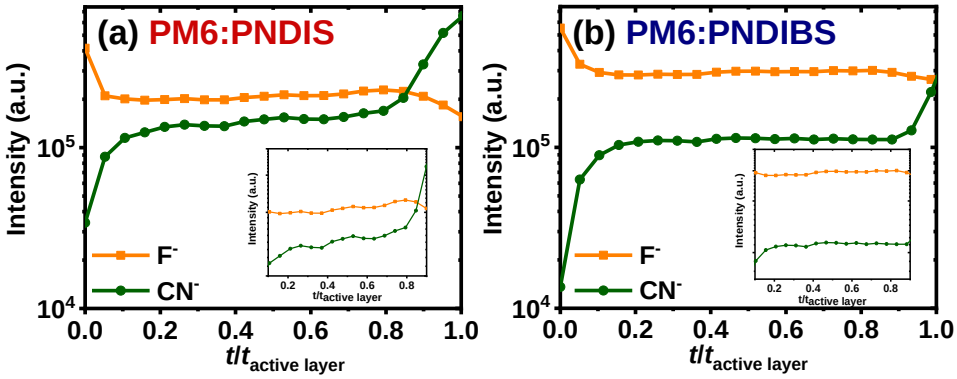

Figure 2-6. (a) TOF-SIM profiles of F^- and CN^- for PM6:PNDIS devices across the active layer thickness. (b) TOF-SIM profiles of F^- and CN^- for PM6:PNDIBS devices across the active layer

thickness. All blends were processed under the optimized conditions from chlorobenzene. Reproduced with permission from Ref.[44] Copyright 2020 American Chemical Society.

2.1.3.6. Surface and Bulk Morphology.

The surface morphology of neat and blend films was investigated by atomic force microscopy (AFM) imaging (Figures 2-7 and A-9). Although neat films of both of the acceptors showed relatively smooth surfaces (R_q ~ 1.1 nm), neat films of PNDIS showed a rather amorphous surface with no distinct features while neat films of PNDIBS exhibited homogenous fibrillar structures indicative of the highly crystalline nature of this polymer (Figure A-9).[29] Despite the clear differences in the surface morphology of neat PNDIS and PNDIBS films, their blend films (PM6:PNDIS and PM6:PNDIBS) showed similar morphology with distinctive needle-like features with comparable surface roughness (R_q ~ 2 nm) and domain size (~ 22 – 25 nm) (Figure 2-7).

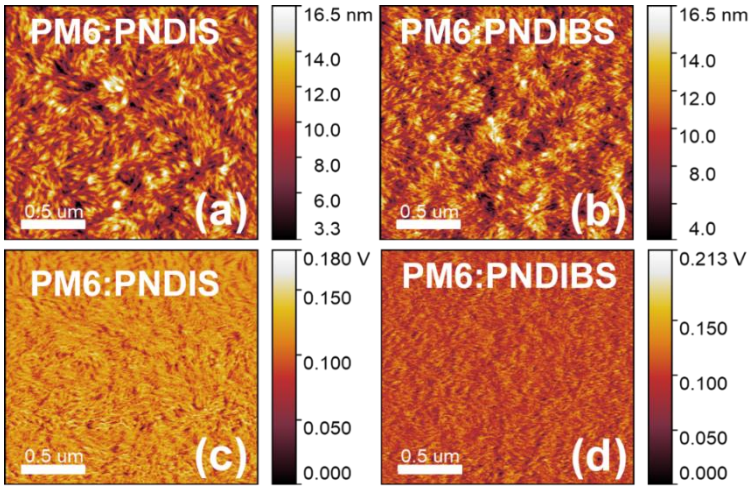

Figure 2-7. AFM height (a, b) and phase (c, d) images (2 μm x 2 μm) of the surfaces of PM6:PNDIS (a, c) and PM6:PNDIBS (b, d) blend films processed from optimized conditions in chlorobenzene. The scale bars are 500 nm. Reproduced with permission from Ref.[44] Copyright 2020 American Chemical Society.

To gain more insights into the bulk morphology of the blend films, 2D-grazing incident wide-angle X-ray scattering (2D-GIWAXS) measurements were carried out on both the neat films and blend films. The 2D-GIWAXS images and the corresponding line cuts for the neat donor and acceptor films are presented in Figure A-10, while those of the blend films are shown in Figure 2-8. The peak positions as well as the *d*-spacings for both the neat and blend films are summarized in Table A-6. The neat films of donor polymer PM6 exhibit distinct (100) diffraction peaks in both the in-plane (IP) and the out-of-plane (OOP) directions at around 0.30 $Å^{-1}$ and 0.33 $Å^{-1}$ (Figures A-10d and A-10e), which corresponds to a *d*-spacing of 19.04 – 20.94 Å, respectively (Table A-6). The (010) peaks were also present in both IP and OOP directions of neat PM6 films, centering at 1.68 – 1.71 $Å^{-1}$ (Figure A-10d and A-10e) with a *d*-spacing of 3.67 – 3.74 Å. The pronounced (100) and (010) diffraction peaks in both the IP and the OOP directions indicate the coexistence of both *face-on* and *edge-on* molecular orientations in neat PM6 films, which is consistent with previous reports.[46]

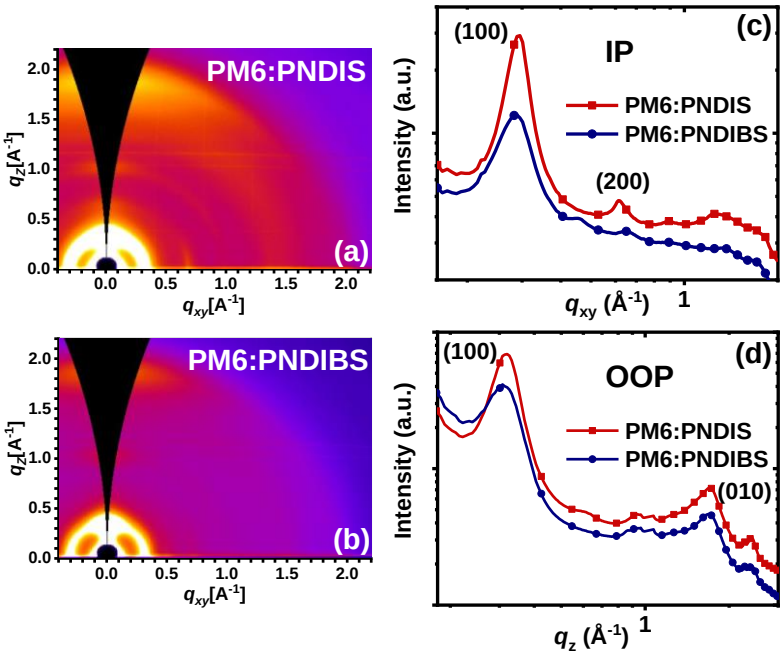

Figure 2-8. 2D-GIWAXS patterns of (a) PM6:PNDIS blend film and PM6:PNDIBS blend film. (b) In-plane (IP) and out-of-plane (OOP) line-cuts GIWAXS patterns for PM6:PNDIS and PM6:PNDIBS blend films. Reproduced with permission from Ref.[44] Copyright 2020 American Chemical Society.

Neat films of PNDIS and PNDIBS had intense (100) diffraction peaks in the IP direction at q_{xy} of 0.29 and 0.26 $Å^{-1}$, respectively, corresponding to *d*-spacings of 21.67 Å and 24.17 Å (Table A-6). The larger lamellar distance observed in neat PNDIBS films can be attributed to its longer 2-octyldodecyl side chains relative to the 2-hexyldecyl side chains in PNDIS. These lamellar packing distances in both PNDIS and PNDIBS are significantly shorter than expected from their alkyl chain lengths, clearly indicating interdigitation of the alkyl side chains between adjacent polymer backbones.[142] Higher order reflections of the lamellar packings were also present in the neat acceptor polymer films as evidenced by the (200) peaks in the IP direction (Figure A-10b). Pronounced (010) peaks in the OOP direction were also observed in both PNDIS and PNDIBS neat films (q_z = 1.57 – 1.58 $Å^{-1}$) with a π- π stacking distance of 3.98 – 4.00 Å (Table A-6). Compared to PNDIS, PNDIBS exhibited slightly broader and more intense (100) and (010) peaks in the IP and OOP directions, respectively. While PNDIBS had a rather weak (100) peak in the OOP direction, PNDIS exhibited a more pronounced (100) diffraction peak at 0.29 $Å^{-1}$. These observations collectively suggested that PNDIBS predominantly adopted *face-on* molecular orientation while PNDIS exhibited mixed *face-on* and *edge-on* populations.

In the blend films, the (100) peaks in the OOP direction, which mainly originated from the PM6 donor polymer, became sharper, more intense, and shifted to a lower q_z value (q_z = 0.31 – 0.32 $Å^{-1}$) that lied between the q_z values of the donor and the acceptor polymers (Table A-6); thereby suggesting well-mixed blends. Pronounced (100) diffraction peaks in the IP direction were also observed (q_{xy} = 0.29 $Å^{-1}$) in both PM6:PDNIS and PM6:PNDIBS blends. Moreover,

the lamellar *face-on* (200) ordering peaks were preserved in PM6:PNDIS blend but disappeared in PM6:PNDIBS blend (Figure 2-8c). The crystal coherence length (L_c) calculated using Scherrer equation was found to be 10.5 nm and 8.1 nm for PM6:PNDIS and PM6:PNDIBS blends, respectively. The higher L_c values and the presence of highly ordered lamellar peaks observed in PM6:PDNIS blends indicated that PNDIS retained its crystallinity upon blending with the donor polymer PM6 while the crystallinity of PNDIBS decreased in blend films. Moreover, the L_c of PM6:PNDIS blends (10.5 nm) is comparable to the typical exciton diffusion length[143, 144] enabling highly efficient exciton diffusion and charge photogeneration as explained earlier. Compared to the neat acceptor polymer films, the (010) peaks in the OOP direction shifted to higher q_z values of 1.69 $Å^{-1}$ for PM6:PNDIBS blends and 1.71 $Å^{-1}$ for PM6:PNDIS blends. The observation of sharp and intense (100) and (010) peaks in the IP and OOP directions, respectively, in the PM6:PNDIS blends clearly show that the polymer chains exhibit preferential *face-on* molecular orientation in the blends, which is favorable for charge transport across the electrical contacts.

2.1.4. Conclusions

We have investigated how a fluorinated donor polymer (PM6) influences the photovoltaic properties, blend morphology, and blend photophysics of all-PSCs based on NDI-arylene copolymer acceptors. We found that pairing of PM6 respectively with PNDIS and PNDIBS led to dramatically different photovoltaic, blend morphology, and blend photophysics results. PM6:PNDIS all-PSCs combined the expected enhancement in V_{oc} (0.967 V) with high fill factor (0.70) to enable 9.1% PCE due to the vertical phase stratification and predominant *face-on* molecular orientations in the blend nanomorphology. In addition, the blend photophysics of PM6:PNDIS featured high charge photogeneration rate, strongly suppressed geminate and

bimolecular recombinations, and near unity charge collection probability. However, despite a favorable low optical bandgap energy loss (0.475 eV) and enhanced V_{oc} (0.925 V) in PM6:PNDIBS all-PSCs, compared to similar blends of the non-fluorinated PBDB-T, they showed poor performance (3.1% PCE) that originated from bulk phase separation with both *face-on* and *edge-on* molecular orientations, poor charge collection probability (66%) and high electron-hole recombination rate. These results show that in addition to the expected enhancement of V_{oc}, a fluorinated polymer in all-PSCs can also dramatically influence the blend morphology and blend photophysics with consequent negative or positive impact on the photovoltaic performance. The results also demonstrate that PM6:PNDIS all-PSCs are promising efficient devices that are robust to various processing methods and to active layer thicknesses of up to 300 nm.

2.2. Elucidating Impact of Molecular Weight on Morphology, Charge Transport, Photophysics, and Performance of All-Polymer Solar Cells.

2.2.1. Introduction

Advances in molecular design of materials and device engineering strategies have enabled substantial progress in raising the efficiency of organic photovoltaics (OPVs) over the past several years.[11-46] Among the various OPV technologies, all-polymer solar cells (all-PSCs) where the photoactive layer is composed of a blend of an electron-donating (donor) conjugated polymer and an electron-accepting (acceptor) conjugated polymer – the so-called bulk heterojunction (BHJ) architecture – offer unique advantages, including the facile tuning of optoelectronic properties of polymers,[11-46] their superior photochemical stability,[43, 61, 62] their excellent durability under thermal and mechanical stresses,[45, 63-68] and their potential for large scale manufacture.[40, 64] These features of all-PSCs make them especially appealing candidates for commercial applications in many areas. Although the power conversion efficiency (PCE) of all-PSCs has recently exceeded 10-11% in several different binary blend systems,[16, 28, 36, 37, 39, 41-43, 46] it lags behind the PCE of small-molecule non-fullerene acceptors (SM-NFAs) based solar cells where the PCEs has reached over 16%.[95, 96, 145] From a device engineering perspective, the major bottlenecks hindering further advances in the photovoltaic performance of all-PSCs include the low photocurrent density (J_{sc})[11, 12, 17, 18, 23, 24, 26-28, 32, 40] and low fill factor (FF).[11, 12, 17, 18, 30, 32, 40] The photocurrent is limited by the low electron mobility of the acceptor polymer component and the overall lack of greater complementary light-harvesting of the solar light by both blend components.[11, 12, 17, 18, 23, 24, 26-28, 32, 40] The small fill factor is primarily due to the non-optimal

blend morphology, which in turn is influenced by polymer molecular weight[21, 22, 25, 29, 33] and polymer/polymer interchain interactions.[15, 24, 30, 37, 40]

Advancing all-PSCs from a materials chemistry point of view, includes not only finding ways to harvest more of the solar spectrum,[16, 23, 29, 41, 42] increase the carrier mobilities of the donor and acceptor conjugated polymers,[29, 36, 41, 42] and to control and fine-tune the blend morphology[15, 24, 30, 37, 40, 72] and blend photophysics[41, 44, 67] but also to understand the underlying structure-property-performance relationships. A fundamental molecular parameter that can substantially influence the physical properties of the component materials, the thermodynamics of all-polymer blends, and the efficiency of all-PSCs is polymer molecular weight.[11, 21, 22, 25, 29, 33, 81, 82] Although several prior studies have been devoted to the effects of the molecular weights of the acceptor polymer and donor polymer on the photovoltaic properties of all-polymer solar cells, the results gave rise to divergent conclusions.[21, 22, 25, 29, 33, 81, 82] It was found that increasing the molecular weight of either the donor polymer or the acceptor polymer led to significantly enhanced power conversion efficiency (PCE) of all-PSCs due to the synergistic improvement of the short-circuit current (J_{sc}) and the fill factor (FF) while the open-circuit voltage (V_{oc}) remained relatively constant.[21, 22, 29, 81, 82] In contrast, other reports have found simultaneous drop in both J_{sc} and FF, and thus the power conversion efficiency, with increasing polymer molecular weight.[25, 33] The decline of J_{sc} and FF with increasing molecular weight was attributed to non-optimal blend morphology featuring either coarser domains due to large liquid-liquid phase separations[33] or greater molecular miscibility between the blend components,[25] both of which led to increased charge recombination and poorer charge photogeneration and charge extraction rates. Among the limitations of these prior studies of the impact of the number-average molecular weight (M_n) on the performance of all-PSCs include the relatively narrow range of M_n of the polymers

investigated. Very few of these studies reported M_n values measured at high temperature (> 100 ^oC)[25, 33, 81] and hence the effects of actual molecular weight of the conjugated polymer could not be delineated from those due to effects of chain aggregation.[22, 25, 29, 82] Nearly all prior studies, except one,[33] were focused on the acceptor polymer poly([N,N′-bis(2-octyldodecyl)-naphthalene-1,4,5,8-bis(dicarboximide)-2,6-diyl]-alt-5,5′-(2,2′-bithiophene)) (PNDIOD-T2 or N2200) and various non-high performing donor polymers.[21, 25, 81, 82]

Towards the resolution of the current conflicting views on how polymer molecular weight impacts the photovoltaic properties of all-PSCs,[21, 22, 25, 33, 81, 82] we aim to address this problem by employing an entirely new binary blend system whose components have not previously been involved in studies of the effects of M_n, including the well-known high-performance donor polymer, poly[(2,6-(4,8-bis(5-(2-ethylhexyl)thiophen-2-yl)-benzo[1,2-b:4,5-b']dithiophene))-alt-(5,5-(1',3'-di-2-thienyl-5'.7'-bis(2-ethylhexyl)benzo[1',2'-c:4',5'-c']dithiophene-4,8-dione], (PBDB-T) (Figure 2-9a).[146] We decided to focus on the direct heteroarylation polymerization (DHAP)-prepared poly([N,N′-bis(2-octyldodecyl)-naphthalene-1,4,5,8-bis(dicarboximide)-2,6-diyl]-alt-5,5′-(2,2′-biselenophene)) (PNDIBS) (Figure 2-9a) as the acceptor polymer component in the proposed M_n dependent studies. DHAP has been shown to be a simple and environmental-friendly pathway to synthesize highly efficient organic photovoltaic materials with minimal structural defects.[75, 147-150] Compared to previously well-studied N2200,[21, 25, 81, 82] our group has shown Stille-derived PNDIBS, which incorporates biselenophene units instead of bithiophene units, to have a narrower optical bandgap, increased crystallinity, and enhanced bulk charge transport and photovoltaic properties.[29, 37, 97] Thus well-defined DHAP-derived PNDIBS of sufficiently broad range of M_n values can be expected to

advance our understanding of the impact of molecular weight on photovoltaic properties while enabling development of high performance all-PSCs.

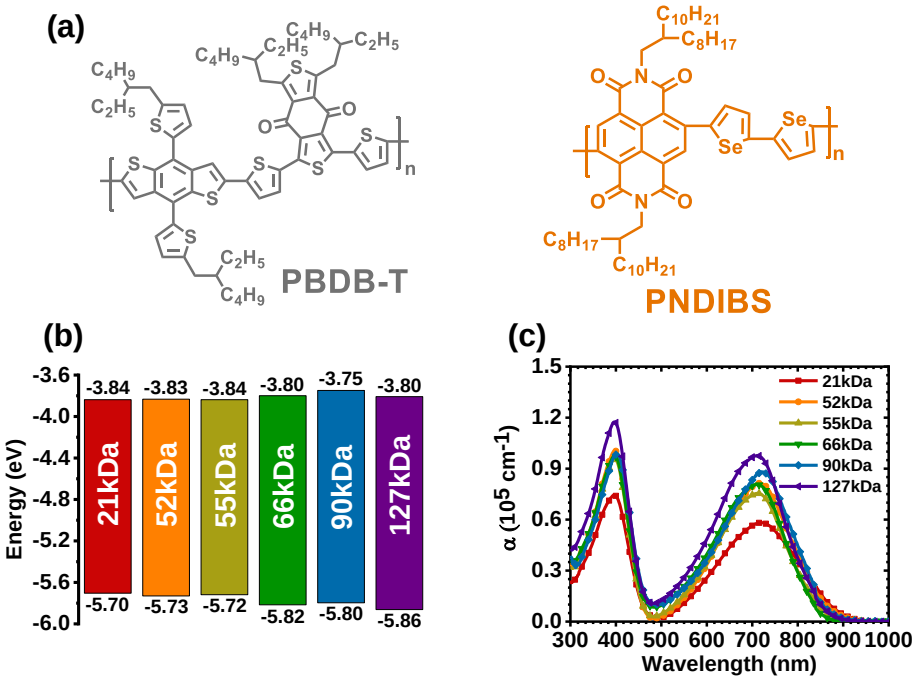

Figure 2-9. (a) Molecular structures of donor polymer (PBDB-T) and acceptor polymer (PNDIBS). (b) HOMO/LUMO energy levels of the acceptor polymer of varying number-averaged molecular weight M_n. (c) Thin-film optical absorption spectra of the PNDIBS acceptor copolymer at different number-average molecular weights M_n. Reproduced with permission from Ref.[69] Copyright 2020 Royal Society of Chemistry.

In this paper, we report a comprehensive investigation of the effects of the number-average molecular weight (M_n) of the acceptor polymer on the blend charge transport, blend photophysics, blend morphology, and photovoltaic properties of all-PSCs. The binary blend devices paired the donor polymer PBDB-T respectively with the DHAP-prepared acceptor copolymer PNDIBS at six different M_n values from 21 to 127 kDa. We found that the key photovoltaic parameters of the PBDB-T:PNDIBS blend devices, PCE and J_{sc}, both increased with increasing M_n until reaching peaks at an optimal molecular weight of 55 – 66 kDa and subsequently decreased with further increases in M_n. The observed peak in photovoltaic

performance at M_n of 55 kDa coincided with an optimal blend morphology composed of a bi-continuous network of ordered crystalline features of predominantly *face-on* molecular orientations and 5.5-6.5 nm domain sizes. The optimal or critical M_n value also marked peaks in charge photogeneration rate and symmetric charge transport. Outside of the optimal M_n range, the blend morphology evolved from finely and tightly packed in the 21 kDa blends to disordered and amorphous structures with large phase separation, leading to severe charge recombination and space-charge build-up, which are detrimental to photovoltaic device performance. At the critical M_n value of 55 kDa, the all-PSCs had a maximum PCE of 10.2% with an average of 9.3% as a result of the favorable blend charge transport properties, blend photophysics, and blend morphology. We also found that the M_n has a significant impact on the sensitivity of the device efficiency to the active layer thickness. While the PCE of the optimal M_n was rather insensitive to the active layer thickness, the efficiency of all-PSCs at the higher M_n was strongly dependent on the layer thickness and in this case, the thinner photoactive layer afforded the highest PCE. Overall, this study and results provide a broader and unified understanding of how the molecular weight of a polymer component of all-polymer solar cells impacts the blend charge transport, blend photophysics, blend morphology, and photovoltaic properties as well as give new structure-property relationships for a promising n-type semiconducting copolymer.

2.2.2. Experimental Methods

Materials. Naphthalene-1,4,5,8-tetracarboxylic dianhydride was obtained from TCI America and used without any further purification. Selenophene, tris(dibenzylideneacetone) dipalladium (0), pivalic acid, cesium carbonate and other precursors for the preparation of the 2-octyl-1-dodecylamine were obtained from Sigma-Aldrich and used without further purifications. Extra dry chlorobenzene was obtained from Accros Organic and de-gassed with Argon for 15 min

prior to utilization. Other starting materials were purchased from Sigma-Aldrich, TCI America or Alfa Aesar. The donor polymer PBDB-T was synthesized in our lab.

Synthesis of Materials. The preparation of the 2,6-dibromonaphthalene-1,4,5,8-diimide monomer was realized following to the literature approach.[75] The preparation of 2,2'-biselenophene (Figure B-1), was performed according to the conditions of the literature.[97] Then, a further step was taken to obtain the 5,5'-bistrimethylstannyl-2, 2'-biselenophene (Figure B-2).[97, 151] The DHAP and Stille protocols for the polymer synthesis were performed according to the literature methods.[75, 97] The details are given in the Appendix B.

Fabrication and Characterization of all-PSCs. Solar cells devices were fabricated with an inverted architecture of ITO/ZnO/PEI/Blend/MoO_3/Ag. ITO-coated substrates (15 Ω/square, Shanghai B. Tree Tech, Shanghai, China) were cleaned sequentially in ultrasonic baths with acetone, deionized water, and isopropyl alcohol for 30 min, dried using nitrogen gas, and followed by 10 mins of O_2 plasma cleaning. The ZnO precursor solution was spin-coated onto the ITO and followed by thermal annealing at 250 °C for 30 min to make ~30 nm thick ZnO layer. A 0.05 wt% solution of polyethylenimine (PEI) in 2-methoxyethanol was spin-coated onto the ZnO layer and dried at 120 °C for 10 min. The PBDB-T:PNDIBS (1:0.8 wt/wt) blends were prepared in chlorobenzene, mixed and stirred overnight at 85^{o}C in the glovebox. The blend solutions were spin-coated at 1000 rpm for 50s, followed by thermal annealing at 110^{o}C for 10 min in the Argon-filled glovebox. All the active layers had a thickness of 105 ± 5 nm. MoO_3 (0.5 nm) and Ag (100 nm) were thermally deposited onto the active layer. An aperture mask with area of 3.14 mm^2 was applied during measurements to define the illuminated device area. After evaporation of the electrode, the photovoltaic cells were tested under AM 1.5G solar illumination at 100 mW/cm^2 in ambient air by using a solar simulator (Model 16S, Solar Light Co.,

Philadelphia, PA) with a 200W Xenon Lamp Power Supply (Model XPS 200, Solar Light Co., Philadelphia, PA) calibrated by NREL certified Si photodiode (Model 1787-04, Hamamatsu Photonics K.K., Japan) and a HP4155A semiconductor parameter analyzer (Yokogawa Hewlett Packard, Japan). After the *J*-*V* measurements, the external quantum efficiency (EQE) spectra were measured by using a solar cell quantum efficiency measurement system (Model QEX10, PV Measurements, Inc., Boulder, CO) with a 2 mm^2 (2 mm × 1 mm) size masked incident light source and TF Mini Super measurement apparatus for multiple devices in a single substrate. The EQE system was calibrated with a Si photodiode before measurement.

Fabrication and Characterization of SCLC devices. Current-voltage (*J*-*V*) characteristics of the SCLC devices were measured by using a HP4155A semiconductor parameter analyzer (Yokogawa Hewlett-Packard, Tokyo). The carrier mobility was deduced by fitting the *J*-*V* curves to the Mott−Gurney equation where *J* is the current density, ε_0 is the permittivity of free space, ε is the relative permittivity, μ is the zero-field mobility, *V* is the voltage, *L* is the thickness of active layer.

$$J = \frac{9}{8}\varepsilon_0\varepsilon\mu\frac{V^2}{L^3}$$

The SCLC device structures for electron-only and hole-only were ITO/ZnO/PEI/Blend/LiF (1nm)/Al (100nm) and ITO/PEDOT: PSS/Blend/MoO_3 (7.5nm)/Ag (100nm), respectively. Each active layer of both neat and blend films was processed at the optimized all-PSC devices condition as described above and spin-coated at 1000 rpm for 50s and followed by thermal annealing at 110^{o}C for 10 min inside glovebox.

Fabrication and Characterization of OFETs. TFT devices were fabricated on highly doped n-type Si (100) wafer with a 300 nm thick SiO_2 treated with self-assembled monolayer of n-

octadecyltrimethoxysilan (OMTS), according to the reported method.[152] Before use, the OTMS monolayer was rinsed subsequently with toluene, acetone, and isopropyl alcohol and dried under a nitrogen stream. Static water contact angles of the OTMS substrates measured by Edmund Scientific goniometer were higher than 105 degree. The solutions (5 mg/mL) of polymer semiconductor for transistor devices were prepared by dissolving the polymer in chlorobenzene at 80°C for 30 min and then spin-cast on the OTMS substrates with controlled thickness at ~40 nm. The as-prepared thin films were thermally annealed at 170°C for 1 hour in N_2-filled glove box. A top-contact gold electrode (70 nm) was subsequently deposited by evaporation through a shadow mask with a channel length (L) and width (W) defined as 50 and 1000 μm, respectively. The transistor characteristics were measured by Keithley 4200 semiconductor parameter analyzer (Keithley Instruments Inc., Cleveland, OH, USA) in an N_2 filled glove box at room temperature. The effect of molecular weight on μ_e^{FET} can be inferred from the standard FET relation by calculating derivative charge mobility using the equation for I_{ds} in the saturation region.

$$I_{ds} = \frac{WC_i}{2L}\mu(V_{gs} - V_T)^2$$

AFM Imaging. Atomic force microscopy (AFM) characterization of the surface morphology was done on the active layers of the actual polymer solar cells, used in the photovoltaic measurements, by using a Bruker Dimension scanning probe microscope (SPM) system.

GIWAXS. Grazing incidence X-ray scattering (GIWAXS) experiments were conducted at the Japan Synchrotron Radiation Facility SPring-8 by using the beamlines BL46XU. Thin film samples of the neat donor polymer (PBDB-T) and acceptor polymers (PNDIBS) were spin-coated on the top of glass substrates and annealed at 110 °C for 10 min. The binary blend films were prepared in the same manner as the actual all-PSC devices on ZnO/PEI-coated ITO

substrates. The X-ray beam was monochromatized by a double-crystal Si (111) monochromator, and the X-ray energy in this experiment was 12.40 keV (λ = 0.1 nm). The angle of incident X-ray to sample surface was 0.12° with a Huber diffractometer. The scattered profile from the film sample was detected using an area detector (PILATUS 300K) for 1 s at room temperature, and the distance between the sample and detector was 175.0 mm. The crystal coherence length (L_c) of samples was determined by using the Scherrer equation: $L_c = 2\pi K/\Delta q$, where K is a shape factor (typically 0.89) and Δq is the full width at half-maximum (FWHM) of the diffraction peak. Here, the L_c (100) was obtained from the FWHM of the (100) diffraction peak in the-plane (q_{xy}) line cut.

2.2.3. Results and Discussion

2.2.3.1. Synthesis and Characterization.

The monomers, 2,6-dibromonaphthalene-1,4,5,8-diimide and 2,2'-biselenophene, were synthesized following the conditions reported in the literature, and a detailed protocol is available in Appendix B.[75, 97] We have previously reported DHAP-based synthesis of the *bithiophene*-NDI copolymer, PNDIOD-T2, and observed that a more regioregular polymer was achieved than the same polymer made by conventional Stille coupling polymerization.[75] Here, we wanted to confirm the reproducibility and robustness of the DHAP approach by applying it under similar conditions to prepare the *biselenophene*-NDI copolymer, PNDIBS, and by optimization of the DHAP polymerization time to produce a series of polymers with different molecular weights (Table B-1). In the case of the Stille-prepared PNDIBS, we used the same conditions reported earlier.[29, 97] Scheme S1 presents the general conditions for the copolymerization of 2,6-dibromonaphthalene-1,4,5,8-diimide and 2,2'-Biselenophene by DHAP and by Stille, respectively.

The ^{1}H NMR spectra of both the Stille and DHAP PNDIBS samples are shown in Figures B-3 and B-4. Despite the limited solubility of both polymer samples in 1,1,2,2-tetrachloroethane-D2, the spectra are clear enough to identify structural differences between the two polymers. The DHAP-prepared PNDIBS exhibit a 2:3.98 ratio between the NDI and the biselenophene protons in the aromatic region, which deviates only marginally from the expected ratio of 2:4. On the other hand, the Stille-prepared PNDIBS sample showed a ratio of 2:4.23 between the NDI and biselenophene protons, clearly indicating some homocoupling of the tin derivative monomers. Moreover, the broader peak at 8.6 to 8.75 ppm can be associated to the unbrominated NDI end-groups. The debromation of the NDI monomer has been previously shown to induce the homocoupling of the other monomer, notably the tin derivative monomer in our Scheme S1.[153] Thermogravimetric analysis (TGA) showed onset degradation temperature (T_d) of over 400^{o}C (Figure B-5) suggesting that the DHAP-prepared PNDIBS polymers had excellent thermal stability. Differential scanning calorimetry (DSC) scans (Figure B-6) showed that the DHAP-prepared PNDIBS samples had a higher melting temperature (T_m = 357^{o}C) compared to the previously reported Stille-prepared PNDIBS of comparable molecular weight.[29] These results clearly indicated that NDI-based copolymers prepared via DHAP method can afford higher regioregularity by minimizing homocoupling defects than the conventional Stille-prepared polymers. The molecular weight and dispersity of the PNDIBS samples were characterized by size exclusion chromatography (SEC) using 1,2,4-trichlorobenzene (TCB) eluent at 110 °C relative to polystyrene standards. The molecular weight data are summarized in Table 2-4. We note that the solubility of the PNDIBS samples depended on the molecular weight. Specifically, the higher molecular weight samples (M_n > 55kDa) required a higher temperature (T > 80^{o}C) and longer stirring time to achieve complete dissolution and formation of true solutions.

The electronic structure of the series of PNDIBS of varying molecular weight was characterized in terms of cyclic voltammetry (CV) derived HOMO/LUMO energy levels, which are shown in Figure 2-9b and summarized in Table 2-4. The cyclic voltammograms for the reduction and oxidation processes in PNDIBS are shown in Figures B-7 and B-8, respectively. The HOMO and LUMO energy levels of PNDIBS with M_n of 21 kDa, 52 kDa, and 55 kDa are nearly identical at -5.70 – -5.73 eV and -3.83 – -3.84 eV, respectively. The LUMO energy level of PNDIBS with higher M_n values was slightly upshifted to -3.75 – -3.80 eV. A similar trend was also observed in the HOMO energy levels of the higher molecular weight PNDIBS, where the HOMO downshifted -5.80 – -5.86 eV (Figure 2-9b). These HOMO/LUMO energy levels of PNDIBS are comparable to literature results.[29, 97] More interestingly, the large range of M_n (21-127 kDa) investigated here has enabled observation of impact of molecular weight on the electronic structure of the acceptor polymer PNDIBS. It is to be noted that similar effects of M_n on electronic structure has been observed for the donor polymer poly(3-hexylthiophene) (P3HT);[154-156] however, previous studies of other NDI-based copolymers found the LUMO/HOMO energy levels to be virtually independent of the polymer molecular weight.[22, 25] Our observed shifts of the LUMO/HOMO energy levels with increasing M_n suggest that the higher molecular weight PNDIBS samples have either more intrachain disorder due to backbone twisting[155] or an increase in density of amorphous regions.[155-157]

Thin film absorption spectra of the series of DHAP-prepared PNDIBS of different number-average molecular weight (M_n) are presented in Figure 2-9c, and the numerical optical parameters are summarized in Table 2-4. As expected and in good agreement with previous reports,18, 57 these absorption spectra have two characteristic peaks at ~400 nm and 710 – 718 nm, which represent the π-π* transition and the intramolecular charge transfer (ICT) bands,

respectively. We note that the absorption spectra of the DHAP-prepared PNDIBS have a slightly wider but molecular weight independent optical bandgap ($E_g^{opt.}$) of 1.42-1.44 eV (Table 2-4), which is very similar to that of the Stille-prepared PDNIBS with E_g^{opt} of 1.40 eV (Figure B-9). Clearly, this suggests that the polymerization method has only marginal impact on the optical bandgap of this semiconducting polymer. However, subtle and gradual hypsochromic shift of the ICT band with increasing M_n from 21kDa to 66kDa is observed (Table 2-4), and this means that intramolecular charge transfer between the NDI electron-accepting moiety and the biselenophene electron-donating moiety is increasingly weakened by backbone distortion and conformational disorder with increasing polymer chain length.[158] The slight bathochromic shift in the ICT band observed in higher M_n samples (90kDa and 127kDa) signify significant chain aggregation at increasing M_n. Interestingly, we also observed that the absorption coefficient (α_{max}) increased monotonically with increasing M_n (Figure 2-9c) from 0.75 x 10^5 cm^{-1} at 21 kDa to 1.17 x 10^5 cm^{-1} at 127 kDa. The absorption coefficients of PNDIBS copolymers are much higher than other typical NDI-based copolymers due to increased backbone planarity, increased interchain overlap, and higher crystallinity.[13, 19, 97] The observed increase of the absorption coefficient α_{max} with increasing molecular weight can be explained by the increased solid-state packing density as a result of chain folding at the higher M_n. Although not previously explained, similar effects of molecular weight on absorption coefficient have been observed in other donor-acceptor conjugated copolymers.[21, 81, 159]

Table 2-4. Molecular Weight, Electronic Structure, and Optical Properties of Acceptor Polymer PNDIBS and Donor Polymer PBDB-T. Reproduced with permission from Ref.[69] Copyright 2020 Royal Society of Chemistry.

M_n (kDa)	M_w (kDa)	PDI	λ_{max} (nm)	α_{max} (10^5 cm^{-1})	λ_{ICT} (nm)	λ_{onset} (nm)	$E_g^{opt.(a)}$ (eV)	E_{HOMO} (eV)	E_{LUMO} (eV)
21	36	1.7	397	0.75	718	885	1.40	-5.70	-3.84
52	172	3.3	398	1.01	715	873	1.42	-5.73	-3.83
55	132	2.4	397	0.96	713	868	1.42	-5.72	-3.84
66	172	2.6	397	0.97	711	859	1.44	-5.82	-3.80
90	270	3.0	399	1.04	722	872	1.42	-5.80	-3.75
127	292	2.3	397	1.17	710	870	1.42	-5.86	-3.80

[(a)] $E_g^{opt.} = 1240/\lambda_{onset}$

We characterized the electron transport properties of one of the present DHAP-prepared PNDIBS (21 kDa) by using organic field-effect transistors (OFETs) with bottom-gate top-contact architecture as detailed in the Experimental Method section. For comparison, we similarly characterized the field-effect electron mobility of the Stille-prepared PNDIBS. The transfer curves and output curves are shown in Figure B-10 while the saturation region field-effect electron mobility (μ_e^{FET}) is presented in Table B-2. The Stille-prepared PNDIBS films annealed at 170 °C showed an average μ_e^{FET} of 0.15 cm^2/Vs with an on/off current ratio (I_{on}/I_{off}) of 1 x 10^5 (Table B-2). If the same PNDIBS films annealed only at room temperature (25 °C) the field-effect electron mobility drops to 0.04 cm^2/Vs, which suggests that thermal annealing at high temperature enhances electron transport by the increased crystallinity and favorable intermolecular packing. The DHAP-prepared PNDIBS films annealed at 170 °C had an average μ_e^{FET} of 0.16 cm^2/Vs with an on/off current ratio (I_{on}/I_{off}) of 4 x 10^6 (Table B-2), which is comparable to that of the Still-prepared PNDIBS. However, the over one order of magnitude

enhancement in on/off current ratio is notable and an indication of some of the advantages of the DHAP method in synthesizing defect-free, high regioregularity, and high mobility semiconducting polymers.

2.2.3.2. Photovoltaic properties of PBDB-T:PNDIBS Blend Devices.

We exploited the series of DHAP-prepared PNDIBS of different number-average molecular weight M_n to investigate the effects of the acceptor polymer M_n on the photovoltaic properties of all-PSCs. The photoactive layer of the devices thus comprised binary blend of the donor polymer PBDB-T and acceptor polymer PNDIBS. The all-PSCs were constructed with an inverted device architecture: ITO/ZnO/PEI/Blend/MoO_3/Ag, where polyethyleneimine (PEI) was used as a cathode interlayer.[121] The PBDB-T:PNDIBS blend devices were optimized by varying the donor polymer/acceptor polymer (D:A) ratio, annealing temperature, and use of solvent processing additives. The optimal processing conditions were found to be spin-coating of the blend solutions with D:A ratio of 1:0.8 wt/wt, thermal annealing at 110^{o}C for 10 min, and *without* use of any solvent processing additive. The *J-V* responses and the EQE spectra of the optimized all-PSC devices for each PNDIBS molecular weight are presented in Figure 2-10 whereas the corresponding photovoltaic properties are summarized in Table 2-5. All the photovoltaic parameters, including J_{sc}, V_{oc}, FF, and PCE, are presented as a function of the PNDIBS molecular weight in Figure 2-11.

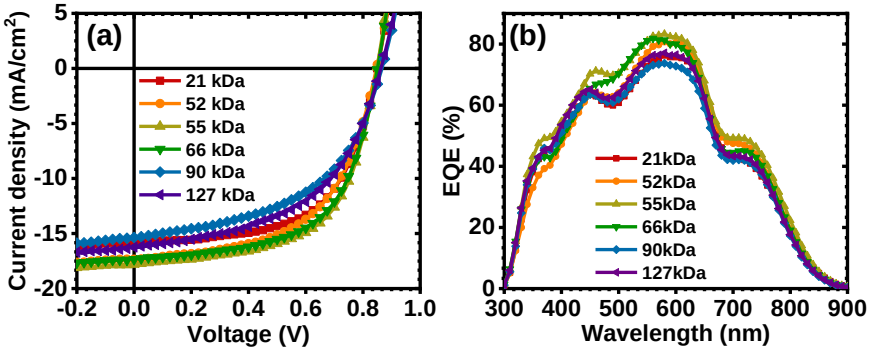

Figure 2-10. The acceptor polymer PNDIBS number-averaged molecular weight (M_n) dependence of photovoltaic properties of optimized PBDB-T:PNDIBS devices: (a) *J-V* curves; and (b) EQE spectra. Reproduced with permission from Ref.[69] Copyright 2020 Royal Society of Chemistry.

Table 2-5. Dependence of Photovoltaic Properties of Optimized PBDB-T:PNDIBS Blends on Acceptor Polymer PNDIBS Molecular Weight M_n. Reproduced with permission from Ref.[69] Copyright 2020 Royal Society of Chemistry.

Blend	J_{sc} (mA/cm^2)	V_{oc} (V)	FF	$PCE_{average}$[(a)] (%)	PCE_{max} (%)	$J_{sc}^{calc.}$ (mA/cm^2)
PBDB-T:PNDIBS (21 kDa)	15.89 (± 0.26)	0.85 (± 0.003)	0.60 (± 0.02)	8.13 (± 0.24)	8.65	15.63
PBDB-T:PNDIBS (52 kDa)	17.34 (± 0.63)	0.85 (± 0.004)	0.56 (± 0.03)	8.37 (± 0.50)	9.12	16.35
PBDB-T:PNDIBS (55 kDa)	17.94 (± 0.68)	0.85 (± 0.005)	0.61 (± 0.01)	9.28 (± 0.37)	10.2	17.45
PBDB-T:PNDIBS (66 kDa)	17.36 (± 0.59)	0.85 (± 0.006)	0.60 (± 0.03)	8.91 (± 0.25)	9.35	16.50
PBDB-T:PNDIBS (90 kDa)	15.37 (± 0.43)	0.87 (± 0.006)	0.51 (± 0.02)	6.84 (± 0.28)	7.18	15.24
PBDB-T:PNDIBS (127 kDa)	16.24 (± 0.22)	0.86 (± 0.005)	0.52 (± 0.02)	7.32 (± 0.37)	8.12	15.84

[(a)]Average of over 10 devices

The dependence of J_{sc} on M_n, as shown in Figure 2-11a, exhibits a rise to a peak value at 55 kDa followed by a large decline. In particular, the photocurrent J_{sc} exhibits a peak of 17.94 mA/cm^2 at M_n of 55kDa, and subsequently decreases to a minimum value of 15.37 mA/cm^2 at 90 kDa before slightly rising again to 16.24 mA/cm^2 at 127 kDa (Table 2-5). As we will discuss later, further insights to this evolution of the photocurrent as a function of molecular weight can be gained by observed correlations with the blend charge transport properties, blend photophysics and blend film morphology. The V_{oc} as a function of M_n is relatively constant at 0.85 – 0.87 V although a slight increase at the highest M_n values could be argued (Figure 2-11b); this observation is in agreement with the marginal changes in the LUMO energy level of

PNDIBS as a function of molecular weight. The FF fluctuated around 0.60 – 0.64 for M_n between 21 kDa to 66 kDa before decreasing to 0.51 – 0.53 at higher M_n of 90-127 kDa (Figure 2-11c). These dependencies of the photovoltaic parameters J_{sc}, V_{oc}, and FF on M_n thus combined to produce the observed dependence of PCE on M_n shown in Figure 2-11d. The PCE rises with M_n to a maximum PCE of 10.2% at 55 kDa and significantly declines with further increases in M_n. Clearly, the M_n dependence of the PCE closely resembles the dependence of J_{sc} on molecular weight given the dominant role of the changes in photocurrent. Overall, we conclude from these observations that there exists an optimal or critical molecular weight of the acceptor polymer that optimizes the efficiency and photovoltaic properties of all-PSCs; the optimal value is in the range of 55-66 kDa in the case of the present PBDB-T:PNDIBS blend devices.

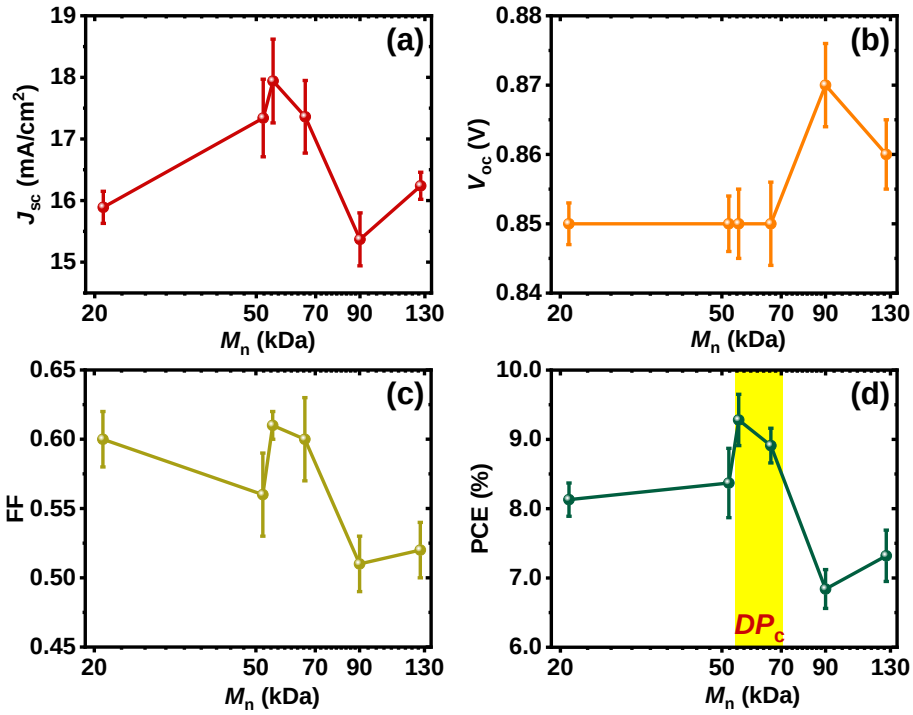

Figure 2-11. The relationships of photovoltaic parameters (J_{sc}, V_{oc}, FF, and PCE) with the number-averaged molecular weight M_n of acceptor polymer PNDIBS in PBDB-T:PNDIBS all-PSC devices: (a) J_{sc} vs. M_n, (b) V_{oc} vs. M_n, (c) FF vs. M_n, and (d) PCE vs. M_n. The error bars

were generated from over 10 devices at each M_n. Reproduced in part with permission from Ref.[69] Copyright 2020 Royal Society of Chemistry.

We note that the photovoltaic properties of a binary blend of donor polymer PBDB-T and a similarly DHAP-prepared PNDI2OD-T2 acceptor polymer of much higher M_n (M_n = 76kDa) (PCE = 7.3%)[75] are inferior to those of the PBDB-T:PNDIBS blends of lower PNDIBS M_n. This observation suggests the benefits of moving from *bithiophene*-NDI copolymers to *biselenophene*-NDI copolymers.

The EQE spectra of the optimized devices for all M_n values investigated are shown in Figure 2-10b. The photocurrent response of all devices spanned the 885 nm to 300 nm range, which matched well with the complementary absorption spectra of the donor and the acceptor polymers in the PBDB-T:PNDIBS blends. Thus, it is clear that the photocurrent generated in the 460 – 670 nm region comes from the photoinduced electron transfer from the donor polymer, whereas the photocurrent produced in the 350 – 460 nm and 680 – 880 nm regions originate from the photoinduced hole transfer from the acceptor polymer.[124] The maximum EQE value is found around 570 – 580 nm for each M_n, varying from 73.7% for the 90kDa devices to 83.3% for the 55kDa, which mirrored the observed trend in J_{sc} (Figure 2-11a). Moreover, the optimized all-PSC devices fabricated from the optimal PNDIBS molecular weight of 52kDa – 66kDa had superior quantum efficiency response throughout the whole spectral range, which is in good agreement with the observed enhanced J_{sc} at these M_n values. The photocurrent J_{sc} values obtained by integrating the EQE spectra were found to be within 2-6% mismatch with the values obtained directly from the *J-V* measurements (Table 2-5).

We found the photovoltaic properties of the all-PSCs at each molecular weight have different sensitivity towards the photoactive layer thickness. Thus, we chose all-PSC devices based on PNDIBS of 66 kDa and 90 kDa M_n values to probe the photoactive layer thickness

dependence of the photovoltaic properties (Figure B-11). The average PCE of the PNDIBS-66kDa devices is relatively constant at ~9.0% as the active layer thickness decreased from 100 nm to 80nm; the PCE decreased to ~8.0% as the thickness was further reduced to 70 nm. which was indicative of its weak dependence on the film thickness. In contrast, the efficiency of the PNDIBS-90kDa devices progressively increased from 5.4 to 7.3% as the active layer decreased from 110 nm to 70 nm. The much-improved photovoltaic properties of the 90 kDa devices at thinner active layers can be attributed to the strongly suppressed charge recombination and the reduced space-charge accumulation/formation. This observation suggests that blends of the higher molecular weight PNDIBS have potential applications in developing semi-transparent inverted all-polymer solar cells.

2.2.3.3. Charge Photogeneration and Charge Recombination of PBDB-T:PNDIBS Blend Devices.

To investigate the effects of molecular weight of the acceptor polymer PNDIBS on the charge recombination kinetics, we characterized the J_{sc} and V_{oc} as a function of the incident light intensity (P_{light}). The dependence of V_{oc} on the light intensity can be generalized as $\frac{dV_{oc}}{dln(P_{light})} \propto s\frac{kT}{q}$, where k is the Boltzmann constant, T is absolute temperature, and q is elementary charge. The value of the proportionality coefficient, s, is a measure of whether bimolecular recombination (s = 1) or trap-assisted recombination (s = 2) is dominant in the charge recombination dynamics.[133, 134, 160] The s value determined from the plot of V_{oc} versus ln (P_{light}) for all-PSC devices of different PNDIBS molecular weights (Figure 2-12a) varied from 1.02 in M_n of 21 kDa to 1.15 in M_n of 127 kDa. Clearly, the near unity s coefficient measured at all the

M_n values means that bimolecular recombination is the dominant charge recombination mechanism in these all-PSC blends.

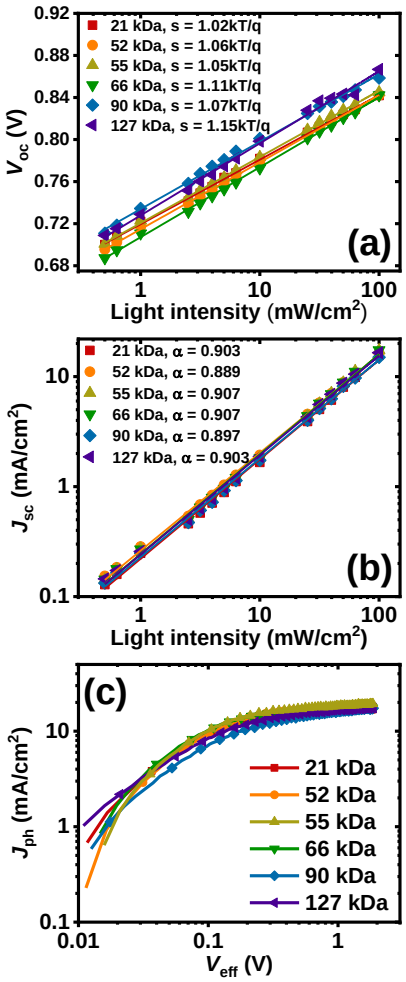

Figure 2-12. Dependence of photovoltaic parameters on incident light intensity for the optimized PBDB-T:PNDIBS devices of various acceptor polymer molecular weight M_n: (a) V_{oc} vs. P_{light}; (b) J_{sc} vs. P_{light} (c) J_{ph} vs V_{eff} for optimized PBDB-T:PNDIBS devices of various acceptor polymer molecular weight M_n. Reproduced in part with permission from Ref.[69] Copyright 2020 Royal Society of Chemistry.

The relationship between J_{sc} and P_{light} can be modelled as $J_{sc} \propto P_{light}{}^{\alpha}$, where linearity ($\alpha$ = 1) indicates that all charge carriers are collected at electrodes prior to recombination whereas significant deviation from linearity implies otherwise.[133, 134, 161] From the exponential coefficient α values extracted from Figure 2-12b, we observed a significant deviation from unity

for all devices at all of the M_n values (α = 0.897 – 0.907). These results suggest the existence of severe bimolecular recombination in all-PSC devices from all PNDIBS molecular weights investigated. The slightly higher α value observed at 55kDa and 66kDa (α = 0.907) might reflect weaker bimolecular recombination as suggested by the slight improvement in FF (0.60 – 0.61). Moreover, the much lower exponential coefficient especially in the 90kDa devices (α = 0.897) coupled with the unbalanced charge transport to be discussed below suggest that the performance of these all-PSC devices is hindered not only by bimolecular recombination but also by space-charge effects;[161] we note that this observation is consistent with our observed enhanced efficiency in devices with thinner active layers discussed above. The high degree of bimolecular recombination in these blends is further confirmed by examining the trend of FF with respect to the incident light intensity. As shown in Figure B-12a, the fill factor of the PBDB-T:PNDIBS devices at all M_n values increased with decreasing light intensity. This improvement in FF at low light intensity can be rationalized by the strongly suppressed bimolecular recombination due to decreased charge carrier density. Overall, these results demonstrate that the nature of charge recombination kinetics in these PBDB-T:PNDIBS devices is independent of the molecular weight of PNDIBS and that the all-PSCs are dominated by bimolecular recombination, which appears to lead to the relatively low FF values (0.52 – 0.61) when compared to other reported high-performing all-PSCs.

We investigated the molecular weight dependence of the charge generation kinetics of the present all-PSC devices by evaluating the maximum photoinduced charge photogeneration rate (G_{max}) and charge extraction rate ($P(E,T)$) via the relationship between the photocurrent ($J_{ph} = J_{light} - J_{dark}$, where J_{light} is the current density under illumination, and J_{dark} is the dark current density) and the effective voltage ($V_{eff} = V_o - V_a$, where V_o is the built-in voltage, and V_a is the

applied voltage). The plot of J_{ph} versus V_{eff} is given in Figure 2-12c whereas the *P(E,T)* and G_{max} values are summarized in Table B-3. All the devices at all M_n values, with the exception of the 90kDa devices, showed saturated photocurrents at a relatively low effective voltage of 0.8V (Figure 2-12c). This observation suggest that apart from the 90kDa devices which exhibit a poor charge extraction probability of 89.3%, all photogenerated excitons in the all-PSCs at all other M_n values were essentially dissociated into free charge carriers that were effectively collected at the electrodes as evidenced by the high *P(E,T)* under short-circuit condition (93.7% – 94.5%) (Table B-3). The M_n dependence of the maximum charge photogeneration rate (G_{max}) was found to parallel the trend observed in the above photovoltaic properties and the blend charge transport properties discussed below. Specifically, the G_{max} rose from 1.06 x 10^{28} $m^{-3}s^{-1}$ in the 21kDa devices, peaked at 1.21 x 10^{28} $m^{-3}s^{-1}$ in the 55kDa devices, and then declined to 1.09 x 10^{28} $m^{-3}s^{-1}$ in the 90-127kDa devices (Table B-3). Since the thin film absorption coefficient was marginally affected by the polymer molecular weight, we conclude that the observed difference in the charge photogeneration rate as a function of M_n can be attributed primarily to the variation in morphology at the various molecular weights as will be discussed in detail below.

To further confirm the formation of space-charge region (SCR) in the 90kDa and 127kDa blend devices, the relationship of J_{ph} and V_{eff} as a function of incident light intensity was characterized, and results for the optimized PBDB-T:PNDIBS devices of different M_n values are showed in Figure 2-13. The characteristic space-charge limited photocurrent is expected to have a square-root dependency on the effective voltage.[162] As shown in Figures 2-13a-d, the SCR remained within V_{eff} of lower than 0.3V; thus, indicating that the formation of space-charge is relatively weak. On the other hand, the SCR in 90kDa and 127kDa devices extended to much higher V_{eff} of 0.4 – 0.5V (Figures 2-13e-f). Moreover, the square-root region was found to persist

and shift to lower V_{eff} at lower incident light intensity. These observations suggested that the space-charge formation in the 90kDa and 127kDa devices was more severe; thereby, explaining the poor photovoltaic properties and corroborating the increasing PCE at thinner films. The presence of space-charge effects can also be proved by investigating the dependency of saturation voltage (V_{sat}) extracted from Figures 2-13, which is the transition voltage from the saturation region to the square-root region, on the incident light intensity[162] as shown in Figure B-12b. The V_{sat} of the optimized PBDB-T:PNDIBS devices fabricated from the lower molecular weight acceptor polymers (21kDa, 52kDa, 55kDa, and 66kDa) exhibited nearly independency on P_{light} where the slopes were found to be around 0.03 – 0.16; thus, suggesting weak space-charge formation. The relationship of V_{sat} and P_{light} of the 90kDa and 127kDa devices showed a slope of 0.45 and 0.34, respectively, which is in good agreement with the theoretical prediction of space-charge region (slope = 0.5).[162] These analyses collectively confirm that there is significant space-charge formation in the 90kDa and 127kDa devices, which explain the decreased photovoltaic properties compared to the lower M_n based devices as observed earlier.

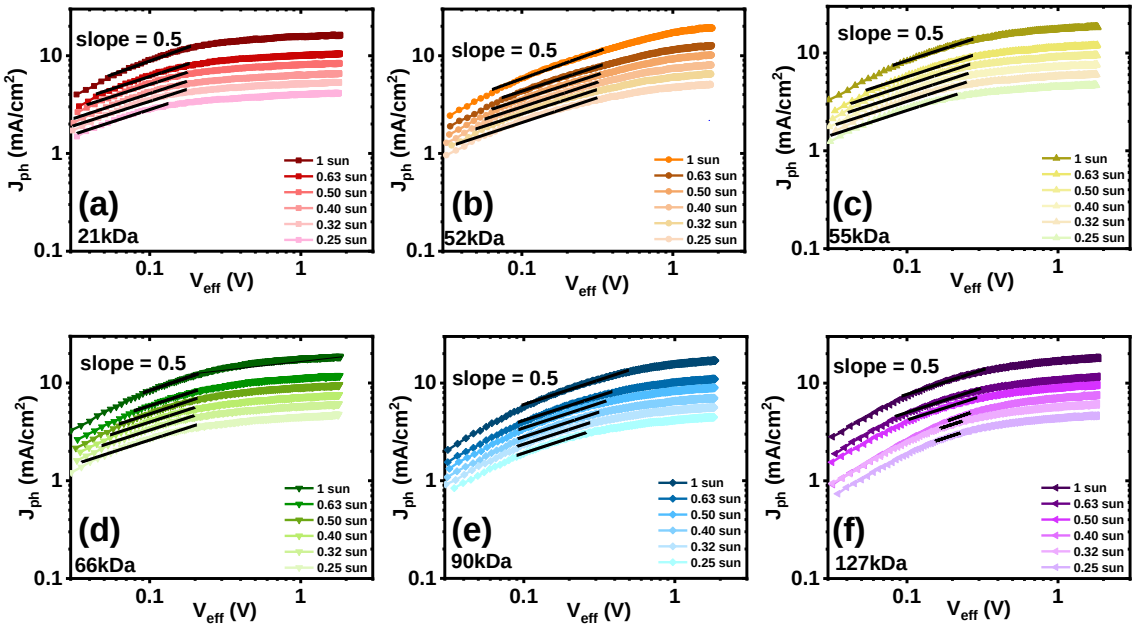

Figure 2-13. J_{ph} vs. V_{eff} for optimized PBDB-T:PNDIBS devices at various PNDIBS molecular weight and at different incident light intensity: (a) 21kDa, (b) 52kDa, (c) 55kDa, (d) 66kDa, (e) 90kDa, and (f) 127kDa. Reproduced with permission from Ref.[69] Copyright 2020 Royal Society of Chemistry.

2.2.3.4. Charge Transport Properties of PBDB-T:PNDIBS Blend Films.

We characterized the PNDIBS molecular weight (M_n) dependence of bulk charge transport in the all-PSC devices by measuring the space-charge limited current (SCLC) charge carrier mobilities of PBDB-T:PNDIBS blend films processed at the same optimal conditions as used to fabricate the all-PSC devices. The *J-V* curves and SCLC fitting lines for hole-only devices and electron-only devices are shown in Figures B-13 and B-14, respectively. The M_n dependence of the electron mobility (μ_e), the hole mobility (μ_h), and the ratio μ_h/μ_e for the PBDB-T:PNDIBS blend films are shown in Figure 2-14. Both μ_e and μ_h exhibit very similar trends, increasing to their peak values at 55 kDa and subsequently decreasing as the molecular weight increased to 127kDa (Figure 2-14). Specifically, the electron mobility of the blend films increased 3.4-fold from the 21 kDa value to a maximum of 1.96 x 10^{-4} cm^2/Vs at 55kDa and then dropped to 3.60 x 10^{-5} cm^2/Vs at 127 kDa (Table 2-6). On the other hand, the corresponding hole mobility of the blend films increased 1.7-fold from 1.91 x 10^{-4} cm^2/Vs at 21 kDa to the peak value of 3.21 x 10^{-4} cm^2/Vs at 55 kDa and then decreased to 1.14 x 10^{-4} cm^2/Vs at 127 kDa (Table 2-6). These measured values of both hole and electron mobilities are comparable with previous reports for all-PSC devices containing the present donor and acceptor polymers.[29] Further analysis reveals that the blend charge transport becomes more symmetric with the μ_h/μ_e ratio approaching unity (μ_h/μ_e = 1.12 – 1.64) around the optimal molecular weight range of 55-66 kDa (Figure 2-14). The poor electron and hole mobilities accompanied by the highly asymmetric charge transport observed in the 90 kDa and127 kDa PBDB-T:PNDIBS blends is

consistent with space-charge effects and their observed inferior photovoltaic device performance. It is also clear that the higher carrier mobilities and more symmetric charge transport observed at the optimal molecular weight range (M_n = 55-66 kDa) are in good agreement with the higher J_{sc} and FF values observed in the photovoltaic properties discussed earlier.

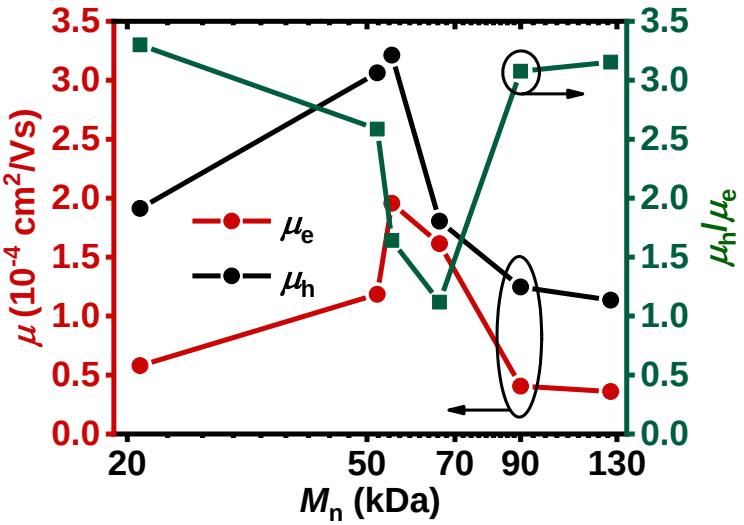

Figure 2-14. PNDIBS molecular weight (M_n) dependence of the space-charge limited current (SCLC) charge carrier mobilities of PBDB-T:PNDIBS blend films processed at the same optimal conditions used to fabricate the all-PSC devices. Reproduced in part with permission from Ref.[69] Copyright 2020 Royal Society of Chemistry.

Table 2-6. Dependence of SCLC Charge Carrier Mobilities of Optimized PBDB-T:PNDIBS Blend Films on Acceptor Polymer PNDIBS Molecular Weight. Reproduced with permission from Ref.[69] Copyright 2020 Royal Society of Chemistry.

Blend	μ_e (cm^2/Vs)	μ_h (cm^2/Vs)	μ_h/μ_e
PBDB-T:PNDIBS (21kDa)	5.80 x 10^{-5}	1.91 x 10^{-4}	3.30
PBDB-T:PNDIBS (52kDa)	1.18 x 10^{-4}	3.06 x 10^{-4}	2.59
PBDB-T:PNDIBS (55kDa)	1.96 x 10^{-4}	3.21 x 10^{-4}	1.64
PBDB-T:PNDIBS (66kDa)	1.51 x 10^{-4}	1.81 x 10^{-4}	1.12
PBDB-T:PNDIBS (90kDa)	4.05 x 10^{-5}	1.25 x 10^{-4}	3.08
PBDB-T:PNDIBS (127kDa)	3.60 x 10^{-5}	1.14 x 10^{-4}	3.15

2.2.3.5. Surface and Bulk Morphology of PBDB-T:PNDIBS Blend Films.

The PNDIBS molecular weight M_n dependence of the surface morphology of the PBDB-T:PNDIBS blend films was investigated by atomic force microscopy (AFM) imaging (Figure 2-15). The PBDB-T:PNDIBS blend films of increasing PNDIBS molecular weight evolved from tightly spaced fibrils with small domain sizes of around 24 nm in the 21 kDa to a well-connected network of needle-like features having extended domains of about 30 – 40 nm (52, 55, and 66 kDa) to featureless structures with larger domains of approximately 50 nm (90 and 127 kDa) (Figure 2-15). Combining these observations with the earlier charge photogeneration analysis, it can be concluded that the PBDB-T:PNDIBS blends that exhibit intermediate domain sizes of around 30 – 40nm are more suitable for exciton dissociation and charge generation. Although the much finer phase separation seen in the 21kDa blends could facilitate efficient exciton diffusion and dissociation, the generated charges are more likely to encounter one another and recombine prior to being extracted and thereby limit the overall photogeneration rate. On the other hand, the larger- scale phase separation in the 90 kDa and 127 kDa blends could inhibit exciton diffusion to the donor/acceptor blend interface and thus hamper the charge photogeneration rate as well. These changes of the blend surface morphology suggest two transition points from the less aggregating (21 kDa) to crystalline and well-ordered domains (52 – 66 kDa) and subsequently to the more amorphous and highly disordered structures (90 – 127 kDa). The blend morphology evolution with molecular weight parallel observations in the M_n dependencies of photovoltaic and charge transport properties, where the highest efficiencies (PCEs) and largest charge carrier mobilities occurred only in blends that exhibit intermediate domain sizes and well-ordered crystalline regions.

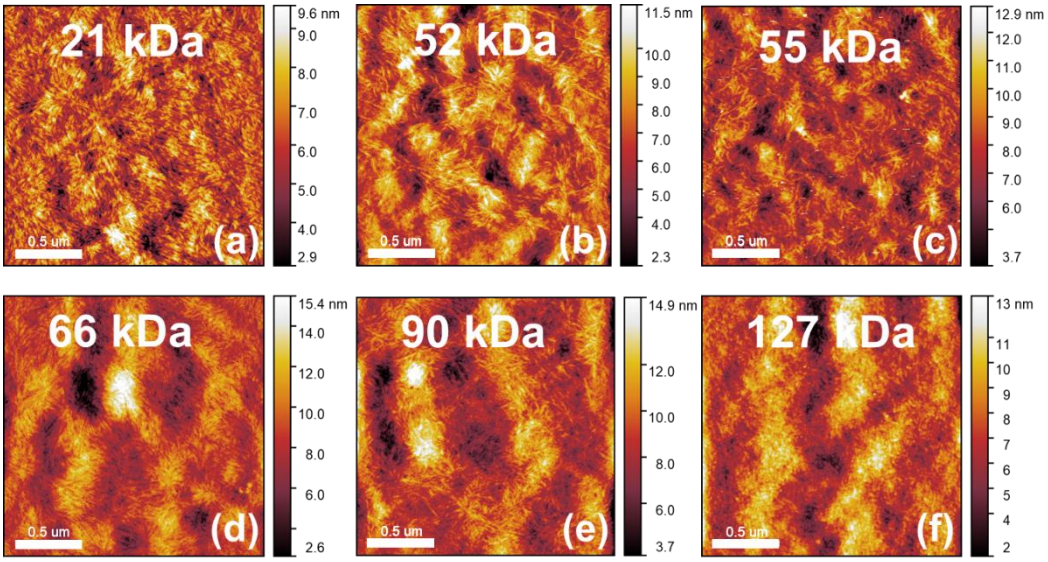

Figure 2-15. AFM height images (2μm x 2μm) of PBDB-T:PNDIBS blend films at various acceptor polymer PNDIBS molecular weight. All active layers were processed at the optimal conditions. Reproduced in part with permission from Ref.[69] Copyright 2020 Royal Society of Chemistry.

Two-dimensional (2D) grazing incident wide-angle X-ray scattering (2D-GIWAXS) measurements were carried out on the optimized PBDB-T:PNDIBS blend films of various PNDIBS molecular weights M_n. The 2D-GIWAXS images and the 1D line cuts for the PBDB-T:PNDIBS blend films are presented in Figure 2-16 and those for the neat PBDB-T films are given in Figure B-15. All blend films exhibited pronounced (100) diffraction peaks in the in-plane (IP) direction at q_{xy} = 0.25 – 0.27 Å^{-1} (Table B-4) which are similar to the values observed in the neat acceptor polymer thin films.[29] The higher order diffraction peaks (*h*00) which are characteristic of highly ordered PNDIBS had disappeared, which suggest that the polymer chain packing is less ordered upon blending with the donor polymer PBDB-T. In the out-of-plane (OOP) direction, a distinct (010) diffraction peak is observed at q_z = 1.61 – 1.66 Å^{-1} (Table B-4) for all blend films except for the 66kDa blend film. Surprisingly, the (010) peak of the 66kDa blend film shifted to a much lower q_z of 1.52 Å^{-1}. The presence of the sharp and intense (100) peak and (010) peak in the IP and OOP directions (Figure 2-16), respectively, strongly indicate

that the most crystallites in all of the PBDB-T:PNDIBS blends preferentially adopt the *face-on* orientation. Moreover, compared to the blend films of other molecular weights, the 55kDa and 66kDa blend films exhibited extremely broad and weak (100) diffraction peaks in the OOP direction. These results suggest that among all of the blend films, the highest population of *face-on* oriented crystallites can be expected in the 55kDa and 66kDa blend films, which can explain their observed better charge transport (μ_e, μ_h, and μ_h/μ_e) and their improved photovoltaic parameters (J_{sc}, FF, and PCE).

Table 2-7. Summary of d-spacing, π- π Distance, and Crystalline Coherence Length (L_c) Derived from In-Plane (IP) and Out-of-Plane (OOP) Line Cuts in 2-D GIWAXS of Blend Thin Films. Reproduced with permission from Ref.[69] Copyright 2020 Royal Society of Chemistry.

Polymer	d-spacing (Å)	π- π distance (Å)	L_c (nm) (100) IP
PBDB-T	22.0	3.73	5.2
PBDB-T:PNDIBS (21kDa)	23.5	3.85	7.8
PBDB-T:PNDIBS (52kDa)	23.5	3.79	6.9
PBDB-T:PNDIBS (55kDa)	23.5	3.85	6.5
PBDB-T:PNDIBS (66kDa)	24.7	4.14	5.5
PBDB-T:PNDIBS (90kDa)	24.1	3.85	6.2
PBDB-T:PNDIBS (127kDa)	24.7	3.90	6.5

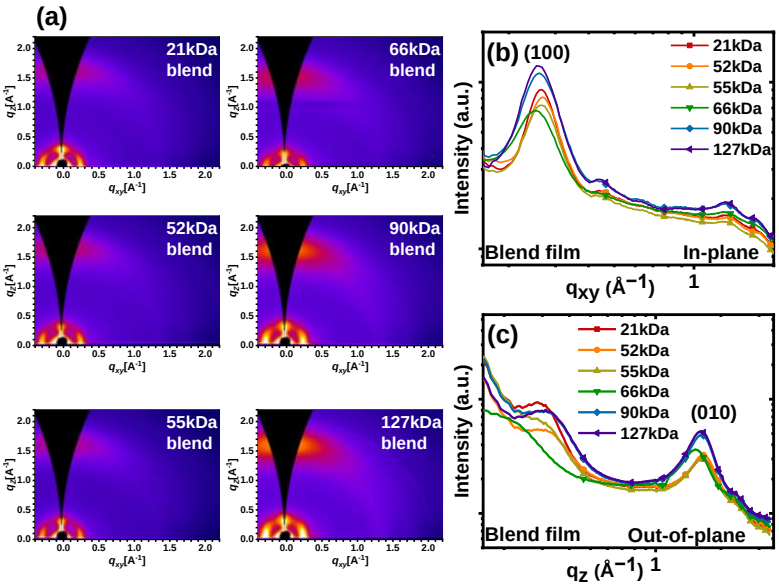

Figure 2-16. PNDIBS molecular weight dependence of 2D-GIWAXS data for PBDB-T:PNDIBS blend active layers processed at the optimal conditions: (a) 2D-GIWAXS patterns; (b, c) 1D line cuts of GIWAXS patterns in the in-plane (IP) (b) and the out-of-plane (OOP) direction (c). Reproduced with permission from Ref.[69] Copyright 2020 Royal Society of Chemistry.

The crystalline coherence length (L_c) estimated from the Scherrer's equation for all PBDB-T:PNDIBS blend films was found to decrease from 7.8 nm in the PNDIBS-21kDa blend (Table 2-7) to a minimum value of 5.5 nm in PNDIBS-66kDa blend (Table 2-7) and then rises to 6.5 nm in the PNDIBS-127kDa blend (Table 2-7 and Figure 2-17). Adding the M_n dependent photovoltaic efficiency to Figure 2-17 shows that the PCE and blend L_c trends are related, suggesting that there are perhaps three distinct blend morphology regions that impact the performance of these all-PSCs devices. In the optimal M_n region of ~ 55-66kDa, the blend film exhibits a phase-separated bi-continuous morphology with intermediate nanocrystalline domains (L_c ~ 5.5-6.5 nm) that enable good mixing of the donor and acceptor polymer counterparts, which in turn increases the donor/acceptor interfacial area and hence facilitates large exciton dissociation, charge photogeneration, and charge transport for overall enhanced PCE, J_{sc}, and FF. On the lower M_n side, the morphology is characterized by relatively large crystalline domains (L_c ~ 7-8 nm), which while enabling good charge transport lacks sufficient donor/acceptor interfacial area and charge photogeneration essential to achieve optimal performance. At higher M_n (90-127kDa), although the crystalline coherence length remains moderate (L_c ~ 6.2 – 6.5 nm), the morphology is dominated by large scale disordered microstructure evidenced by the featureless AFM images which lacked microfibrils (Figure 2-15). Consequently, blend devices at these higher M_n values suffered from severe bimolecular recombination and space-charge effects mainly due to the poor charge transport properties and lower charge extraction rate, which explain the decrease in the photovoltaic properties (PCE, J_{sc}, and FF).

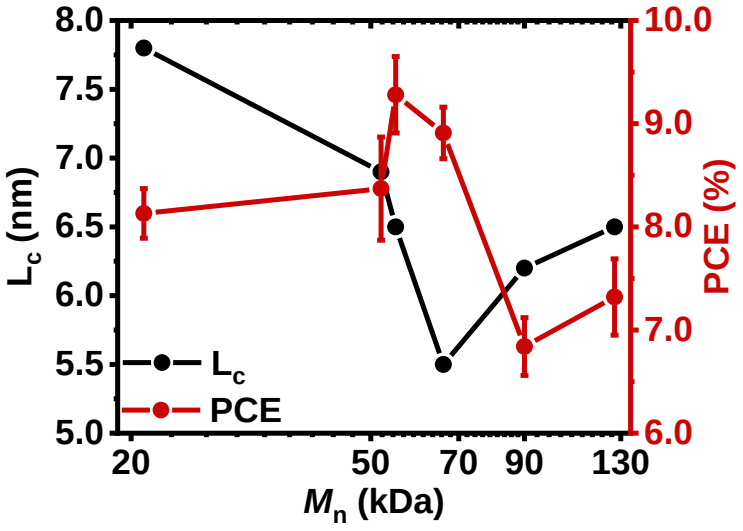

Figure 2-17. Dependencies of the power conversion efficiency (PCE) of PBDB-T:PNDIBS all-polymer solar cells and the blend crystal coherence length (L_c) on the acceptor polymer PNDIBS M_n. Reproduced in part with permission from Ref.[69] Copyright 2020 Royal Society of Chemistry.

2.2.4. Conclusions

We have synthesized six well-defined number-average molecular weight (M_n) values (21-127 kDa) of the n-type semiconducting biselenophene-naphthalenediimide copolymer (PNDIBS) via direct heteroarylation polymerization (DHAP) and used them to investigate the influence of polymer molecular weight on the morphology, photophysics, charge transport, and photovoltaic properties of all-polymer solar cells (all-PSCs). Both short-circuit current (J_{sc}) and power conversion efficiency (PCE) of the PBDB-T:PNDIBS blend devices were found to increase with increasing M_n until they peaked at an optimal M_n of 55 kDa and thereafter decreased with further increases in M_n. The maximum and average PCE of 10.2% and 9.3%, respectively, observed at the optimal M_n value of 55 kDa coincided with optimal blend charge transport properties, blend photophysics, and blend morphology at this critical molecular weight. At the optimal M_n, the blend morphology was characterized by a bi-continuous network of 5.5-6.5 nm crystalline domains with predominantly *face-on* molecular orientations whereas on the higher M_n side a

relatively disordered microstructure with larger scale phase separation was evident from 2D-GIWAXS and AFM imaging while a more finely packed crystalline microstructure was observed at 21 kDa. In particular, the observed decrease of photovoltaic parameters at higher M_n could be explained by the larger scale phase separation, decrease in electron mobility, severe bimolecular recombination, and formation of space-charge region. The sensitivity of the all-PSC device efficiency to the active layer thickness was found to depend on the acceptor polymer molecular weight. The PCE of devices at around the optimal M_n was relatively constant with active layer thickness whereas at the higher M_n the efficiency varied significantly with layer thickness, suggesting the potential of using the high molecular weight PNDIBS for semi-transparent all-PSC applications. Overall, the results of this study demonstrate the importance of tuning the molecular weight of the polymer components to optimize the morphology, charge transport, photophysics and efficiency of all-polymer solar cells. The results also provide new insights on structure-property relationships for the n-type semiconducting copolymer PNDIBS.

Chapter 3. Unified Understanding of Molecular Weight Dependence of Electron Transport in Naphthalene Diimide-Based n-Type Semiconducting Polymers

The results in this chapter are reprinted with permission from Tran, D. K.; Robitaille, A.; Hai, I. J.; Kuzuhara, D.; Koganezama, T.; Chiu, Y-C.; Leclerc, M.; Jenekhe, S. A. Unified Understanding of Molecular Weight Dependence of Electron Transport in Naphthalene Diimide-Based n-Type Semiconducting Polymers. *Chem. Mater.* **2022**, *34*, 9644-9655. Copyright 2022 American Chemical Society.

3.1. Introduction

Semiconducting polymers with good charge transport properties have paved the way for the rise of low-cost thin film organic electronic devices, including organic field-effect transistors (OFETs),[5-10] organic light-emitting diodes (OLEDs) for commercial displays and lighting,[4] organic solar cells (OSCs),[11-16] organic thermoelectrics (OTEs),[47-49] and bioelectronics.[50, 51] Understanding of the structure-property relationships in semiconducting polymers has been essential to the design and synthesis of new materials with enhanced properties that advance these device applications.[4-16, 47-52] The charge carrier mobility (μ) of semiconducting polymers in particular is a key property, which has been studied and substantially improved over the past 2 decades, leading to some polymers that now outperform polycrystalline silicon (μ > 10 cm^2/Vs).[7, 9]

Previous studies have demonstrated that high *hole* mobility can be achieved by increasing the polymer molecular weight (Figure C-1a)[163-167] in p-type semiconducting polymers such as regioregular poly(3-hexylthiophene) (P3HT) (Figure 3-1a), poly(dodecylquarterthiophene)

(PQT) (Figure 3-1a), poly(2,5-bis(3-alkylthiophen-2-yl)thieno-[3,2*b*]thiophene) (PBTTT) (Figure 3-1a). Recent studies of a broad range of polymer chain lengths in these p-type semiconducting polymers[157, 168, 169] as well as other p-type polymers with polycyclic cores such as indacenodithiophene (IDTBT)[170, 171] and fluorene (F8BT)[172] have showed that the hole mobility reaches a saturated value at a critical degree of polymerization (DP_c) and then levels off rather than continuous increase with increasing *DP*. In particular, the hole mobility was found to depend on intercrystallite connectivity for $DP < DP_c$ and local lattice disorder for $DP \geq DP_c$.[157, 168-170] As a result, the hole mobility rises steeply to its maximum value once sufficient intercrystallite connectivity is established and levels off since the local lattice disorder remains relatively constant (Figure C-1a).

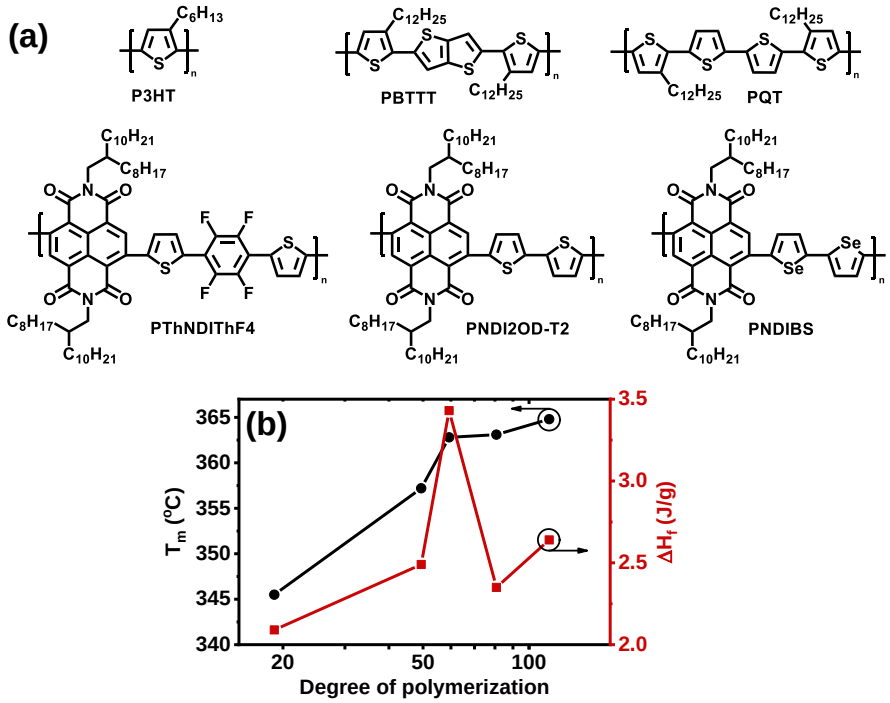

Figure 3-1. (a) Molecular structures of semicrystalline p-type semiconducting polymers (P3HT, PBTTT, and PQT) and weakly ordered n-type semiconducting polymers (PThNDIThF4, PNDI2OD-T2, and PNDIBS). (b) Degree of polymerization dependence of thermal properties of PNDIBS. Reproduced with permission from Ref.[173] Copyright 2022 American Chemical Society.

The synthesis and investigation of the charge transport properties of n-type semiconducting polymers have generally lagged behind those of p-type conjugated polymers.[7, 8] Nevertheless, high electron mobility (μ > 3 cm^2/Vs) has been achieved in some classes of n-type semiconducting polymers.[83, 85, 86, 174] The most extensively studied n-type semiconducting polymers have a donor-acceptor architecture[175, 176] as exemplified by various naphthalene diimide (NDI)-based copolymers.[7-9, 52, 177] Although the influences of the polymer molecular weight on the blend morphology, blend photophysics, and photovoltaic properties have been previously examined,[25, 29, 33, 69, 81] the dependence of electron mobility on polymer chain length and the physics governing electron transport in n-type semiconducting polymers remain scarcely explored.

Previous studies of polymer chain length effects on electron mobility in n-type conjugated polymers[33, 178-181] have shown different and even contradictory results (Figure C-1b). For instance, a study of poly(naphthalene diimide-*alt*-bithiophene) (PNDI2OD-T2) (Figure 3-1a) showed that shorter polymer chain lengths facilitate improved electron mobility (Figure C-1b) due to enhanced crystallinity.[179] However, this study did not specify whether the molecular weight was number-average or weight-average and how the molecular weight was characterized (solvent and temperature).[179] Additionally, the "higher crystallinity leads to higher mobility" rationalization is in disagreement with current understanding that lower molecular weight conjugated polymer with high degree of crystallinity exhibit lower carrier mobility due to defined grain boundaries acting as charge trapping sites.[163, 180] A different study of the same PNDI2OD-T2 polymer has similarly reported that the polymer with lower molecular weight had enhanced electron mobility compared to the higher molecular weight ones (Figure C-1b).[180] We note that this study has overlooked the impacts of polydispersity index (PDI), which increased

with increasing polymer molecular weight, where the PDI of the highest M_n sample (PDI = 3.0) was twice of that of the lowest M_n sample (PDI = 1.40);[180] thus, the observed increasing mobility with decreasing molecular weight might have been influenced by the lower PDI values. A recent study has tried to delineate the effects of PDI and M_n on the electron mobility of PNDI2OD-T2 by ensuring a relatively narrow molecular weight distributions (PDI ~ 1.2 – 1.4) and found that the electron mobility increases with increasing polymer molecular weight (Figure C-1b) due to the enhanced tie-chain fraction.[181] However, the PNDI2OD-T2 films were processed by drop-casting and subjected to solvent vapor annealing;[181] thus, even though maximal chain alignment can be achieved, the observed electron mobility even at the highest molecular weight is much lower than previously reported values (Figure C-1b).[178-180] On the other hand, another study reported that the electron mobility reached a peak at an optimal chain length (Figure C-1b), which was attributed to an optimal degree of crystallinity.[178] Furthermore, comprehensive understanding of molecular weight dependence of *bulk* electron transport in NDI-based n-type semiconducting polymers remains to be explored. In summary, results of prior studies of effects of polymer chain length on electron mobility of n-type semiconducting polymers have been contradictory, and the offered explanations have been unsatisfactory.

In this paper, we report studies of the effects of polymer chain length *DP* on *electron* transport and thin-film microstructure of poly(naphthalene diimide-*alt*-biselenophene) (PNDIBS) (Figure 3-1a), a model system for n-type semiconducting polymers with donor-acceptor architecture. The series of PNDIBS samples, prepared via direct hetero(arylation) polymerization (DHAP) method, had a sufficiently broad range of *DP* from 19 to 117. The *field-effect* electron mobility (μ_{OFET}) was measured by using organic-field effect transistors (OFETs), and the *bulk* electron mobility (μ_{SCLC}) was measured via the space-charge limited current (SCLC) technique.

We show that both μ_{OFET} and μ_{SCLC} of PNDIBS exhibit a peak at the same range of critical degree of polymerization (DP_c) of 45 – 60 repeat units. To facilitate connection of the macroscopic electron transport to the thin-film microstructure of PNDIBS, we combined atomic force microscopy (AFM) imaging and 2D-grazing incidence wide-angle X-ray scattering (2D-GIWAXS) analyses to probe the thin film multiscale polymer packings as a function of chain length *DP*. We found that when *DP* is less than DP_c, the rate-limiting step for efficient electron transport is intercrystallite transport due to insufficient electrical connectivity between ordered domains. In contrast, when *DP* is greater than DP_c, the rate-limiting step becomes intrachain, interchain, and intracrystallite transport due to backbone twisting, chain entanglements, and randomly distributed local fields acting as electron traps. Further analyses of paracrystallinity disorder, which is the local lattice disorder within a crystallite, along the polymer stacking in the lamellar and π-π stacking directions revealed the physical sources of local lattice disorder to be backbone twisting, chain folding and entanglement, and random side chain conformational disorder. Available literature data on other NDI-based copolymers were found to also correspond to this unified picture of electron transport physics of this class of n-type semiconducting polymers.

3.2. Experimental Methods

Materials. The synthesis and characterization of the series of PNDIBS samples of five different molecular weights, prepared by using the DHAP method, have previously been reported by our groups.[69]

Characterizations. The number-average (M_n) and weight-average (M_w) molecular weights were determined by size exclusion chromatography (SEC) using a high temperature Varian Polymer Laboratories GPC220 equipped with an RI detector and a PL BV400 HT Bridge

Viscometer. The column set consists of 2 PL gel Mixed C (300 x 7.5 mm) columns and a PL gel Mixed C guard column. The flow rate was fixed at 1mL/min using 1,2,4-trichlorobenzene (TCB) (with 0.0125% w/v Butylated hydroxytoluene (BHT) as an antioxidant) as the eluent. The temperature of the system was set at 110 °C. The samples (2 mg) were dissolved in 2 mL of TCB in 5 mL chromatography vials then stirred and heated to 110 °C for 1 hour for a complete dissolution. Then, the polymer solution is filtered through a 0.45 μm cellulose fiber film into a 5 mL chromatography vial to ensure a homogenous polymeric solution. The reported molecular weight data are based on polystyrene standards (Easi-Vials PS-M from Varian Polymer Laboratories) dissolved in TCB. The differential scanning calorimetry (DSC) analysis was performed on a TA Instrument Q100 under N_2 flow by scanning from -10 to 400^{o}C at heating and cooling rates of 10^{o}C/min.

Fabrication and Characterization of OFETs at TAIWAN TECH. OFET devices were fabricated on highly doped n-type Si(100) wafers with a 300-nm thick SiO_2 layer treated with a n-octadecyltrimethoxysilane (OTMS) self-assembled monolayer according to the reported method.[152] Before use, the OTMS monolayer was rinsed sequentially with toluene, acetone, and isopropyl alcohol and dried under a N_2 stream. Static water contact angles of the OTMS substrates were higher than 105^o when measured by using an Edmund Scientific goniometer. The solutions (5 mg/mL) of polymer semiconductor for transistor devices were prepared by dissolving the polymer in chlorobenzene at 80°C for 30 min and then spin-casted onto the OTMS-modified Si/SiO_2 substrates with controlled thickness at ~40 nm. The as-prepared thin films were thermally annealed at 170°C for 1 hour in a N_2-filled glove box. A top-contact gold electrode (70 nm) was subsequently deposited by evaporation through a shadow mask with a channel length (L) and width (W) defined as 50 and 1000 μm, respectively. The transistor

characteristics were measured by using a Keithley 4200 semiconductor parameter analyzer (Keithley Instruments Inc., Cleveland, OH, USA) in a N_2 filled glove box at room temperature. The saturation region field-effect electron mobility, μ_{OFET}, was calculated from the standard FET relationship:

$$I_{ds} = \left(\frac{WC_i}{2L}\right)(V_{gs} - V_T)^2\mu \qquad (Eq.\,3.1)$$

Fabrication and Characterization of OFETs at the University of Washington. OFET devices were fabricated on heavily n-doped silicon (<0.005Ωcm; 500μm) with a 300nm-thick silicon dioxide layer. The surface of the cleaned substrate was treated with air plasma before immersing in octadecyltrichlorosilane (OTS-18):Toluene (1:500, v:v) overnight to form a self-assembled monolayer (SAM). Afterwards, the treated substrates were washed and sonicated in toluene to remove excess physiosorbed OTS-18, and then they were thermally annealed at 100°C for 10 min in ambient air. Solutions of PNDIBS (5 – 7 mg/mL) were prepared by dissolving the polymer in chlorobenzene and stirred at 85°C for at least 1 hour inside a N_2-filled glovebox. The PNDIBS solutions were spin-coated onto the OTS18-modified Si/SiO_2 substrates, and the resulting PNDIBS films were thermally annealed at 170°C for 1 hour in a N_2-filled glove box. Source and drain electrodes were defined by thermal evaporation of gold electrodes (60 nm). Channel length (L) and width (W) were 100μm and 1000μm, respectively. The transistor characteristics were measured by using a Keithley 4200 SCS semiconductor parameter analyzer (Keithley Instruments Inc., Cleveland, OH, USA) in a N_2-filled glove box at room temperature. The saturation region field-effect electron mobility, μ_{OFET}, was calculated from the standard FET relationship (Equation 1).

Fabrication and Characterization of SCLC Devices. Current-voltage (*J*-*V*) characteristics of the SCLC devices were measured by using a HP4155A semiconductor parameter analyzer

(Yokogawa Hewlett-Packard, Tokyo). The carrier mobility was deduced by fitting the *J-V* curves to the Mott−Gurney equation where *J* is the current density, ε_o is the permittivity of free space, ε is the relative permittivity, μ_{SCLC} is the zero-field mobility, *V* is the voltage, *L* is the thickness of semiconducting polymer layer:

$$J = \frac{9}{8}\varepsilon_0\varepsilon\mu\frac{V^2}{L^3} \qquad (Eq.3.2)$$

The SCLC device structure was ITO/ZnO/PEI/PNDIBS/LiF (1nm)/Al (100nm). ZnO and polyethyleneimine (PEI) solutions were prepared as previously reported.[121, 182] The ZnO precursor solution was spin-coated onto ITO substrates and annealed at 200°C for 30 min in ambient air. Afterwards, the PEI solution was spin-coated onto the dried ZnO layer and thermally annealed at 120°C for 10 min. The ITO/ZnO/PEI coated substrates were then transferred to an Argon-filled glovebox to deposit the polymer semiconductor layer. The PNDIBS film was spin-coated at 1000 rpm for 50s and followed by thermal annealing at 110°C for 10 min inside an Argon-filled glovebox.

AFM Imaging. Atomic force microscopy (AFM) characterization of the surface morphology of the PNDIBS films was done using a Bruker Dimension scanning probe microscope (SPM) system. Films of PNDIBS of different number-average molecular weight values were spin-coated at 1000 rpm for 50 s and followed by thermal annealing at 110°C for 10 min inside an Argon-filled glovebox.

GIWAXS. Grazing incidence X-ray scattering (GIWAXS) experiments were conducted at the Japan Synchrotron Radiation Facility SPring-8 by using the beamlines BL46XU. Thin film samples of PNDIBS were spin-coated on the top of glass substrates and annealed at 110 °C for 10 min. The X-ray beam was monochromatized by a double-crystal Si(111) monochromator, and the X-ray energy in this experiment was 12.40 keV (λ = 0.1 nm). The angle of incident X-ray to

sample surface was 0.12° with a Huber diffractometer. The scattered profile from the film sample was detected using an area detector (PILATUS 300K) for 1 s at room temperature, and the distance between the sample and detector was 175.0 mm. The crystal coherence length (L_c) of samples was determined by using the Scherrer equation: $L_c = 2\pi K/\Delta q$, where K is a shape factor (typically 0.9) and Δq is the full width at half-maximum (FWHM) of the diffraction peak. Here, the L_c (100) and L_c (010) were obtained respectively from the FWHM of the (100) diffraction peak in the in-plane (q_{xy}) line-cut and the FWHM of the (010) diffraction peak in the out-of-plane (q_z) line-cut.

3.3. Results and Discussion

3.3.1. Optical and Thermal Properties.

Thin-film optical absorption spectra of PNDIBS of various number-average molecular weight (M_n) values have been previously reported by our group.[29, 69] Two absorption bands centered at 397 – 399 nm and at 711 – 718 nm were observed (Figure C-2a), which are assigned to the π-π* transition and intramolecular charge transfer (ICT).[69] The main effect of M_n is a small progressive blue shift of the ICT band from 718 nm to 711 nm with increasing M_n, with the exception of the 90kDa sample, indicating that the intramolecular charge transfer interaction between the NDI moiety and the biselenophene moiety is weakened due to backbone distortion.[69] The slight bathochromic shift in the ICT band of the 90kDa films suggests significant chain aggregation which might be caused by the slightly higher PDI value (Table 3-1) compared to the other polymer samples.

The polymer chain length dependence of the thermal properties of PNDIBS, as characterized by differential scanning calorimetry (DSC) scans (Figures C-2b and C-2c), including melting temperature (T_m), crystallization temperature (T_c), enthalpy of fusion (ΔH_f),

and the entropy of fusion (ΔS_f), are summarized in Table 3-1 and presented in Figure 3-1b. The T_m progressively increased from 345.5°C at *DP* ~ 19 to 364.8°C at *DP* ~ 117, which can be rationalized by increased chain folding and chain entanglements at the higher *DP*.[178, 180] In contrast, the crystallization temperature T_c remained relatively constant at around 347.5°C – 348.5°C for *DP* varying between 19 and 117 (Table 3-1). The independence of T_c on *DP* can be explained by supercooling effects as exemplified by the temperature offset between the T_m and T_c (2K – 16K) and the vertical lines after nucleation in the cooling traces (Figure C-2c). In this case, the polymers crystallize rapidly even at a slow cooling rate of 10°C/min; thus, the T_c appeared independent of the *DP*. The enthalpy of fusion ΔH_f reached its peak value of 3.43 J/g at DP ~ 60 and subsequently decreased as *DP* increased further. The entropy of fusion ΔS_f followed a similar *DP* dependence as ΔH_f, reaching a maximum at DP ~ 60 (Table 3-1). Since the change in entropy of fusion can be expressed as:

$$\Delta S_f = S_{melt} - S_{crystal} = k\left(ln\Omega_{melt} - ln\Omega_{crystal}\right) \qquad (Eq.\,3.3)$$

where k is the Boltzmann constant and Ω_i is the total possible microscopic configurations of the polymer chains in state i, the observed maximum ΔS_f at *DP* ~ 60 implies that $S_{crystal}$ and $\Omega_{crystal}$ are minimized and thus suggests highly ordered crystallites that enable efficient intrachain and interchain packings.

Table 3-1. Molecular Weight, Optical Properties, and Thermal Properties of PNDIBS. Reproduced with permission from Ref.[173] Copyright 2022 American Chemical Society.

M_n (kDa)	PDI	DP[(a)]	T_m (°C)	T_c (°C)	ΔH_f (J/g)[(b)]	ΔS_f (10^{-3} J/gK)[(c)]
21	1.7	19.4	345.5	347.5	2.09	3.4
55	2.4	50.8	357.2	348.5	2.49	4.0
66	2.6	60.9	362.8	348.2	3.43	5.4

90	3.0	83.1	363.1	348.1	2.35	3.7
127	2.3	117.2	364.8	348.5	2.64	4.1

[(a)] DP = M_n/M, where M is the molecular weight of a repeat unit.
[(b)] ΔH_f calculated from the differential scanning calorimetry (DSC) traces of the 2nd cooling cycle.
[(c)] ΔS_f calculated from $\Delta S_f = \Delta H_f/T_m$ assuming $\Delta G_f = 0$ for equilibrium.

3.3.2. Field-Effect Electron Transport.

We characterized the *field-effect* electron transport properties of several PNDIBS samples with different *DP* values by using n-channel organic field-effect transistor (OFET) devices fabricated and characterized independently at the University of Science and Technology (TAIWAN TECH) and the University of Washington (UW). The TAIWAN TECH devices were fabricated using a bottom-gate/top-contact architecture with channel dimensions of 50μm/1000μm (L/W), while the UW devices were fabricated using a bottom-gate/top-contact architecture with channel dimensions of 100μm/1000μm (L/W) . The output curves and transfers curves for the TAIWAN TECH devices are given in Figures C-3 and C-4, respectively while those of the UW devices are presented in Figures C-5 and C-6. The OFET parameters for all devices are shown in Table 3-2. The saturated *field-effect* electron mobility (μ_{OFET}) as a function of *DP* is presented in Figure 3-2a. The on/off current ratio (I_{on}/I_{off}) of the devices was generally very high (> 10^4 – 10^6) for all the *DP* values. The average electron mobility μ_{OFET} obtained from the TAIWAN TECH devices increased from 0.16 cm^2/Vs at *DP* ~ 19 to a peak of 0.26 cm^2/Vs at *DP* ~ 50 and subsequently decreased to 0.08 cm^2/Vs at *DP* ~ 117. A similar trend in the μ_{OFET} as a function of DP was also observed for the UW devices where μ_{OFET} rose from 0.034 cm^2/Vs at *DP* ~ 19 to a maximum of 0.20 cm^2/Vs at *DP* ~ 60 and dropped to 0.07 cm^2/Vs at *DP* ~ 117. The slight difference in the absolute μ_{OFET} values obtained by the two institutions likely originated from the subtle differences in device fabrication procedures. Nevertheless, these results suggest

that there exists a critical degree of polymerization (DP_c) range between 50 – 60 repeat units where the *field-effect* electron mobility is maximized. The observation of a rise in electron mobility of PNDIBS with chain length to a peak value followed by decline past the DP_c regime is interesting and to be contrasted with known chain length dependence of the *hole* transport properties of classic semi-crystalline p-type semiconducting polymers, where the hole mobility does not decline from its peak value (Figure C-1a).[157, 168-172]

Table 3-2. Electron Transport Properties of PNDIBS. Reproduced with permission from Ref.[173] Copyright 2022 American Chemical Society.

M_n (kDa)	DP	μ_{SCLC} (10^{-4} cm^2/Vs)[(a)]	μ_{FET} (cm^2/Vs)[(b)]	I_{on}/I_{off} [(b)]	V_t [(b)] (V)	μ_{FET} (cm^2/Vs)[(c)]	I_{on}/I_{off} [(c)]	V_t [(c)] (V)
21	19.4	1.68 ± 0.42	0.034 ± 0.006	$>10^5$	11.7	0.16 ± 0.003	$>10^6$	27.6
55	50.8	3.89 ± 0.97	0.15 ± 0.03	$>10^5$	14.6	0.26 ± 0.05	$>10^6$	29.0
66	60.9	4.91 ± 0.63	0.20 ± 0.06	$>10^5$	15.5	0.23 ± 0.05	$>10^6$	31.2
90	83.1	1.22 ± 1.50	0.10 ± 0.03	$>10^4$	5.9	0.20 ± 0.01	$>10^6$	27.5
127	117.2	0.91 ± 0.31	0.07 ± 0.01	$>10^4$	4.3	0.08 ± 0.02	$>10^6$	23.9

[(a)]Average values were obtained from four different devices.
[(b)]Average values were obtained from at least six different devices which were fabricated and characterized at the UW.
[(c)]Average values were obtained from six different devices which were fabricated and characterized at TAIWAN TECH.

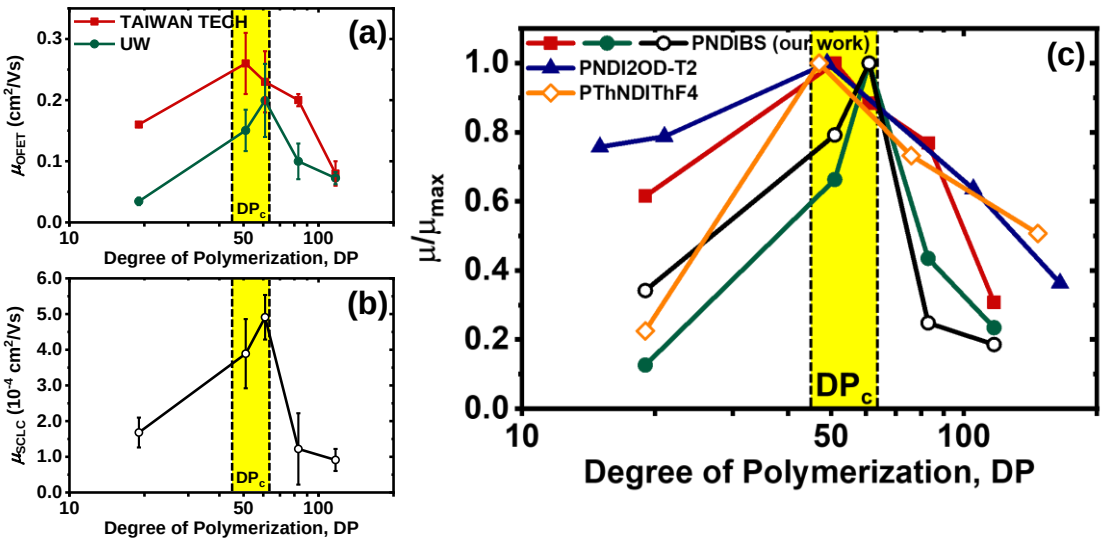

Figure 3-2. (a) Dependence of *field-effect* electron mobility (μ_{OFET}) on degree of polymerization of PNDIBS for devices fabricated independently at TAIWANTECH and at the UW. Error bars represent +/- standard deviation. (b) Dependence of bulk electron mobility (μ_{SCLC}) on degree of polymerization of PNDIBS. Error bars represent +/- standard deviation. (c) Normalized (μ/μ_{max}) *field-effect* electron mobility (filled symbols) and *bulk* electron mobility (unfilled symbols) as a function of the degree of polymerization of n-type semiconducting polymers including our present work and literature data.[33, 178] Reproduced with permission from Ref.[173] Copyright 2022 American Chemical Society.

3.3.3. Bulk Electron Transport.

Towards a broader understanding of the chain length dependence of electron transport in PNDIBS, we next focused on using the space-charge limited current (SCLC) method to characterize the *bulk* electron transport in the films. Unlike OFET-derived electron mobility μ_{OFET}, which is sensitive to only a few nanometers of the semiconductor near the dielectric interface, the SCLC electron mobility (μ_{SCLC}) characterizes the *bulk* electron mobility over a few hundred nanometers of the semiconductor layer sandwiched between the electrodes. Details of the fabrication and characterization procedures for the electron-only SCLC devices, ITO/ZnO/PEI/PNDIBS/LiF/Al, are outlined in the Experimental Methods. The SCLC *J-V* curves and the Mott-Gurney equation fit lines are given in Figure C-7, and the average SCLC electron mobility values are summarized in Table 3-2. The dependence of the *bulk* electron mobility

μ_{SCLC} on the degree of polymerization is shown in Figure 3-2b. The average electron mobility increases monotonically from 1.68 x 10^{-4} cm^2/Vs to a peak at 4.91 x 10^{-4} cm^2/Vs as the polymer chain elongates from around 20 repeat units to around 50-60 repeat units beyond which the μ_{SCLC} value steeply decreases to 0.91 x 10^{-4} cm^2/Vs (Table 3-2). This result indicates that there is also a critical polymer chain length region between 50-60 repeat units where the *bulk* electron mobility is maximized. The fact that both the *field-effect* electron mobility and the *bulk* electron mobility are maximized at the same DP_c range between 50 – 60 repeat units for PNDIBS is very significant since this has not been previously identified in the literature.

To arrive at a more complete understanding of the physics of electron transport in *n-type* semiconducting polymers, we collected the few available literature data on polymer molecular weight dependence of electron mobility,[33, 178] where the conjugated polymers were processed from common solvent (chlorobenzene or chloroform) and deposition methods (i.e. spin-coating), and the polymer molecular weights were characterized at high temperature (T > 80°C). The normalized electron mobility (μ/μ_{max}) as a function of the degree of polymerization *DP* for the present PNDIBS along with the literature data for various naphthalene diimide (NDI)-based conjugated polymers are shown in Figure 3-2c. It is clear from the data in Figure 3-2c that the maximum electron mobility is observed in a narrow range of critical degree of polymerization of about 45 – 60 repeat units for all the polymers, suggesting generality of the observed dependence of electron transport on polymer molecular weight beyond PNDIBS.

The observed peak in the dependence of *electron* mobility on *DP* of n-type semiconducting polymers is in sharp contrast with the known chain length dependence of *hole* mobility of p-type semiconducting polymers, where the *hole* mobility saturates and levels off once interdomain connectivity is established (Figure C-1a). What this difference in *DP*

dependence suggests is that factors limiting efficient electron transport in n-type semiconducting polymers are different from those limiting hole transport in p-type semiconducting polymers.[157, 168-172] Furthermore, we note that the different NDI-based n-type semiconducting polymers, whose electron transport data in Figure 3-2c show similar trend, have a donor-acceptor architecture with very different donor moieties; this implies that the physics governing multiscale electron transport is universal across at least this class of n-type semiconducting polymers. Thus, to elucidate the underlying mechanisms governing the chain length dependence of electron transport properties in the class of NDI-based n-type semiconducting polymers, we sought to understand the morphology of PNDIBS thin films by using AFM and GIWAXS characterization results presented below.

3.3.4. Surface Morphology.

AFM height images of PNDIBS thin films are shown in Figure C-8, and the calculated two-dimensional Fast Fourier transformed (2D-FFT) images are presented in Figure C-9. Thin films of PNDIBS within the DP_c range exhibited highly ordered and elongated fibrillar structures (Figures C-8b-c) whereas films of PNDIBS outside the DP_c range were featureless (Figures C-8a, d, and e). Moreover, the root-mean-square surface roughness (R_q) of films within the DP_c range was found to be the smallest (R_q = 0.68 – 0.72 nm) suggesting a homogenous and well-connected network of crystalline domains. Further examination of the orientational alignment of the fibrils by means of 2D-FFT images showed that samples where DP is higher than DP_c exhibited a uniform radial distribution (Figures C-9d-e), indicating that the fibrils are randomly oriented with no preferential directionality across the film surfaces.[180, 183] In contrast, samples where $DP \leq DP_c$ showed anisotropic 2D-FFT images (Figures C-9a-c), which suggests strong fiber alignment along certain directions over several micrometers[180, 183] and thus very surprising

since the films were prepared by spin coating and not by any processing technique that could induce preferential orientation (e.g. blade coating, solution shearing, or inkjet printing). The presence of strong fibrillar directionality in the thin-film microstructure of PNDIBS in the DP_c range is expected to be beneficial to the multiscale electron transport properties as further discussed below.

3.3.5. Bulk Thin Film Morphology.

Two-dimensional grazing incidence wide-angle X-ray scattering (2D-GIWAXS) measurements were carried out on thin films of PNDIBS of various molecular weights. The 2D-GIWAXS images and the 1D line cuts for PNDIBS films are presented in Figure 3-3. The peak positions are summarized in Table C-1 whereas the lamellar spacings, the π-π stacking distance, the crystalline coherence length (L_c), and the paracrystallinity disorder (g) are presented in Table 3-3.

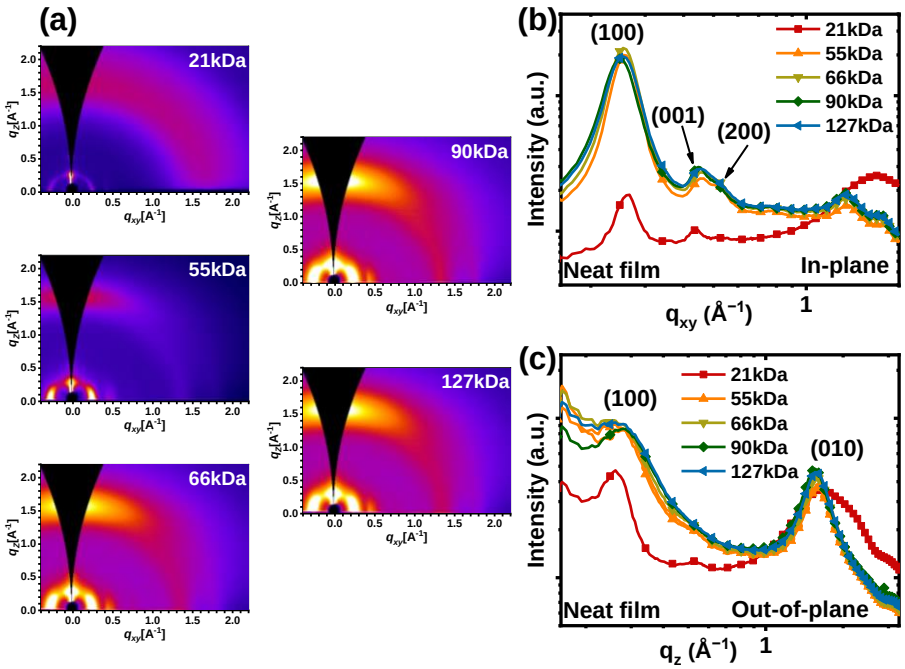

Figure 3-3. Molecular weight dependence of 2D-GIWAXS data for PNDIBS thin films: (a) 2D-GIWAXS patterns; (b and c) 1D line cuts of GIWAXS patterns in the in-plane (IP) direction (b)

and the out-of-plane (OOP) direction (c). Reproduced with permission from Ref.[173] Copyright 2022 American Chemical Society.

Film of PNDIBS of various molecular weights had an intense (100) diffraction peak in the in-plane (IP) direction at q_{xy} = 0.25 – 0.27 Å^{-1} (Table C-1) which corresponds to varying lamellar *d*-spacing of 23.5 – 25.3 Å (Table 3-3). These lamellar packing distances in PNDIBS films are significantly shorter than expected from their alkyl chain lengths, which is indicative of strong inter-digitation of the alkyl side chains between adjacent polymer backbones.[142] Except for the lowest molecular weight sample (M_n = 21kDa), films of the higher molecular weight PNDIBS also exhibited higher order diffraction peaks (*h*00) in the in-plane direction (Figure 3-3b). In the out-of-plane (OOP) direction, the PNDIBS-21kDa thin films showed a distinct (100) peak and a very broad (010) peak at q_z of 0.26 Å^{-1} and 1.64 Å^{-1}, respectively, suggesting that the low molecular weight PNDIBS adopts both *edge-on* and *face-on* molecular orientations. Films of all the higher molecular weight PNDIBS samples exhibited sharp and intense (010) diffraction peak at q_z = 1.55 – 1.59 Å^{-1} (Table C-1) accompanied by a broad and weak (100) peak in the OOP direction, which suggests that most of the crystallites were oriented *face-on* with respect to the substrates. The π-π stacking distances in the PNDIBS thin films of various M_n values are found to be 3.83 – 4.06 Å (Table 3-3), which are comparable to previous reports of π-π stacking distances in majority of NDI-based semiconducting copolymers.[142]

Table 3-3. Summary of Lamellar *d*-Spacing Distance, π-π Stacking Distance, Crystalline Coherence Length (L_c) in the In-Plane (IP) and Out-of-Plane (OOP) Directions, and the Paracrystallinity Disorder in the Lamellar (g_{lam}) and the π-Stacking Directions (g_π) of PNDIBS Films at Various Number-Average Molecular Weight (M_n) values. Reproduced with permission from Ref.[173] Copyright 2022 American Chemical Society.

M_n (kDa)	DP	d-spacing (Å)	π- π distance (Å)	L_c (nm) (100) IP	L_c (nm) (010) OOP	g_{lam} (%) (100) IP	g_π (%) (010) OOP
21	19.4	23.5	3.83	14.0	0.54	15.7	30.9
55	50.8	24.7	3.94	11.4	1.24	17.5	21.4
66	60.9	24.7	3.96	10.7	1.26	18.2	21.2
90	83.1	25.3	4.06	9.6	1.36	19.4	20.6
127	117.2	24.7	4.00	9.3	1.30	19.5	20.9

An interesting visualization of how the thin-film microstructure evolves as a function of the polymer chain length is obtained in Figure 3-4 by displaying the dependence of the lamellar d-spacing and π-π stacking distance versus degree of polymerization *DP* (Figure 3-4a). Three distinct regions, including $DP < DP_c$, $DP = DP_c$, and $DP > DP_c$, can be identified, each of which represents a specific polymer packing motif as illustrated in Figure 3-4b. In region I ($DP < DP_c$), the shortest d-spacing and π-π stacking distances indicate that these short polymer chains are packed efficiently featuring high backbone planarity and improved intermolecular π-orbital overlapping.[184] In region II ($DP = DP_c$), both the lamellar distance and the π-π stacking distance increase, which can be seen as consequences of some degree of backbone twisting. In region III ($DP > DP_c$), further increases in the lamellar distance and the π-stacking distance are observed, suggesting significant chain folding, chain entanglements, and random rotational conformation of the flexible alkyl side chains. We note that the slightly higher lamellar and π-π stacking distance observed in the 90kDa sample compared to the 127kDa sample could be due to

increased chain aggregation as evidenced by the previously discussed bathochromic shift in the optical absorption. Nevertheless, the proposed microstructural pictures (Figure 3-4b) are well corroborated by the optical and thermal properties as well as the paracrystallinity disorder as discussed below. We also note that our proposed evolution of thin film microstructures as a function of polymer chain length is in good accordance with a study on diketopyrrolopyrrole (DPP)-based semiconducting polymers.[185] Clearly, the observed evolution of intramolecular and intermolecular packings as a function of chain length can significantly influence the multiscale electron transport in PNDIBS films as further discussed below.

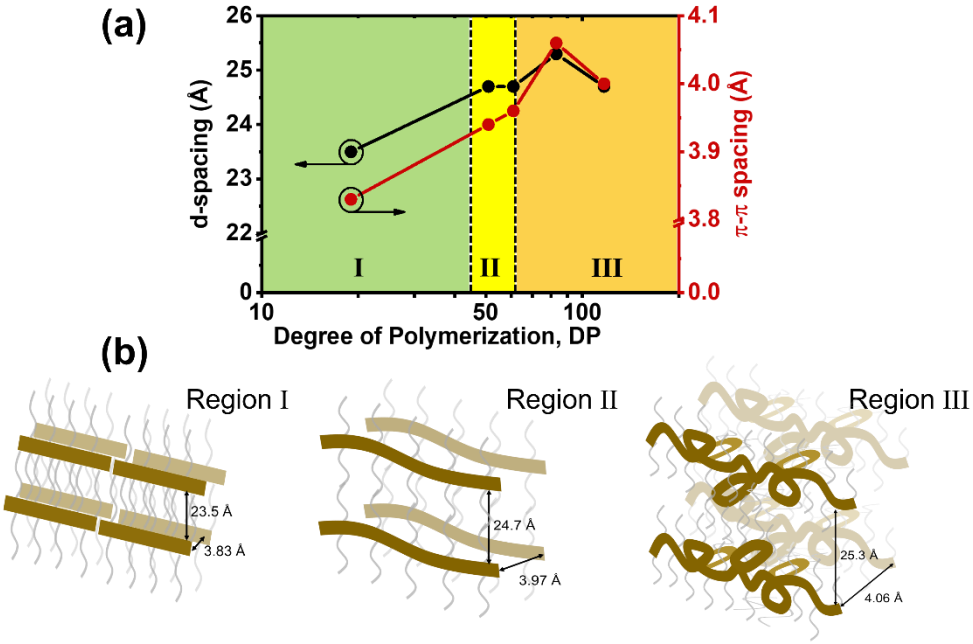

Figure 3-4. (a) Effects of degree of polymerization on the intermolecular packing distances in the lamellar direction (d-spacings) and in the π-direction (π-π spacings), and (b) Schematics of the solid-state packings as a function of polymer chain length. Reproduced with permission from Ref.[173] Copyright 2022 American Chemical Society.

The crystalline coherence length (L_c) estimated from the full-width at half-maxima of both the (100) diffraction peak in the IP direction and the (010) diffraction peak in the OOP direction are presented in Table 3-3 while the chain length dependence of L_c values are shown in

Figure 3-5a. The IP direction L_c (100) value is found to monotonically decrease with increasing degree of polymerization from 14.0 nm at *DP* ~19 to 9.3 nm at *DP* ~ 117, which means that the crystallite sizes and the crystallinity progressively decrease as the polymer chain grows. In addition, the OOP direction L_c (010) value increases with increasing chain length (Figure 3-5a) from 0.54 nm (*DP* ~ 19) to 1.24 - 1.26 nm (*DP* ~ 60) and to 1.30 – 1.36 nm (*DP* > 80). The observed progressive increase in values of L_c (010) suggests slightly enhanced long-range ordering as the polymer chain grows.[186]

The paracrystallinity disorder was also estimated using the single-peak fit approximation method[157, 187] in both the lamellar direction (g_{lam}) and the π-stacking direction (g_π) to quantify the degree of intracrystallite disorder. The numerical values of g_{lam} and g_π are summarized in Table 3-3 while the relationships between the degree of polymerization and *g* values are shown in Figure 3-5b. With the exception of the lowest molecular weight sample (*DP* ~ 19) where g_π is likely to be overestimated due to the extremely broad (010) diffraction peak in the OOP direction (Figure 3-3c), the g_π values of the other samples remain constant at around 21%. This result implies that the local disorder within a crystallite along the π-stacking direction is independent of polymer chain length. On the other hand, the g_{lam} values are found to gradually increase with increasing degree of polymerization from around 16% (*DP* ~ 19) to 18% (*DP* ~ 60) and to 20% (*DP* > 80). This observation suggests that the physical source of local lattice disorder of n-type semiconducting polymers, which has remained unclear thus far,[188] lies in chain folding, kinks, and random side chain entanglements which can be worsened at longer polymer chain lengths. The increasing disorders in the lamellar direction could significantly disrupt efficient stackings and render the polymer more amorphous, which further corroborates the proposed

microstructural pictures (Figure 3-4b) and is in good agreement with the observed trend in the IP direction L_c (100) values.

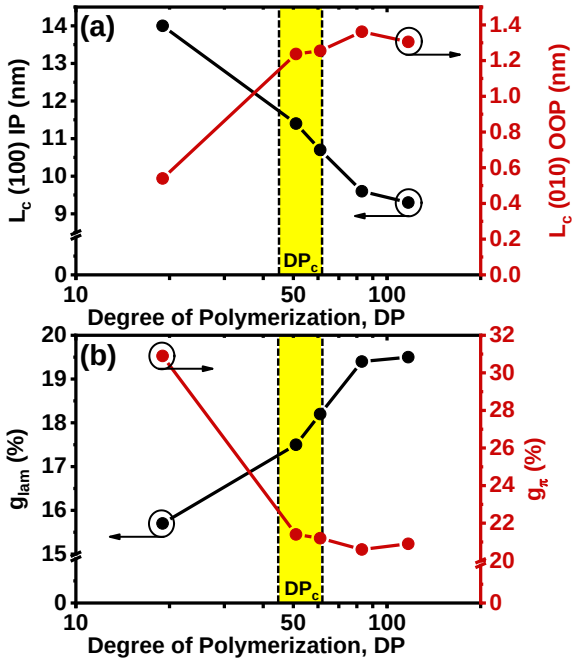

Figure 3-5. (a) Effects of polymer chain length on crystalline coherence length (L_c), and (b) Effects of polymer chain length on paracrystallinity disorder (g). Reproduced with permission from Ref.[173] Copyright 2022 American Chemical Society.

3.3.6. Understanding Electron Transport in n-Type Semiconducting Polymers.

The key experimental observations on the electron transport properties and the thin-film morphology of PNDIBS can be summarized as follows: (i) Both the *field-effect* electron mobility and *bulk* electron mobility are found to be concurrently maximized at a critical range of polymer chain length DP_c of 45 – 60 repeat units. This important structure-property relationship finding for NDI-based semiconducting polymers is likely to be broadly applicable to other classes of n-type D-A copolymers; (ii) Preferential alignment of fibrils over several micrometers across the film surface is observed for $DP \leq DP_c$; (iii) Three distinct microstructure regimes, $DP < DP_c$, $DP = DP_c$, and $DP > DP_c$, were found to characterize the evolution of the lamellar distance and the π-π stacking distance as a function of polymer chain length; (iv) Polymer crystallinity

decreases monotonically with increasing polymer chain length; and (v) Paracrystallinity disorder in the π-stacking direction is independent of the polymer chain length, whereas the paracrystallinity disorder in the lamellar direction scales approximately linearly with the polymer chain length.

Increasing the polymer molecular weight in order to maximize the crystallinity is one of the long-standing material design rules for achieving efficient charge transport in conjugated polymers.[8, 165, 189] However, our results in conjunction with available literature data show that there is rather a weak correlation between crystallite size and electron mobility in NDI-based n-type semiconducting polymers (Figure C-10). This finding suggests that there are other factors, beyond material crystallinity and maximal polymer chain length, that hinder efficient macroscopic electron transport in NDI-based n-type semiconducting polymers.

Based on the above results on polymer chain length dependent electron transport properties and thin film microstructure results from AFM imaging and 2D-GIWAXS analyses, we propose a schematic to visualize the multiscale packing of polymers as a function of chain length (Figure 3-6). We use the schematic in Figure 3-6 to guide the delineation of various factors that limit electron transport in PDNIBS and other n-type semiconducting polymers. The overall macroscopic electron mobility can be expressed as the sum of a series of mobilities[190] spanning over multiscale[191, 192] from intrachain ($\mu_{\text{intrachain}}$) and interchain ($\mu_{\text{interchain}}$) to intracrystallite ($\mu_{\text{intracrystallite}}$) and intercrystallite ($\mu_{\text{intercrystallite}}$):

$$\frac{1}{\mu} = \frac{1}{\mu_{intrachain}} + \frac{1}{\mu_{interchain}} + \frac{1}{\mu_{intracrystallite}} + \frac{1}{\mu_{intercrystallite}} \qquad (Eq.\,3.4)$$

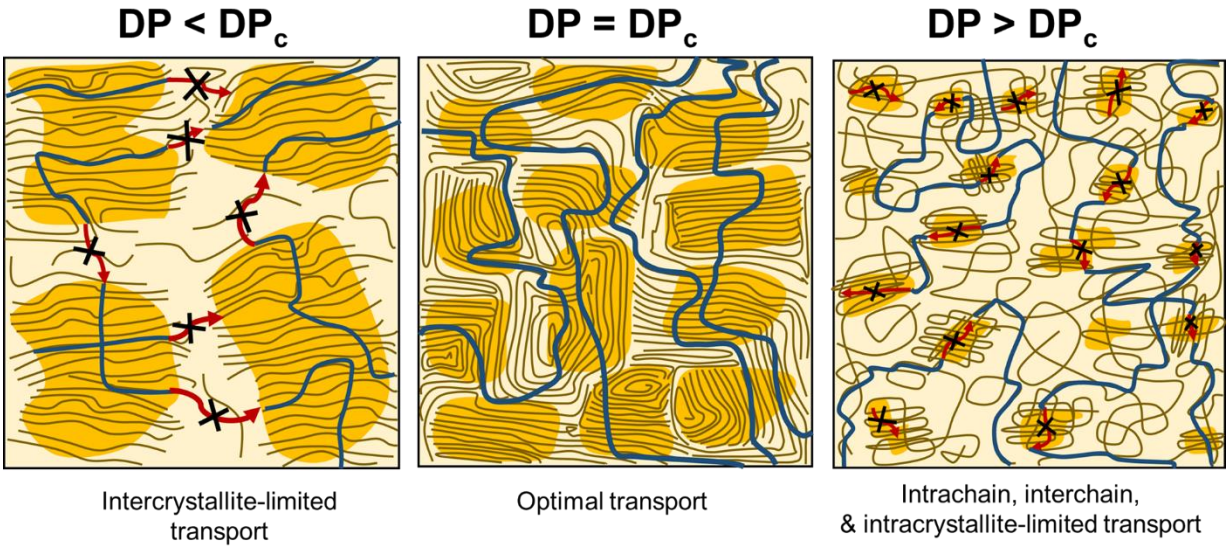

Figure 3-6. Schematic of proposed picture of how polymer chain length influences macroscopic charge transport in n-type semiconducting polymers. Reproduced with permission from Ref.[173] Copyright 2022 American Chemical Society.

In the case of $DP < DP_c$, the polymer chains are the least coiled, ensuring maximum backbone planarity and thus enabling efficient *intrachain* mobility. Moreover, polymer chains in this regime also exhibit shorter intermolecular packing distances in the π-stacking direction, as described earlier, leading to improved *interchain* electronic coupling and increased electron hopping rate and thus overall enhanced *interchain* mobility. However, the short polymer chain length severely limits electron transport between crystallites due to insufficient intercrystallite connectivity; thus, inhibiting the intercrystallite mobility. As a result, the $DP < DP_c$ regime is characterized by intercrystallite-limited electron transport (Figure 3-6):

$$\frac{1}{\mu} \sim \frac{1}{\mu_{intercrystallite}} \quad , \qquad for\ DP < DP_c \qquad (Eq.\ 3.5)$$

In the case of $DP > DP_c$, the intercrystallite transport is no longer the rate-limting step since sufficient electrical connectivity can be provided by the much longer polymer chains. The above 2D-GIWAXS results revealed that although the paracrystallinity disorder in the π-π direction remained relatively constant, the paracrystallinity disorder along the lamellar direction

increased dramatically in the longer polymer chains due to intrachain folding, interchain entanglements, and random conformational disorder of the flexible alkyl side chains; thereby, reducing intracrystallite ordering. Severe chain folding and chain entanglements also result in inefficient intermolecular packing featuring larger π-π stacking distances, and consequently diminished short-range ordering and hindered intrachain charge delocalization and interchain hopping rate. Furthermore, the lack of a preferential fibrillar directionality suggests that the long polymer chains are likely to be randomly oriented across the film surface. Consequently, intrinsic dipole moments of the polymer chains can act as random local fields that trap electrons and significantly reduce the mobility.[193] Thus, the $DP > DP_c$ regime can be categorized as intrachain, interchain, and intracrystallite-limited electron transport (Figure 3-6):

$$\frac{1}{\mu} \sim \frac{1}{\mu_{intrachain}} + \frac{1}{\mu_{interchain}} + \frac{1}{\mu_{intracrystallite}} \quad , \qquad for\ D > DP_c \qquad (Eq. 3.6)$$

In the critical chain length range, $DP = DP_c$, sufficient intercrystallite connectivity, efficient intrachain electron delocalization, fast interchain hopping rate, combined with strong fiber alignment across several micrometers of film surface facilitate maximal electron transport (Figure 3-6). Thus, in this critical degree of polymerization range the electron mobility is best described by *Eq*. 3.4.

The reason why the dependence of charge transport on polymer molecular weight in n-type polymers intrinsically differs from that of p-type polymers is likely to originate from the polymer architectures. The trend of hole mobility as a function of *DP* in p-type polymers has been reported mostly for either semicrystalline homopolymers (P3HT, PBTTT, and PQT)[157, 163-167, 194] or donor-acceptor polymers with polycyclic cores (indacenodithiophene and fluorene).[170-172] These p-type polymers bear linear alkyl side chains which allow for better interdigitation, efficient packing, and more resistance to entanglement as evidenced by the relatively constant

structural disorder,[157, 168-170, 172] implying that once sufficient intercrystallite connectivity is achieved, the hole mobility in p-type polymers remains relatively constant. We speculate that if bulky and branch side chains were incorporated into p-type polymers instead of linear chains, increased structural disorder would be inevitable. In that case, the chain length dependence of hole mobility would likely be similar to the observed trend in our present study that is, μ_h would rise to a maximum value representing intercrystallite-limited transport regime and subsequently decrease, signifying intrachain-, interchain-, and intracrystallite-limited transport regime. Indeed, a recent study of DPP-based semiconducting polymers bearing 4-hexyldodecyl side chains shows that the hole mobility is optimized at an intermediate molecular weight.[185] On the other hand, a common design motif for not only NDI-based polymers but also other high-performing n-type polymers is donor-acceptor architecture with large branched alkyl side chains for sufficient solubility. The long alkyl chains are susceptible to entanglement, and significant backbone torsional disorder can be expected between the donor moiety and the acceptor moiety causing chain folding/kinks. As a result, maximum electron mobility can only be observed within the DP_c regime where intrachain mobility, interchain mobility, intracrystallite mobility, and intercrystallite mobility are simultaneously optimized.

Additional future studies of other classes of n-type semiconducting polymers with donor-acceptor architectures are needed to strengthen this picture of electron transport in n-type semiconducting polymers. Nevertheless, we believe that the present results and analyses provide a foundation for understanding of electron transport in PNDIBS and other n-type semiconducting polymers. A new guide to materials design towards high electron mobility n-type conjugated polymers that emerges from this unified understanding is that rather than aiming to maximize molecular weight and crystallinity *per se*, the goal should be to achieve a polymer molecular

weight in the critical range ($DP = DP_c$), which globally optimizes contributions from intrachain, interchain, intracrystallite, and intercrystallite transport.

3.4. Conclusions

In conclusion, we have used the donor-acceptor copolymer PNDIBS as a model system to investigate the polymer chain length dependence of electron transport in naphthalene diimide-based n-type semiconducting polymers. We found that both the *field-effect* electron mobility and the *bulk* electron mobility measured by the SCLC technique are maximized within the same range of critical polymer chain length (DP_c) of 45 – 60 repeat units of PNDIBS and other NDI-based n-type semiconducting polymers. A parallel characterization of the thin-film microstructure evolution with PNDIBS degree of polymerization by AFM and GIWAXS analyses has enabled a mechanistic understanding of the observed electron mobility dependence on *DP*. Thus, outside of the critical polymer chain length range, the decreased electron transport is shown to arise from intercrystallite limitations for $DP < DP_c$ whereas intrachain, interchain, and intra-crystallite transport constrained electron mobility for $DP > DP_c$.

The present results also suggest that unlike long-standing understanding of the critical role of maximal crystallinity on the hole mobility of poly(3-hexylthiophene) and other p-type semiconducting polymers, electron transport in n-type semiconducting polymers is only weakly correlated with crystallinity. The distinct behaviors of the paracrystallinity disorder along the lamellar and the π-π stacking directions have facilitated unmasking of the physical sources of local lattice disorder in this series of PNDIBS to be random side chain conformational disorder, chain folding, and chain entanglements. Finally, we highlight a guide to materials design towards high electron mobility n-type conjugated polymers that emerges from our present results: It is that rather than aiming to maximize molecular weight and crystallinity *per se*, the goal should be

to target a polymer molecular weight in the critical range (DP_c), since this can globally optimize contributions from intrachain, interchain, intracrystallite, and intercrystallite transport.

Chapter 4. Chain Length Dependence of Electron Transport in an n-Type Conjugated Polymer with a Rigid-Rod Chain Topology

4.1. Introduction

Semiconducting polymers combine good charge transport properties with mechanical flexibility, solution processability, and molecular tailorability of electronic properties have enabled a wide range of organic electronic device applications, including organic light-emitting diodes (OLEDs),[4] organic field-effect transistors (OFETs),[5-10] organic photovoltaics (OPVs),[11-16, 37, 44, 69] organic thermoelectric (OTE),[47-49] and organic electrochemical transistors (OECTs).[50, 195] Advances in device performance in the past several years has been driven primarily by improving understanding of the structure-property relationships of the materials and improving electron mobility of n-type semiconducting polymers towards parity with hole mobility of p-type semiconducting polymers. Nevertheless, knowledge and understanding of the structure-property relationships and underlying electron transport physics of n-type semiconducting polymers still lag behind those of p-type conjugated polymers.

Previous studies have shown that polymer chain length is a critical molecular factor that significantly influence the charge transport properties of both p-type and n-type semiconducting polymers. In particular, the chain length dependent hole mobility in p-type conjugated polymers (e.g. P3HT, IDTBT, F8BT) is characterized by two regimes: a region of continuous increase of charge carrier mobility with increasing degree of polymerization (*DP*) until a peak in hole mobility is reached, further increase in *DP* results in a constant mobility due to structural disorder along the charge transport direction (Figure D-1a).[157, 163-170, 172] We recently investigated and elucidated the chain length dependent electron transport in naphthalene-diimide (NDI) based

n-type conjugated polymers.[173] The electron mobility was found to increase with increase *DP*, reach a peak at a critical DP_c, and then significantly decreased with further growth of chain length.[173] A critical *DP* is required (Figure D-1b) to concurrently establish sufficient intercrystallite connectivity and suppress structural disorder such that contributions from intrachain mobility, interchain mobility, intracrystallite mobility, and intercrystallite mobility are globally optimized.[173] It is important to emphasize that both the hole mobility in p-type semiconducting polymers and electron mobility in n-type semiconducting polymers are limited by an upper limit (Figure D-1) imposed by structural disorder that originates from the ***semi-flexible*** nature of their polymer backbones as well as their flexible alkyl side chains.

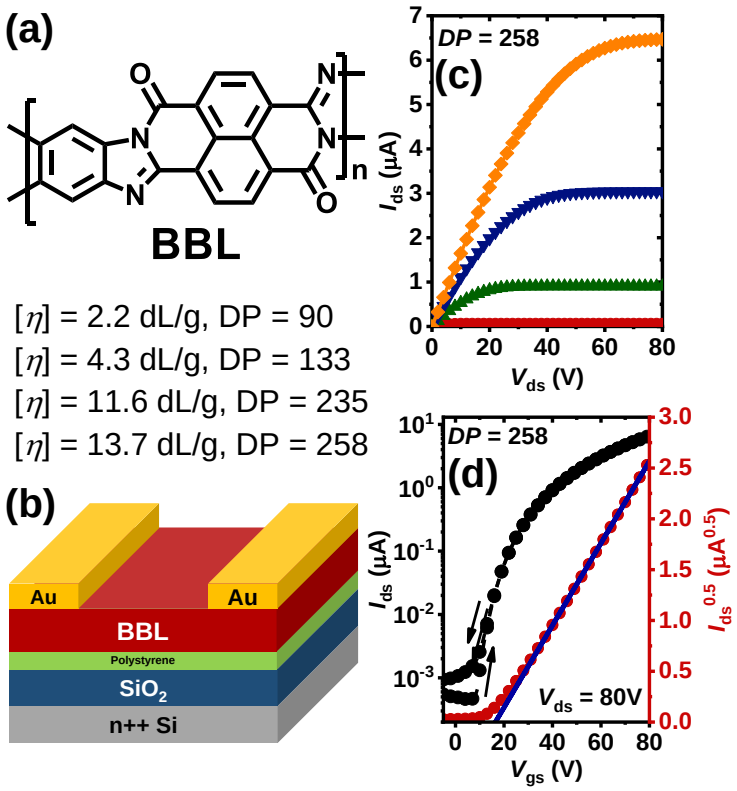

Figure 4-1. (a) Molecular structure of ladder poly(benzimidazobenzophenanthroline) (BBL); (b) Schematic of BBL n-channel organic field-effect transistor (OFET) using a bottom-gate/top-contact device architecture; (c-d) Representative output curves (c) and transfer curves (d) of n-channel BBL OFET devices.

In this paper, we report investigation of the electron transport physics, including the polymer chain length dependence of field-effect electron mobility, of an n-type semiconducting polymer that has a rigid-rod chain topology. We used the π-conjugated ladder polymer, poly(benzimidazobenzophenanthroline) (BBL) (Figure 4-1a) as the model rigid-rod polymer system. BBL has a known large persistence length (ρ = 153 nm),[196] zero conformational disorder, efficient intrachain electron delocalization, and excellent photochemical/thermal stability owing to the unique double-stranded structure and the ribbon-like topology.[5, 197] We show that the field-effect electron mobility of BBL grows linearly with increasing polymer chain length while the threshold voltage decays exponentially as a function of polymer chain length. Both relationships are unique to the class of rigid-rod conjugated ladder polymers, and the underlying charge transport physics has been elucidated in terms of chain length dependent *structural disorder* and *energetic disorder*. The thin film microstructure as a function of polymer chain length was characterized by a combination of atomic force microscopy (AFM), transmission electron microscopy (TEM), and 2D grazing incidence wide-angle X-ray scattering (GIWAXS), revealing improved long-range ordering along the π-stacking direction, tighter interdomain spacing, and overall lower structural disorder with increasing chain length. Our variable temperature electron transport measurements combined with Grünewald's numerical analysis of the trap density of states (DOS) showed a lowered activation energy, narrower trap depth, and reduced trap concentration as the polymer chain length increases. Finally, our findings have elucidated the mechanism of electron transport in n-type conjugated ladder polymers with rigid-rod chain topology and contributed new insights to the design of next-generation semiconducting polymers.

4.2. Experimental Methods

Materials. Ladder poly(benzimidazobenzophenanthroline) (BBL) of different intrinsic viscosities were synthesized by our group following previously reported procedure.[198] Methanesulfonic acid (MSA) and polystyrene (MW = 280 kg/mol) were purchased from Sigma-Aldrich. Gold pellets (99.999%) were purchased from Kurt J. Lesker.

Characterization of Intrinsic Viscosity and Molecular Weight. The intrinsic viscosity ($[\eta]$) of the BBL ladder polymers was determined using a Cannon-Ubbelohde dilution viscometers suspended in a water bath at 30.0°C. The polymer solutions in methanesulfonic acid (MSA) were adjusted such that the elution time of the polymer solution was 1.1 – 1.8 times that of the pure solvent ($1.1<\eta_{relative}<1.8$). The intrinsic viscosity was determined by extrapolation of the inherent viscosity ($\eta_{inherent}$) and the reduced viscosity ($\eta_{reduced}$) of five polymer solutions to infinite dilution according to the relations:

$$\eta_{reduced} = \frac{\eta_{sp}}{c} = [\eta] + k'[\eta]^2 c + k''[\eta]^3 c^2 + \cdots (Eq. 4-1)$$

$$\eta_{inherent} = \frac{\ln \eta_{rel}}{c} = [\eta] - \left(\frac{1}{2} - k'\right)[\eta]^2 c + \left(\frac{1}{3} - k' + k''\right)[\eta]^3 c^2 + \cdots \ (Eq. 4-2)$$

$$\eta_{sp} = \frac{1}{\eta_{rel}} \ (Eq. 4-3)$$

Since BBL ladder polymers behave as long and rigid rods, the intrinsic viscosity $[\eta]$ can be written as:[196]

$$[\eta] = K_R \left(\frac{L}{d}\right)^2 f\left(\frac{L}{d}, \frac{\rho}{d}, \frac{b}{d}\right) \ (Eq. 4-4)$$

assuming $M_L = 26.51\ dalton/\text{Å}$ and $d = hydrodynamic\ diameter = 12\text{Å}$. The polymer molecular weights (*M*) are obtained by solving the nonlinear equation 4-4, and the degree of

polymerization is calculated by normalizing the polymer molecular weight to the monomer molecular weight (M_o = 334 g/mol). The [η] values were found to be 2.2 dL/g, 4.3 dL/g, 11.6 dL/g, and 13.7 dL/g corresponding respectively to M_v values of 29.9kDa, 44.4kDa, 78.5kDa, and 86.3kDa (Table 4-1).[196] The degree of polymerization (*DP*) of the series of BBL ladder polymer was calculated to be 90, 133, 235, and 258 (Table 4-1).

Fabrication and Characterization of n-Channel BBL Field-Effect Transistors. N-channel organic field-effect transistors (OFETs) were fabricated in a bottom-gate top-contact device architecture with a polymer buffer layer (Figure 4-1b). The substrate is comprised of heavily n-doped silicon (< 0.005 S/cm; 500 cm) with a 300 nm-thick silicon oxide layer. The substrates were cleaned by sequentially sonicating in acetone, DI water, and isopropyl alcohol. The cleaned substrates were then treated with air plasma for 10 mins. Insulating polystyrene (PS) was dissolved in anhydrous toluene (5 mg/mL) and stirred at room temperature overnight. The BBL polymers of different intrinsic viscosities were dissolved in methanesulfonic acid (MSA; 6 – 15 mg/mL) and stirred at elevated temperature (> 85^{o}C) for a few days to ensure complete dissolution. The PS solution was spin-coated onto the substrates at 3000 rpm for 60 seconds to produce a 17.0 nm (± 0.12 nm) thick layer, followed by drying in vacuum at 60^{o}C overnight. On top of the PS-coated substrates, the BBL thin films were deposited by spin-coating the BBL solutions at 4500 – 5000 rpm for 30 seconds. The acidic solvent was immediately removed by immersing the polymer films into isopropanol (IPA) several times over 12 hours. The polymer films were then dried in vacuum at 60^{o}C overnight and then annealed at 170^{o}C on a hot plate for 10 minutes in a Nitrogen-filled glovebox. Source and drain electrodes were defined by thermal evaporation of gold electrodes (60 nm). Channel width (*W*) and length (*L*) were 1000μm and 100μm, respectively. The transistors were tested by using a Keithley 4200 semiconductor

characterization system inside a nitrogen atmosphere. The field-effect electron mobility was extracted by analyzing the current – voltage data with the saturation-region equation:

$$I_{ds} = \frac{\mu W C_i}{2L}(V_G - V_T)^2 \ (Eq. 5)$$

where I_{DS} is the source-drain current, μ is field-effect mobility, C_i is the capacitance of gate insulator (10.6 nF/cm^2), V_{GS} is source-gate voltage bias, and V_T is threshold voltage.

Atomic Force Microscopy (AFM) Imaging. AFM characterization of the surface morphology of the BBL films was carried out in quantum nanomechanical (QNM) mode using a Bruker Dimension scanning probe microscope (SPM) system. Films of BBL of different molecular weight values were prepared as described earlier.

Transmission Electron Microscopy (TEM) and Selected Area Electron Diffraction (SAED). The BBL polymers of various intrinsic viscosities were dissolved in methanesulfonic acid (0.5 – 2 mg/mL) and stirred at 85ºC for a few days. The polymer solutions were spin-coated at 1500 rpm for 30 seconds onto clean glass substrates. The films were submerged immediately into deionized water to simultaneously remove the acidic solvent and lift off from the supporting substrates. The floating BBL thin films were transferred onto carbon coated copper grid and dried under vacuum at room temperature overnight. TEM images were collected using a FEI Tecnai G2 F20 SuperTwin system (200kV) supplied with a Gatan Ulttrascan CCD digital camera.

Grazing Incidence Wide-Angle X-ray Scattering (GIWAXS). GIWAXS measurements were conducted at the Advanced Light Source (ALS) at Lawrence Berkley National Laboratory by using the beamlines 7.3.3 and a Pilatus 2M area detector. The images were taken with a beam energy of 10 keV and an incidence angle 0.14º with 5s exposure time. Data were processed using

Nika and WAXStools[199] in Igor Pro. Peak positions were determined by Lorentzian peak fittings. The crystal coherence length (L_c) of samples was determined by using the Scherrer equation: $L_c = 2\pi K/\Delta q$, where K is a shape factor (typically 0.9) and Δq is the full width at half maximum (FWHM) of the diffraction peak. Here, the L_c (100) and L_c (010) were obtained respectively from the FWHM of the (100) diffraction peak in the in-plane (q_{xy}) line-cut and the FWHM of the (010) diffraction peak in the out-of-plane (q_z) line-cut.

Variable Temperature Electron Transport Measurements. Temperature-dependent electron transport measurements of BBL n-channel organic field-effect transistor devices were performed in a PPMS system (Quantum Design, 1.75 K/9T). The OFET devices were fabricated as outlined above. Channel width (W) and length (L) were 1000μm and 50μm, respectively. After the top contacts were thermally evaporated, the complete devices were moved from the N_2-filled glovebox to ambient atmosphere and wire-bonded/glued to Rotator Universal Sample Boards (Quantum Design, P103C). Once the devices were secured on the sample board, they were attached to a multi-functional probe (Quantum Design) and loaded into the PPMS system. The system was purged and sealed with helium gas at least 2 times to remove any oxygen and water impurities prior to varying the temperature. Initial electrical measurements were performed at 300 K to ensure the transistors operate properly without any short-circuit or open-voltage problems before sweeping the temperature. Subsequent measurements were performed at every 10 K interval with a rate of 1 – 2 K/min to allow sufficient time for thermal equilibrium. Voltage biases are only applied during the measurements when the desired temperature was reached to avoid any potential bias stresses.

4.3. Results and Discussion

4.3.1. Electron Transport Properties.

The chain length dependent electron transport properties of BBL were measured by using organic field-effect transistors (OFETs) as the experimental platform. The OFET devices were fabricated by using a bottom-gate/top-contact architecture (Figure 4-1b) with channel dimensions of 100μm/1000μm (length/width). Insulating polystyrene (PS) was used as a low-*k* polymer buffer layer to passivate electron traps on the SiO_2 surface, which has been showed to yield the highest electron mobility in BBL n-channel FETs.[200, 201] The output curves and transfer curves for the n-channel OFET devices at each *DP* value are shown in Figures 4-1c, 4-1d, and D-3. The electron transport parameters, including the average saturation region field-effect electron mobility (μ_{ave}) and threshold voltage (V_T) are summarized in Table 4-1, and the relationships between these parameters and the polymer chain length are presented in Figures 4-2. The field-effect electron mobility (μ_e) was found to increase from $(0.48 \pm 0.07)\text{x}10^{-2}$ cm^2/Vs at a *DP* of 90 to $(2.74 \pm 0.24)\text{x}10^{-2}$ cm^2/Vs when *DP* was 258 (Table 4-1). The observed average μ_e values of the highest *DP* sample are in good agreement with our previous result using samples of comparable intrinsic viscosity.[5] The field-effect electron mobility of shows a linear dependence on the degree of polymerization (Figure 4-2a), which means that the room-temperature field-effect electron mobility of this rigid-rod polymer grows with the polymer chain.

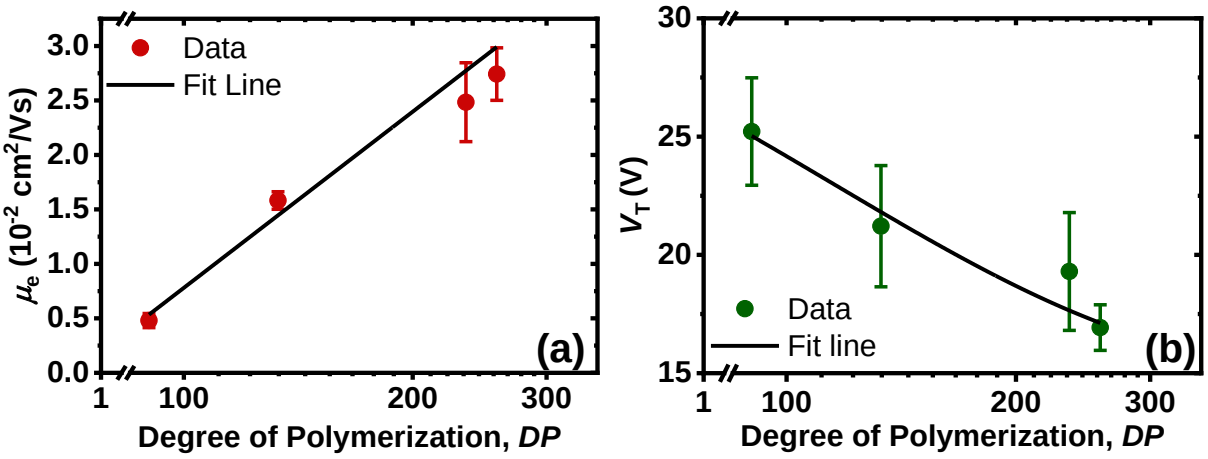

Figure 4-2. Dependence of field-effect electron mobility (μ_e) on degree of polymerization (*DP*) of BBL; (d) Dependence of threshold voltage (V_T) on *DP* of. Note that each data point in both (a) and (b) is an average of 20 – 50 devices.

Table 4-1. Electron Transport Properties of BBL Ladder Polymer.

$[\eta]$ (dL/g)	M_w (kDa)	*DP*	$\mu_{ave}^{(a)}$ (10^{-2} cm^2/Vs)	$V_T^{(b)}$ (V)	$I_{on}/I_{off}^{(c)}$
2.2	29.9	90	0.48 ± 0.07	25.2 ± 2.3	10^3
4.3	44.4	133	1.58 ± 0.08	21.2 ± 2.6	10^3 - 10^4
11.6	78.5	235	2.48 ± 0.36	19.3 ± 2.5	10^4
13.7	86.3	258	2.74 ± 0.24	16.9 ± 1.0	10^4

$^{(a)}\mu_{ave}$, average *field-effect* electron mobility (+/- one standard deviation); $^{(b)}V_T$, average threshold voltage (+/- one standard deviation);$^{(c)}I_{on}/I_{off}$, on/off current ratio. Average values and standard deviations at each degree of polymerization were calculated from at least 19 different devices.

The threshold voltage (V_T) was found to also depend on the degree of polymerization exhibiting an exponential decay (Figure 4-2b). In particular, the average V_T value of 25.2 ± 2.3 V at *DP* = 90 decreased 16.9 ± 1.0 V at *DP* = 258 (Table 4-1). An exponential decay fit, $V_T = A \exp(-DP/DP_0) + B$, to the threshold voltage versus *DP* data (Figure 4-2b) resulted in a pre-exponential coefficient A = 22.5 V, an exponential decay coefficient DP_0 = 115, and a constant B = 14.7 V. This result suggests that when the polymer chain has grown sufficiently long beyond the decay coefficient ($DP \gg 115$), the room-temperature V_T for BBL n-channel field-effect transistors fabricated using the same device architecture can be as low as 14.7 V. The observed decay of V_T as a function of *DP* values suggests that the density of trap states should strongly depend on the polymer chain length such that the longer the polymer chain length, the lower the number of traps present. The origins of these trap states and how they depend on the polymer chain length will be described in the following sections.

We also want to emphasize that the observed exponential decay dependence of threshold voltage on polymer chain length has not been previously observed in either semi-flexible *p-type* or *n-type* semiconducting polymers (Figure D-4).[33, 157, 163-170, 172, 178-180, 185] Thus, our findings that both the electron mobility as well as the threshold voltage can be simultaneously controlled by one material's physical property, the polymer chain length, are highly valuable. They suggest that high-current, low-voltage organic electronic devices with fast switching behavior could be potentially developed based on rigid-rod ladder polymers.

The observed linear increase of electron mobility with polymer chain length in the rigid-rod ladder polymer, BBL, is to be contrasted with the chain length dependence of *electron* transport properties of semi-flexible n-type semiconducting polymers[33, 173, 178] and *hole* transport properties of semi-flexible p-type semiconducting polymers.[157, 163-170, 172, 185] In particular, the charge carrier mobilities of semi-flexible polymers, be it *hole* or *electron,* are limited by an upper bound (Figure D-1) imposed by the structural disorder arising from the semi-flexible backbone and their long alkyl side chains. On the other hand, our results demonstrate that the charge carrier mobility of rigid-rod ladder polymers increases linearly as a function of polymer chain length, suggesting that electron mobility exceeding 1-10 cm^2/Vs could potentially be accessible if sufficiently high molecular-weight polymers can be synthesized. To further understand the physics underlying the chain length dependent electron transport properties of the class of rigid-rod ladder polymers, we have quantitatively examined both ***structural disorder*** by using a variety of morphology characterizations techniques and ***electronic disorder*** by investigating variable temperature electron mobility and performing spectral analysis on the trap density of states.

4.3.3. Chain Length Dependent Thin Film Microstructure and Structural Disorder.

A complement of characterization techniques including atomic force microscopy (AFM), transmission electron microscopy (TEM), and two-dimensional grazing-incidence X-ray scattering (2D-GIWAXS) were employed to probe the evolution of thin film microstructure as well as examine the relationship between structural disorder and polymer chain length in BBL thin films. AFM height and phase images of BBL thin films of different *DP* values are presented in Figures 4-3a – d, and the power spectral density (PSD) profiles of the AFM phase images are shown in Figure D-5. Films of lower *DP* samples (Figures 4-3a and 4-3b) were featureless suggesting a relatively low crystallinity, whereas films of higher *DP* samples (Figures 4-3c and 4-3d) exhibited hints of short yet well-connected fibrillar features indicating enhanced degree of crystallinity, which would be beneficial for electron transport. Analyses of the PSD profiles of the AFM phase images revealed a gradual decrease in spatial periodicity from ~ 157 nm to ~ 78 nm as the *DP* increased from 90 to 258 repeat units. In other words, the crystallites in films of high molecular weight polymers are not only situated much closer to one another but are also within the persistence length of BBL (ρ = 153 nm);[196] thereby, enabling highly efficient intercrystallite electron transport and corroborating the observed linear increase in electron mobility with polymer chain length.

TEM images of BBL thin films of various *DP* values are shown in Figures 4-3e and 4-3h. Nanoplatelets oriented randomly throughout the films are observed which is in good agreement with our previous result.[202] The main effect of increasing *DP* on the bulk morphology of BBL thin films is the enlargement of these sheet-like features as *DP* increases. Based on the TEM and AFM results, a schematic depicting the 2D thin film microstructures of BBL thin films as a function of *DP* is proposed in Figure 4-2i. At low *DP* value, randomly dispersed clusters of

relatively small crystalline domains are situated far away from each other and beyond the contour length of BBL chains (Figure 4-2i); insufficient intercrystallite connectivity results and thus hindering macroscopic electron transport. As the polymer chains increase, the crystalline domains grow larger and position themselves within the persistence length of BBL polymer, providing a well-percolated network of polymer chains and facilitating efficient intercrystallite electron transport.

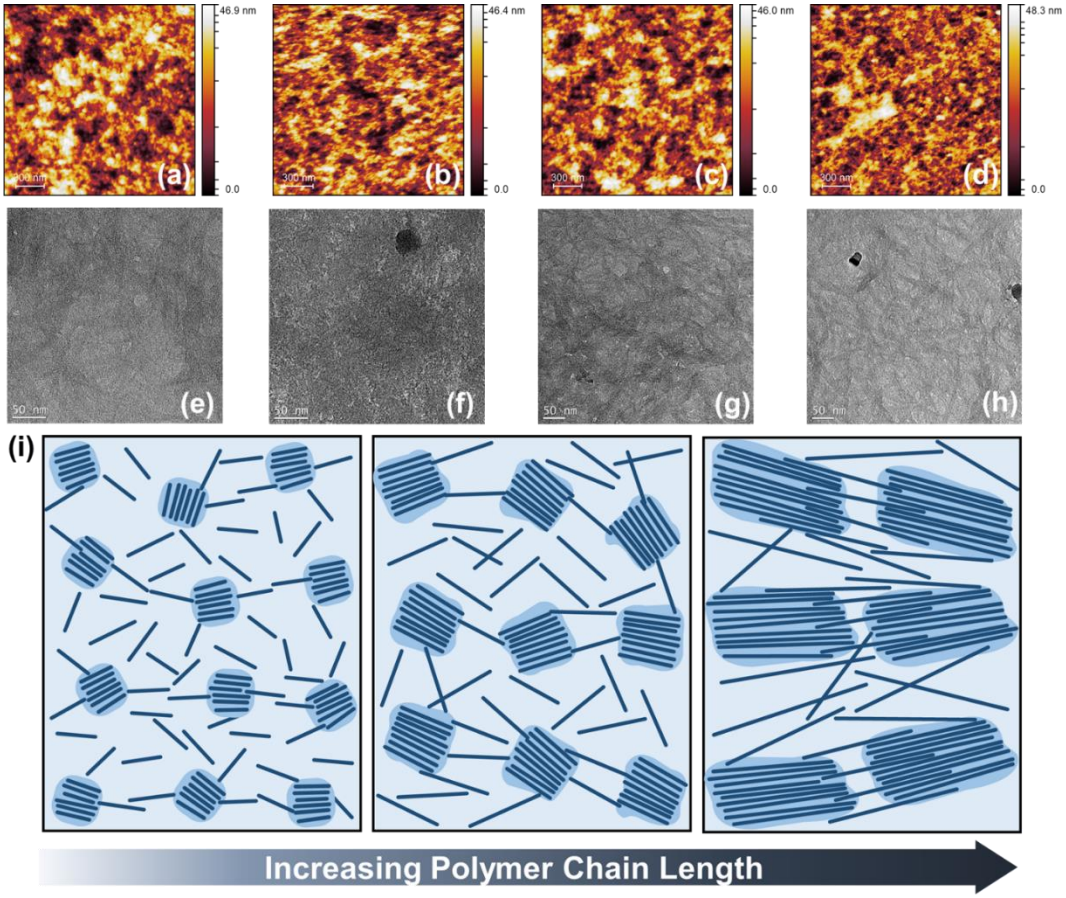

Figure 4-3. (a-d) AFM height images of BBL thin films at different degree of polymerization (*DP*): (a) *DP* = 90, (b) *DP* = 133, (c) *DP* = 235, (d) *DP* = 258; (e-h) TEM images of BBL thin films at different DP values: (e) *DP* = 90, (f) *DP* = 133, (g) *DP* = 235, (h) *DP* = 258; (i) Schematics of BBL thin film microstructures as a function of polymer chain length based on AFM and TEM analyses.

We performed two-dimensional grazing incidence wide X-ray scattering (2D GIWAXS) measurements on BBL thin films of different molecular weights to gain insights into the thin

film microstructures at higher spatial resolution. The 2D diffraction patterns and 1D line cuts in both in-plane (IP) and out-of-plane (OOP) directions are shown in Figures D-6a and D-6b. The diffraction peak positions (q_{xy} and q_z) are summarized in Table D-1, whereas interplanar spacings along (100) OOP and (010) IP directions, the crystalline coherence length (L_c), and the paracrystallinity disorder (g) are presented in Table 4-2.

Pronounced (100) diffraction peaks in the out-of-plane (OOP) direction at q_z = 0.78 – 0.79 $Å^{-1}$ accompanied by a broad (010) diffraction peak at q_z = 1.74 – 1.76 $Å^{-1}$ were observed in BBL films of various polymer chain length. The lamellar spacing distance was calculated to be around 8 Å for all polymer molecular weights (Table 4-2), which is significantly shorter than that of semi-flexible conjugated polymers bearing long alkyl side chains. In the in-plane (IP) direction, all thin films showed a sharp and pronounced (010) diffraction peak at q_{xy} = 1.87 – 1.88 $Å^{-1}$, corresponding to a π-π stacking distance of 3.34 – 3.36 Å. Both the lamellar and π-π stacking distances of BBL were found to be independent of polymer chain length, which might be due to the side-chain free architecture and is thus different from that of semi-flexible conjugated polymers bearing long alkyl side chains.[173] Furthermore, the presence of the pronounced (010) IP and (100) OOP diffraction peaks indicated that most BBL crystallites preferentially stack *edge-on* with respect to the substrates. Analysis of the pole figure (Figure D-6d) revealed that the volume fraction of *edge-on* oriented crystallites increased from ~ 73% to ~ 78% with increasing polymer chain length (Figure D-7), promoting better in-plane electron transport across the electrodes in OFET device configurations. This result is in agreement with the improved electron mobility seen in higher molecular weight samples.

Table 4-2. Summary of Interplanar Spacing (d), Crystalline Coherence Length (L_c), Number of Stacked Layers Within a Crystallite (N), and Paracrystallinity Disorder (g) in Both Lamellar and π-Stacking Directions of BBL Thin Films at Different Degree of Polymerization (DP) Values.

DP	$d_{(100)\ OOP}$ (Å)	$d_{(010)\ IP}$ (Å)	$L_{c,\ (100)\ OOP}$ (nm)	$L_{c,\ (010)\ IP}$ (nm)	$N_{(100)\ OOP}$ (layers)	$N_{(010)\ IP}$ (layers)	$g_{lam,\ (100)\ OOP}$ (%)	$g_{\pi,\ (010)\ IP}$ (%)
90	7.98	3.35	0.90	2.43	2.1	8.2	35.7	14.1
133	7.98	3.35	0.90	2.61	2.1	8.8	35.9	13.6
235	8.03	3.34	0.96	2.64	2.2	8.9	34.7	13.5
258	8.07	3.36	1.00	2.77	2.2	9.3	34.0	13.2

The crystalline coherence length (L_c) estimated from the full-width at half-maxima of both the (100) diffraction peak in the OOP direction and the (010) diffraction peak in the IP direction are showed in Table 4-2 while the dependence of L_c on the degree of polymerization is presented in Figure 4-4a. The L_c value of the (100) OOP direction was found to marginally enhance from 0.90 nm at DP = 90 to 1.00 nm at DP = 258, which suggests that each crystallite consists of about 2 monolayers of polymer chains in the lamellar direction regardless of the polymer chain length (Table 4-2). On the other hand, the L_c value in the (010) IP direction was found to depend more on the degree of polymerization where the L_c value increased monotonically from 2.43 nm at DP = 90 to 2.77 nm at DP = 258 (Figure 4-4a) indicating larger crystallite sizes and better long-rang ordering in high molecular weight samples. In fact, the observed L_c values along with the d-spacings revealed that approximately 8 – 9 monolayers of polymer chains are packed tightly in the π-direction within a single crystallite (Table 4-2), which is significantly improved compared to that of semi-flexible naphthalene diimide (NDI) based n-type semiconducting polymers (~ 3 – 4 monolayers).[173, 203] The larger crystallite sizes and

excellent long-range ordering especially in the charge transport direction is in good agreement with the observed linear increase in electron mobility with increasing polymer chain length.

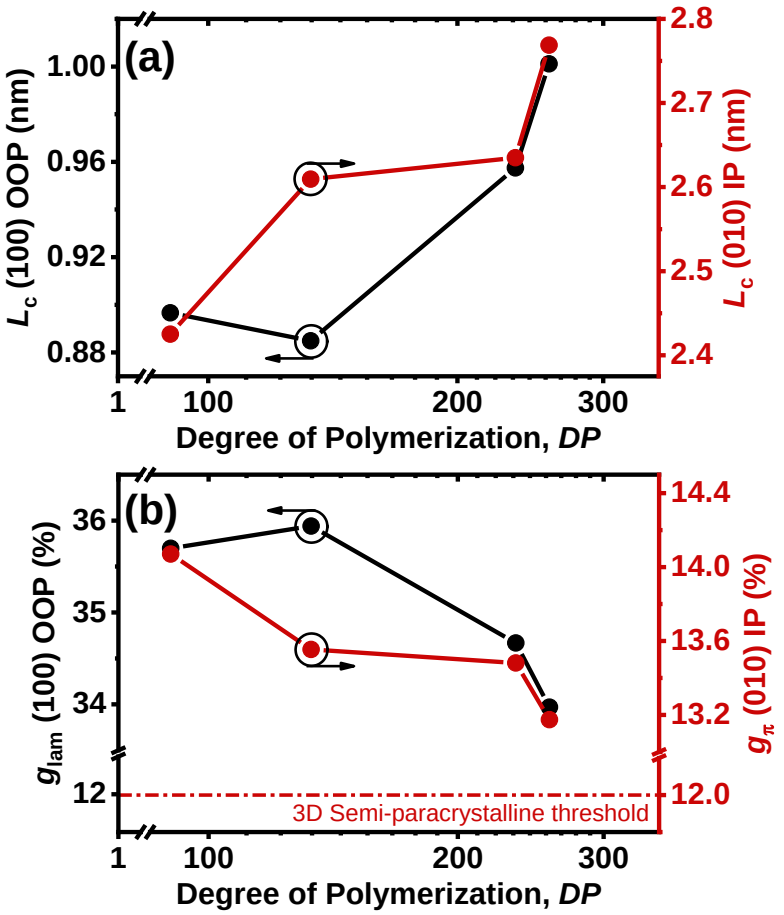

Figure 4-4. (a) Dependence of crystalline coherence length (L_c) in both lamellar, (100) OOP, and π, (010) IP, directions on degree of polymerization; (b) Dependence of paracrystallinity disorder (g) in both lamellar (g_{lam}) and π-stacking (g_π) directions on degree of polymerization.

The paracrystallinity disorder was also estimated using the single-peak fit approximation method[157, 187, 203] in both the lamellar direction (g_{lam}) and the π-stacking direction (g_π) to quantify the degree of lattice distortion or structural disorder. The numerical values of g_{lam} and g_π are summarized in Table 4-2 while the relationships between the degree of polymerization and g values are shown in Figure 4-4b. The structural disorder in the π-stacking direction was found to

slightly decrease from 14.1% to 13.2% with increasing *DP* from 90 to 258, all of which were within the range of other high-mobility 2D semi-paracrystalline organic materials (g_π ~ 12% – 15).[203] Moreover, the g_π values of BBL are lower than those of semi-flexible conjugated polymers (Figure 4-4a), which could be explained by the enhanced π-π intermolecular interaction between the highly planar backbone of this ladder polymer. The strong attraction forces would ensure highly ordered chain registry, suppress deviations in the π-stacking distances, and promote long-range ordering. In contrast, the frequent chain folding and kinks along the backbone common in semi-flexible conjugated polymers hamper intermolecular interactions resulting in large deviations in the lamellar packing distance and cumulative structural disorder.

In the lamellar direction, the lattice disorder was found to slightly decrease from 35.7% to 34.0% when *DP* increases from 90 to 258. The large lattice disorder of BBL along the lamellar axis indeed corroborates with a recently proposed model for hydration of side-chain free polymers where ions and water molecules are easily injected and housed between the polymer chains in the lamellar direction.[195] Moreover, the inverse proportionality of g_{lam} on *DP* seen in BBL is to be contrast to the direct proportionality of g_{lam} on *DP* in semi-flexible NDI-based semiconducting polymers, which has been previously demonstrated to originate from side chain entanglements and backbone twisting.[173]

Interestingly, however, the magnitude of the lattice distortion in the lamellar direction of the rigid-rod ladder polymer BBL (g_{lam} ~ 34 – 36%) is nearly 2-fold higher than that of semi-flexible conjugated polymers (g_{lam} ~ 16 – 20%) even at the same degree of polymerization (Figure 4-5a).[173] We speculate that the large difference in g_{lam} between these two topologically distinct classes of polymers likely originates from the presence/absence of side chains as illustrated in Figures 4-5b and 4-5c. For semi-flexible polymers, although the side chains are

susceptible to entanglement especially in the high molecular weight polymers and could impede the polymer backbone from crystallizing efficiently,[173, 203, 204] they can be leveraged as anchoring points to lock the polymer chains in place[205] as proposed in Figure 4-5b; thus, reducing large variations in the lamellar packing distance, suppressing lattice distortion, enabling larger crystallites, and promoting long-range ordering in the lamellar direction. On the other hand, the lack of side chains in BBL causes the polymer chains to easily slip away from each other introducing substantial lattice disorder along the lamellar axes (Figure 4-5c) and preventing large crystal growth. Additionally, the electrostatic repulsions between the protonated imine bonds ($-C=NH^+$)[206, 207] on each polymer chains (Figure 4-5c) would prevent tight interplanar packings during the initial film formation when processing from acidic solutions; thereby, worsening the lattice disorder and severely limiting long-range ordering. Therefore, future studies should explore additional strategies to minimize lattice distortion along the (100) direction such that crystals of rigid-rod ladder polymers can achieve long-range ordering in all three crystallographic axes, i.e. lamellar, π-stacking, and backbone. For instance, incorporation of alkyl side chains onto the polymer backbone as anchor points or installing functional substituents capable of H-bonding or other non-covalent intermolecular interactions are potential molecular engineering strategies to enhance lamellar long-range ordering of conjugated ladder polymers. From a device engineering perspective, kinetically controlled rate of the film deprotonation after spin-coating from acidic solutions could be a key to promote the growth of large and highly ordered crystals.

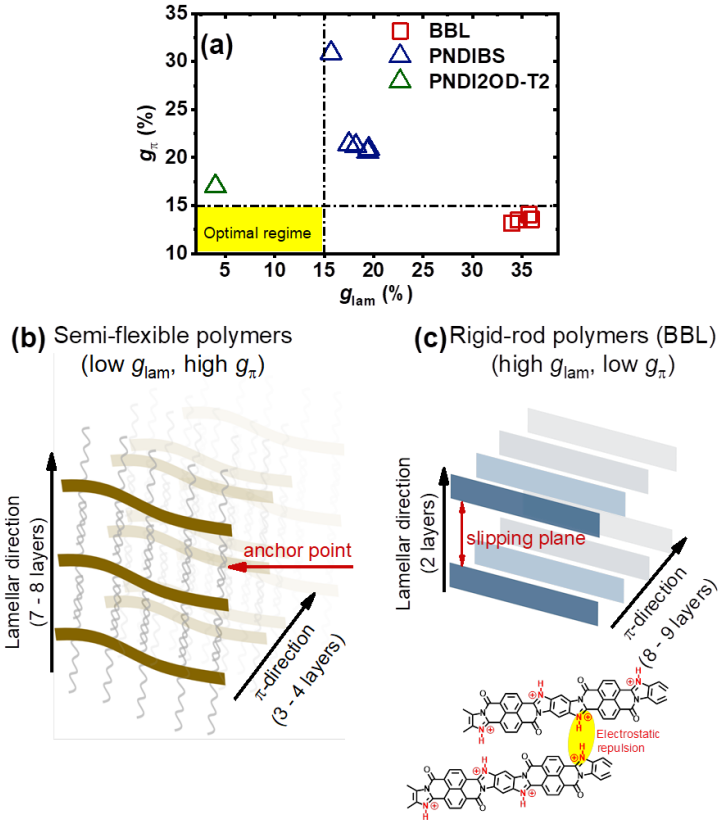

Figure 4-5. (a) Trade-off between paracrystallinity in the lamellar direction (g_{lam}) and paracrystallinity π-stacking direction (g_π) in rigid-rod polymers (BBL) and semi-flexible polymers (PNDIBS and PNDI2OD-T2); (b and c) Schematic of the proposed mechanism for low g_{lam} and high g_π in semi-flexible conjugated polymers (b) and mechanism for high g_{lam} and low g_π in rigid-rod conjugated ladder polymers (c).

In summary, our thin film microstructure characterization results have demonstrated that even though the interplanar spacings along the (100) and (010) axes are rather insensitive to polymer chain length, the crystallite sizes, crystallite spacings, volume fraction of *edge-on* oriented crystallites, and paracrystallinity disorder all exhibit significant chain length dependence. As the polymer chains elongate, the crystallites not only situate closer to each other but also grow larger in both lamellar and π-stacking directions with improved lattice ordering and preferential *edge-on* orientation with respect to the substrates. These microstructural features are optimal for efficient in-plane charge transport across the electrodes in the field-effect

transistor configuration; thus, explaining the observed linear dependence of electron mobility on degree of polymerization of rigid-rod ladder polymers.

4.3.4. Chain Length Dependent Electronic Disorder of BBL Thin Films.

We performed variable temperature electron transport measurements to investigate the electronic disorder in BBL thin films and thus to provide additional insights on the origins of chain length dependent electron mobility and threshold voltage in this model rigid-rod conjugated polymer. Detailed procedures for the variable temperature measurements are described in the Experimental Section. Briefly, after the devices were loaded into the Physical Property Measurement System (PPMS), an initial transfer curve was taken at 300K to ensure that the transistors functioned properly. The cooling/heating rate is controlled at 1 – 2 K/min with a temperature interval of 10 K to allow sufficient time for thermal equilibrium. We note that gate and drain voltage biases are only applied when the desired temperature is reached and ready for measurements to avoid any unnecessary voltage bias stresses. The temperature dependent transfer curves at different *DP* values are shown in Figures D-8. Little to no hysteresis between the forward and reverse scans was observed in all the devices within the measured temperature range (Figure D-8) indicating that any observed changes in the electron mobility are solely due to temperature rather than device degradation.

The saturated electron mobility of all the OFET devices was found to decrease with decreasing temperature following an Arrhenius relationship (Figure 4-6a) as shown in the following formula: $\mu \propto \exp\left(\frac{-E_a}{k_B T}\right)$, where E_a is the apparent activation energy, k_B is the Boltzmann constant, and T is the absolute temperature (K). This result is indicative of a thermally activated charge transport process in BBL thin films. The activation energy for electron transport (E_a) obtained from the monoexponential relationship between μ_e and 1/T is

presented as a function of degree of polymerization in Figure 4-6b. The E_a values were found to dramatically decrease with increasing polymer chain length decreasing from 302 meV for *DP* = 90 to 139 meV for *DP* = 258. The observed monotonic decrease of E_a with increasing *DP* indicates a lower degree of energetic disorder in the higher *DP* samples, and this observation agrees with the measured higher electron mobility and lower threshold voltage at the higher *DP*. Nevertheless, the observed E_a values of BBL thin films are unexpectedly higher than reported values for other high-performing conjugated polymers (E_a ~ 40 – 120 meV)[157, 208] considering the torsional-free and highly rigid-rod backbone of BBL. We attribute the high activation energy seen in these BBL OFETs to a combination of mechanical strain and thermal strain induced by a large mismatch in coefficient of thermal expansion (α) between SiO_2 (α = 4.1 ppm/K),[209] polystyrene (α = 72 ppm/K),[209] and the rigid-rod polymer (α ~ -6 – 10 ppm/K).[210-212] Local distortions in positions of polymer chains arisen from the coefficient of thermal expansion mismatch would result in large lattice disorder and induce modifications to the band structures at the dielectric-semiconductor interface.[209] These effects would lead to the formation of additional trap states[209] that might not be present in the initial devices; thereby, skewing the activation energy to be much higher.

As an alternative, we employed Grünewald's method to determine the trap density of states (DOS) spectra which can provide insights into the trap depth (E_o) and total concentration of trap states (N_{trap}) and help to deconvolute the impacts of coefficient of thermal expansion mismatch on the activation energy. This numerical method has been widely adopted by the community to probe the trap DOS of various organic semiconductors.[80, 213-218] The resulting trap DOS spectra plotted as a function of energy with respect to the LUMO energy level of BBL devices at different *DP* values are presented in Figure D-9. The data were fitted to an exponential

distribution to model shallow trap states situated within a few k_BT away from the LUMO energy level (< 0.1 eV) and a Gaussian distribution to represent deep trap states (E > 0.1 eV) where appropriate. The parameters used to model these distributions are summarized in Table D-2 whereas the chain length dependent trap depth (E_o) and total concentration of shallow trap states ($N_{shallow}$) are shown in Figure 4-5c.

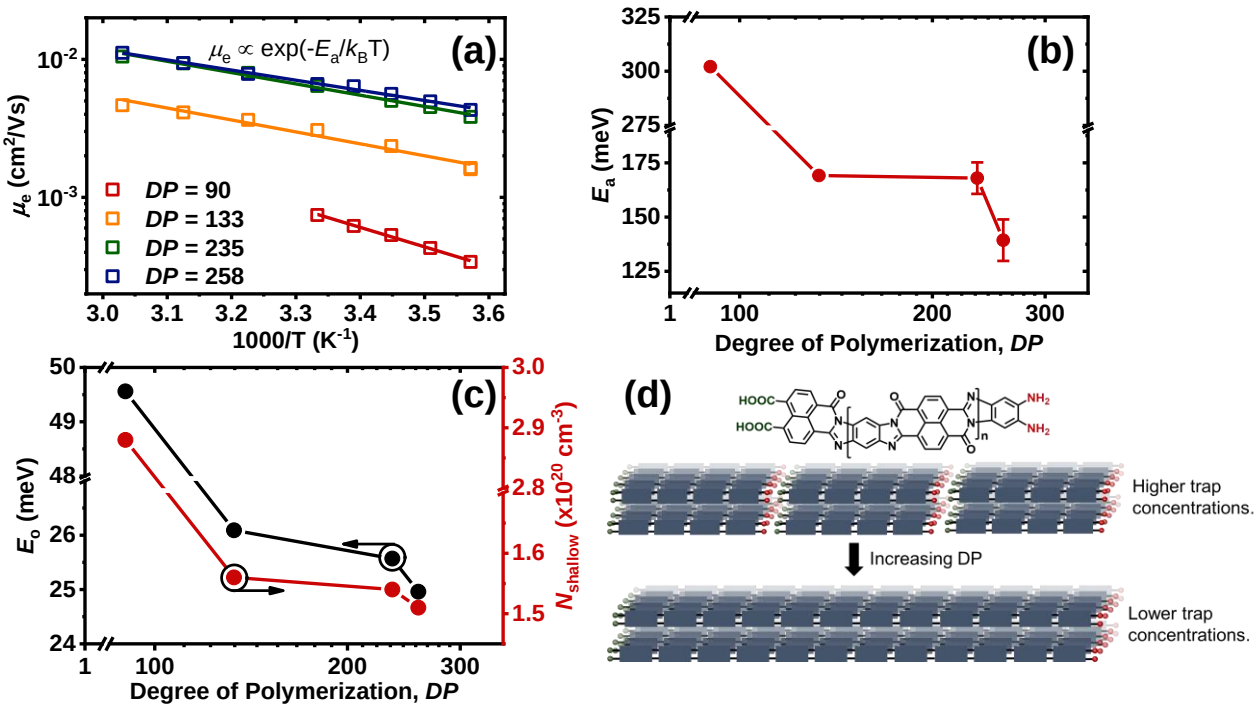

Figure 4-6. (a) Temperature dependent electron mobility (μ_e) of BBL ladder polymers at different degree of polymerization. Data are fitted to an Arrhenius relationship: $\mu_e \propto \exp\left(-\frac{E_a}{k_BT}\right)$, where E_a is the apparent activation energy, k_B is the Boltzmann constant, and T is the absolute temperature; (b) Chain length dependent activation energy (E_a) of BBL ladder polymers; (c) Chain length dependent trap depth (E_0) extracted from an exponential trap distribution and volumetric density of traps (N_{trap}); (d) Schematic of proposed picture of the origin of charge trapping sites in BBL ladder polymers and how polymer chain length influences the concentration of traps.

The trap DOS spectra of BBL devices of all *DP* values showed an exponential distribution as a function of energy within a few k_BT away from the LUMO energy level (E_{LUMO} - E < 0.1 eV). The exponential trap distribution is in fact characteristic of polycrystalline organic

semiconductors and has been shown to originate from thermal fluctuations or structural defects.[80] In particular, the trap DOS spectrum of BBL devices at *DP* = 90 had an extremely broad exponential tail of 49.6 meV suggesting a large distribution of trap states located closed to the band edge. As the polymer chain length increased, the width of the exponential distribution was found to rapidly decrease to 26.1 meV for *DP* = 133 and subsequently reduce to 25.6 meV for *DP* = 235 and eventually to 25.0 meV for *DP* = 258. The observed narrowing of the trap DOS spectra with increasing degree of polymerization is equivalent to a strong correlation between trap depth and polymer chain length as shown in Figure 4-6c and agrees well with the observed relationship between E_a and *DP* demonstrated earlier. Therefore, we believe that the true activation energy for electron transport in BBL thin films should be on the same order of magnitude as the trap depth E_o and smaller than the aforementioned E_a due to the elimination of temperature induced thermal strain and mechanical strain in the Grünewald's method.

Our further analysis of the trap DOS spectra of the low molecular weight BBL devices (*DP* = 90) showed a broad peak (Figure D-9a) which can be fitted to a Gaussian distribution featuring a peak center at E_1 = 150 meV and a peak width σ of 8.1 meV (Table D-2). This Gaussian peak represents discrete electronic states within the bandgap of the semiconducting polymer which can be highly detrimental to the macroscopic charge transport process.[80, 214] The Gaussian distribution of trap sites was found to not only shift farther away from the band edge (E_1 = 192 meV) but also reduce in amplitude and became narrower (σ = 4.3 meV) in higher molecular weight BBL devices (*DP* = 133) (Figure D-9b), correlating with the improved electron mobility and lower threshold voltage. We note that the disappearance of the peak in *DP* = 235 and *DP* = 258 devices (Figures D-9c and D-9d) can be interpreted as either that no discrete sub-gap electronic states are present in these devices, or that these deep traps have shifted sufficiently

far away from the band edge and thus have minimal impacts on the electron transport properties. Our findings that show a simultaneous reduced trap depth and gradual shift of intermediate/deep traps away from the band edge with increasing *DP* are indicative of a lower degree of electronic disorder with increasing polymer chain length, which is in good agreement with the enhanced electron mobility as a function of *DP*.

Moreover, the total concentration of shallow trap states located a few k_BT from the band edge was calculated by performing an integration of the exponential trap distribution from E_{LUMO} - E = 0 eV to E_{LUMO} - E = -0.1 eV, and the resulting value is presented as a function of polymer chain length in Figure 4-6c. The concentration of shallow traps was found to quickly decrease from 2.88 x 10^{20} states/cm^3 in the lowest molecular weight BBL devices (*DP* = 90) to 1.51 x 10^{20} states/cm^3 in the highest molecular weight BBL devices (*DP* = 258) (Table D-2). The rapid decay of the trap concentrations as a function of polymer chain length corroborates the relationship between V_T and *DP*, since threshold voltage is the gate voltage required to fill all the trap states before mobile charges can be accumulated in the transistor channel.[80] The high trap concentrations seen in low *DP* samples would result in a larger threshold voltage to turn-on the devices compared to that of the high *DP* devices. Our results have again emphasized the importance of increased polymer chain length to simultaneously decrease trap depth and suppress charge trapping density such that a synergistic improvement in electron mobility and threshold voltage can be achieved for the class of conjugated rigid-rod ladder polymers.

We have thus far established the effects of polymer chain length on the energetic disorder (i.e. large activation energy, broad distribution of traps, and high concentration of traps) and how charge carrier trapping influences the electron transport properties of the prototype rigid-rod conjugated polymer, BBL. However, the origin of these charge trapping sites seems unclear.

Previous reports have pointed out several possible sources of traps in organic semiconductors including dynamic disorder, static disorder (e.g. structural defects and chemical impurities), interfacial effects, environmental effects, and bias stress effects.[80] Although there might be multiple sources of traps working in tandem and contributing to the overall concentration of traps in BBL ladder polymers, we propose that the most probable dominant source of traps lies in the unreacted amine ($-NH_2$) groups and carboxylic acid (-COOH) present at the end of the polymerization reaction as illustrated in Figure 4-6d. The lower molecular weight BBL samples would have higher density of these unreacted functional groups dangling at each end of the polymer chains acting as charge trapping sites (Figure 4-5d). As the polymer chain length increases, the number of these unreacted end groups would reduce significantly per unit volume resulting in an overall lower concentration of trap sites. Thus, from an energetic point of view, the electron transport in BBL is constrained by the trap frequency at these defect sites where lower molecular weight samples will have lower electron mobility and require higher threshold voltage to de-trap these localized electrons and excite them to the mobile states.[79, 80, 219, 220]

4.3.5. Mechanism of Electron Transport in Conjugated Ladder Polymers with Rigid-Rod Chain Topology.

Taking all the data together, we now propose a mechanism to explain the physics underlying the observed chain length dependent electron transport in π-conjugated polymers with rigid-rod chain topology from ***structural disorder*** and ***energetic disorder*** points of view (Figure 4- 7).

In the case of low *DP* polymers, the crystalline domains are relatively small and consist of at most one or two crystallites with a low fraction of *edge-on* oriented crystallites as evidenced from a combination of AFM, TEM, and GIWAXS results (Figure 4-7); thus, hindering efficient

intracrystallite electron transport especially in the in-plane direction. Furthermore, these crystalline domains are situated far away from each other beyond the contour length of the polymer chains; thereby, limiting intercrystallite electron transport. The intercrystallite transport is additionally suppressed by the high energetic disorder induced by the large concentration of charger carrier trapping sites which originate from unreacted end groups in the low *DP* polymers (Figure 4-6). As a result, electrons are prone to be trapped at these defects, which would not only slow down the macroscopic charge transport but also require sufficiently high gate voltage to de-trap and release them back to the mobile states. Therefore, the combination of large structural disorder and severe energetic disorder has resulted in poor electron transport properties (i.e. low μ and high V_T) in the low molecular weight rigid-rod ladder polymers.

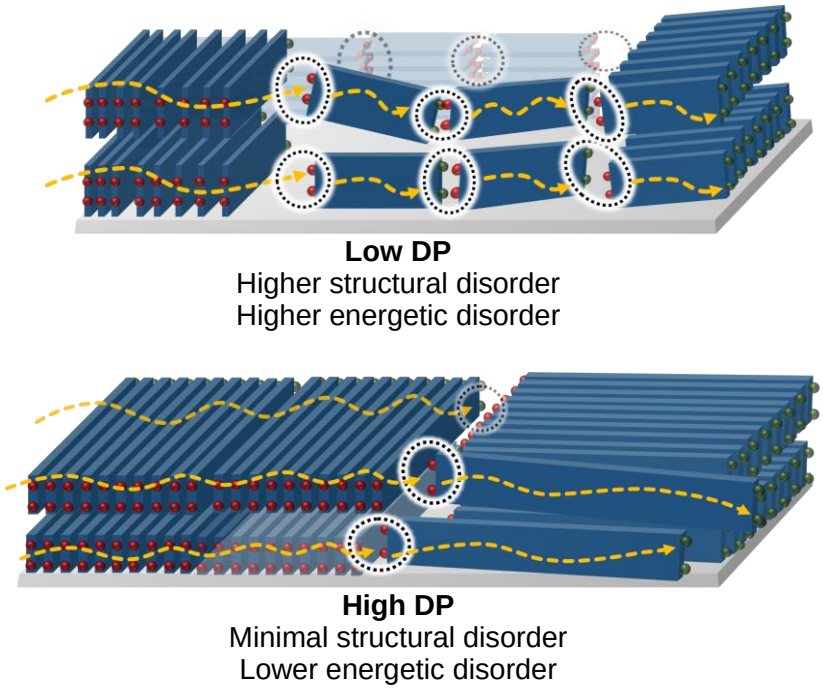

Figure 4-7. Schematic of proposed mechanism of chain length dependent electron transport properties of BBL rigid-rod conjugated ladder polymer.

As the *DP* increases, the larger crystalline domains comprised of several *edge-on* oriented crystallites and low lattice distortion collectively lead to a significant improvement in intracrystallite electron mobility. Moreover, the tighter intercrystallite distance below both the persistence length and the contour length of the polymer chains enables more efficient intercrystallite transport whereby electrons can easily traverse between domains via delocalization along the defect-free rigid-rod backbone of BBL. In addition, the lower volumetric density of trap sites as a result of the longer polymer chain length results in decreased density of electronic defects and reduced frequency of charge trapping events. Thus, the synergistic effects of minimal structural disorder and lower energetic have improved the electron transport properties (i.e. enhanced μ and low V_T) in rigid-rod ladder polymers of high molecular weight.

4.4. Conclusions

In conclusion, we have investigated the chain length dependent electron transport properties of a n-type semiconducting ladder polymer and examined the underlying physics in terms of ***structural disorder*** and ***energetic disorder***. Using organic field-effect transistors as the experimental platform, we have demonstrated a linear dependence of electron mobility on polymer chain length along with an exponential decay of threshold voltage as a function of chain length, both of which are distinctive to the class of rigid-rod ladder polymers and have not been previously observed in the class of semi-flexible polymers. Results from AFM, TEM, and 2D GIWAXS analyses have collectively revealed an optimal thin film microstructures for efficient electron transport in high *DP* polymers featuring *edge-on* oriented crystallites with excellent long-range ordering along the π-stacking direction, decreased lattice distortion, and large crystalline domain sizes with tight intercrystallite spacings. Furthermore, both variable temperature electron transport measurements and Grünewald's method indicated a lower degree

of energetic disorder showing decreased activation energy for electron transport in high *DP* polymers which can be rationalized by the reduced density of charge trapping sites. Therefore, the combination of optimal morphological features and favorable electronic landscapes have resulted in the observed chain length dependent electron transport properties in BBL ladder polymer.

The trade-off between paracrystallinity disorders along the (100) and (010) crystallographic axes in rigid-rod polymers and semi-flexible polymers is also highlighted whereby the origins for such differences are proposed to lie in the presence/absence of the side chains and the processing nature of BBL polymers from acidic medium. Finally, our findings collectively have provided mechanistic understanding on charge transport properties in semiconducting polymers, contributed fundamental insights to the design of high-mobility rigid-rod ladder polymers, and offered useful design guidelines towards the development of next-generation semiconducting polymers.

Chapter 5. Probing the Formation of Polarons, Polaron Pairs, and Bipolarons in n-Type Poly(Benzimidazobenzophenanthroline) Based π-Conjugated Redox Polymer

5.1. Introduction

Organic electrochemical transistors (OECTs) have been garnering significant research interest and spotlighted as the main building block for versatile applications including complementary logic circuits,[221-224] biosensors,[225, 226] neuromorphic computing,[227, 228] etc. Advances in the device performance of OECTs have been primarily driven by one main material design rule that is incorporation of hydrophilic side chains onto known high-performing p-type (e.g. polythiophene) and n-type (e.g. napthalenene diimide based copolymers) polymers to facilitate ion uptake and transport.[50, 229, 230] Also central to the OECT device performance are the electrochemical reactivity and electrochemical stability of the polymer backbone as well as the nature of charge carriers, be it *electron-polaron* or *electron-bipolaron*. However, fundamental studies to explore the structure-electrochemical properties-device performance remain scarce, especially for n-type π-conjugated polymers, due in part to the inability of the polymer backbone to store and stabilize large amounts of injected electrons upon doping.[231] As a result, there still exists a large knowledge gap regarding the electrochemical reactivity of the polymers and how tuning of such material property will influence the transient and steady-state performance of OECT devices.

An effective strategy to tackle the poor stability and structural degradation of n-type π-conjugated polymers upon electron injection is to incorporate redox active sites into the polymer backbone, which can reversibly and stably store multiple electrons per repeat units.[231, 232] This

class of material is called π-conjugated redox polymers since they combine electron-transporting property along the π-conjugated backbone with the robust charging/discharging of redox sites.[231, 233-238] Nevertheless, this approach has only been applied to carbonyl group (-C=O-) containing polymers such as naphthalene diimide (NDI) based copolymers,[231, 233-235] pyromellitic diimide copolymers,[236] and diketopyrrolopyrrole (DPP) based copolymers.[237, 238] Within these limited examples, questions regarding the nature of charged species (bipolaron vs. polaron pairs), their formation mechanism, and their electronic band structure still remain unanswered.

Here, we investigate the formation of polaron, polaron pairs, and bipolarons using a novel phenazine-substituted poly(benzimidazobenzophenanthroline) (BBL-P) n-type π-conjugated redox polymer whose molecular structure is shown in Scheme 5-1. The highly planar rigid-rod backbone of BBL-P endows large delocalization length to stabilize the charged species upon formation, and the six total redox active sites consisting of two carbonyl groups and four imine sites (Scheme 5-1) will also facilitate multiple reversible and rapid electron injections. Thus, a high doping level can be stably and reversible achieved, which will aid to distinguish whether polaron pairs or bipolarons are the multiply charged species. Furthermore, the more disordered nature of BBL-P[239] will help to stabilize the formation of multiply charged species,[87, 89] which otherwise would be harder in their more crystalline parent polymer, BBL (Scheme 5-1).

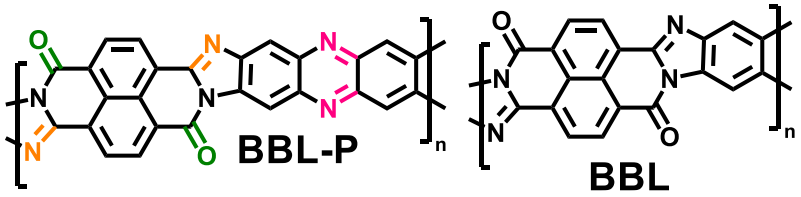

Scheme 5-1. Molecular structures of BBL and BBL-P ladder polymers.

We found that BBL-P can undergo three acid-base coupled redox reactions corresponding to different molecular redox sites with decreasing pK_a from carbonyl to naphthalene imine to

phenazine imine. Each redox reaction is shown to involve two protons per one electron transferred, which is unusual and deviates from the prevailing one-proton/one-electron pattern of BBL[206] and several other materials.[240, 241] By using a variety of characterization tools, we elucidate the underlying mechanism for the multiple redox reactions of BBL-P both from a molecular level and a macroscopic perspective towards mapping out the formation of polaron and bipolaron. The first redox reaction is related to the reduction of BBL-P at the carbonyl group ($1H^+/1e^-$), which leads to a spontaneous protonation ($1H^+$) at the phenazine imine site to stabilize the increased electron density upon electron injection. A low doping level of around one electron per four to five repeat units is found at the first redox process. The second redox reaction is associated with the reduction of BBL-P at the protonated naphthalene imine sites ($1H^+/1e^-$) followed by a protonation ($1H^+$) of the phenazine imine groups. At this stage, about three to four electrons are injected per four repeat units, which induces a pro-quinoidal polymer structures. Highly delocalized singlet polarons are the primary charge carriers upon the first and second redox reactions with the polaron density reaching its maximum at the second redox event. The third redox reaction corresponds to the reduction of BBL-P at the protonated phenazine imine sites accompanied by a protonation of the naphthalene imine functional groups. An average of five electrons are injected per four repeat units leading to the coexistence of singly charged and multiply charged states within the same polymer films. By means of spectroelectrochemistry, we show that a ternary mixture of singlet polaron, polaron pairs (triplet bipolarons), and singlet bipolarons are in equilibrium upon the third redox event, all of which are rather localized on a pro-benzoidal polymer structure. Further increase of the doping level beyond the third redox process leads to annihilation of singlet polarons and singlet bipolarons, and polaron pairs became the dominating charge carriers. Our results have thus provided the first experimental evidence for

the coexistence of different polaronic species upon electrochemical doping, elucidated the mechanism of their formation, as well as mapped out the transformation from singly charged state to multiply charged state as the doping level increased. These findings will provide fundamental frameworks to molecular engineer the next-generation of π-conjugated redox polymers for high-performing OECT devices and other related applications (batteries, supercapacitors, and electrocatalysis).

5.2. Experimental Methods

Chemicals. The phenazine-substituted poly(benzimidazobenzophenanthroline) ladder polymer (BBL-P) was synthesized in house according to reported procedure.[239] Methanesulfonic acid (MSA) was purchased from Sigma-Aldrich.

Preparation of BBL-P Films of Electrodes. The BBL-P polymer was dissolved in methanesulfonic acid (MSA; 15 mg/mL) and stirred at elevated temperature (> 100^{o}C) for several days. The polymer solution was filtered through 1 μm pore size Grade GF/B Glass Microfiber Filters (Whatman GF/B w/ GMF) immediately before use. The filtered polymer solution was spin-coated at 1500 rpm for 30 seconds onto ITO substrates for cyclic voltammetry, FTO substrates for spectroelectrochemistry, and gold coated glass substrates for *in-operando* Raman spectroscopy. The acidic solvent was immediately removed by immersing the polymer films into a mixture of isopropanol (IPA) and ethylene glycol (EG) (IPA:EG = 1:1, v:v) several times over 12 hours. The polymer films were then dried in vacuum at 90^{o}C overnight and then annealed at 170^{o}C on a hot plate for 10 minutes in ambient conditions.

Cyclic Voltammetry. Cyclic voltammetry was performed in conventional three-electrode cells with Ag/AgCl pellet as the reference electrode (World Precision Instrument) and Pt mesh as the counter electrode. Cyclic voltammetry measurements were performed at room temperature using

EG&G Princeton Applied Research, model 273A potentiostat. The BBL-P film prepared as described above served as the working electrode. The supporting electrolyte consisted of 0.1M KCl in deionized (DI) water, and its pH values were tuned by adding either KOH or HCl such that the final solution always contained at least 0.1M KCl. The 0.1M $KCl_{(aq)}$ was purged with a nitrogen stream for at least 15 minutes before any measurements. A stream of N_2 was also constantly flown on top of the electrolyte surface during measurements to minimize oxygen diffusion.

Optical Absorption and Spectroelectrochemistry. Optical absorption spectra of the BBL-P films were taken on a Perkin-Elmer Lambda 900 spectrometer. For spectroelectrochemistry, BBL-P thin film was coated on FTO substrates which were inserted into a cuvette filled with 0.1 M $KCl_{(aq)}$ as the electrolyte. Three-electrode configuration containing Ag/AgCl pellet as the reference electrode, Pt mesh as the counter electrode, and FTO/BBL-P as the working electrode was used. A Metrohm Autolab PDSTAT204 potentiostat was used to control the potential via the Metrohm NOVA software (Version 2.1.6). The BBL-P working electrodes were biased at different potential for 60s for doping to equilibrated before collecting the optical spectra. The films were thoroughly de-doped by applying +0.5V (vs. Ag/Ag^+) between each doping cycle. Both the doping and the de-doping currents were simultaneously collected during the optical measurements for coulometry analysis. The electrolyte was degassed by sparging with N_2 stream for at least 20 mins prior to measurements.

***In-operando* Raman Spectroscopy.** Raman spectra of BBL-P thin films were collected using a Thermo Scientific DXR2 Raman microscope. A 532-nm laser with a power of 2 mW was focused onto BBL-P film surface through a 10x objective lens. *In-operando* Raman spectra were taken at different bias potentials and different pH values. A three-electrode cells consisting of

BBL-P on gold coated glass substrate as the working electrode, Pt mesh as the counter electrode, and Ag/AgCl pellet as the reference electrode, and a Metrohm Autolab PDSTAT204 potentiostat was used to control the potential via the Metrohm NOVA software (Version 2.1.6).

5.3. Results and Discussion

5.3.1. Cyclic Voltammetry of BBL-P in Aqueous Electrolyte.

Cyclic voltammetry (CV) was performed first to investigate the electrochemical properties of BBL-P in aqueous environment. A three-electrode electrochemical cell consisting of Ag/AgCl pellet as the reference electrode, Pt mesh as the counter electrode, and BBL-P coated on conductive ITO substrate as the working electrode was used. The aqueous electrolyte always contained at least 0.1M $KCl_{(aq)}$, and the pH of the electrolyte solution was varied by adding either hydrochloric acid (HCl) or potassium hydroxide (KOH). Additionally, acetonitrile was also titrated to the electrolyte at 10 vol% to poison the Pt electrode and suppress any hydrogen evolution reaction. The applied potentials were also kept within the stability window of water as a function of pH to ensure that no undesirable side reactions took place. The final electrolyte solution was de-oxygenated by purging with nitrogen (N_2) for 20 minutes before any measurements, and a constant N_2 stream was also maintained atop of the electrolyte surface to ensure an oxygen-free environment during the measurements. Cyclic voltammograms of BBL-P thin films with varying electrolyte's pH from pH = 4.11 to pH = 0.06 are shown in Figure 5-1. Depending on the number of observable features in the voltammograms, the pH-dependent electrochemical properties of BBL-P can be categorized into three separate regions:

Region 1. In the case of pH > 3.1 up to 8.1, the voltametric patterns showed marginal dependence on the electrolyte's pH (Figure 5-1a). Indeed, only one voltametric feature, *wave I*, with poorly resolved cathodic and anodic waves can be observed with a formal potential ($E_{1/2}$) of

-0.32V (vs. Ag/Ag^+) and significant peak splitting (ΔE_p) of 138.8 ± 5.8 meV. As the pH value decreased approaching the second region (Figure 5-1b), both the forward and return waves became more apparent with peak positions shifted towards more positive potentials featuring $E_{1/2}$ of -0.037 V (vs. Ag/Ag^+) and smaller peak splitting (ΔE_p = 75.6 ± 11.5 meV at 25mV/s).

Region 2. In the case of 1 < pH < 3.1, the voltammograms showed two pairs of well-resolved and quasi-reversible reduction and oxidation waves consisting of the previously observed *wave I* and an emerging *wave II* at more negative potentials (Figures 5-1c-g). Both the formal potential and the peak splitting of *wave I* and *wave II* were found to strongly depend on the electrolyte's pH. In particular, the $E_{1/2}$ value of *wave I* gradually shifted from -0.017 V (vs. Ag/Ag^+) to 0.14 V (vs. Ag/Ag^+) whereas that of *wave II* moved from -0.29 V (vs. Ag/Ag^+) to -0.09 V (vs. Ag/Ag^+) as the solution pH changed from 3.13 to 1.07. Furthermore, the ΔE_p value of *wave I* was found to decrease from 58.4 meV to 8.44 meV while that of *wave II* was found to diminish from 143.4 meV to 38.4 meV as the solution pH was lowered. Brilliant changes in the film color were clearly visible during the scans with excellent stability and reversibility under anaerobic conditions. The first reduction process showed minimal color changes; however, the second reduction process changed the initially lavender violet film to become gray.

Region 3. In the case of pH < 1, the voltammograms exhibited three sets of well-resolved and quasi-reversible waves consisting of the previously observed *waves I and II* and an emerging *wave III* at most negative potentials. Similar to the voltametric behavior seen in region 2, the $E_{1/2}$ and ΔE_p of all three waves showed intense pH dependence whereby the formal potentials progressively shifted positively with greatly reduced peak splitting. Robust electrochromic effects were also observed in this region whereby the third reduction process changed the color of the film from gray to bright green. The presence of three reversible electrochemical activity

indicates that BBL-P can undergo three proton-coupled electron transfer events which is more than that of the parent BBL ladder polymer.[206] Considering the molecular structures of BBL and BBL-P (Scheme 5-1), the additional redox reaction at pH < 1 must originate from the phenazine unit.

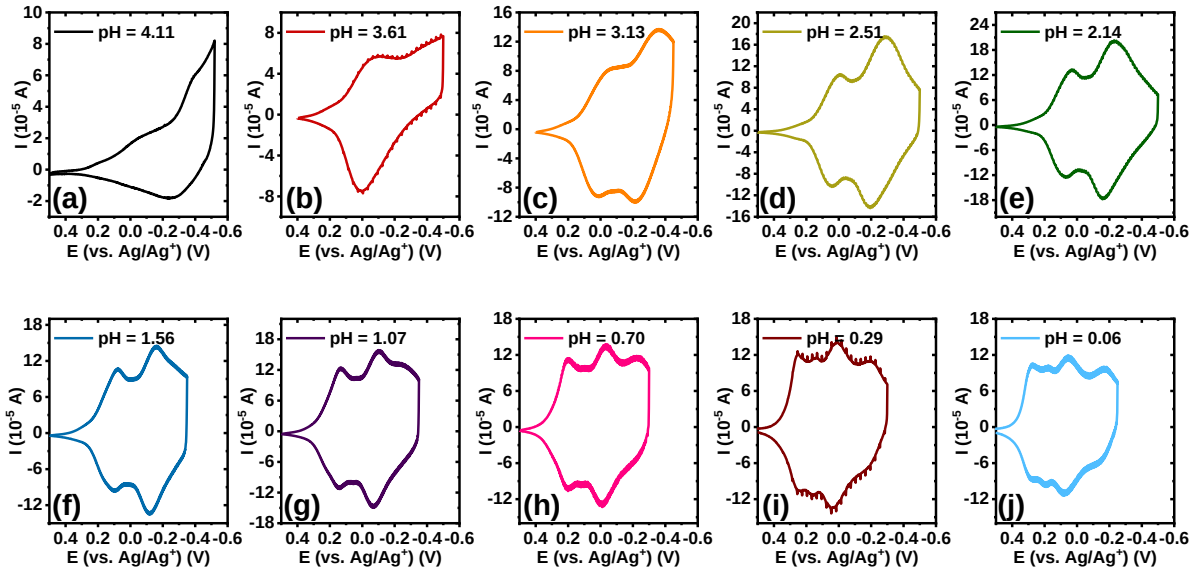

Figure 5-1. pH-dependent cyclic voltammograms of BBL-P thin films collected in 0.1M $KCl_{(aq)}$ supporting electrolyte with a scan rate of 25 mV/s using a 3-electrode configuration with ITO/BBL-P as the working electrode, Pt mesh as the counter electrode, and Ag/AgCl as the reference electrode.

Our results suggest that BBL-P can undergo two acid-base equilibrium in aqueous KCl solution with an average pK_a of 2.5 and 1 corresponding respectively to the protonation at the naphthalene imine site (HBBL-P^+) and the phenazine imine site (HBBL-$P^{+'}$). Indeed, the parent BBL polymer has been shown to exhibit a pK_a around 2.2 for the naphthalene imine site in aqueous tetrabutylammonium sulfate,[206] whereas phenazine small molecules are known to undergo protonation with a pK_a around 1.2.[242, 243]

Quantitative analysis of the pH-dependent formal potentials of each redox event via Pourbaix diagram (Figure 5-2) revealed average slopes of 99.3 ± 0.8, 116.3 ± 1.1, and 109.6 ±

6.8 mV/pH for the first, second, and third redox reaction, respectively. These results have indicated that each redox reaction of BBL-P consumed two protons per one electron, which is twice of that of the parent BBL polymer (Figure E-1).[206] The deviation of the prevailing one-proton/one-electron of BBL-P is very intriguing and worth further investigation. We hypothesize that the extra proton involved in each electrochemical event must be associated with the imine sites on the phenazine unit, and the proposed the multiple electrochemical reduction reactions of BBL-P in aqueous acid is shown in Scheme 5-2.

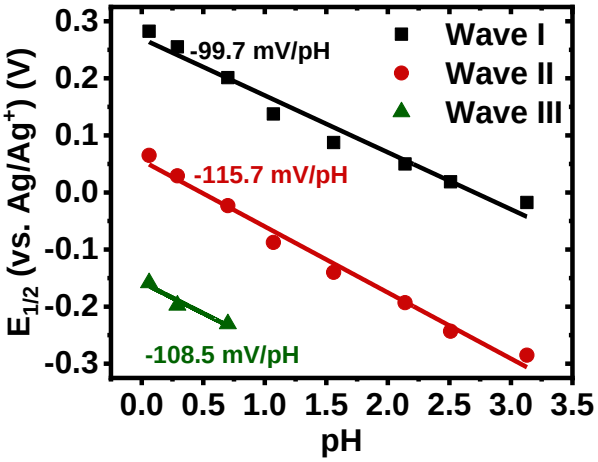

Figure 5-2. Representative Pourbaix diagram of BBL-P thin films in 0.1M$_{(aq)}$ KCl at a scan rate of 25 mV/s.

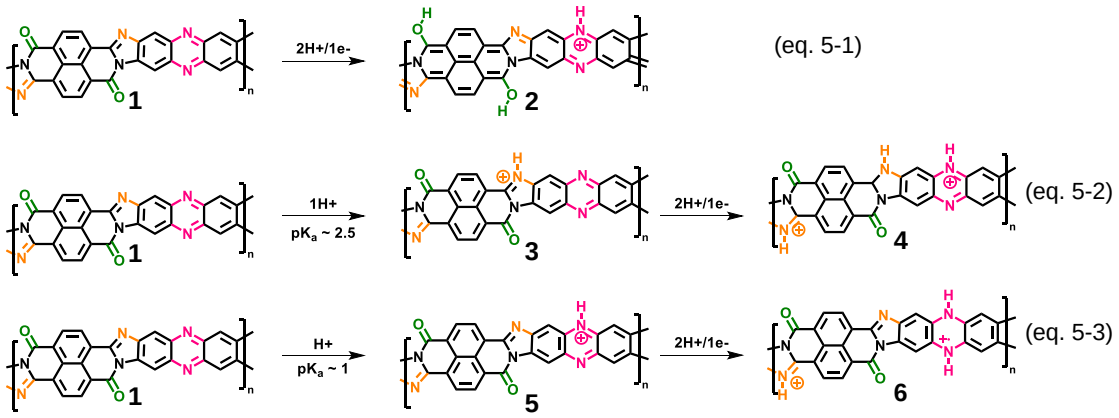

Scheme 5-2. Proposed electrochemical reduction reactions of BBL-P in aqueous KCl electrolyte.

To confirm our hypothesis and arrive at a more comprehensive understanding of the multiple electrochemical redox reactions of BBL-P in acidic electrolyte, we examined the thermodynamics and kinetics of each reduction process by density functional theory (DFT) calculations and variable scan rate cyclic voltammetry, respectively. Results from these analyses will provide macroscopic insights on the feasibility of the proposed mechanism. Furthermore, a combination of characterization techniques such as spectroelectrochemistry, coulometry, and *in-operando* Raman spectroscopy will be used to probe the evolution of optoelectronic properties, doping level, and structural properties of BBL-P, all of which are to be discussed in detailed *vide infra* to provide molecular insights into the electrochemical reduction processes.

5.3.2. Thermodynamics of Electrochemical Doping Reactions of BBL-P.

We first examined the feasibility of the proposed electrochemical redox reactions of BBL-P from a thermodynamics perspective. Density functional theory (wB97XD/6-31G (d,p)) of the dimers of the proposed structures (**1** – **6**) were performed to gain insights into the polymer chain conformations as well as their free energy. The optimized geometries of **1**, **2**, **4**, and **6** structures all exhibited completely planar chain conformation (Figures E-2) suggesting that the formation of polaron would not introduce any detrimental torsional defects into the rigid-rod polymer backbone.

A quantitative comparison of the driving force for each of the reduction reaction is presented in Figure E-3. The Gibbs free energy change (ΔG) of all three reactions was found to be negative indicating that the reduced products (**2**, **4**, and **6**) are thermodynamically favorable. Furthermore, the ΔG value was largest for the 1 → 2 reaction (ΔG_{12} = -84 eV) meaning that the conversion from neutral BBL-P to its reduced unprotonated form (Equation 5-1) is readily accessible; thus, requiring a low doping potential. The ΔG value of the 1 → 4 reaction was

intermediate (ΔG_{14} = -67 eV) implying that the observed second reduction wave would correspond to the reduction of protonated BBL-P at the naphthalene imine sites(Equation 5-2). Moreover, the smallest ΔG value (ΔG = -66 eV) corresponding to the 1 → 6 conversion suggests that protonated BBL-P at the phenazine imine sites (Equation 5-3) would be slightly harder to reduce compared to the protonated naphthalene imine and thus require substantially negative potentials. These findings are in excellent agreement with the experimental CV data and have confirmed that the proposed electrochemical reduction reaction scheme of BBL-P is valid from a thermodynamic standpoint.

5.3.3. Kinetics of Electrochemical Reduction Reactions of BBL-P.

The kinetics of each electrochemical event of BBL-P was also investigated to quantitatively distinguish between the slow diffusion-limited and the fast surface-controlled processes. Representative cyclic voltammograms of BBL-P with varying scan rate (v) collected in electrolyte solution of pH ranging from 4.1 to 0.06 are shown in Figures 5-3a-j. Notably, the voltametric responses of BBL-P showed marginal changes with increasing scan rate showing well-resolved cathodic and anodic peaks up to 150 mV/s at all pH value. A power law is applied to describe the electrochemical reduction kinetics:

$$i = av^b$$

where i is the current, v is the scan rate, a is a constant, and b is the power-law coefficient.

The relationship between log(i) and log (ν) with varying electrolyte solution pH are shown in Figures E-4 whereby the slope of the linear fit represents the b-value. The pH-dependence of b-value for each electrochemical reduction event is presented in Figures 5-3k-m. In general, a b-value of 1 indicates a rapid surface-controlled pseudocapacitive electrochemical process whereas a b-value of 0.5 represents a battery-like slow diffusion-limited process.[244, 245] In

the case of the first reduction event, average *b*-values of both the cathodic peak and the anodic peak were found to gradually increase from $b = 0.87 – 0.89$ to near unity ($b = 1.00$) as the pH values were lowered from 3.1 to 0.06 (Figure 5-3k). This result suggests that the reduction of unprotonated BBL-P showed a dominating pseudocapacitive behavior especially in highly acidic electrolytes. In the case of the second reduction process, the *b*-value exhibited a steep increase from around 0.6 – 0.7 to 0.9 – 1.0 as the solution pH decreased from ~3 to ~2.5 (Figure 5-3l) indicating a transition from a slow diffusion-limited process to a fast surface-limited redox process which also coincided with the transition from region 1 to region 2 discussed earlier. The charge storage mechanism remained to be pseudocapacitive with decreasing pH down to 0.06 as evidenced by the relatively constant *b*-value around 1.0 (Figure 5-3l). The kinetics of the third reduction process also showed a dominating pseudocapacitive behavior with average *b*-value around 0.9 – 1.1 regardless of the electrolyte solution pH (Figure 5-3m). These results collectively have suggested that the kinetics of electrochemical reduction of BBL-P can be controlled by the electrolyte's pH where protonation of the polymer offers an effective means to overcome the kinetics barrier leading to rapid reduction processes. Furthermore, the charge storage mechanism of BBL-P follows a pseudocapacitive behavior even at high scan rate indicating the remarkable rate capabilities of BBL-P.[246] Therefore, BBL-P ladder polymer could be a promising electrode materials for future applications in all-polymer proton supercapacitors[247-249] or proton batteries.[250-253]

We have thus far demonstrated that the proposed electrochemical reduction reactions are valid from a macroscopic thermo-kinetic perspective. To further our understanding of the multiple redox states of BBL-P from a molecular level, we employed a complement of *in-operando* characterization techniques as discussed in the following sections.

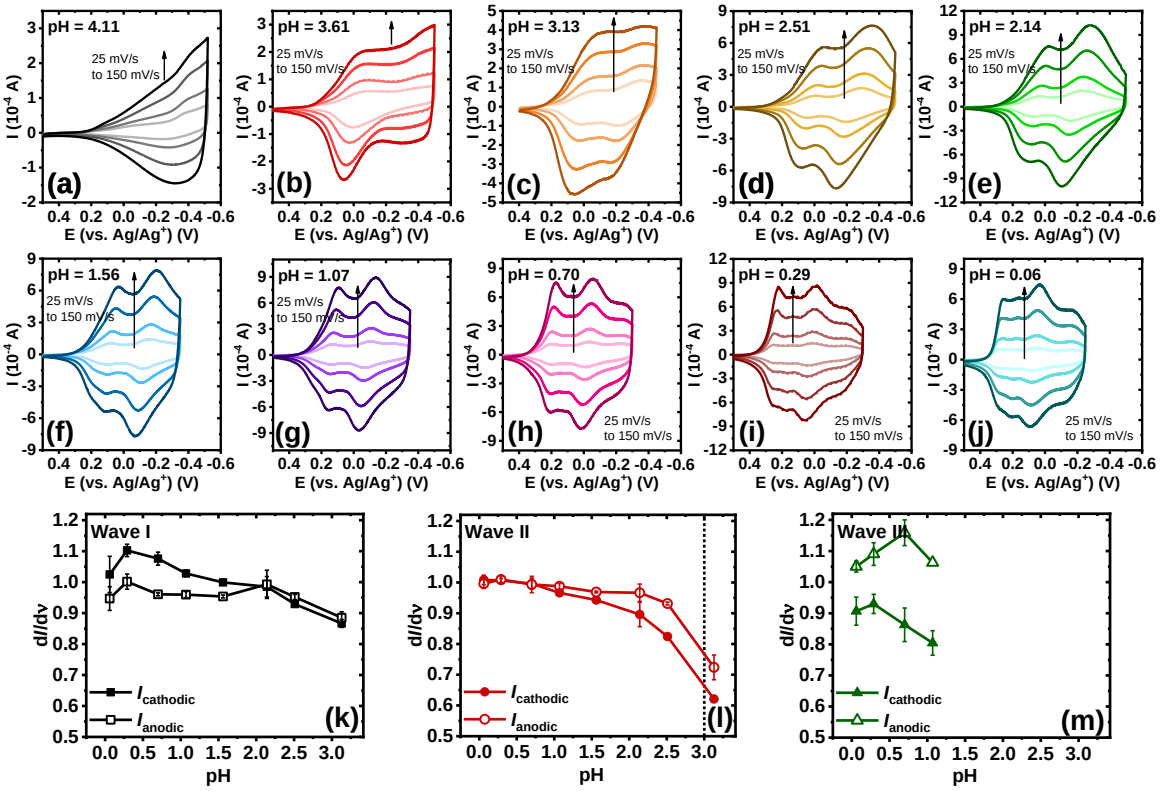

Figure 5-3. (a-j) pH-dependent cyclic voltammograms of BBL-P thin films collected in 0.1M $KCl_{(aq)}$ supporting electrolyte at various scan rates from 25 mV/s to 150 mV/s. (k – m) Dependence of *b*-value (dI/dv) on the electrolyte pH for the first redox event (k), the second redox event (l), and the third redox event (m).

5.3.4. Spectroelectrochemistry of BBL-P Films in Aqueous Solution.

We used spectroelectrochemistry to examine the evolution of optoelectronic properties upon electrochemical reduction as well as to probe the formation of polaron and bipolaron. The optical absorption spectra of undoped BBL-P with varying electrolyte's pH are shown in Figure E-5. Even when BBL-P is protonated (pH < 3 and pH <1), the spectral shapes remain relatively constant showing a main absorption feature centered at around 490 – 495 nm and a poorly resolved shoulder at around 630 nm. This result suggests that neither the electronic structures nor the polymer chain conformation were affected upon protonation, which is a unique characteristic of rigid-rod ladder polymers.[197]

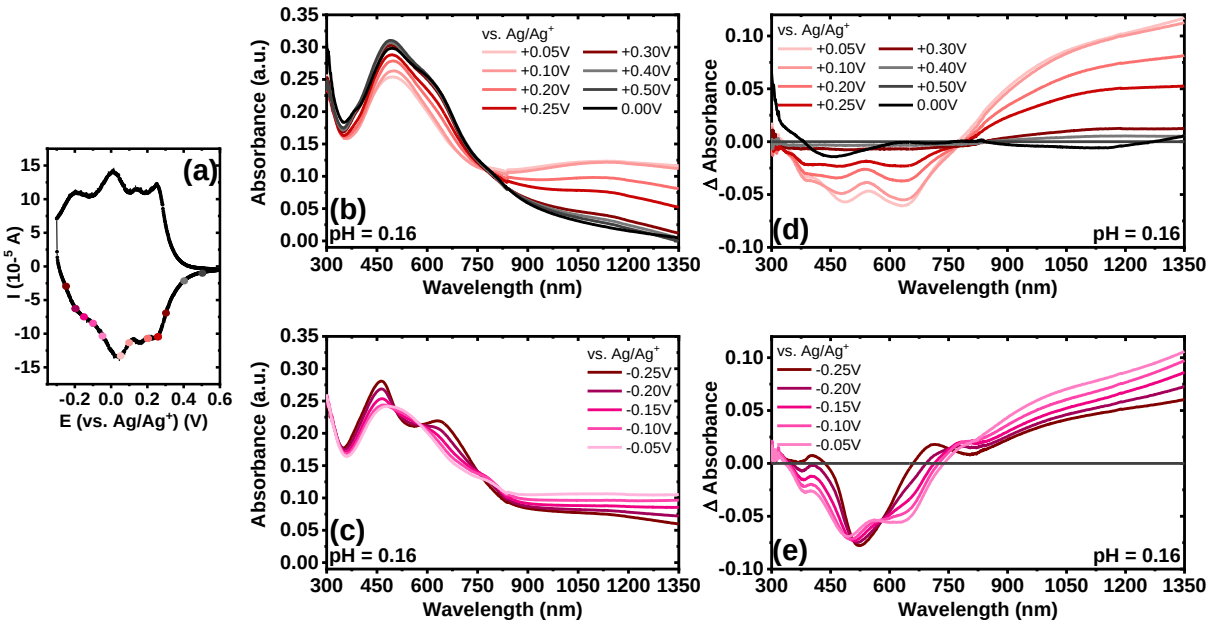

Figure 5-4. (a) Cyclic voltammogram of BBL-P thin films in aqueous KCl electrolyte of pH 1.07 collected at a scan rate of 25 mV/s; (b – c) UV-Vis-NIR optical absorption spectra under different potentials of BBL-P thin films in electrolyte of pH = 1.04; (d – e) Differential UV-Vis-NIR optical absorption spectra under different potentials of BBL-P thin films. The baseline spectrum was taken at +0.50V to de-dope the films prior to each doping step.

Spectroelectrochemistry of BBL-P was performed in a three-electrode configuration with BBL-P coated on conducting transparent substrate as the working electrode, Pt mesh as the counter electrode, and Ag/AgCl pellet as the reference electrode. The optical properties of BBL-P thin films at various doping potentials collected in aqueous KCl electrolyte solution of pH 0.16, 1.04, and 2.43 are shown in Figures 5-4, E-6, and E-7, respectively. The points on the voltammograms (Figures 5-4a, E-6a, and E-7a) indicate the potentials at which the films were doped before collecting the spectra. The current was monitored to ensure that the polymer doping has reached a steady state before optical measurements took place. We note that the polymer films were thoroughly de-doped at +0.50V (vs. Ag/Ag^+) between each doping step. In each case, the potential was applied from negative to positive directions. The differential absorption spectra of BBL-P thin films as a function of doping potentials and solution pH are also shown in Figures 5-4d-e, E-6d-e, and E-7d-e. Since results obtained in electrolyte solution

of pH 1.04 and 2.46 (Figures E-6 and E-7) are essentially snapshots of those collected in extremely low pH regime, we will focus our discussion on the spectroelectrochemistry of BBL-P in highly acidic electrolyte solution (pH < 1) where all three redox reactions coexist in equilibrium (Eqs. 5-1 – 5-3).

The spectral responses of BBL-P in highly acidic electrolyte (pH = 0.16) can be divided into two potential ranges as illustrated in Figures 5-4b and 5-4c. As the applied potential approached the first redox peak at around +0.25 V (vs. Ag/Ag^+) (Figure 5-4a) from +0.50V, the π-π* transition of the ground state (λ_{max} = 496 nm) decreased in intensity accompanied by a new broad absorption band in the near infrared (near-IR) region centered at 1115 nm (Figure 5-4b and 5-4d), which indicates the formation of polaron. As the applied potential was swept towards the second redox event (E = +0.05V, vs. Ag/Ag^+), a combination of progressive increase of the near-IR absorption band (λ = 1115 nm) and gradual bleaching of the visible absorption band (λ = 496 nm) was observed (Figures 5-4b and 5-4d), which means the density of polaron increased with increasing doping level. Within this potential range from +0.50V to +0.05V (vs. Ag/Ag^+), only one isosbestic point at around 770 nm (Figures 5-4b and 5-4d) can be observed indicating the direct conversion of neutral to singly charged state of BBL-P. Furthermore, the density of polaron was found to be maximized at the second redox event (E = +0.05V, vs. Ag/Ag^+) as evidenced by the highest intensity of the near-IR band (Figures 5-4d and E-8). The differential absorption spectra also suggested that the density of polaron at the first redox event is about 2-2.5 times lower than that of the second redox event (Figures E-8).

As the applied potential approached the third redox event (E < 0 V, vs. Ag/Ag^+), the π-π* transition of the ground state (λ_{max} = 496 nm) was significantly bleached giving rise to two sharp absorption bands centered at 461 nm and 640 nm. The intensity of the near-IR absorption band (λ

= 1115 nm) was also found to decrease from its maximum (Figure E-8), which suggests the transition of singly charged polaron to multiply charged species. Indeed, three isosbestic points at 505 nm, 580 nm, and 755 nm (Figures 5-4c and 5-4e) can be seen indicating the conversion of singly charged to multiply charged states of BBL-P. Thus, our results have showed that the visible absorption bands at 461 nm and 640 nm can be assigned to the absorption of multiply charged BBL-P whereas the near-IR absorption band at 1115 nm is associated with the singly charged BBL-P. The extremely broad absorption features of BBL-P seen at applied potentials of -0.15 – -0.05V (vs. Ag/Ag^+) (Figure 5-4c) can be explained by the coexistence of both singly and multiply charged states leading to an overlapping of several absorption features; thus, distorting the optical absorption spectra. As a result, both singly charged as well as multiply charged species can charge carriers in the third redox event of BBL-P ($E_{1/2}$ = -0.17 V, vs. Ag/Ag^+).

5.3.5. Coulometry of BBL-P Films as a Function of pH.

Next, we quantified the doping level by calculating the number of electrons per repeat unit (eru) via coulometry assay, which would also enable us to also cross-check the spectroelectrochemistry results. To avoid the effects of oxygen reduction reaction (ORR) and overestimation of charge integration, we used the de-doping current to calculate the electron density in the reduced BBL-P films after the optical absorption measurements.[195] The number of electron per repeat unit was calculated by normalizing the total charge generated in the reduced BBL-P films obtained by integration of the de-doping current to the number of monomers present on the electrode following previously reported method.[254] The pH-dependence of the doping level is shown in Figure 5-5a.

In highly acidic electrolyte (pH = 0.16), the first reduction event ($E_{1/2}$ = + 0.25V, vs. Ag/Ag^+) resulted in a relatively low electron density with an average eru of 0.22 ± 0.02. This

means that about one electron is produced per four to five repeat unit of reduced unprotonated BBL-P. Further decrease of doping potential led to gradual increase of the electron density (Figure 5-5a) showing an average doping level of 0.78 ± 0.07 eru upon the second reduction event; thus, suggesting that approximately three to four electrons are injected per four repeat units of reduced protonated BBL-P at the naphthalene imine sites. These findings indeed corroborate the spectroelectrochemistry results indicating that the electron density of the second redox process is about 3-fold higher than that of the first redox reaction. At an applied potential of -0.15V (vs. Ag/Ag^{+}) corresponding to the third redox process, the doping level reached 1.33 ± 0.07 eru which is equivalent to about five electrons are injected per four repeat units. These results indicate that multiply charged species must exist; thus, agreeing with the optical absorption spectroscopy results.

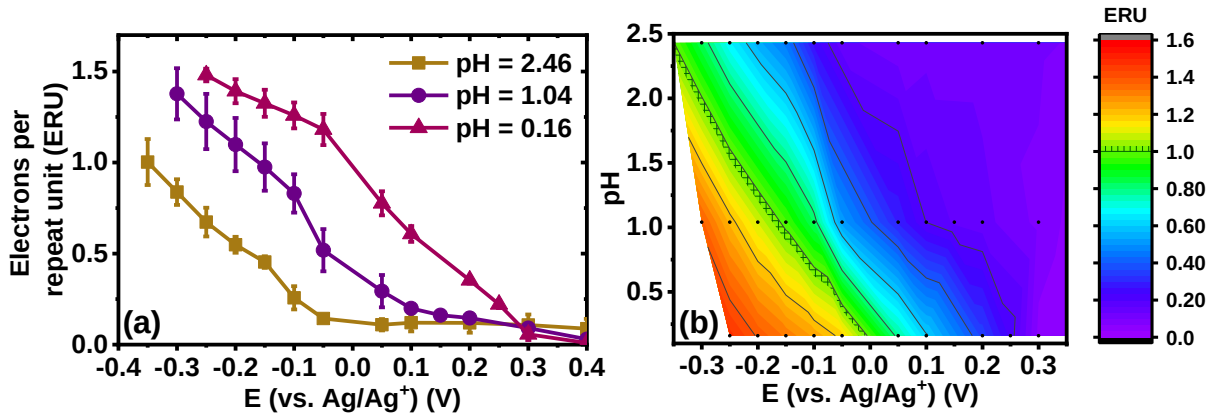

Figure 5-5. (a) Evolution of doping level (number of electrons per repeat unit) as a function of doping potential. (b) Dependence of doping level on electrolyte pH and doping potentials.

It is important to note that the electron density as a function of pH is in excellent agreement with the observed CV and Pourbaix's diagram presented earlier. For example, a horizontal line representing a doping level of 0.75 eru was found to intersect the pH = 1.04 line at -0.086 V and the pH = 2.46 line at -0.27 V, both of which are the formal potential of the second reduction event of BBL-P in respective electrolyte solution. Using the calculated electron

density at three different pH values, we can also interpolate and generate a heat map to illustrate the number of electrons per repeat unit as a function of doping potentials and electrolyte pH as shown in Figure 5-5b. The doping level of the parent BBL ladder polymer in neutral aqueous electrolyte has been previously shown to reach 0.75 – 1.00 eru at much larger doping potentials between -0.5 – -0.9 V (vs. Ag/Ag^+) depending on the polymer molecular weights and the electrolyte.[195, 255] In our case, by tuning the electrolyte's pH value, we can achieve comparable doping level (i.e. 0.75 – 1.00 eru) at significantly lower doping potentials suggesting that potential BBL-P OECT devices that operate in acidic environment could have reduced threshold voltage and lower power consumption.

5.3.6. Probing the Formation of Polaron, Polaron Pairs, and Bipolarons.

The unique optical signatures of neutral, singly charged, and multiply charged species of BBL-P (Figure 5-6a) enable us to track their formation upon electrochemical doping and quantitatively construct the evolution of electronic band structure as a function of doping level (Figure 5-6b). Neutral BBL-P exhibited a medium bandgap of around 2.5 eV (Figure 5-6) which is in good agreement with previously reported DFT results. As the polymer chains are reduced to an intermediate doping level (0.7 – 1.0 eru) corresponding to the second redox event, singlet polarons are formed featuring two mid-gap bands at 1.1 eV and 1.4 eV(Figure 5-6) where the former is related to the transition from the valence band (VB) to the polaron bonding state. It is important to highlight that the band gap remains a finite value at 0.3 eV primarily due to the Peierls instability forbidding the formation of metallic state in one-dimensional π-conjugated polymers. As the polymer is further reduced to very high doping level (~ 1.5 eru), the electronic band is widened from 2.5 eV to 2.7 eV (Figures 5-6a) which agrees with the formation of multiply charged species.[92] The absorption peak at 1.9 eV (Figure 5-6a) can be assigned to the

transition from the valence band to the anti-bonding state of the charged species; thus, implying that the gap between the VB and the bonding state of the charged species is 0.8 eV. This result initially seems to contradict the traditional picture where the transition from the VB to the empty bonding state of bipolaron is higher energy than that of polarons.[89, 91, 256, 257] However, a recent study has suggested that strongly coupled polarons with lower energy transition or red-shifted optical absorption could be more favorably formed in electrochemically doped poly(3-hexylthiophene) (P3HT) depending on the experimental conditions (e.g. potential bias, counterion size, counterion mobility, etc.).[89] As a result, we assign strongly coupled polaron pairs (triplet bipolarons) rather singlet bipolarons to be the main carriers in heavily reduced BBL-P. Although this result is different from the reported DFT results for BBL polymer[258] whereby bipolarons are formed in heavily doped samples (> 1.3 eru), such discrepancies can be explained by the use of single oligomer chain in DFT, overlooking the interchain electronic coupling, solvent effects, and interaction between counterions with the polymer chains.[258]

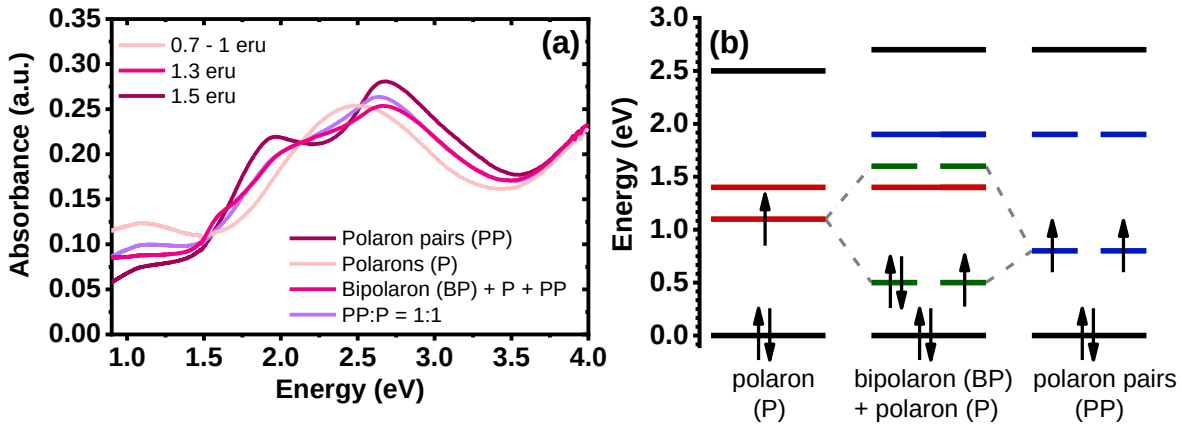

Figure 5-6. (a) Optical signatures of singlet polarons (P), polaron pairs (PP), and singlet bipolarons (BP); (b) Electronic band structure of different polaronic species including polaron, bipolaron, and polaron pairs.

As mentioned earlier in the spectroelectrochemistry results, the optical absorption spectra corresponding to the third redox event of BBL-P (1.3 eru) were severely distorted suggesting the

coexistence of different polaronic species. We thus performed linear superpositions of the optical signatures of polaron (P) and polaron pairs (PP) to quantify the distribution of these polaronic species in the reduced BBL-P films. Despite varying PP:P compositions, the superimposed spectra could only match the main electronic excitations in the visible (4 – 1.7 eV) and near-IR (0.9 – 1.5 eV) regions and failed to capture the electronic transition at 1.6 eV (Figure E-5b). This result suggests that there must be some electronic interactions between polarons and polaron pairs to give rise to a new charged species with an electronic transition of 1.6 eV. Indeed, two isosbestic points at 1.65 eV and 1.52 eV are observed which can be associated to the transformation between PP/new species and P/new species, respectively. In other words, the third redox process of BBL-P should consist of a ternary mixture of polaron, polaron pairs, and a new multiply charged species.

We propose that this new multiply charged species is a singlet bipolaron arising from the hybridization between the bonding states of polaron and polaron pairs (Figure 5-6b). The optimal energy level distribution of polaron and polaron pairs enables the formation of two new mid-gap bands at 0.5 eV and 1.6 eV (Figure 5-6b) where the latter is associated with the transition from the valence band to the non-bonding state of the singlet bipolaron. Our findings have thus provided the first experimental evidence on the coexistence of polaron, polaron pairs, and bipolaron in n-type π-conjugated redox polymer and clearly mapped out the transition between each polaronic species in energy space. We note that previously reported DFT calculations have predicted the coexistence of polaron and bipolaron on the same polymer chain of BBL;[258] however, no insights were provided as to how polaron pairs can turn into bipolaron.

In summary, we have experimentally provided for the first time a complete picture of the formation and transition of different polaronic species in the class of ladder

poly(benzimidazobenzophenanthroline). At a low to intermediate doping level of 0.1 – 1.0 eru, singlet polaron is the main charge carrier showing two mid-gap transitions of 1.1 eV and 1.4 eV corresponding to the electronic transition from the valence band to the polaron bonding state and the polaron nonbonding state, respectively. At a very high doping level of 1.5 eru, strongly coupled polaron pairs, rather than bipolarons, are the dominating charge carriers showing a wider bandgap accompanied by two mid-gap transitions of 0.8 eV and 1.9 eV. At an intermediate-high doping level of ~ 1.3 eru, polaron and polaron pairs coexist in equal amount, and the hybridization between their bonding states gives rise to singlet bipolarons; thus, a ternary combinations of polaron, polaron pairs, and bipolarons are in equilibrium.

5.3.7. *In-operando* Raman spectroscopy of BBL-P Films.

We then used *in-operando* Raman spectroscopy to probe the structural and electronic evolution of BBL-P upon electrochemical doping. We will similarly focus our discussion on results obtained in solution of pH < 1 as all three redox states of BBL-P coexist in equilibrium under this condition. The Raman spectra of BBL-P in highly acidic electrolyte (pH = 0.19) are shown in Figure 5-7, and the close-up spectra of relevant vibrational modes are shown in Figures 5-7b–g. The Raman intensity decreased over the whole measurement ranges indicating the formation of polaronic species upon electrochemical reduction.[255, 259] The most intense Raman vibrational modes of undoped BBL-P are located at w_1 = 1713 cm^{-1}, w_2 = 1630 cm^{-1}, w_3 = 1601 cm^{-1}, w_4 = 1538 cm^{-1}, w_5 = 1385 cm^{-1}, w_6 = 1319 cm^{-1}, and w_7 = 1157 cm^{-1}. The w_1 Raman mode can be assigned to the symmetric C=O vibrations which gradually decreased and was completely bleached at E < +0.05V (vs. Ag/Ag^+) (Figure 5-7b). The disappearance of the w_1 vibrational modes implies a very high doping level beyond 1.0 eru was obtained at more negative potential,[255] which corroborates well with our coulometry results.

The w_2 Raman mode (1630 cm^{-1}) can be assigned to the C=N stretch of the phenazine unit[260] whereas the w_3 mode (1601 cm^{-1}) originates from the C=C/C-C vibrations. Upon electrochemical doping, the w_3 peak intensity decreased and gradually shifted to lower frequency (Figures 5-7c and E-10b). In particular, the w_3 Raman band was found at 1589 cm^{-1} (12 cm^{-1} shift) upon the second redox reaction (E = +0.05V, vs. Ag/Ag^+). The substantial frequency decrease suggests that the polarons that are formed cause the structure to adopt a more quinoidal character.[93, 258, 261] As the polymer chains are further reduced (E = -0.15 – -0.20V, vs. Ag/Ag^+), the w_3 vibrational mode increased in intensity and shifted back to higher frequency centering at 1620 cm^{-1} (Figures 5-7c and E-10b). This result implies that the strongly coupled polaron pairs and bipolarons that are formed upon the third redox event results in a pro-benzoidal structure. As a results, these multiply charged species would be much less delocalized compared to the singlet polarons.

Moreover, the w_2 Raman band (1630 cm^{-1}) was found to progressively shift to higher wavenumber as the applied potential was swept from positive to negative (Figure E-10a). In particular, this vibrational mode centered at 1637 cm^{-1} for E = +0.05V (vs. Ag/Ag^+) and at 1663-1664 cm^{-1} for E = -0.15 – -0.20V (vs. Ag/Ag^+). The significant red-shift is indicative of the protonation of the imine bond to yield $-C=N^+-$ on both the phenazine rings and the naphthalene rings.[262] The higher Raman intensity and more red-shifted Raman band seen at -0.15 – -0.20V compared to that at +0.05V suggests that the concentration of $-C=N^+-$ is higher in this reduced form of BBL-P. We note that at low doping level (E = +0.25V, vs. Ag/Ag^+), the -C=N- vibrational mode exhibited marginal shift which means that very few number of imine sites are protonated at this potential.

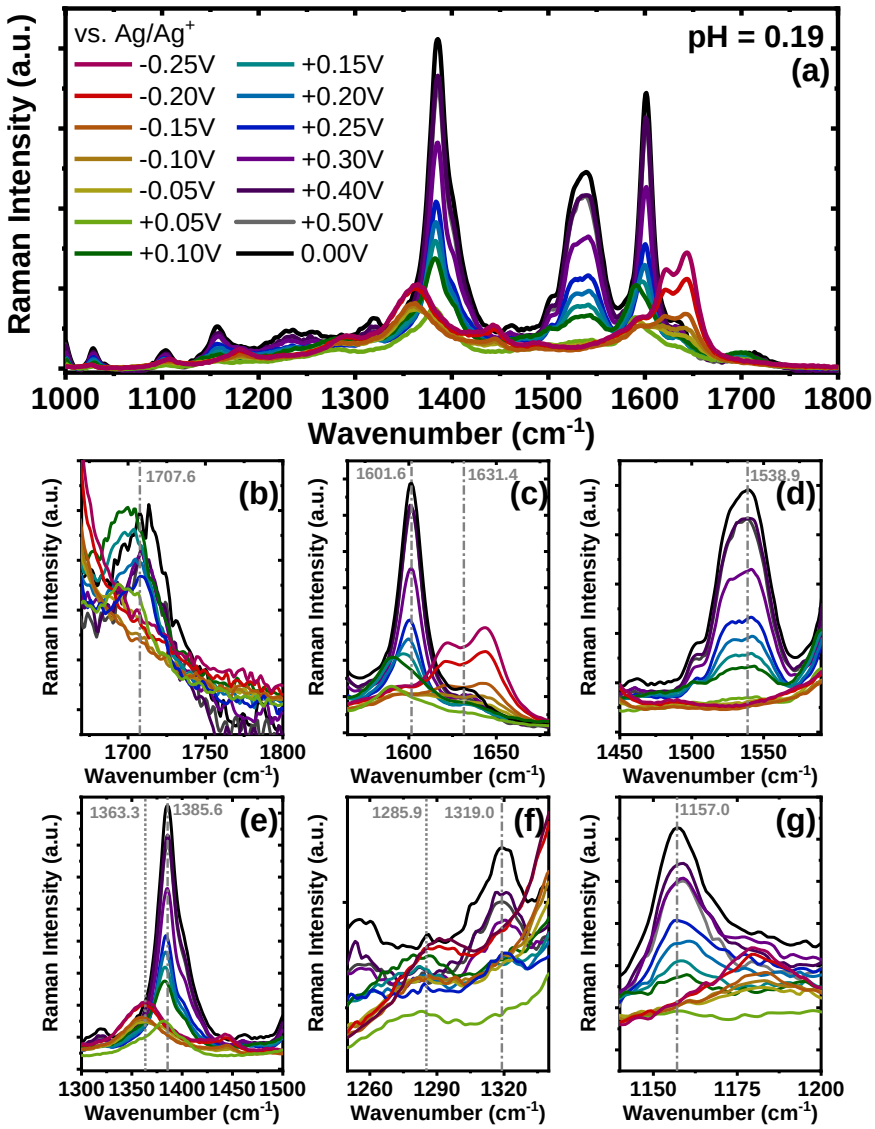

Figure 5-7. (a) *In-operando* Raman spectra of BBL-P films with 532 nm excitation in the range of 1000 – 1800 cm^{-1} region. (b-g) Zoomed in Raman spectra of BBL-P films in the regions of (b) 1125 – 1220 cm^{-1}, (c) 1250 – 1350 cm^{-1}, (d) 1300 – 1500 cm^{-1}, (e) 1450 – 1590 cm^{-1}, (f) 1565 – 1680 cm^{-1}, and (g) 1670 – 1800 cm^{-1}. Raman measurements were collected from BBL-P films coated on gold covered glass substrates as the working electrode with 0.1M $KCl_{(aq)}$ (pH = 0.19) as the electrolyte, Pt mesh as the counter electrode, Ag/AgCl pellet as reference electrode positioned away from the illuminated area.

The w_4 mode (1538 cm^{-1}) corresponds to the aromatic C-C and C-N skeletal vibrations. The slight intensity decrease seen at E = +0.25V (Figure 5-7d) suggests that there are marginal conformational changes in the polymer backbone, which makes sense given the low doping level

(~ 0.2 eru). However, the w_4 Raman band was completely bleached at more negative potentials (E < +0.05V) suggesting significant structural changes upon polaron formation.[259] This finding indeed corroborates the high doping level (> 1.0 eru) explained by coulometry earlier.

The w_5 mode (1385 cm^{-1}) can be assigned to the -C-N- single bond stretching.[239] As the doping level increased, the Raman intensity was found to gradually decrease, and the peak position shifted to lower wavenumber (Figures 5-7e and E-10c). In particular, the peak shifting can be divided into three regions where the first region (E > 0.3V) showed minimal change in frequency, the second region (0 < E < 0.3V) featured a 4 cm^{-1} shift, and the third region (E < 0V) had a substantial shift of 23 cm^{-1} (Figure E-10c). The significant peak shift of this -C-N- vibrational mode seen in the second and third region is indicative of formation of charged species as previously reported for polyaniline and its derivatives.[261, 263] Moreover, the substantial peak shift corroborates the formation of strongly coupled polaron pairs and bipolarons upon the third redox reaction whereas polarons are the main charge carrier in the second redox reaction.

The w_6 Raman mode (1319 cm^{-1}) in undoped BBL-P can be assigned to the -C-N- stretching of the phenazine ring. This vibrational mode was shifted to much lower energy (1285 cm^{-1}) (Figure 5-7f) which can be ascribed to the formation of radical cation segment. Lastly, the w_7 Raman mode (1157 cm^{-1}) corresponding to in-plane C-H bending was substantially upshifted to 1179 cm^{-1} upon the third reduction reaction (Figure 5-7g). This large decrease in vibrational energy of this mode can be explained by the -C-H- vibrational of the radical cation segment.

In summary, our *in-operando* Raman spectroscopy results have provided important structural and electronic insights of BBL-P upon electrochemical doping, all of which are found to be in excellent agreement with spectroelectrochemistry and coulometry analyses. The first reduction reaction of BBL-P results in minimal structural changes mainly due to the low and

non-uniform distribution of polaron across the polymer backbone (1 electron per 4 – 5 repeat unit). The second reduction reaction of BBL-P leads to polaron formation accompanied by significant conformational changes featuring more quinoidal characteristics and an intermediate concentration of protonated imine sites. The third reduction reaction of BBL-P comprised to polaron, polaron pairs, and bipolarons induces greater structural changes showing more benzoidal characteristics and a high concentration of protonated imine sites.

5.3.8. Proposed Schemes for BBL-P Electrochemical Reactions.

Taking all the data together, we now provide a more comprehensive scheme to explain the multiple elusive electrochemical reduction reactions of BBL-P in acidic aqueous electrolytes.

At pH > 3, the BBL-P film remains to be unprotonated and facilely undergoes a redox reaction to form the first reduced form (Scheme 5-3). At this stage, the doping level is rather low featuring about 1 electron per 4 – 5 repeat unit as suggested by spectroelectrochemistry and coulometry results. As a result, minimal changes in the structural properties are observed as evidenced by the *in-operando* Raman spectroscopy analysis.

At 1 < pH < 3, part of the BBL-P film is protonated specifically at the naphthalene imine bond which then undergoes a redox reaction at a more negative potential to form the second reduced form. The density of polaron in this structure is shown to be around 3 – 4 electrons per 4 repeat units via spectroelectrochemistry and coulometry. *In-operando* Raman spectroscopy reveals that this reduced form adopts a more quinoidal character than the undoped unprotonated BBL-P. The molecular structure of this reduced form is thus shown in Scheme 5-4.

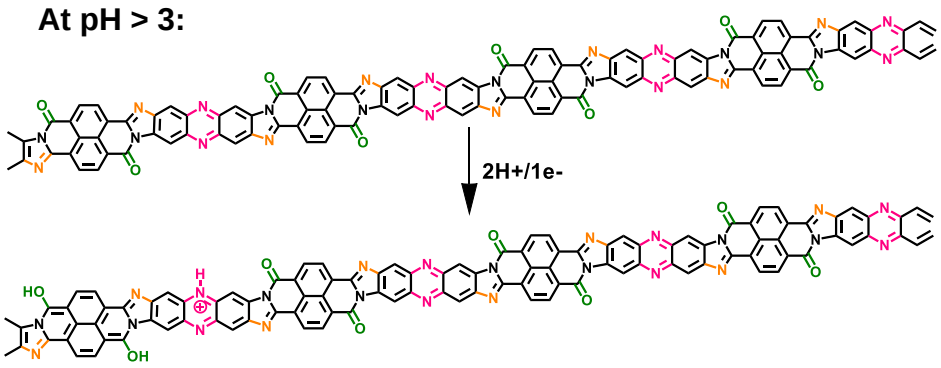

Scheme 5-3. A two-proton/one-electron electrochemical doping reaction of BBL-P at pH > 3.

At pH < 1, the imine bonds of the phenazine rings are protonated, and the protonated polymer undergoes a redox reaction to form the third reduced form at significantly more negative potential. Multiply charged BBL-P with a high doping level of approximately 5 electrons per 4 repeat units are found via spectroelectrochemistry and coulometry. The polymer structure of this reduced state preferentially adopts a more benzoidal character featuring large concentration of -C=N^+- sites on both the phenazine rings and the naphthalene rings. The molecular structure of this reduced state of BBL-P is thus illustrated in Scheme 5-5.

It is important to reiterate that all three final products are formed as a result of a two-proton/one-electron redox reaction, which is to be contrasted with commonly seen one-proton/one-electron. The extra proton insertion to the polymer backbone implies that all reduced products of BBL-P should have higher redox capacity and volumetric capacitance than the parent BBL. Our results have therefore established important fundamental frameworks regarding the electrochemical reactivity and resulting optoelectronic and structural evolution of BBL-P, all of which are broadly applicable to future device applications.

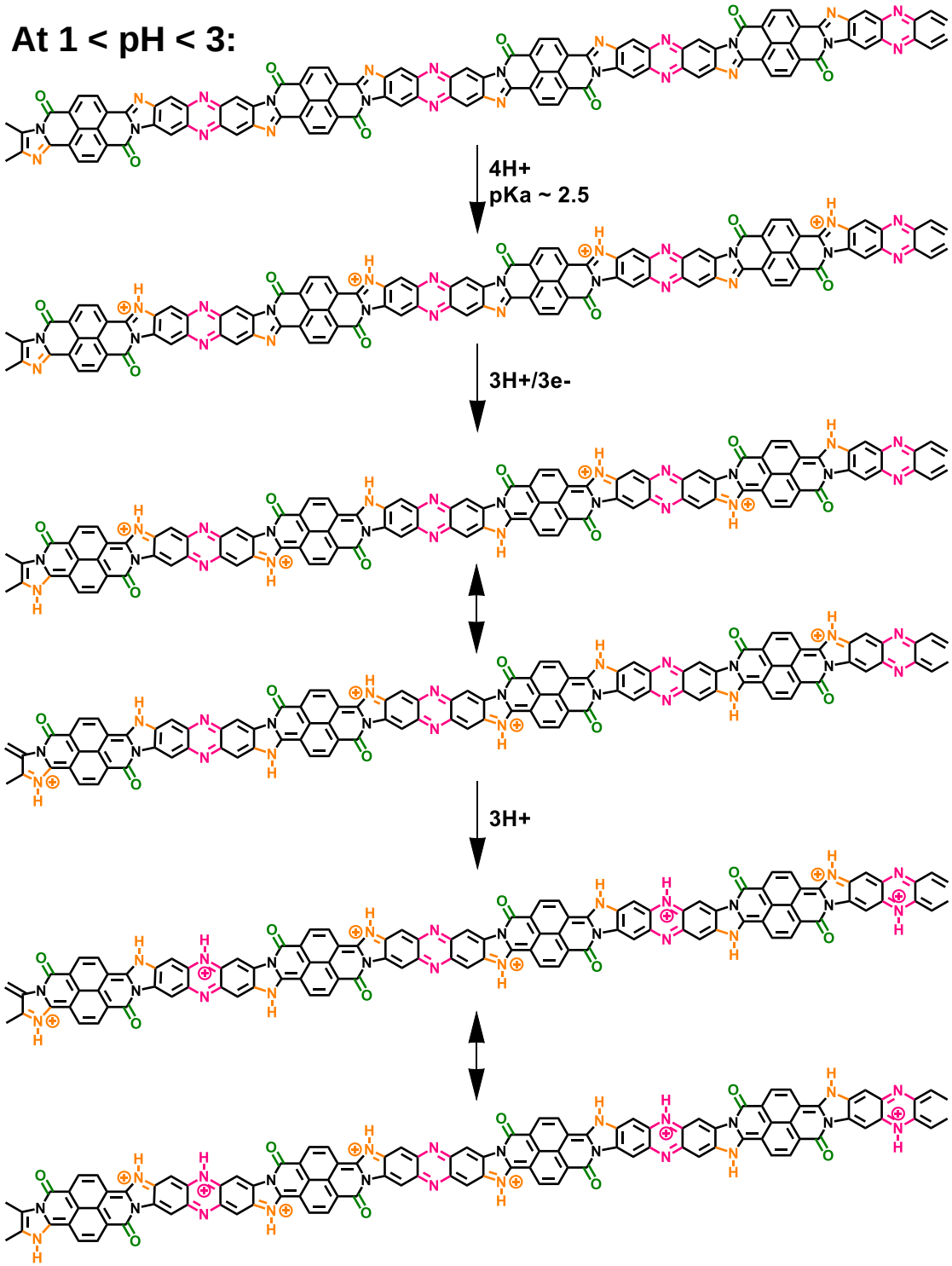

Scheme 5-4. A two-proton/one-electron electrochemical doping reaction of BBL-P at 1<pH<3.

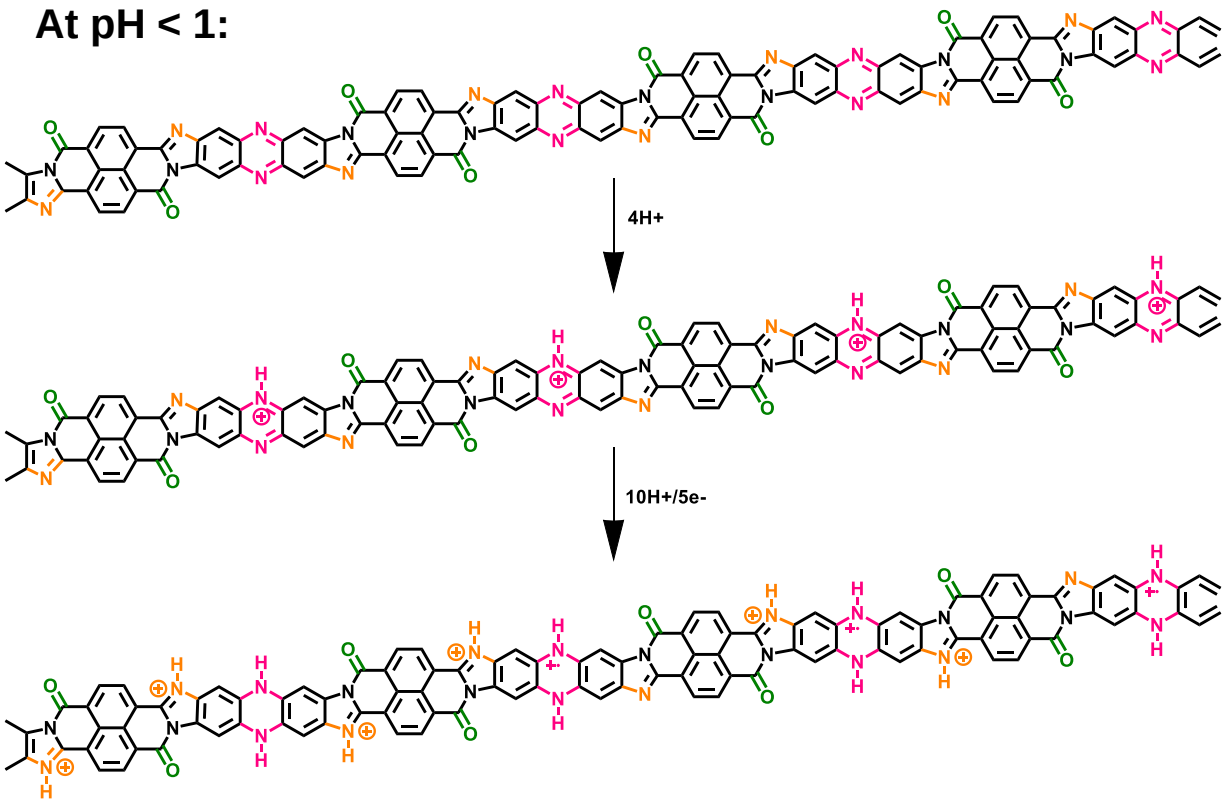

Scheme 5-5. A two-proton/one-electron electrochemical doping reaction of BBL-P at pH < 3.

5.3.9. Redox Capacity of BBL-P Films as a Function of pH and Applied Potentials.

We also explore the charge storage capability of BBL-P in acidic environment towards future applications in organic electrochemical transistors, all-organic proton batteries, and proton supercapacitors. The redox capacity (ρ) is defined as the change in volumetric charge density per infinitesimal change of equilibrium potential relative to a reference electrode.[264, 265]

$$\rho = \frac{dq}{dE_{eq}} = \frac{d\left(\frac{Q}{V}\right)}{dE_{eq}}$$

where ρ is the redox capacity (F/cm^3), Q is the charge stored in the electrode (C), V is the volume of the electrode (cm^3), and E_{eq} is the equilibrium potential.

Using the total charge obtained from coulometry analysis, we computed the redox capacity of BBL-P with respect to the doping potential in electrolyte of pH < 1 as shown in

Figure 5-8a, and the heatmap showing the evolution of redox capacity as a function of both doping potential and electrolyte pH is illustrated in Figure 5-8b. The redox capacity of BBL-P in highly acidic electrolyte exhibited three different peaks at around +0.25V, +0.05V, and -0.15V (vs. Ag/Ag^{+}) which coincided with the formal potential of the first, second, and third redox event, respectively. This result makes sense since electrons are injected into the polymer films at these potentials. Moreover, the maximum ρ value of BBL-P in acidic electrolyte (ρ = 1272 F/cm^3) is significantly higher than that of the parent BBL in neutral aqueous environment (540 – 1000 F/cm^3)[184, 195] and neutral non-aqueous environment (~ 150 F/cm^3).[266] We note that the molecular weight of BBL-P used in this study is considered to be relatively low with an intrinsic viscosity around 1.1 dL/g; thus, further enhanced redox capacity can be expected when higher molecular weight sample is synthesized.[195] Our results have demonstrated that the unique molecular design of BBL-P featuring multiple basic sites with varying pK_a values enables remarkably high redox capacity upon protonation and reduction.

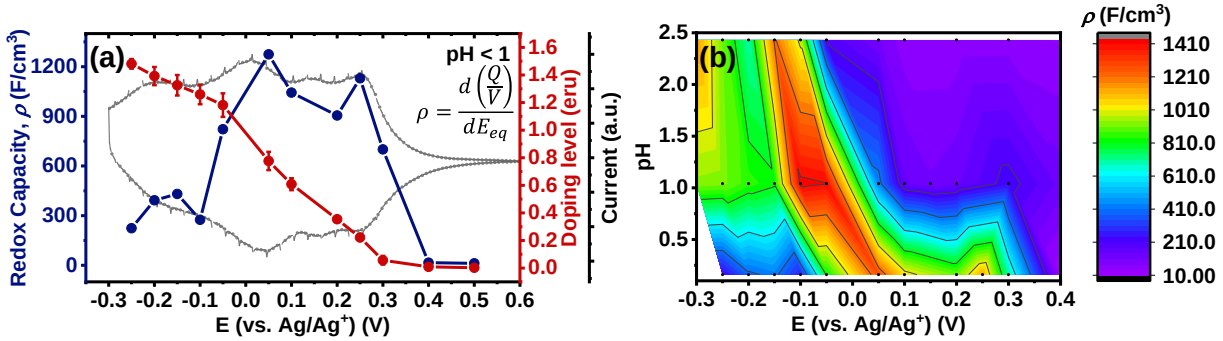

Figure 5-8. (a) Evolution of redox capacity (ρ) and doping level (eru) of BBL-P thin films as a function of doping potential in electrolyte of pH < 1; (b) Dependence of redox capacity of BBL-P thin films as a function of electrolyte pH and doping potentials.

5.4. Conclusions

In conclusion, we have investigated the formation of polaron, polaron pairs, and bipolarons in a novel polybenzimidazobenzophenanthroline) based n-type π-conjugated redox

polymer. By means of electrochemical doping in highly acidic aqueous electrolyte, we have showed that BBL-P can undergo three sequential acid-based coupled redox reactions featuring unusual two-proton/one-electron transfer process. A complement of *in-operando* characterization tools and macroscopic thermo-kinetic analyses were employed to explain the underlying mechanism of electrochemical reduction as well as to elucidate the nature of charged species at each redox event.

The first redox reaction ($pK_a > 3$) is related to the $1H^+/1e^-$ reduction at the carbonyl position showing a low doping level with an average one electron injected per four repeat unit followed by a spontaneous protonation ($1H^+$) at the phenazine imine sites. The second redox reaction ($1 < pK_a < 3$) is associated with the $1H^+/1e^-$ reduction at the protonated naphthalene imine position resulting in an intermediate doping level with an average three electrons injected per four repeat unit accompanied by further protonation ($1H^+$) at the phenazine imine. The third redox reaction ($pK_a < 1$) corresponds to the $1H^+/1e^-$ reduction at the protonated phenazine imine position leading to a high doping level with an average of five electrons injected per four repeat units, which promotes additional protonation ($1H^+$) at the naphthalene imine sites.

At a low to intermediate doping level corresponding to the first and second redox event, singlet polarons are the primary charge carriers that are highly delocalized along a pro-quinoidal polymer backbone. At a higher doping level associated with the third redox event, a ternary mixture of polarons, polaron pairs, and bipolarons coexist in equilibrium whereby bipolarons are shown to originate from the hybridization between the bonding states of polaron and polaron pairs. The coexistence of multiple polaronic species results in significant structural changes that favor a more benzoidal polymer structure and large concentration of protonated imine sites. Further increase of the doping level beyond that of the third redox event causes the singlet

bipolarons to dissociate, and polaron pairs became the dominating charge carriers. Lastly, a superior redox capacity (> 1000 F/cm^3) is demonstrated suggesting remarkable charging capability and tremendous potentials for future applications in organic electrochemical transistors as well as all-polymer energy storage systems.

Chapter 6. Conclusions and Outlook

6.1. Conclusions

Throughout this work, I have investigated factors that govern the charge transport and photovoltaic properties of n-type semiconducting polymers and elucidated the underlying physics towards arriving at more quantitative guidelines to molecular engineer next-generation semiconducting polymers and organic electronic devices. The multiple projects presented in this dissertation have tackled several long-standing challenges and shortcomings in the field of organic electronics including molecular control over the macroscopic phase-separated morphology of polymer blends in all-polymer solar cells, lack of understanding on the electron transport mechanism of n-type semiconducting polymers, and large gaps in the knowledge between fundamental electrochemical reactivity and the nature of charged species n-type π-conjugated redox polymers.

My studies presented in Chapter 2 have addressed the overarching question: What molecular and supramolecular factors govern the photovoltaic properties of all-polymer solar cells (all-PSCs), which are composed of binary blends of n-type and p-type semiconducting polymers? I have investigated several binary polymer blend systems and demonstrated that surface energy and polymer molecular weight of the blend components have profound impacts on the blend photophysics, charge transport, and morphology, all of which control the photovoltaic properties of all-PSC devices.

In particular, a comparative study between PM6:PNDIS and PM6:PNDIBS blends presented in Chapter 2.1 shows that asymmetric surface energy between the blend components seen in the PM6:PNDIS system would induce a thermodynamically favorable blend morphology featuring optimal lateral thin film microstructure with large crystalline domain sizes combined

with preferential *face-on* molecular orientations and vertical phase stratification. As a result, the PM6:PNDIS blend devices exhibited enhanced charge photogeneration, high and balanced blend charge transport properties, suppressed charge recombination, highly efficient charge extraction with near unity charge collection probability, and high device efficiency. In contrast, comparable surface energies between PM6 and PNDIBS result in excessive molecular miscibility and poor domain purity leading to suboptimal photophysical processes and much lower photovoltaic properties.

I have also investigated the effects of polymer molecular weight on the morphology, photophysics, charge transport, and performance of all-polymer solar cells as presented in Chapter 2.2. The device efficiency is shown to reach a maximum value within a narrow range of critical polymer molecular weight (M_n) between 55 – 66 kDa, which can be explained by the highly efficient photophysical processes, combining enhanced charge photogeneration with improved charge transport properties, and optimal morphological features showing a bi-continuous network of 5 – 6 nm crystalline domains with predominantly *face-on* molecular orientations. The drop-off in efficiency at two molecular weight extremes above and below the critical M_n range is rationalized by the decreased charge carrier mobilities, formation of space-charge region, large scale phase separation. Therefore, these results have demonstrated that tuning of polymer molecular weight is an effective molecular engineering strategy to concurrently optimize the morphology, photophysics, charge transport, and efficiency of all-polymer solar cells.

Studies of how polymer chain topology and polymer chain length influence the electron transport physics of n-type semiconducting polymers were conducted and presented in Chapter 3 and Chapter 4. Using organic field-effect transistors as the main experimental platform in

conjunction with a model semi-flexible conjugated polymer and a model rigid-rod conjugated polymer, I have showed completely different chain length dependent electron mobility in these two topological classes of polymers. Various morphological characterization tools were employed to probe the thin film microstructure whereas variable temperature measurements and numerical modeling were used to examine the degree of energetic disorder towards deconvoluting the underlying physics.

I showed that severe structural disorder arising from chain folding/kinks and side chain entanglement which is intrinsic to the molecular designs of semi-flexible conjugated polymers imposes an upper limit on their electron mobility. A maximum electron mobility can only be achieved at a critical degree of polymerization (DP_c) between 45 – 60 repeat units. The decreased electron mobility outside DP_c is rationalized by intercrystallite limitation when $DP < DP_c$ whereas intrachain, interchain, and intracrystallite transport are factors that constrain efficient macroscopic electron transport when $DP > DP_c$.

In contrast, the rigid-rod conjugated polymer combines suppressed structural disorder and favorable electronic landscapes, which results in a linear increase of electron mobility with increasing polymer chain length. Furthermore, I also discovered an exponential decay of threshold voltage with respect to polymer chain length which has not been previously observed in semi-flexible conjugated polymers. I demonstrated that the observed chain length dependent threshold voltage is primarily due to reduced trap density and lower trap depth with increasing polymer chain length. In addition, a unique trade-off of structural disorder between these two topological classes of polymers is also highlighted.

Finally, I investigated the formation of polaron, polaron pairs, and bipolarons in a novel phenazine substituted poly(benzimidazobenzophenanthroline) n-type π-conjugated redox

polymer upon electrochemical doping as presented in Chapter 5. Three acid-based coupled redox reactions featuring unusual two-proton/one-electron transfer process are observed, and the underlying mechanism of these multiple redox states are explained both from a molecular level and a macroscopic thermo-kinetic perspective. The nature of charged species upon electrochemical doping is also unraveled by a complement of *in-operando* characterization techniques. Up to a doping level of about one electron per repeat unit (eru), singlet polarons are the only charge carriers that are highly delocalized along a pro-quinoidal polymer structure. As the doping level reaches ~ 1.3 eru, singlet polarons, polaron pairs, and singlet bipolarons coexist in equilibrium where bipolarons are shown to arise from the hybridization between the bonding states of singlet polarons and polaron pairs. Further increase of the doping level results in polaron pairs as the dominating charge carriers. These findings have thus contributed important fundamental insights regarding the formation mechanism of different polaronic species in n-type π-conjugated redox, which would be broadly applicable to various device applications (e.g. organic electrochemical transistors, energy storage systems, and electrocatalysis).

Overall, the works presented in this dissertation have contributed new knowledge and paved the way towards innovative advances for both the field of semiconducting polymer and the organic electronics research community. Insights gained from these studies provide important design guidelines to engineer the next generation of high-performing semiconducting polymer and organic electronic devices with advanced functionalities. Further investigations should be continued to push the boundaries of understandings of collective properties of semiconducting polymers as well as to usher in transformative technological advances.

6.2. Outlook

On the polymer solar cells front, despite rapid increase in the device efficiency approaching the 20% commercialization benchmark achieved in a few systems, the device stability including shelf stability, chemical stability, thermal stability, and operational stability, sustainability, and large-scale processability remain to be improved in order to fully realize their potentials. Comprehensive understandings of the thermal stability, chemical stability, and the device operational stability under constant illumination are currently lacking. As a result, future studies should examine the degradation mechanism of polymer solar cell devices as well as perform accelerated lifetime measurements such that useful strategies to improve the device stability to meet commercialization specifications can be established. Moreover, studies on the use of non-toxic solvents such as non-halogenated solvents during device fabrication should be prioritized. At the same time, large-area device fabrication techniques such as blade-coating, roll-to-roll printing, and inkjet printing should be explored to ensure minimal losses in the device efficiency and device stability during device scale-up process. In addition, given the large data sets available from hundreds of publications, a data-driven approach can be developed to guide the device optimization of polymer solar cells where the most crucial task would be to determine a suitable descriptor to capture the complex nature of blend morphology.

Regarding the electron transport properties of n-type semiconducting polymers, future studies should continue to explore the influences of intrinsic molecular and supramolecular factors as well as extrinsic environmental factors on the electron transport properties. My results in Chapter 4 have shown that despite its promising potential, BBL suffers from a large density of trap states which are highly detrimental to the electron mobility and the threshold voltage in organic field-effect transistors. Towards this end, one example studies to be done in the near

future is to examine the effects of different trap passivation strategies on the electron transport properties of BBL. From a polymer chemistry point of view, end-capping can be used to ensure no unreacted polar end groups will be dangling at the end of the polymerization; thus, minimizing the number of chemical defects. From a device engineering perspective, blending BBL with other non-conjugated polymers to dilute the trap densities, or blending BBL with electron-donating small molecules to fill the trap are straightforward approaches to passive the trap sites and enhance the electron transport properties.

Although my studies have demonstrated that rigid-rod conjugated polymers are immune from the structural disorder limited electron transport, the observable electron mobility remains modest compared to semi-flexible naphthalene diimide based n-type semiconducting polymers. However, the rigid-rod polymer backbone free of conformational disorder is expected to endow large electron delocalization and high charge carrier mobility. In fact, an intrachain mobility as high as 600 cm^2/Vs has been previously reported for ladder type poly(*p*-phenylenes) via microwave measurements of mobility.[267] As a result, understanding the nature of charge carriers (*electron-polaron* vs. *electron-bipolaron*) in π-conjugated rigid-rod ladder polymer under organic field-effect transistors (OFETs) operation condition is critical to bridge the gap in theoretical calculations and experimental electron mobility values. Towards this end, pulsed and quasi-static measurements of OFET devices can be investigated in conjunction with charge modulation spectroscopy (CMS) to examine the transient device characteristic,[268] track the formation of charge carriers, and identify the nature of such charge carriers. Results and insights presented in Chapter 5 can also provide some frameworks to distinguish between different charge carrier species.

Remarkably high redox capacity has been demonstrated for the novel n-type π-conjugated redox polymer suggesting its promising potentials as anode materials for lithium or proton batteries and electrocatalysts for carbon dioxide reduction. An example study that can be carried out in the near future is to investigate the electronic conductivity, proton conductivity, and the catalytic activity towards developing a triple-phase boundary within a single material which is highly desirable for electrocatalysis applications.[269]

Bibliography

1. Chiang, C. K.; Fincher, C. R.; Park, Y. W.; Heeger, A. J.; Shirakawa, H.; Louis, E. J.; Gau, S. C.; MacDiarmid, A. G. Electrical Conductivity in Doped Polyacetylene. *Phys. Rev. Lett.* **1977,** *39*, 1098-1101.
2. Shirakawa, H. The Discovery of Polyacetylene Film: The Dawning of an Era of Conducting Polymers (Nobel Lecture). *Angew. Chem. Int. Ed.* **2001,** *40*, 2574-2580.
3. MacDiarmid, A. G. "Synthetic Metals": A Novel Role for Organic Polymers (Nobel Lecture). *Angew. Chem. Int. Ed.* **2001,** *40*, 2581-2590.
4. Kulkarni, A. P.; Tonzola, C. J.; Babel, A.; Jenekhe, S. A. Electron Transport Materials for Organic Light-Emitting Diodes. *Chem. Mater.* **2004,** *16*, 4556-4573.
5. Babel, A.; Jenekhe, S. A. High Electron Mobility in Ladder Polymer Field-Effect Transistors. *J. Am. Chem. Soc.* **2003,** *125*, 13656-13657.
6. Mei, J.; Diao, Y.; Appleton, A. L.; Fang, L.; Bao, Z. Integrated Materials Design of Organic Semiconductors for Field-Effect Transistors. *J. Am. Chem. Soc.* **2013,** *135*, 6724-6746.
7. Quinn, J. T. E.; Zhu, J.; Li, X.; Wang, J.; Li, Y. Recent progress in the development of n-type organic semiconductors for organic field effect transistors. *J. Mater. Chem. C* **2017,** *5*, 8654-8681.
8. Paterson, A. F.; Singh, S.; Fallon, K. J.; Hodsden, T.; Han, Y.; Schroeder, B. C.; Bronstein, H.; Heeney, M.; McCulloch, I.; Anthopoulos, T. D. Recent Progress in High-Mobility Organic Transistors: A Reality Check. *Adv. Mater.* **2018,** *30*, 1801079.
9. Kim, M.; Ryu, S. U.; Park, S. A.; Choi, K.; Kim, T.; Chung, D.; Park, T. Donor-Acceptor-Conjugated Polymer for High-Performance Organic Field-Effect Transistors: A Progress Report. *Adv. Funct. Mater.* **2019,** *30*, 1904545.
10. Fratini, S.; Nikolka, M.; Salleo, A.; Schweicher, G.; Sirringhaus, H. Charge transport in high-mobility conjugated polymers and molecular semiconductors. *Nat. Mater.* **2020,** *19*, 491-502.
11. Lee, C.; Lee, S.; Kim, G.-U.; Lee, W.; Kim, B. J. Recent Advances, Design Guidelines, and Prospects of All-Polymer Solar Cells. *Chem. Rev.* **2019,** *119*, 8028-8086.
12. Genene, Z.; Mammo, W.; Wang, E.; Andersson, M. R. Recent Advances in n-Type Polymers for All-Polymer Solar Cells. *Adv. Mater.* **2019,** *31*, 1807275.
13. Earmme, T.; Hwang, Y.-J.; Murari, N. M.; Subramaniyan, S.; Jenekhe, S. A. All-Polymer Solar Cells with 3.3% Efficiency Based on Naphthalene Diimide-Selenophene Copolymer Acceptor. *J. Am. Chem. Soc.* **2013,** *135*, 14960-14963.
14. Hwang, Y.-J.; Courtright, B. A. E.; Ferreira, A. S.; Tolbert, S. H.; Jenekhe, S. A. 7.7% Efficient All-Polymer Solar Cells. *Adv. Mater.* **2015,** *27*, 4578-4584.
15. Hwang, Y.-J.; Earmme, T.; Courtright, B. A. E.; Eberle, F. N.; Jenekhe, S. A. n-Type Semiconducting Naphthalene Diimide-Perylene Diimide Copolymers: Controlling Crystallinity, Blend Morphology, and Compatibility Toward High-Performance All-Polymer Solar Cells. *J. Am. Chem. Soc.* **2015,** *137*, 4424-4434.
16. Jia, T.; Zhang, J.; Zhong, W.; Liang, Y.; Zhang, K.; Dong, S.; Ying, L.; Liu, F.; Wang, X.; Huang, F.; Cao, Y. 14.4% efficiency all-polymer solar cell with broad absorption and low energy loss enabled by a novel polymer acceptor. *Nano Energy* **2020,** *72*, 104718.
17. Wang, G.; Melkonyan, F. S.; Facchetti, A.; Marks, T. J. All-Polymer Solar Cells: Recent Progress, Challenges, and Prospects. *Angew. Chem. Int. Ed.* **2019,** *58*, 4129-4142.

18. Benten, H.; Mori, D.; Ohkita, H.; Ito, S. Recent research progress of polymer donor/polymer acceptor blend solar cells. *J. Mater. Chem. A* **2016,** *4*, 5340-5365.
19. Earmme, T.; Hwang, Y.-J.; Subramaniyan, S.; Jenekhe, S. A. All-Polymer Bulk Heterojuction Solar Cells with 4.8% Efficiency Achieved by Solution Processing from a Co-Solvent. *Adv. Mater.* **2014,** *26*, 6080-6085.
20. Hwang, Y.-J.; Earmme, T.; Subramaniyan, S.; Jenekhe, S. A. Side chain engineering of n-type conjugated polymer enhances photocurrent and efficiency of all-polymer solar cells. *Chem. Commun.* **2014,** *50*, 10801-10804.
21. Kang, H.; Uddin, M. A.; Lee, C.; Kim, K.-H.; Nguyen, T. L.; Lee, W.; Li, Y.; Wang, C.; Woo, H. Y.; Kim, B. J. Determining the Role of Polymer Molecular Weight for High-Performance All-Polymer Solar Cells: Its Effect on Polymer Aggregation and Phase Separation. *J. Am. Chem. Soc.* **2015,** *137*, 2359-2365.
22. Jung, J.; Lee, W.; Lee, C.; Ahn, H.; Kim, B. J. Controlling Molecular Orientation of Naphthalenediimide-Based Polymer Acceptors for High Performance All-Polymer Solar Cells. *Adv. Energy Mater.* **2016,** *6*, 1600504.
23. Gao, L.; Zhang, Z.-G.; Xue, L.; Min, J.; Zhang, J.; Wei, Z.; Li, Y. All-Polymer Solar Cells Based on Absorption-Complementary Polymer Donor and Acceptor with High Power Conversion Efficiency of 8.27%. *Adv. Mater.* **2016,** *28*, 1884-1890.
24. Li, Z.; Xu, X.; Zhang, W.; Meng, X.; Ma, W.; Yartsev, A.; Inganäs, O.; Andersson, M. R.; Janssen, R. A. J.; Wang, E. High Performance All-Polymer Solar Cells by Synergistic Effects of Fine-Tuned Crystallinity and Solvent Annealing. *J. Am. Chem. Soc.* **2016,** *138*, 10935-10944.
25. Zhou, N.; Dudnik, A. S.; Li, T. I. N. G.; Manley, E. F.; Aldrich, T. J.; Guo, P.; Liao, H.-C.; Chen, Z.; Chen, L. X.; Chang, R. P. H.; Facchetti, A.; Olvera de la Cruz, M.; Marks, T. J. All-Polymer Solar Cell Performance Optimized via Systematic Molecular Weight Tuning of Both Donor and Acceptor Polymers. *J. Am. Chem. Soc.* **2016,** *138*, 1240-1251.
26. Zhang, Z.-G.; Yang, Y.; Yao, J.; Xue, L.; Chen, S.; Li, X.; Morrison, W.; Yang, C.; Li, Y. Constructing a Strongly Absorbing Low-Bandgap Polymer Acceptor for High-Performance All-Polymer Solar Cells. *Angew. Chem. Int. Ed.* **2017,** *56*, 13503-13507.
27. Li, Z.; Xu, X.; Zhang, W.; Meng, X.; Genene, Z.; Ma, W.; Mammo, W.; Yartsev, A.; Andersson, M. R.; Janssen, R. A. J.; Wang, E. 9.0% power conversion efficiency from ternary all-polymer solar cells. *Energy & Environ Sci.* **2017,** *10*, 2212-2221.
28. Fan, B.; Ying, L.; Zhu, P.; Pan, F.; Liu, F.; Chen, J.; Huang, F.; Cao, Y. All-Polymer Solar Cells Based on a Conjugated Polymer Containing Siloxane-Functionalized Side Chains with Efficiency over 10%. *Adv. Mater.* **2017,** *29*, 1703906.
29. Kolhe, N. B.; Lee, H.; Kuzuhara, D.; Yoshimoto, N.; Koganezawa, T.; Jenekhe, S. A. All-Polymer Solar Cells with 9.4% Efficiency from Naphthalene Diimide-Biselenophene Copolymer Acceptor. *Chem. Mater.* **2018,** *30*, 6540-6548.
30. Liu, X.; Zhang, C.; Duan, C.; Li, M.; Hu, Z.; Wang, J.; Liu, F.; Li, N.; Brabec, C. J.; Janssen, R. A. J.; Bazan, G. C.; Huang, F.; Cao, Y. Morphology Optimization via Side Chain Engineering Enables All-Polymer Solar Cells with Excellent Fill Factor and Stability. *J. Am. Chem. Soc.* **2018,** *140*, 8934-8943.
31. Xu, X.; Li, Z.; Wang, J.; Lin, B.; Ma, W.; Xia, Y.; Andersson, M. R.; Janssen, R. A. J.; Wang, E. High-Performance All-Polymer Solar Cells Based On Fluorinated Naphthalene

Diimide Acceptor Polymers With Fine-Tuned Crystallinity And Enhanced Dielectric Constants. *Nano Energy* **2018,** *45*, 368-379.
32. Xu, X.; Li, Z.; Zhang, W.; Meng, X.; Zou, X.; Di Carlo Rasi, D.; Ma, W.; Yartsev, A.; Andersson, M. R.; Janssen, R. A. J.; Wang, E. 8.0% Efficient All-Polymer Solar Cells with High Photovoltage of 1.1 V and Internal Quantum Efficiency near Unity. *Adv. Energy Mater.* **2018,** *8*, 1700908.
33. Deshmukh, K. D.; Matsidik, R.; Prasad, S. K. K.; Connal, L. A.; Liu, A. C. Y.; Gann, E.; Thomsen, L.; Hodgkiss, J. M.; Sommer, M.; McNeill, C. R. Tuning the Molecular Weight of the Electron Accepting Polymer in All-Polymer Solar Cells: Impact on Morphology and Charge Generation. *Adv. Funct. Mater.* **2018,** *28*, 1707185.
34. Yuan, J.; Ford, M. J.; Xu, Y.; Zhang, Y.; Bazan, G. C.; Ma, W. Improved Tandem All-Polymer Solar Cells Performance by Using Spectrally Matched Subcells. *Adv. Energy Mater.* **2018,** *8*, 1703291.
35. Zhang, K.; Xia, R.; Fan, B.; Liu, X.; Wang, Z.; Dong, S.; Yip, H.-L.; Ying, L.; Huang, F.; Cao, Y. 11.2% All-Polymer Tandem Solar Cells with Simultaneously Improved Efficiency and Stability. *Adv. Mater.* **2018,** *30*, 1803166.
36. Yao, H.; Bai, F.; Hu, H.; Arunagiri, L.; Zhang, J.; Chen, Y.; Yu, H.; Chen, S.; Liu, T.; Lai, J. Y. L.; Zou, Y.; Ade, H.; Yan, H. Efficient All-Polymer Solar Cells based on a New Polymer Acceptor Achieving 10.3% Power Conversion Efficiency. *ACS Energy Lett.* **2019,** *4*, 417-422.
37. Kolhe, N. B.; Tran, D. K.; Lee, H.; Kuzuhara, D.; Yoshimoto, N.; Koganezawa, T.; Jenekhe, S. A. New Random Copolymer Acceptors Enable Additive-Free Processing of 10.1% Efficient All-Polymer Solar Cells with Near-Unity Internal Quantum Efficiency. *ACS Energy Lett.* **2019,** *4*, 1162-1170.
38. Sun, H.; Tang, Y.; Koh, C. W.; Ling, S.; Wang, R.; Yang, K.; Yu, J.; Shi, Y.; Wang, Y.; Woo, H. Y.; Guo, X. High-Performance All-Polymer Solar Cells Enabled by an n-Type Polymer Based on a Fluorinated Imide-Functionalized Arene. *Adv. Mater.* **2019,** *31*, 1807220.
39. Wu, J.; Meng, Y.; Guo, X.; Zhu, L.; Liu, F.; Zhang, M. All-polymer solar cells based on a novel narrow-bandgap polymer acceptor with power conversion efficiency over 10%. *J. Mater. Chem. A* **2019,** *7*, 16190-16196.
40. Wu, Y.; Schneider, S.; Walter, C.; Chowdhury, A. H.; Bahrami, B.; Wu, H.-C.; Qiao, Q.; Toney, M. F.; Bao, Z. Fine-Tuning Semiconducting Polymer Self-Aggregation and Crystallinity Enables Optimal Morphology and High-Performance Printed All-Polymer Solar Cells. *J. Am. Chem. Soc.* **2020,** *142*, 392-406.
41. Feng, K.; Huang, J.; Zhang, X.; Wu, Z.; Shi, S.; Thomsen, L.; Tian, Y.; Woo, H. Y.; McNeill, C. R.; Guo, X. High-Performance All-Polymer Solar Cells Enabled by n-Type Polymers with an Ultranarrow Bandgap Down to 1.28 eV. *Adv. Mater.* **2020,** *32*, 2001476.
42. Fan, Q.; Ma, R.; Liu, T.; Su, W.; Peng, W.; Zhang, M.; Wang, Z.; Wen, X.; Cong, Z.; Luo, Z.; Hou, L.; Liu, F.; Zhu, W.; Yu, D.; Yan, H.; Wang, E. 10.13% Efficiency All-Polymer Solar Cells Enabled by Improving the Optical Absorption of Polymer Acceptors. *Sol. RRL* **2020,** *4*, 2000142.
43. Du, J.; Hu, K.; Meng, L.; Angunawela, I.; Zhang, J.; Qin, S.; Liebman-Pelaez, A.; Zhu, C.; Zhang, Z.; Ade, H.; Li, Y. High-Performance All-Polymer Solar Cells: Synthesis of Polymer Acceptor by a Random Ternary Copolymerization Strategy. *Angew. Chem. Int. Ed.* **2020,** *59*.

44. Tran, D. K.; Kolhe, N. B.; Hwang, Y.-j.; Kuzuhara, D.; Koganezawa, T.; Jenekhe, S. A. Effects of a Fluorinated Donor Polymer on the Morphology, Photophysics, and Performance of All-Polymer Solar Cells Based on Naphthalene Diimide-Arylene Copolymer Acceptors. *ACS Appl. Mater. Interfaces* **2020,** *12*, 16490-16502.
45. Fan, Q.; Su, W.; Chen, S.; Kim, W.; Chen, X.; Lee, B.; Liu, T.; Mendez-Romero, U. A.; Ma, R.; Yang, T.; Zhuang, W.; Li, Y.; Li, Y.; Kim, T.-S.; Hou, L.; Yang, C.; Yan, H.; Yu, D.; Wang, E. Mechanically Robust All-Polymer Solar Cells from Narrow Band Gap Acceptors with Hetero-Bridging Atoms. *Joule* **2020,** *4*, 658-672.
46. Meng, Y.; Wu, J.; Guo, X.; Su, W.; Zhu, L.; Fang, J.; Zhang, Z.-G.; Liu, F.; Zhang, M.; Russell, T. P.; Li, Y. 11.2% Efficiency all-polymer solar cells with high open-circuit voltage. *Sci. China Chem.* **2019,** *62*, 845-850.
47. Lu, Y.; Wang, J.-Y.; Pei, J. Strategies To Enhance the Conductivity of n-Type Polymer Thermoelectric Materials. *Chem. Mater.* **2019,** *31*, 6412-6423.
48. Sun, Y.; Di, C.-A.; Xu, W.; Zhu, D. Advances in n-Type Organic Thermoelectric Materials and Devices. *Adv. Electron. Mater.* **2019,** *5*, 1800825.
49. Xu, K.; Sun, H.; Ruoko, T.-P.; Wang, G.; Kroon, R.; Kolhe, N. B.; Puttisong, Y.; Liu, X.; Fazzi, D.; Shibata, K.; Yang, C.-Y.; Sun, N.; Persson, G.; Yankovich, A. B.; Olsson, E.; Yoshida, H.; Chen, W. M.; Fahlman, M.; Kemerink, M.; Jenekhe, S. A.; Mueller, C.; Berggren, M.; Fabiano, S. Ground-state electron transfer in all-polymer donor-acceptor heterojunctions. *Nat. Mater.* **2020,** *19*, 738-744.
50. Rivnay, J.; Inal, S.; Salleo, A.; Owens, R. M.; Berggren, M.; Malliaras, G. G. Organic electrochemical transistors. *Nat. Rev. Mater.* **2018,** *3*, 17086.
51. Paulsen, B. D.; Tybrandt, K.; Stavrinidou, E.; Rivnay, J. Organic mixed ionic–electronic conductors. *Nat. Mater.* **2020,** *19*, 13-26.
52. Sun, H.; Wang, L.; Wang, Y.; Guo, X. Imide-Functionalized Polymer Semiconductors. *Chem. Eur. J.* **2019,** *25*, 87-105.
53. Jenekhe, S. A.; Lu, L.; Alam, M. M. New Conjugated Polymers with Donor-Acceptor Architectures: Synthesis and Photophysics of Carbazole-Quinoline and Phenothiazine-Quinoline Copolymers and Oligomers Exhibiting Large Intramolecular Charge Transfer. *Macromolecules* **2001,** *34*, 7315-7324.
54. Zhu, Y.; Champion, R. D.; Jenekhe, S. A. Conjugated Donor−Acceptor Copolymer Semiconductors with Large Intramolecular Charge Transfer: Synthesis, Optical Properties, Electrochemistry, and Field Effect Carrier Mobility of Thienopyrazine-Based Copolymers. *Macromolecules* **2006,** *39*, 8712-8719.
55. Teo, Y. C.; Lai, H. W. H.; Xia, Y. Synthesis of Ladder Polymers: Developments, Challenges, and Opportunities. *Chem. Eur. J.* **2017,** *23*, 14101-14112.
56. Cao, Z.; Leng, M.; Cao, Y.; Gu, X.; Fang, L. How rigid are conjugated non-ladder and ladder polymers? *J. Polym. Sci.* **2021,** *1*.
57. Tian, X.; Stranks Samuel, D.; You, F. Life cycle energy use and environmental implications of high-performance perovskite tandem solar cells. *Sci. Adv.* **2020,** *6*, eabb0055.
58. Riede, M.; Spoltore, D.; Leo, K. Organic Solar Cells—The Path to Commercial Success. *Adv. Energy Mater.* **2021,** *11*, 2002653.
59. Heliatek TÜV Rheinland certified - Ultra-low carbon footprint. https://www.heliatek.com/en/technology/sustainability/.

60. Lunardi, M. M.; Dias, P. R.; Deng, R.; Corkish, R. Life Cycle Environmental Assessment of Different Solar Photovoltaic Technologies. In *Photovoltaic Sustainability and Management*, AIP Publishing LLC: 2021; pp 5-1-5-34.
61. Xu, Y.; Yuan, J.; Zhou, S.; Seifrid, M.; Ying, L.; Li, B.; Huang, F.; Bazan, G. C.; Ma, W. Ambient Processable and Stable All-Polymer Organic Solar Cells. *Adv. Funct. Mater.* **2019,** *29*, 1806747.
62. Lee, S.; Kim, Y.; Wu, Z.; Lee, C.; Oh, S. J.; Luan, N. T.; Lee, J.; Jeong, D.; Zhang, K.; Huang, F.; Kim, T.-S.; Woo, H. Y.; Kim, B. J. Aqueous-Soluble Naphthalene Diimide-Based Polymer Acceptors for Efficient and Air-Stable All-Polymer Solar Cells. *ACS Appl. Mater. Interfaces* **2019,** *11*, 45038-45047.
63. Zhang, Y.; Xu, Y.; Ford, M. J.; Li, F.; Sun, J.; Ling, X.; Wang, Y.; Gu, J.; Yuan, J.; Ma, W. Thermally Stable All-Polymer Solar Cells with High Tolerance on Blend Ratios. *Adv. Energy Mater.* **2018,** *8*, 1800029.
64. Kim, T.; Kim, J.-H.; Kang, T. E.; Lee, C.; Kang, H.; Shin, M.; Wang, C.; Ma, B.; Jeong, U.; Kim, T.-S.; Kim, B. J. Flexible, highly efficient all-polymer solar cells. *Nat. Commun.* **2015,** *6*, 8547.
65. Lee, J.-W.; Ma, B. S.; Choi, J.; Lee, J.; Lee, S.; Liao, K.; Lee, W.; Kim, T.-S.; Kim, B. J. Origin of the High Donor-Acceptor Composition Tolerance in Device Performance and Mechanical Robustness of All-Polymer Solar Cells. *Chem. Mater.* **2020,** *32*, 582-594.
66. Choi, J.; Kim, W.; Kim, S.; Kim, T.-S.; Kim, B. J. Influence of Acceptor Type and Polymer Molecular Weight on the Mechanical Properties of Polymer Solar Cells. *Chem. Mater.* **2019,** *31*, 9057-9069.
67. Zhang, Q.; Yuan, X.; Feng, Y.; Larson, B. W.; Su, G. M.; Maung Maung, Y.; Rujisamphan, N.; Li, Y.; Yuan, J.; Ma, W. Understanding the Interplay of Transport-Morphology-Performance in PBDB-T-Based Polymer Solar Cells. *Sol. RRL* **2020,** *4*, 1900524.
68. Xu, Y.; Yuan, J.; Liang, S.; Chen, J.-D.; Xia, Y.; Larson, B. W.; Wang, Y.; Su, G. M.; Zhang, Y.; Cui, C.; Wang, M.; Zhao, H.; Ma, W. Simultaneously Improved Efficiency and Stability in All-Polymer Solar Cells by a P-i-N Architecture. *ACS Energy Lett.* **2019,** *4*, 2277-2286.
69. Tran, D. K.; Robitaille, A.; Hai, I. J.; Ding, X.; Kuzuhara, D.; Koganezawa, T.; Chiu, Y.-C.; Leclerc, M.; Jenekhe, S. A. Elucidating the impact of molecular weight on morphology, charge transport, photophysics and performance of all-polymer solar cells. *J. Mater. Chem. A* **2020,** *8*, 21070-21083.
70. You, H.; Kim, D.; Cho, H.-H.; Lee, C.; Chong, S.; Ahn, N. Y.; Seo, M.; Kim, J.; Kim, F. S.; Kim, B. J. Shift of the Branching Point of the Side-Chain in Naphthalenediimide (NDI)-Based Polymer for Enhanced Electron Mobility and All-Polymer Solar Cell Performance. *Adv. Funct. Mater.* **2018,** *28*, 1803613.
71. Lee, C.; Giridhar, T.; Choi, J.; Kim, S.; Kim, Y.; Kim, T.; Lee, W.; Cho, H.-H.; Wang, C.; Ade, H.; Kim, B. J. Importance of 2D Conjugated Side Chains of Benzodithiophene-Based Polymers in Controlling Polymer Packing, Interfacial Ordering, and Composition Variations of All-Polymer Solar Cells. *Chem. Mater.* **2017,** *29*, 9407-9415.
72. Yuan, J.; Xu, Y.; Shi, G.; Ling, X.; Ying, L.; Huang, F.; Lee, T. H.; Woo, H. Y.; Kim, J. Y.; Cao, Y.; Ma, W. Engineering the morphology via processing additives in multiple all-polymer solar cells for improved performance. *J. Mater. Chem. A* **2018,** *6*, 10421-10432.

73. Ye, L.; Jiao, X.; Zhao, W.; Zhang, S.; Yao, H.; Li, S.; Ade, H.; Hou, J. Manipulation of Domain Purity and Orientational Ordering in High Performance All-Polymer Solar Cells. *Chem. Mater.* **2016,** *28*, 6178-6185.
74. Shi, G.; Yuan, J.; Huang, X.; Lu, Y.; Liu, Z.; Peng, J.; Ding, G.; Shi, S.; Sun, J.; Lu, K.; Wang, H.-Q.; Ma, W. Combinative Effect of Additive and Thermal Annealing Processes Delivers High Efficiency All-Polymer Solar Cells. *J. Phys. Chem. C* **2015,** *119*, 25298-25306.
75. Robitaille, A.; Jenekhe, S. A.; Leclerc, M. Poly(naphthalene diimide-alt-bithiophene) Prepared by Direct (Hetero)arylation Polymerization for Efficient All-Polymer Solar Cells. *Chem. Mater.* **2018,** *30*, 5353-5361.
76. Kim, Y. J.; Ahn, S.; Wang, D. H.; Park, C. E. A Mechanistic Understanding of a Binary Additive System to Synergistically Boost Efficiency in All-Polymer Solar Cells. *Sci. Rep.* **2015,** *5*, 18024.
77. Nobel Prize in Physics Awarded to Transistor Inventors. *Bell System Technical Journal* **1956,** *35*, i-iv.
78. Sze, S. M.; Li, Y.; Ng, K. K. *Physics of semiconductor devices*. John wiley & sons: 2021.
79. Murari, N. M.; Hwang, Y.-J.; Kim, F. S.; Jenekhe, S. A. Organic nonvolatile memory devices utilizing intrinsic charge-trapping phenomena in an n-type polymer semiconductor. *Org. Electron.* **2016,** *31*, 104-110.
80. Haneef, H. F.; Zeidell, A. M.; Jurchescu, O. D. Charge carrier traps in organic semiconductors: a review on the underlying physics and impact on electronic devices. *J. Mater. Chem. C* **2020,** *8*, 759-787.
81. Chen, S.; An, Y.; Dutta, G. K.; Kim, Y.; Zhang, Z.-G.; Li, Y.; Yang, C. A Synergetic Effect of Molecular Weight and Fluorine in All-Polymer Solar Cells with Enhanced Performance. *Adv. Funct. Mater.* **2017,** *27*, 1603564.
82. Fan, B.; Ying, L.; Wang, Z.; He, B.; Jiang, X.-F.; Huang, F.; Cao, Y. Optimisation of processing solvent and molecular weight for the production of green-solvent-processed all-polymer solar cells with a power conversion efficiency over 9%. *Energy & Environ Sci.* **2017,** *10*, 1243-1251.
83. Zhao, Z.; Yin, Z.; Chen, H.; Zheng, L.; Zhu, C.; Zhang, L.; Tan, S.; Wang, H.; Guo, Y.; Tang, Q.; Liu, Y. High-Performance, Air-Stable Field-Effect Transistors Based on Heteroatom-Substituted Naphthalenediimide-Benzothiadiazole Copolymers Exhibiting Ultrahigh Electron Mobility up to 8.5 cm^2/Vs. *Adv. Mater.* **2017,** *29*, 1602410.
84. Dou, J.-H.; Zheng, Y.-Q.; Yao, Z.-F.; Lei, T.; Shen, X.; Luo, X.-Y.; Yu, Z.-A.; Zhang, S.-D.; Han, G.; Wang, Z.; Yi, Y.; Wang, J.-Y.; Pei, J. A Cofacially Stacked Electron-Deficient Small Molecule with a High Electron Mobility of over 10 $cm^2V^{-1}s^{-1}$ in Air. *Adv. Mater.* **2015,** *27*, 8051-8055.
85. Zheng, Y.-Q.; Lei, T.; Dou, J.-H.; Xia, X.; Wang, J.-Y.; Liu, C.-J.; Pei, J. Strong Electron-Deficient Polymers Lead to High Electron Mobility in Air and Their Morphology-Dependent Transport Behaviors. *Adv. Mater.* **2016,** *28*, 7213-7219.
86. Wang, Y.; Guo, H.; Harbuzaru, A.; Uddin, M. A.; Arrechea-Marcos, I.; Ling, S.; Yu, J.; Tang, Y.; Sun, H.; López Navarrete, J. T.; Ortiz, R. P.; Woo, H. Y.; Guo, X. (Semi)ladder-Type Bithiophene Imide-Based All-Acceptor Semiconductors: Synthesis, Structure–Property Correlations, and Unipolar n-Type Transistor Performance. *J. Am. Chem. Soc.* **2018,** *140*, 6095-6108.

87. Cavassin, P.; Holzer, I.; Tsokkou, D.; Bardagot, O.; Réhault, J.; Banerji, N. Electrochemical Doping in Ordered and Disordered Domains of Organic Mixed Ionic–Electronic Conductors. *Adv. Mater.* **2023,** *n/a*, 2300308.
88. Scholes, D. T.; Yee, P. Y.; Lindemuth, J. R.; Kang, H.; Onorato, J.; Ghosh, R.; Luscombe, C. K.; Spano, F. C.; Tolbert, S. H.; Schwartz, B. J. The Effects of Crystallinity on Charge Transport and the Structure of Sequentially Processed F4TCNQ-Doped Conjugated Polymer Films. *Adv. Funct. Mater.* **2017,** *27*, 1702654.
89. Wu, E. C.; Salamat, C. Z.; Ruiz, O. L.; Qu, T.; Kim, A.; Tolbert, S. H.; Schwartz, B. J. Counterion Control and the Spectral Signatures of Polarons, Coupled Polarons, and Bipolarons in Doped P3HT Films. *Adv. Funct. Mater.* **2023,** *33*, 2213652.
90. Enengl, C.; Enengl, S.; Pluczyk, S.; Havlicek, M.; Lapkowski, M.; Neugebauer, H.; Ehrenfreund, E. Doping-Induced Absorption Bands in P3HT: Polarons and Bipolarons. *ChemPhysChem* **2016,** *17*, 3836-3844.
91. Voss, M. G.; Challa, J. R.; Scholes, D. T.; Yee, P. Y.; Wu, E. C.; Liu, X.; Park, S. J.; León Ruiz, O.; Subramaniyan, S.; Chen, M.; Jenekhe, S. A.; Wang, X.; Tolbert, S. H.; Schwartz, B. J. Driving Force and Optical Signatures of Bipolaron Formation in Chemically Doped Conjugated Polymers. *Adv. Mater.* **2021,** *33*, 2000228.
92. Brédas, J. L.; Scott, J. C.; Yakushi, K.; Street, G. B. Polarons and bipolarons in polypyrrole: Evolution of the band structure and optical spectrum upon doing. *Phys. Rev. B* **1984,** *30*, 1023-1025.
93. Nightingale, J.; Wade, J.; Moia, D.; Nelson, J.; Kim, J.-S. Impact of Molecular Order on Polaron Formation in Conjugated Polymers. *J. Phys. Chem. C* **2018,** *122*, 29129-29140.
94. Genene, Z.; Mammo, W.; Wang, E.; Andersson, M. R. Recent Advances in n-Type Polymers for All-Polymer Solar Cells. *Adv. Mater.* **2019,** *31*, 1807275.
95. Yuan, J.; Zhang, Y.; Zhou, L.; Zhang, G.; Yip, H.-L.; Lau, T.-K.; Lu, X.; Zhu, C.; Peng, H.; Johnson, P. A.; Leclerc, M.; Cao, Y.; Ulanski, J.; Li, Y.; Zou, Y. Single-Junction Organic Solar Cell with over 15% Efficiency Using Fused-Ring Acceptor with Electron-Deficient Core. *Joule* **2019,** *3*, 1140-1151.
96. Cui, Y.; Yao, H.; Zhang, J.; Zhang, T.; Wang, Y.; Hong, L.; Xian, K.; Xu, B.; Zhang, S.; Peng, J.; Wei, Z.; Gao, F.; Hou, J. Over 16% efficiency organic photovoltaic cells enabled by a chlorinated acceptor with increased open-circuit voltages. *Nat. Commun.* **2019,** *10*, 2515.
97. Hwang, Y.-J.; Ren, G.; Murari, N. M.; Jenekhe, S. A. n-Type Naphthalene Diimide–Biselenophene Copolymer for All-Polymer Bulk Heterojunction Solar Cells. *Macromolecules* **2012,** *45*, 9056-9062.
98. Wu, Y.; Schneider, S.; Walter, C.; Chowdhury, A. H.; Bahrami, B.; Wu, H.-C.; Qiao, Q.; Toney, M. F.; Bao, Z. Fine-Tuning Semiconducting Polymer Self-Aggregation and Crystallinity Enables Optimal Morphology and High-Performance Printed All-Polymer Solar Cells. *J. Am. Chem. Soc.* **2019,** *142*, 392-406.
99. Fan, B.; Ying, L.; Zhu, P.; Pan, F.; Liu, F.; Chen, J.; Huang, F.; Cao, Y. All-Polymer Solar Cells Based on a Conjugated Polymer Containing Siloxane-Functionalized Side Chains with Efficiency over 10%. *Adv. Mater.* **2017,** *29*, 1703906.
100. Lee, C.; Kang, H.; Lee, W.; Kim, T.; Kim, K.-H.; Woo, H. Y.; Wang, C.; Kim, B. J. High-Performance All-Polymer Solar Cells Via Side-Chain Engineering of the Polymer

Acceptor: The Importance of the Polymer Packing Structure and the Nanoscale Blend Morphology. *Adv. Mater.* **2015,** *27*, 2466-2471.
101. Lee, W.; Lee, C.; Yu, H.; Kim, D.-J.; Wang, C.; Woo, H. Y.; Oh, J. H.; Kim, B. J. Side Chain Optimization of Naphthalenediimide-Bithiophene-Based Polymers to Enhance the Electron Mobility and the Performance in All-Polymer Solar Cells. *Adv. Funct. Mater.* **2016,** *26*, 1543-1553.
102. Li, W.; Ye, L.; Li, S.; Yao, H.; Ade, H.; Hou, J. A High-Efficiency Organic Solar Cell Enabled by the Strong Intramolecular Electron Push-Pull Effect of the Nonfullerene Acceptor. *Adv. Mater.* **2018,** *30*, 1707170.
103. Zhao, W.; Li, S.; Yao, H.; Zhang, S.; Zhang, Y.; Yang, B.; Hou, J. Molecular Optimization Enables over 13% Efficiency in Organic Solar Cells. *J. Am. Chem. Soc.* **2017,** *139*, 7148-7151.
104. Zhang, M.; Guo, X.; Zhang, S.; Hou, J. Synergistic Effect of Fluorination on Molecular Energy Level Modulation in Highly Efficient Photovoltaic Polymers. *Adv. Mater.* **2014,** *26*, 1118-1123.
105. Deng, D.; Zhang, Y.; Zhang, J.; Wang, Z.; Zhu, L.; Fang, J.; Xia, B.; Wang, Z.; Lu, K.; Ma, W.; Wei, Z. Fluorination-enabled optimal morphology leads to over 11% efficiency for inverted small-molecule organic solar cells. *Nat. Commun.* **2016,** *7*, 13740.
106. Wang, Y.; Zhang, Y.; Qiu, N.; Feng, H.; Gao, H.; Kan, B.; Ma, Y.; Li, C.; Wan, X.; Chen, Y. A Halogenation Strategy for over 12% Efficiency Nonfullerene Organic Solar Cells. *Adv. Energy Mater.* **2018,** *8*, 1702870.
107. Stuart, A. C.; Tumbleston, J. R.; Zhou, H.; Li, W.; Liu, S.; Ade, H.; You, W. Fluorine Substituents Reduce Charge Recombination and Drive Structure and Morphology Development in Polymer Solar Cells. *J. Am. Chem. Soc.* **2013,** *135*, 1806-1815.
108. Lu, L.; Yu, L. Understanding Low Bandgap Polymer PTB7 and Optimizing Polymer Solar Cells Based on It. *Adv. Mater.* **2014,** *26*, 4413-4430.
109. Sun, H.; Tang, Y.; Koh, C. W.; Ling, S.; Wang, R.; Yang, K.; Yu, J.; Shi, Y.; Wang, Y.; Woo, H. Y.; Guo, X. High-Performance All-Polymer Solar Cells Enabled by an n-Type Polymer Based on a Fluorinated Imide-Functionalized Arene. *Adv. Mater.* **2019,** *31*, 1807220.
110. Kawashima, K.; Fukuhara, T.; Suda, Y.; Suzuki, Y.; Koganezawa, T.; Yoshida, H.; Ohkita, H.; Osaka, I.; Takimiya, K. Implication of Fluorine Atom on Electronic Properties, Ordering Structures, and Photovoltaic Performance in Naphthobisthiadiazole-Based Semiconducting Polymers. *J. Am. Chem. Soc.* **2016,** *138*, 10265-10275.
111. Yao, C.; Peng, C.; Yang, Y.; Li, L.; Bo, M.; Wang, J. Elucidating the key role of fluorine in improving the charge mobility of electron acceptors for non-fullerene organic solar cells by multiscale simulations. *J. Mater. Chem. C* **2018,** *6*, 4912-4918.
112. Zhou, N.; Facchetti, A. Naphthalenediimide (NDI) polymers for all-polymer photovoltaics. *Mater. Today* **2018,** *21*, 377-390.
113. Yang, J.; Xiao, B.; Tang, A.; Li, J.; Wang, X.; Zhou, E. Aromatic-Diimide-Based n-Type Conjugated Polymers for All-Polymer Solar Cell Applications. *Adv. Mater.* **2019,** *31*, 1804699.
114. Chen, D.; Yao, J.; Chen, L.; Yin, J.; Lv, R.; Huang, B.; Liu, S.; Zhang, Z.-G.; Yang, C.; Chen, Y.; Li, Y. Dye-Incorporated Polynaphthalenediimide Acceptor for Additive-Free High-Performance All-Polymer Solar Cells. *Angew. Chem. Int. Ed.* **2018,** *57*, 4580-4584.

115. Zhang, N.; Xu, Y.; Zhou, X.; Zhang, W.; Zhou, K.; Yu, L.; Ma, W.; Xu, X. Synergistic effects of copolymerization and fluorination on acceptor polymers for efficient and stable all-polymer solar cells. *J. Mater. Chem. C* **2019,** *7*, 14130-14140.
116. Liu, X.; Zou, Y.; Wang, H.-Q.; Wang, L.; Fang, J.; Yang, C. High-Performance All-Polymer Solar Cells with a High Fill Factor and a Broad Tolerance to the Donor/Acceptor Ratio. *ACS Appl. Mater. Interfaces* **2018,** *10*, 38302-38309.
117. Zhang, M.; Guo, X.; Ma, W.; Ade, H.; Hou, J. A Large-Bandgap Conjugated Polymer for Versatile Photovoltaic Applications with High Performance. *Adv. Mater.* **2015,** *27*, 4655-4660.
118. Kulkarni, A. P.; Zhu, Y.; Babel, A.; Wu, P.-T.; Jenekhe, S. A. New Ambipolar Organic Semiconductors. 2. Effects of Electron Acceptor Strength on Intramolecular Charge Transfer Photophysics, Highly Efficient Electroluminescence, and Field-Effect Charge Transport of Phenoxazine-Based Donorв€'Acceptor Materials. *Chem. Mater.* **2008,** *20*, 4212-4223.
119. Luna-Barcenas, G.; Meredith, J. C.; Sanchez, I. C.; Johnston, K. P.; Gromov, D. G.; de Pablo, J. J. Relationship between polymer chain conformation and phase boundaries in a supercritical fluid. *J. Chem. Phys.* **1997,** *107*, 10782-10792.
120. Williams, C.; Brochard, F.; Frisch, H. L. Polymer Collapse. *Annual Review of Physical Chemistry* **1981,** *32*, 433-451.
121. Courtright, B. A. E.; Jenekhe, S. A. Polyethylenimine Interfacial Layers in Inverted Organic Photovoltaic Devices: Effects of Ethoxylation and Molecular Weight on Efficiency and Temporal Stability. *ACS Appl. Mater. Interfaces* **2015,** *7*, 26167-26175.
122. Azzouzi, M.; Kirchartz, T.; Nelson, J. Factors Controlling Open-Circuit Voltage Losses in Organic Solar Cells. *Trends in Chemistry* **2019,** *1*, 49-62.
123. Wang, Y.; Qian, D.; Cui, Y.; Zhang, H.; Hou, J.; Vandewal, K.; Kirchartz, T.; Gao, F. Optical Gaps of Organic Solar Cells as a Reference for Comparing Voltage Losses. *Adv. Energy Mater.* **2018,** *8*, 1801352.
124. Ren, G.; Schlenker, C. W.; Ahmed, E.; Subramaniyan, S.; Olthof, S.; Kahn, A.; Ginger, D. S.; Jenekhe, S. A. Photoinduced Hole Transfer Becomes Suppressed with Diminished Driving Force in Polymer-Fullerene Solar Cells While Electron Transfer Remains Active. *Adv. Funct. Mater.* **2013,** *23*, 1238-1249.
125. Duan, C.; Peng, Z.; Colberts, F. J. M.; Pang, S.; Ye, L.; Awartani, O. M.; Hendriks, K. H.; Ade, H.; Wienk, M. M.; Janssen, R. A. J. Efficient Thick-Film Polymer Solar Cells with Enhanced Fill Factors via Increased Fullerene Loading. *ACS Appl. Mater. Interfaces* **2019,** *11*, 10794-10800.
126. Zhang, G.; Xia, R.; Chen, Z.; Xiao, J.; Zhao, X.; Liu, S.; Yip, H.-L.; Cao, Y. Overcoming Space-Charge Effect for Efficient Thick-Film Non-Fullerene Organic Solar Cells. *Adv. Energy Mater.* **2018,** *8*, 1801609.
127. Jin, Y.; Chen, Z.; Xiao, M.; Peng, J.; Fan, B.; Ying, L.; Zhang, G.; Jiang, X.-F.; Yin, Q.; Liang, Z.; Huang, F.; Cao, Y. Thick Film Polymer Solar Cells Based on Naphtho[1,2-c:5,6-c]bis[1,2,5]thiadiazole Conjugated Polymers with Efficiency over 11%. *Adv. Energy Mater.* **2017,** *7*, 1700944.
128. Fan, B.; Zhu, P.; Xin, J.; Li, N.; Ying, L.; Zhong, W.; Li, Z.; Ma, W.; Huang, F.; Cao, Y. High-Performance Thick-Film All-Polymer Solar Cells Created Via Ternary Blending of a Novel Wide-Bandgap Electron-Donating Copolymer. *Adv. Energy Mater.* **2018,** *8*, 1703085.

129. Guo, B.; Li, W.; Guo, X.; Meng, X.; Ma, W.; Zhang, M.; Li, Y. High Efficiency Nonfullerene Polymer Solar Cells with Thick Active Layer and Large Area. *Adv. Mater.* **2017,** *29*, 1702291.
130. Zhong, H.; Ye, L.; Chen, J.-Y.; Jo, S. B.; Chueh, C.-C.; Carpenter, J. H.; Ade, H.; Jen, A. K. Y. A regioregular conjugated polymer for high performance thick-film organic solar cells without processing additive. *J. Mater. Chem. A* **2017,** *5*, 10517-10525.
131. Huang, J.; Carpenter, J. H.; Li, C.-Z.; Yu, J.-S.; Ade, H.; Jen, A. K. Y. Highly Efficient Organic Solar Cells with Improved Vertical Donor-Acceptor Compositional Gradient Via an Inverted Off-Center Spinning Method. *Adv. Mater.* **2016,** *28*, 967-974.
132. Wang, Z.; Hu, Y.; Xiao, T.; Zhu, Y.; Chen, X.; Bu, L.; Zhang, Y.; Wei, Z.; Xu, B. B.; Lu, G. Correlations between Performance of Organic Solar Cells and Film-Depth-Dependent Optical and Electronic Variations. *Adv. Optical Mater.* **2019,** *7*, 1900152.
133. Proctor, C. M.; Kuik, M.; Nguyen, T.-Q. Charge carrier recombination in organic solar cells. *Prog. Polym. Sci.* **2013,** *38*, 1941-1960.
134. Cowan, S. R.; Banerji, N.; Leong, W. L.; Heeger, A. J. Charge Formation, Recombination, and Sweep-Out Dynamics in Organic Solar Cells. *Adv. Funct. Mater.* **2012,** *22*, 1116-1128.
135. A. Street, R.; Cowan, S.; J. Heeger, A. Experimental test for geminate recombination applied to organic solar cells. *Phys. Rev. B* **2010,** *82*, 121301(R).
136. Jenekhe, S. A.; Osaheni, J. A. Excimers and Exciplexes of Conjugated Polymers. *Science* **1994,** *265*, 765-768.
137. Xie, B.; Zhang, K.; Hu, Z.; Fang, H.; Lin, B.; Yin, Q.; He, B.; Dong, S.; Ying, L.; Ma, W.; Huang, F.; Yan, H.; Cao, Y. Polymer Pre-Aggregation Enables Optimal Morphology and High Performance in All-Polymer Solar Cells. *Solar RRL* **2019,** *n/a*, 1900385.
138. Kim, M.; Kim, J.-H.; Choi, H. H.; Park, J. H.; Jo, S. B.; Sim, M.; Kim, J. S.; Jinnai, H.; Park, Y. D.; Cho, K. Electrical Performance of Organic Solar Cells with Additive-Assisted Vertical Phase Separation in the Photoactive Layer. *Adv. Energy Mater.* **2014,** *4*, 1300612.
139. Liu, S.; Chen, D.; Zhou, W.; Yu, Z.; Chen, L.; Liu, F.; Chen, Y. Vertical Distribution to Optimize Active Layer Morphology for Efficient All-Polymer Solar Cells by J71 as a Compatibilizer. *Macromolecules* **2019,** *52*, 4359-4369.
140. Huang, L.; Wang, G.; Zhou, W.; Fu, B.; Cheng, X.; Zhang, L.; Yuan, Z.; Xiong, S.; Zhang, L.; Xie, Y.; Zhang, A.; Zhang, Y.; Ma, W.; Li, W.; Zhou, Y.; Reichmanis, E.; Chen, Y. Vertical Stratification Engineering for Organic Bulk-Heterojunction Devices. *ACS Nano* **2018,** *12*, 4440-4452.
141. Jasieniak, J. J.; Treat, N. D.; McNeill, C. R.; de Villers, B. J. T.; Della Gaspera, E.; Chabinyc, M. L. Interfacial Characteristics of Efficient Bulk Heterojunction Solar Cells Fabricated on MoO_x Anode Interlayers. *Adv. Mater.* **2016,** *28*, 3944-3951.
142. Hwang, Y.-J.; Murari, N. M.; Jenekhe, S. A. New n-type polymer semiconductors based on naphthalene diimide and selenophene derivatives for organic field-effect transistors. *Polym. Chem.* **2013,** *4*, 3187-3195.
143. Westenhoff, S.; Howard, I. A.; Friend, R. H. Probing the Morphology and Energy Landscape of Blends of Conjugated Polymers with Sub-10 nm Resolution. *Phys. Rev. Lett.* **2008,** *101*, 016102.
144. Najafov, H.; Lee, B.; Zhou, Q.; Feldman, L. C.; Podzorov, V. Observation of long-range exciton diffusion in highly ordered organic semiconductors. *Nat. Mater.* **2010,** *9*, 938-943.

145. Liu, S.; Yuan, J.; Deng, W.; Luo, M.; Xie, Y.; Liang, Q.; Zou, Y.; He, Z.; Wu, H.; Cao, Y. High-efficiency organic solar cells with low non-radiative recombination loss and low energetic disorder. *Nat. Photonics* **2020,** *14*, 300-305.
146. Qian, D.; Ye, L.; Zhang, M.; Liang, Y.; Li, L.; Huang, Y.; Guo, X.; Zhang, S.; Tan, Z. a.; Hou, J. Design, Application, and Morphology Study of a New Photovoltaic Polymer with Strong Aggregation in Solution State. *Macromolecules* **2012,** *45*, 9611-9617.
147. Bura, T.; Blaskovits, J. T.; Leclerc, M. Direct (Hetero)arylation Polymerization: Trends and Perspectives. *J. Am. Chem. Soc.* **2016,** *138*, 10056-10071.
148. Bura, T.; Beaupre, S.; Legare, M.-A.; Quinn, J.; Rochette, E.; Blaskovits, J. T.; Fontaine, F.-G.; Pron, A.; Li, Y.; Leclerc, M. Direct heteroarylation polymerization: guidelines for defect-free conjugated polymers. *Chem. Sci.* **2017,** *8*, 3913-3925.
149. Morin, P.-O.; Bura, T.; Sun, B.; Gorelsky, S. I.; Li, Y.; Leclerc, M. Conjugated Polymers a la Carte from Time-Controlled Direct (Hetero)Arylation Polymerization. *ACS Macro Lett.* **2015,** *4*, 21-24.
150. Wakioka, M.; Ichihara, N.; Kitano, Y.; Ozawa, F. A Highly Efficient Catalyst for the Synthesis of Alternating Copolymers with Thieno[3,4-c]pyrrole-4,6-dione Units via Direct Arylation Polymerization. *Macromolecules* **2014,** *47*, 626-631.
151. Shi, S.; Yuan, J.; Ding, G.; Ford, M.; Lu, K.; Shi, G.; Sun, J.; Ling, X.; Li, Y.; Ma, W. Improved All-Polymer Solar Cell Performance by Using Matched Polymer Acceptor. *Adv. Funct. Mater.* **2016,** *26*, 5669-5678.
152. Ito, Y.; Virkar, A. A.; Mannsfeld, S.; Oh, J. H.; Toney, M.; Locklin, J.; Bao, Z. Crystalline Ultrasmooth Self-Assembled Monolayers of Alkylsilanes for Organic Field-Effect Transistors. *J. Am. Chem. Soc.* **2009,** *131*, 9396-9404.
153. Espinet, P.; Echavarren, A. M. The Mechanisms of the Stille Reaction. *Angew. Chemie. Int. Ed.* **2004,** *43*, 4704-4734.
154. Tsoi, W. C.; Spencer, S. J.; Yang, L.; Ballantyne, A. M.; Nicholson, P. G.; Turnbull, A.; Shard, A. G.; Murphy, C. E.; Bradley, D. D. C.; Nelson, J.; Kim, J.-S. Effect of Crystallization on the Electronic Energy Levels and Thin Film Morphology of P3HT:PCBM Blends. *Macromolecules* **2011,** *44*, 2944-2952.
155. Ko, S.; Hoke, E. T.; Pandey, L.; Hong, S.; Mondal, R.; Risko, C.; Yi, Y.; Noriega, R.; McGehee, M. D.; Bredas, J.-L.; Salleo, A.; Bao, Z. Controlled Conjugated Backbone Twisting for an Increased Open-Circuit Voltage while Having a High Short-Circuit Current in Poly(hexylthiophene) Derivatives. *J. Am. Chem. Soc.* **2012,** *134*, 5222-5232.
156. Sweetnam, S.; Graham, K. R.; Ngongang Ndjawa, G. O.; Heumuller, T.; Bartelt, J. A.; Burke, T. M.; Li, W.; You, W.; Amassian, A.; McGehee, M. D. Characterization of the Polymer Energy Landscape in Polymer:Fullerene Bulk Heterojunctions with Pure and Mixed Phases. *J. Am. Chem. Soc.* **2014,** *136*, 14078-14088.
157. Noriega, R.; Rivnay, J.; Vandewal, K.; Koch, F. P. V.; Stingelin, N.; Smith, P.; Toney, M. F.; Salleo, A. A general relationship between disorder, aggregation and charge transport in conjugated polymers. *Nat. Mater.* **2013,** *12*, 1038-1044.
158. Li, H.; Hwang, Y.-J.; Courtright, B. A. E.; Eberle, F. N.; Subramaniyan, S.; Jenekhe, S. A. Fine-Tuning the 3D Structure of Nonfullerene Electron Acceptors Toward High-Performance Polymer Solar Cells. *Adv. Mater.* **2015,** *27*, 3266-3272.
159. Intemann, J. J.; Yao, K.; Yip, H.-L.; Xu, Y.-X.; Li, Y.-X.; Liang, P.-W.; Ding, F.-Z.; Li, X.; Jen, A. K. Y. Molecular Weight Effect on the Absorption, Charge Carrier Mobility, and

Photovoltaic Performance of an Indacenodiselenophene-Based Ladder-Type Polymer. *Chem. Mater.* **2013,** *25*, 3188-3195.
160. Koster, L. J. A.; Mihailetchi, V. D.; Ramaker, R.; Blom, P. W. M. Light intensity dependence of open-circuit voltage of polymer:fullerene solar cells. *Appl. Phys. Lett.* **2005,** *86*, 123509.
161. Koster, L. J. A.; Mihailetchi, V. D.; Xie, H.; Blom, P. W. M. Origin of the light intensity dependence of the short-circuit current of polymer/fullerene solar cells. *Appl. Phys. Lett.* **2005,** *87*, 203502.
162. Mihailetchi, V. D.; Wildeman, J.; Blom, P. W. M. Space-Charge Limited Photocurrent. *Phys. Rev. Lett.* **2005,** *94*, 126602.
163. Kline, R. J.; McGehee, M. D.; Kadnikova, E. N.; Liu, J.; Frechet, J. M. J. Controlling the Field-Effect Mobility of Regioregular Polythiophene by Changing the Molecular Weight. *Adv. Mater.* **2003,** *15*, 1519-1522.
164. Goh, C.; Kline, R. J.; McGehee, M. D.; Kadnikova, E. N.; Frechet, J. M. J. Molecular-weight-dependent mobilities in regioregular poly(3-hexyl-thiophene) diodes. *Appl. Phys. Lett.* **2005,** *86*, 122110.
165. Zen, A.; Saphiannikova, M.; Neher, D.; Grenzer, J.; Grigorian, S.; Pietsch, U.; Asawapirom, U.; Janietz, S.; Scherf, U.; Lieberwirth, I.; Wegner, G. Effect of Molecular Weight on the Structure and Crystallinity of Poly(3-hexylthiophene). *Macromolecules* **2006,** *39*, 2162-2171.
166. Kline, R. J.; McGehee, M. D.; Kadnikova, E. N.; Liu, J.; Frechet, J. M. J.; Toney, M. F. Dependence of Regioregular Poly(3-hexylthiophene) Film Morphology and Field-Effect Mobility on Molecular Weight. *Macromolecules* **2005,** *38*, 3312-3319.
167. Tripathi, A. S. M.; Sadakata, S.; Gupta, R. K.; Nagamatsu, S.; Ando, Y.; Pandey, S. S. Implication of Molecular Weight on Optical and Charge Transport Anisotropy in PQT-C12 Films Fabricated by Dynamic FTM. *ACS Appl. Mater. Interfaces* **2019,** *11*, 28088-28095.
168. Koch, F. P. V.; Rivnay, J.; Foster, S.; Müller, C.; Downing, J. M.; Buchaca-Domingo, E.; Westacott, P.; Yu, L.; Yuan, M.; Baklar, M.; Fei, Z.; Luscombe, C.; McLachlan, M. A.; Heeney, M.; Rumbles, G.; Silva, C.; Salleo, A.; Nelson, J.; Smith, P.; Stingelin, N. The impact of molecular weight on microstructure and charge transport in semicrystalline polymer semiconductors - poly(3-hexylthiophene), a model study. *Prog. Polym. Sci.* **2013,** *38*, 1978-1989.
169. Gu, K.; Snyder, C. R.; Onorato, J.; Luscombe, C. K.; Bosse, A. W.; Loo, Y.-L. Assessing the Huang–Brown Description of Tie Chains for Charge Transport in Conjugated Polymers. *ACS Macro Lett.* **2018,** *7*, 1333-1338.
170. Nikolka, M.; Hurhangee, M.; Sadhanala, A.; Chen, H.; McCulloch, I.; Sirringhaus, H. Correlation of Disorder and Charge Transport in a Range of Indacenodithiophene-Based Semiconducting Polymers. *Adv. Electron. Mater.* **2018,** *4*, 1700410.
171. Zhao, B.; Pei, D.; Jiang, Y.; Wang, Z.; An, C.; Deng, Y.; Ma, Z.; Han, Y.; Geng, Y. Simultaneous Enhancement of Stretchability, Strength, and Mobility in Ultrahigh-Molecular-Weight Poly(indacenodithiophene-co-benzothiadiazole). *Macromolecules* **2021,** *54*, 9896-9905.
172. Donley, C. L.; Zaumseil, J.; Andreasen, J. W.; Nielsen, M. M.; Sirringhaus, H.; Friend, R. H.; Kim, J.-S. Effects of Packing Structure on the Optoelectronic and Charge Transport Properties in Poly(9,9-di-n-octylfluorene-alt-benzothiadiazole). *J. Am. Chem. Soc.* **2005,** *127*, 12890-12899.

173. Tran, D. K.; Robitaille, A.; Hai, I. J.; Lin, C.-C.; Kuzuhara, D.; Koganezawa, T.; Chiu, Y.-C.; Leclerc, M.; Jenekhe, S. A. Unified Understanding of Molecular Weight Dependence of Electron Transport in Naphthalene Diimide-Based n-Type Semiconducting Polymers. *Chem. Mater.* **2022,** *34*, 9644-9655.
174. Feng, K.; Guo, H.; Sun, H.; Guo, X. n-Type Organic and Polymeric Semiconductors Based on Bithiophene Imide Derivatives. *Acc. Chem. Res.* **2021,** *54*, 3804-3817.
175. Jenekhe, S. A.; Lu, L.; Alam, M. M. New Conjugated Polymers with Donor−Acceptor Architectures: Synthesis and Photophysics of Carbazole−Quinoline and Phenothiazine−Quinoline Copolymers and Oligomers Exhibiting Large Intramolecular Charge Transfer. *Macromolecules* **2001,** *34*, 7315-7324.
176. Agrawal, A. K.; Jenekhe, S. A. New conjugated polyanthrazolines containing thiophene moieties in the main chain. *Macromolecules* **1991,** *24*, 6806-6808.
177. Guo, X.; Watson, M. D. Conjugated Polymers from Naphthalene Bisimide. *Org. Lett.* **2008,** *10*, 5333-5336.
178. Choi, J.; Kim, W.; Kim, D.; Kim, S.; Chae, J.; Choi, S. Q.; Kim, F. S.; Kim, T.-S.; Kim, B. J. Importance of Critical Molecular Weight of Semicrystalline n-Type Polymers for Mechanically Robust, Efficient Electroactive Thin Films. *Chem. Mater.* **2019,** *31*, 3163-3173.
179. Karpov, Y.; Zhao, W.; Raguzin, I.; Beryozkina, T.; Bakulev, V.; Al-Hussein, M.; Häußler, L.; Stamm, M.; Voit, B.; Facchetti, A.; Tkachov, R.; Kiriy, A. Influence of Semiconductor Thickness and Molecular Weight on the Charge Transport of a Naphthalenediimide-Based Copolymer in Thin-Film Transistors. *ACS Appl. Mater. Interfaces* **2015,** *7*, 12478-12487.
180. Nahid, M. M.; Matsidik, R.; Welford, A.; Gann, E.; Thomsen, L.; Sommer, M.; McNeill, C. R. Unconventional Molecular Weight Dependence of Charge Transport in the High Mobility n-type Semiconducting Polymer P(NDI2OD-T2). *Adv. Funct. Mater.* **2017,** *27*, 1604744.
181. Zhao, K.; Zhang, T.; Zhang, L.; Li, J.; Li, H.; Wu, F.; Chen, Y.; Zhang, Q.; Han, Y. Role of Molecular Weight in Microstructural Transition and Its Correlation to the Mechanical and Electrical Properties of P(NDI2OD-T2) Thin Films. *Macromolecules* **2021,** *54*, 10203-10215.
182. Sun, Y.; Seo, J. H.; Takacs, C. J.; Seifter, J.; Heeger, A. J. Inverted Polymer Solar Cells Integrated with a Low-Temperature-Annealed Sol-Gel-Derived ZnO Film as an Electron Transport Layer. *Adv. Mater.* **2011,** *23*, 1679-1683.
183. Luzio, A.; Criante, L.; D'Innocenzo, V.; Caironi, M. Control of charge transport in a semiconducting copolymer by solvent-induced long-range order. *Sci. Rep.* **2013,** *3*, 3425.
184. Wu, H.-Y.; Yang, C.-Y.; Li, Q.; Kolhe, N. B.; Strakosas, X.; Stoeckel, M.-A.; Wu, Z.; Jin, W.; Savvakis, M.; Kroon, R.; Tu, D.; Woo, H. Y.; Berggren, M.; Jenekhe, S. A.; Fabiano, S. Influence of Molecular Weight on the Organic Electrochemical Transistor Performance of Ladder-Type Conjugated Polymers. *Adv. Mater.* **2022,** *34*, 2106235.
185. Pei, D.; Wang, Z.; Peng, Z.; Zhang, J.; Deng, Y.; Han, Y.; Ye, L.; Geng, Y. Impact of Molecular Weight on the Mechanical and Electrical Properties of a High-Mobility Diketopyrrolopyrrole-Based Conjugated Polymer. *Macromolecules* **2020,** *53*, 4490-4500.
186. Su, N.; Ma, R.; Li, G.; Liu, T.; Feng, L.-W.; Lin, C.; Chen, J.; Song, J.; Xiao, Y.; Qu, J.; Lu, X.; Sangwan, V. K.; Hersam, M. C.; Yan, H.; Facchetti, A.; Marks, T. J. High-

Efficiency All-Polymer Solar Cells with Poly-Small-Molecule Acceptors Having π-Extended Units with Broad Near-IR Absorption. *ACS Energy Lett.* **2021,** *6*, 728-738.
187. Rivnay, J.; Noriega, R.; Kline, R. J.; Salleo, A.; Toney, M. F. Quantitative analysis of lattice disorder and crystallite size in organic semiconductor thin films. *Phys. Rev. B* **2011,** *84*, 045203.
188. Rivnay, J.; Mannsfeld, S. C. B.; Miller, C. E.; Salleo, A.; Toney, M. F. Quantitative Determination of Organic Semiconductor Microstructure from the Molecular to Device Scale. *Chem. Rev.* **2012,** *112*, 5488-5519.
189. Tsao, H. N.; Cho, D. M.; Park, I.; Hansen, M. R.; Mavrinskiy, A.; Yoon, D. Y.; Graf, R.; Pisula, W.; Spiess, H. W.; Müllen, K. Ultrahigh Mobility in Polymer Field-Effect Transistors by Design. *J. Am. Chem. Soc.* **2011,** *133*, 2605-2612.
190. Coropceanu, V.; Cornil, J.; da Silva Filho, D. A.; Olivier, Y.; Silbey, R.; Brédas, J.-L. Charge Transport in Organic Semiconductors. *Chem. Rev.* **2007,** *107*, 926-952.
191. Gu, K.; Loo, Y.-L. The Polymer Physics of Multiscale Charge Transport in Conjugated Systems. *J. Polym. Sci. Part B: Polym. Phys.* **2019,** *57*, 1559-1571.
192. Noriega, R. Efficient Charge Transport in Disordered Conjugated Polymer Microstructures. *Macromol. Rapid Commun.* **2018,** *39*, e1800096.
193. Babel, A.; Jenekhe, S. A. Morphology and Field-Effect Mobility of Charge Carriers in Binary Blends of Poly(3-hexylthiophene) with Poly[2-methoxy-5-(2-ethylhexoxy)-1,4-phenylenevinylene] and Polystyrene. *Macromolecules* **2004,** *37*, 9835-9840.
194. McCulloch, I.; Heeney, M.; Chabinyc, M. L.; DeLongchamp, D.; Kline, R. J.; Colle, M.; Duffy, W.; Fischer, D.; Gundlach, D.; Hamadani, B.; Hamilton, R.; Richter, L.; Salleo, A.; Shkunov, M.; Sparrowe, D.; Tierney, S.; Zhang, W. Semiconducting Thienothiophene Copolymers: Design, Synthesis, Morphology, and Performance in Thin-Film Organic Transistors. *Adv. Mater.* **2009,** *21*, 1091-1109.
195. Guo, J.; Flagg, L. Q.; Tran, D. K.; Chen, S. E.; Li, R.; Kolhe, N. B.; Giridharagopal, R.; Jenekhe, S. A.; Richter, L. J.; Ginger, D. S. Hydration of a Side-Chain-Free n-Type Semiconducting Ladder Polymer Driven by Electrochemical Doping. *J. Am. Chem. Soc.* **2023,** *145*, 1866-1876.
196. Berry, G. C. Properties of an optically anisotropic heterocyclic ladder polymer (BBL) in dilute solution. *J. Polym. Sci. Polym. Symp.* **1978,** *65*, 143-172.
197. Hong, S. Y.; Kertesz, M.; Lee, Y. S.; Kim, O. K. Geometrical and electronic structures of a benzimidazobenzophenanthroline-type ladder polymer (BBL). *Macromolecules* **1992,** *25*, 5424-5429.
198. Van Deusen, R. L. Benzimidazo-benzophenanthroline polymers. *J. Polym. Sci. B Polym. Lett.* **1966,** *4*, 211-214.
199. Oosterhout, S. D.; Savikhin, V.; Zhang, J.; Zhang, Y.; Burgers, M. A.; Marder, S. R.; Bazan, G. C.; Toney, M. F. Mixing Behavior in Small Molecule:Fullerene Organic Photovoltaics. *Chem. Mater.* **2017,** *29*, 3062-3069.
200. Sunjoo Kim, F.; Hwang, D.-K.; Kippelen, B.; Jenekhe, S. A. Enhanced carrier mobility and electrical stability of n-channel polymer thin film transistors by use of low-k dielectric buffer layer. *Appl. Phys. Lett.* **2011,** *99*, 173303.
201. Kim, F. S.; Park, C. H.; Na, Y.; Jenekhe, S. A. Effects of ladder structure on the electronic properties and field-effect transistor performance of Poly(benzobisimidazobenzophenanthroline). *Org. Electron.* **2019,** *69*, 301-307.

202. Briseno, A. L.; Kim, F. S.; Babel, A.; Xia, Y.; Jenekhe, S. A. n-Channel polymer thin film transistors with long-term air-stability and durability and their use in complementary inverters. *J. Mater. Chem.* **2011,** *21*, 16461-16466.
203. Peng, Z.; Ye, L.; Ade, H. Understanding, quantifying, and controlling the molecular ordering of semiconducting polymers: from novices to experts and amorphous to perfect crystals. *Mater. Horiz.* **2022,** *9*, 577-606.
204. Carpenter, J. H.; Ghasemi, M.; Gann, E.; Angunawela, I.; Stuard, S. J.; Rech, J. J.; Ritchie, E.; O'Connor, B. T.; Atkin, J.; You, W.; DeLongchamp, D. M.; Ade, H. Competition between Exceptionally Long-Range Alkyl Sidechain Ordering and Backbone Ordering in Semiconducting Polymers and Its Impact on Electronic and Optoelectronic Properties. *Adv. Funct. Mater.* **2019,** *29*, 1806977.
205. Kline, R. J.; DeLongchamp, D. M.; Fischer, D. A.; Lin, E. K.; Richter, L. J.; Chabinyc, M. L.; Toney, M. F.; Heeney, M.; McCulloch, I. Critical Role of Side-Chain Attachment Density on the Order and Device Performance of Polythiophenes. *Macromolecules* **2007,** *40*, 7960-7965.
206. Wilbourn, K.; Murray, R. W. The electrochemical doping reactions of the conducting ladder polymer benzimidazobenzophenanthroline (BBL). *Macromolecules* **1988,** *21*, 89-96.
207. Ahmed, S. A.; Liao, Q.-B.; Shen, Q.; Ashraf Baig, M. M. F.; Zhou, J.; Shi, C.-F.; Muhammad, P.; Hanif, S.; Xi, K.; Xia, X.-H.; Wang, K. pH-Dependent Slipping and Exfoliation of Layered Covalent Organic Framework. *Chem. Eur. J.* **2020,** *26*, 12996-13001.
208. Xiao, M.; Carey, R. L.; Chen, H.; Jiao, X.; Lemaur, V.; Schott, S.; Nikolka, M.; Jellett, C.; Sadhanala, A.; Rogers, S.; Senanayak, S. P.; Onwubiko, A.; Han, S.; Zhang, Z.; Abdi-Jalebi, M.; Zhang, Y.; Thomas, T. H.; Mahmoudi, N.; Lai, L.; Selezneva, E.; Ren, X.; Nguyen, M.; Wang, Q.; Jacobs, I.; Yue, W.; McNeill, C. R.; Liu, G.; Beljonne, D.; McCulloch, I.; Sirringhaus, H. Charge transport physics of a unique class of rigid-rod conjugated polymers with fused-ring conjugated units linked by double carbon-carbon bonds. *Sci. Adv.* **2021,** *7*, eabe5280.
209. Mei, Y.; Diemer, P. J.; Niazi, M. R.; Hallani, R. K.; Jarolimek, K.; Day, C. S.; Risko, C.; Anthony, J. E.; Amassian, A.; Jurchescu, O. D. Crossover from band-like to thermally activated charge transport in organic transistors due to strain-induced traps. *Proc. Natl. Acad. Sci.* **2017,** *114*, E6739-E6748.
210. Hu, X.-D.; Jenkins, S. E.; Min, B. G.; Polk, M. B.; Kumar, S. Rigid-Rod Polymers: Synthesis, Processing, Simulation, Structure, and Properties. *Macromol. Mater. Eng.* **2003,** *288*, 823-843.
211. Hasegawa, M.; Hoshino, Y.; Katsura, N.; Ishii, J. Superheat-resistant polymers with low coefficients of thermal expansion. *Polymer* **2017,** *111*, 91-102.
212. Nakamae, K.; Nishino, T.; Gotoh, Y.; Matsui, R.; Nagura, M. Temperature dependence of the elastic modulus of the crystalline regions of poly(p-phenylene benzobisthiazole). *Polymer* **1999,** *40*, 4629-4634.
213. Kalb, W. L.; Batlogg, B. Calculating the trap density of states in organic field-effect transistors from experiment: A comparison of different methods. *Phys. Rev. B* **2010,** *81*, 035327.
214. Iqbal, H. F.; Ai, Q.; Thorley, K. J.; Chen, H.; McCulloch, I.; Risko, C.; Anthony, J. E.; Jurchescu, O. D. Suppressing bias stress degradation in high performance solution processed organic transistors operating in air. *Nat. Commun.* **2021,** *12*, 2352.

215. Iqbal, H. F.; Waldrip, M.; Chen, H.; McCulloch, I.; Jurchescu, O. D. Elucidating the Role of Water-Related Traps in the Operation of Polymer Field-Effect Transistors. *Adv. Electron. Mater.* **2021,** *7*, 2100393.
216. Pattanasattayavong, P.; Mottram, A. D.; Yan, F.; Anthopoulos, T. D. Study of the Hole Transport Processes in Solution-Processed Layers of the Wide Bandgap Semiconductor Copper(I) Thiocyanate (CuSCN). *Adv. Funct. Mater.* **2015,** *25*, 6802-6813.
217. Paterson, A. F.; Lin, Y.-H.; Mottram, A. D.; Fei, Z.; Niazi, M. R.; Kirmani, A. R.; Amassian, A.; Solomeshch, O.; Tessler, N.; Heeney, M.; Anthopoulos, T. D. The Impact of Molecular p-Doping on Charge Transport in High-Mobility Small-Molecule/Polymer Blend Organic Transistors. *Adv. Electron. Mater.* **2018,** *4*, 1700464.
218. Paterson, A. F.; Mottram, A. D.; Faber, H.; Niazi, M. R.; Fei, Z.; Heeney, M.; Anthopoulos, T. D. Impact of the Gate Dielectric on Contact Resistance in High-Mobility Organic Transistors. *Adv. Electron. Mater.* **2019,** *5*, 1800723.
219. Gong, X.; Ma, W.; Ostrowski, J. C.; Bechgaard, K.; Bazan, G. C.; Heeger, A. J.; Xiao, S.; Moses, D. End-Capping as a Method for Improving Carrier Injection in Electrophosphorescent Light-Emitting Diodes. *Adv. Funct. Mater.* **2004,** *14*, 393-397.
220. Park, J. K.; Jo, J.; Seo, J. H.; Moon, J. S.; Park, Y. D.; Lee, K.; Heeger, A. J.; Bazan, G. C. End-Capping Effect of a Narrow Bandgap Conjugated Polymer on Bulk Heterojunction Solar Cells. *Adv. Mater.* **2011,** *23*, 2430-2435.
221. Sun, H.; Vagin, M.; Wang, S.; Crispin, X.; Forchheimer, R.; Berggren, M.; Fabiano, S. Complementary Logic Circuits Based on High-Performance n-Type Organic Electrochemical Transistors. *Adv. Mater.* **2018,** *30*, 1704916.
222. Yang, C.-Y.; Stoeckel, M.-A.; Ruoko, T.-P.; Wu, H.-Y.; Liu, X.; Kolhe, N. B.; Wu, Z.; Puttisong, Y.; Musumeci, C.; Massetti, M.; Sun, H.; Xu, K.; Tu, D.; Chen, W. M.; Woo, H. Y.; Fahlman, M.; Jenekhe, S. A.; Berggren, M.; Fabiano, S. A high-conductivity n-type polymeric ink for printed electronics. *Nat. Commun.* **2021,** *12*, 2354.
223. Huang, W.; Chen, J.; Yao, Y.; Zheng, D.; Ji, X.; Feng, L.-W.; Moore, D.; Glavin, N. R.; Xie, M.; Chen, Y.; Pankow, R. M.; Surendran, A.; Wang, Z.; Xia, Y.; Bai, L.; Rivnay, J.; Ping, J.; Guo, X.; Cheng, Y.; Marks, T. J.; Facchetti, A. Vertical organic electrochemical transistors for complementary circuits. *Nature* **2023,** *613*, 496-502.
224. Yang, C.-Y.; Tu, D.; Ruoko, T.-P.; Gerasimov, J. Y.; Wu, H.-Y.; Harikesh, P. C.; Massetti, M.; Stoeckel, M.-A.; Kroon, R.; Müller, C.; Berggren, M.; Fabiano, S. Low-Power/High-Gain Flexible Complementary Circuits Based on Printed Organic Electrochemical Transistors. *Adv. Electron. Mater.* **2022,** *8*, 2100907.
225. Inal, S.; Rivnay, J.; Suiu, A.-O.; Malliaras, G. G.; McCulloch, I. Conjugated Polymers in Bioelectronics. *Acc. Chem. Res.* **2018,** *51*, 1368-1376.
226. Guo, K.; Wustoni, S.; Koklu, A.; Díaz-Galicia, E.; Moser, M.; Hama, A.; Alqahtani, A. A.; Ahmad, A. N.; Alhamlan, F. S.; Shuaib, M.; Pain, A.; McCulloch, I.; Arold, S. T.; Grünberg, R.; Inal, S. Rapid single-molecule detection of COVID-19 and MERS antigens via nanobody-functionalized organic electrochemical transistors. *Nat. Biomed. Eng.* **2021,** *5*, 666-677.
227. Ji, X.; Paulsen, B. D.; Chik, G. K. K.; Wu, R.; Yin, Y.; Chan, P. K. L.; Rivnay, J. Mimicking associative learning using an ion-trapping non-volatile synaptic organic electrochemical transistor. *Nat. Commun.* **2021,** *12*, 2480.

228. Yamamoto, S.; Malliaras, G. G. Controlling the Neuromorphic Behavior of Organic Electrochemical Transistors by Blending Mixed and Ion Conductors. *ACS Appl. Electron. Mater.* **2020,** *2*, 2224-2228.
229. Kukhta, N. A.; Marks, A.; Luscombe, C. K. Molecular Design Strategies toward Improvement of Charge Injection and Ionic Conduction in Organic Mixed Ionic–Electronic Conductors for Organic Electrochemical Transistors. *Chem. Rev.* **2022,** *122*, 4325-4355.
230. Zeglio, E.; Inganäs, O. Active Materials for Organic Electrochemical Transistors. *Adv. Mater.* **2018,** *30*, 1800941.
231. Liang, Y.; Chen, Z.; Jing, Y.; Rong, Y.; Facchetti, A.; Yao, Y. Heavily n-Dopable π-Conjugated Redox Polymers with Ultrafast Energy Storage Capability. *J. Am. Chem. Soc.* **2015,** *137*, 4956-4959.
232. Jin, Z.; Cheng, Q.; Evans, A. M.; Gray, J.; Zhang, R.; Bao, S. T.; Wei, F.; Venkataraman, L.; Yang, Y.; Nuckolls, C. π-Conjugated redox-active two-dimensional polymers as organic cathode materials. *Chem. Sci.* **2022,** *13*, 3533-3538.
233. Tan, S. T. M.; Quill, T. J.; Moser, M.; LeCroy, G.; Chen, X.; Wu, Y.; Takacs, C. J.; Salleo, A.; Giovannitti, A. Redox-Active Polymers Designed for the Circular Economy of Energy Storage Devices. *ACS Energy Lett.* **2021,** *6*, 3450-3457.
234. Szumska, A. A.; Maria, I. P.; Flagg, L. Q.; Savva, A.; Surgailis, J.; Paulsen, B. D.; Moia, D.; Chen, X.; Griggs, S.; Mefford, J. T.; Rashid, R. B.; Marks, A.; Inal, S.; Ginger, D. S.; Giovannitti, A.; Nelson, J. Reversible Electrochemical Charging of n-Type Conjugated Polymer Electrodes in Aqueous Electrolytes. *J. Am. Chem. Soc.* **2021,** *143*, 14795-14805.
235. Trefz, D.; Ruff, A.; Tkachov, R.; Wieland, M.; Goll, M.; Kiriy, A.; Ludwigs, S. Electrochemical Investigations of the N-Type Semiconducting Polymer P(NDI2OD-T2) and Its Monomer: New Insights in the Reduction Behavior. *J. Phys. Chem. C* **2015,** *119*, 22760-22771.
236. Wang, A.; Tan, R.; Breakwell, C.; Wei, X.; Fan, Z.; Ye, C.; Malpass-Evans, R.; Liu, T.; Zwijnenburg, M. A.; Jelfs, K. E.; McKeown, N. B.; Chen, J.; Song, Q. Solution-Processable Redox-Active Polymers of Intrinsic Microporosity for Electrochemical Energy Storage. *J. Am. Chem. Soc.* **2022,** *144*, 17198-17208.
237. Aithal, A.; Samuel, J. J.; Bandyopadhyay, A.; Karrothu, V. K.; Gangadharappa, C.; Patil, S.; Narayan, A.; Aetukuri, N. P. B. Extended Conjugation Acceptors Increase Specific Energy Densities in π-Conjugated Redox Polymers. *J. Phys. Chem. C* **2023,** *127*, 5238-5245.
238. Samuel, J. J.; Karrothu, V. K.; Canjeevaram Balasubramanyam, R. K.; Mohapatra, A. A.; Gangadharappa, C.; Kankanallu, V. R.; Patil, S.; Aetukuri, N. P. B. Ionic Charge Storage in Diketopyrrolopyrrole-Based Redox-Active Conjugated Polymers. *J. Phys. Chem. C* **2021,** *125*, 4449-4457.
239. West, S. M.; Tran, D. K.; Guo, J.; Chen, S. E.; Ginger, D. S.; Jenekhe, S. A. Phenazine-Substituted Poly(benzimidazobenzophenanthrolinedione): Electronic Structure, Thin Film Morphology, Electron Transport, and Mechanical Properties of an n-Type Semiconducting Ladder Polymer. *Macromolecules* **2023,** *56*, 2081-2091.
240. Tyburski, R.; Liu, T.; Glover, S. D.; Hammarström, L. Proton-Coupled Electron Transfer Guidelines, Fair and Square. *J. Am. Chem. Soc.* **2021,** *143*, 560-576.
241. Warburton, R. E.; Soudackov, A. V.; Hammes-Schiffer, S. Theoretical Modeling of Electrochemical Proton-Coupled Electron Transfer. *Chem. Rev.* **2022,** *122*, 10599-10650.

242. Li, W.-H.; Li, X.-Y.; Yu, N.-T. Surface-enhanced hyper-Raman scattering and surface-enhanced Raman scattering studies of electroreduction of phenazine on silver electrode. *Chem. Phys. Lett.* **2000,** *327*, 153-161.
243. Mugnier, Y.; Roullier, L.; Laviron, E. Reduction mechanism of phenazine in tetrahydrofuran. Influence of added proton donors. *Electrochimica Acta* **1991,** *36*, 803-809.
244. Choi, C.; Ashby, D. S.; Butts, D. M.; DeBlock, R. H.; Wei, Q.; Lau, J.; Dunn, B. Achieving high energy density and high power density with pseudocapacitive materials. *Nat. Rev. Mater.* **2020,** *5*, 5-19.
245. Augustyn, V.; Come, J.; Lowe, M. A.; Kim, J. W.; Taberna, P.-L.; Tolbert, S. H.; Abruña, H. D.; Simon, P.; Dunn, B. High-rate electrochemical energy storage through Li+ intercalation pseudocapacitance. *Nat. Mater.* **2013,** *12*, 518-522.
246. Vázquez, R. J.; Quek, G.; McCuskey, S. R.; Llanes, L.; Kundukad, B.; Wang, X.; Bazan, G. C. Increasing the molecular weight of conjugated polyelectrolytes improves the electrochemical stability of their pseudocapacitor gels. *J. Mater. Chem. A* **2022,** *10*, 21642-21649.
247. Xu, T.; Li, Z.; Wang, D.; Zhang, M.; Ai, L.; Chen, Z.; Zhang, J.; Zhang, X.; Shen, L. A Fast Proton-Induced Pseudocapacitive Supercapacitor with High Energy and Power Density. *Adv. Funct. Mater.* **2022,** *32*, 2107720.
248. Wu, X.; Zhang, H.; He, C.; Wu, C.; Huang, K.-J. High-power-energy proton supercapacitor based on interface-adapted durable polyaniline and hexagonal tungsten oxide. *J. Colloid Interface Sci.* **2021,** *601*, 727-733.
249. Xu, T.; Wang, D.; Li, Z.; Chen, Z.; Zhang, J.; Hu, T.; Zhang, X.; Shen, L. Electrochemical Proton Storage: From Fundamental Understanding to Materials to Devices. *Nano-Micro Lett.* **2022,** *14*, 126.
250. Xu, Y.; Wu, X.; Ji, X. The Renaissance of Proton Batteries. *Small Struct.* **2021,** *2*, 2000113.
251. Emanuelsson, R.; Sterby, M.; Strømme, M.; Sjödin, M. An All-Organic Proton Battery. *J. Am. Chem. Soc.* **2017,** *139*, 4828-4834.
252. Zhu, Z.; Wang, W.; Yin, Y.; Meng, Y.; Liu, Z.; Jiang, T.; Peng, Q.; Sun, J.; Chen, W. An Ultrafast and Ultra-Low-Temperature Hydrogen Gas–Proton Battery. *J. Am. Chem. Soc.* **2021,** *143*, 20302-20308.
253. Yan, L.; Huang, J.; Guo, Z.; Dong, X.; Wang, Z.; Wang, Y. Solid-State Proton Battery Operated at Ultralow Temperature. *ACS Energy Lett.* **2020,** *5*, 685-691.
254. Quinto, M.; Jenekhe, S. A.; Bard, A. J. Polymer Films on Electrodes. 30. Electrochemistry and Scanning Electrochemical Microscopy Characterization of Benzimidazolebenzophenanthroline-Type Ladder (BBL) and Semiladder (BBB) Polymer Films. *Chem. Mater.* **2001,** *13*, 2824-2832.
255. Xu, K.; Ruoko, T.-P.; Shokrani, M.; Scheunemann, D.; Abdalla, H.; Sun, H.; Yang, C.-Y.; Puttisong, Y.; Kolhe, N. B.; Figueroa, J. S. M.; Pedersen, J. O.; Ederth, T.; Chen, W. M.; Berggren, M.; Jenekhe, S. A.; Fazzi, D.; Kemerink, M.; Fabiano, S. On the Origin of Seebeck Coefficient Inversion in Highly Doped Conducting Polymers. *Adv. Funct. Mater.* **2022,** *32*, 2112276.
256. Cochran, J. E.; Junk, M. J. N.; Glaudell, A. M.; Miller, P. L.; Cowart, J. S.; Toney, M. F.; Hawker, C. J.; Chmelka, B. F.; Chabinyc, M. L. Molecular Interactions and Ordering in

Electrically Doped Polymers: Blends of PBTTT and F_4TCNQ. *Macromolecules* **2014,** *47*, 6836-6846.
257. Dmitrieva, E.; Harima, Y.; Dunsch, L. Influence of Phenazine Structure on Polaron Formation in Polyaniline: In Situ Electron Spin Resonance−Ultraviolet/Visible−Near-Infrared Spectroelectrochemical Study. *J. Phys. Chem. B* **2009,** *113*, 16131-16141.
258. Ghosh, S.; Gueskine, V.; Berggren, M.; Zozoulenko, I. V. Electronic Structures and Optical Absorption of N-Type Conducting Polymers at Different Doping Levels. *J. Phys. Chem. C* **2019,** *123*, 15467-15476.
259. Tan, E.; Kim, J.; Stewart, K.; Pitsalidis, C.; Kwon, S.; Siemons, N.; Kim, J.; Jiang, Y.; Frost, J. M.; Pearce, D.; Tyrrell, J. E.; Nelson, J.; Owens, R. M.; Kim, Y.-H.; Kim, J.-S. The Role of Long-Alkyl-Group Spacers in Glycolated Copolymers for High-Performance Organic Electrochemical Transistors. *Adv. Mater.* **2022,** *34*, 2202574.
260. Kellenberger, A.; Dmitrieva, E.; Dunsch, L. The stabilization of charged states at phenazine-like units in polyaniline under p-doping: an in situATR-FTIR spectroelectrochemical study. *Phys. Chem. Chem. Phys.* **2011,** *13*, 3411-3420.
261. Ćirić-Marjanović, G.; Trchová, M.; Stejskal, J. The chemical oxidative polymerization of aniline in water: Raman spectroscopy. *J. Raman Spectrosc.* **2008,** *39*, 1375-1387.
262. Alex, S.; Turcotte, P.; Fournier, R.; Vocelle, D. Study of the protonation of simple Schiff bases in solvents of various polarity by means of Raman spectroscopy. *Can. J. Chem.* **1991,** *69*, 239-245.
263. Louarn, G.; Lapkowski, M.; Quillard, S.; Pron, A.; Buisson, J. P.; Lefrant, S. Vibrational Properties of PolyanilineIsotope Effects. *J. Phys. Chem.* **1996,** *100*, 6998-7006.
264. Chidsey, C. E. D.; Murray, R. W. Redox capacity and direct current electron conductivity in electroactive materials. *J. Phys. Chem.* **1986,** *90*, 1479-1484.
265. Estrada, L. A.; Liu, D. Y.; Salazar, D. H.; Dyer, A. L.; Reynolds, J. R. Poly[Bis-EDOT-Isoindigo]: An Electroactive Polymer Applied to Electrochemical Supercapacitors. *Macromolecules* **2012,** *45*, 8211-8220.
266. Wilbourn, K.; Murray, R. W. The d.c. redox versus electronic conductivity of the ladder polymer poly(benzimidazobenzophenanthroline). *J. Phys. Chem.* **1988,** *92*, 3642-3648.
267. Prins, P.; Grozema, F. C.; Schins, J. M.; Patil, S.; Scherf, U.; Siebbeles, L. D. A. High Intrachain Hole Mobility on Molecular Wires of Ladder-Type Poly(p-Phenylenes). *Phys. Rev. Lett.* **2006,** *96*, 146601.
268. Street, R. A.; Salleo, A.; Chabinyc, M. L. Bipolaron mechanism for bias-stress effects in polymer transistors. *Phys. Rev. B* **2003,** *68*, 085316.
269. Hui, S. R.; De Luna, P. How increasing proton and electron conduction benefits electrocatalytic CO2 reduction. *Matter* **2021,** *4*, 1555-1577.
270. Hamilton, R.; Bailey, C.; Duffy, W.; Heeney, M.; Shkunov, M.; Sparrowe, D.; Tierney, S.; McCulloch, I.; Kline, R. J.; DeLongchamp, D. M.; Chabinyc, M. In *The influence of molecular weight on the microstructure and thin film transistor characteristics of pBTTT polymers*, Proc.SPIE, 2006.
271. Zen, A.; Pflaum, J.; Hirschmann, S.; Zhuang, W.; Jaiser, F.; Asawapirom, U.; Rabe, J. P.; Scherf, U.; Neher, D. Effect of Molecular Weight and Annealing of Poly(3-hexylthiophene)s on the Performance of Organic Field-Effect Transistors. *Adv. Funct. Mater.* **2004,** *14*, 757-764.

Appendix A

Appendix A presents supplementary information accompanied Chapter 2, Section 2.1: Effects of a Fluorinated Donor Polymer on the Morphology, Photophysics, and Performance of All-Polymer Solar Cells Based on Naphthalene Diimide-Arylene Copolymer Acceptors.

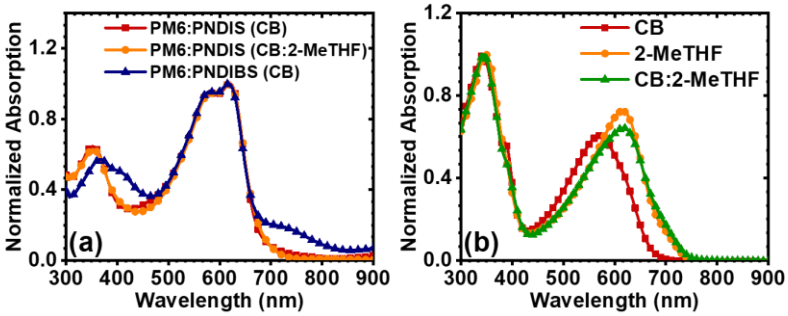

Figure A-1. (a) Normalized thin-film optical absorption spectra of blend film from different solvents. (b) Normalized solution optical absorption spectra of PNDIS acceptor polymers in various solvent systems.

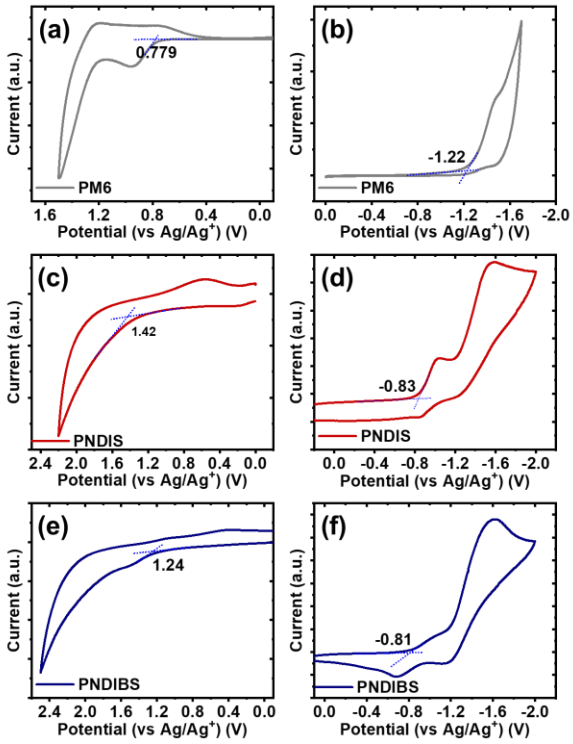

Figure A-2. Cyclic voltammograms of PM6 (a, b), PNDIS (c, d), and PNDIBS (e, f)) in 0.1 M Bu_4NPF_6 solution in acetonitrile at a scan rate of 50 mV/s.

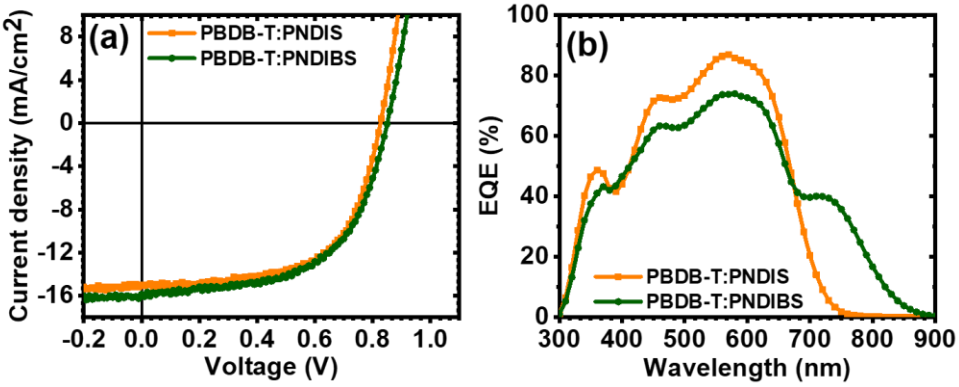

Figure A-3. (a) *J-V* curves for the PBDB-T:PNDIS and PBDB-T:PNDIBS devices. (b) EQE spectra for the PBDB-T:PNDIS and PBDB-T:PNDIBS devices. The PBDB-T:PNDIS and PBDB-T:PNDIBS devices were processed at the exact conditions as those of PM6:PNDIS and PM6:PNDIBS devices, respectively.

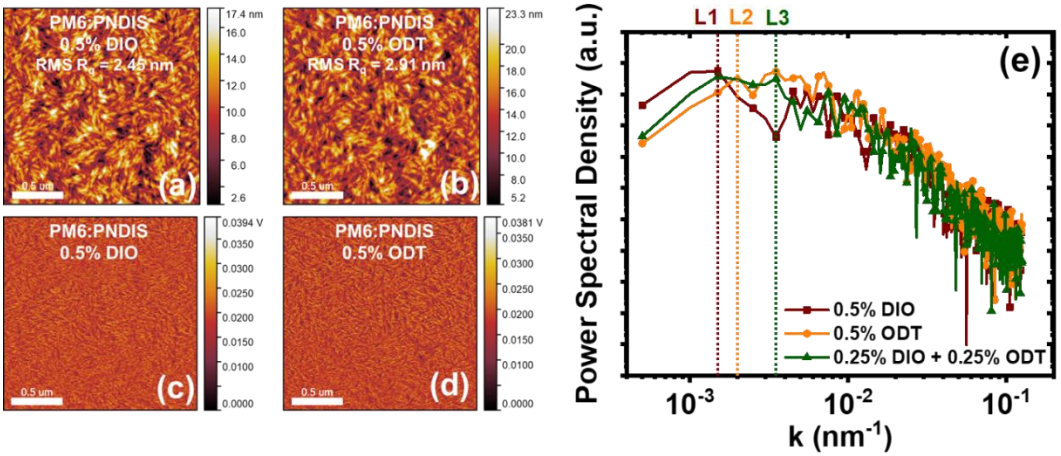

Figure A-4. (a, b) AFM height images and (c, d) phase images (2 μm x 2 μm) of the surfaces of PM6:PNDIS blend films processed using 0.5% DIO or 0.5% ODT as the solvent additive. The scale bars are 500 nm. (e) Power spectra density of PM6:PNDIS blends processed using 0.5% DIO, 0.5% ODT, and a combination of 0.25% DIO + 0.25% ODT.

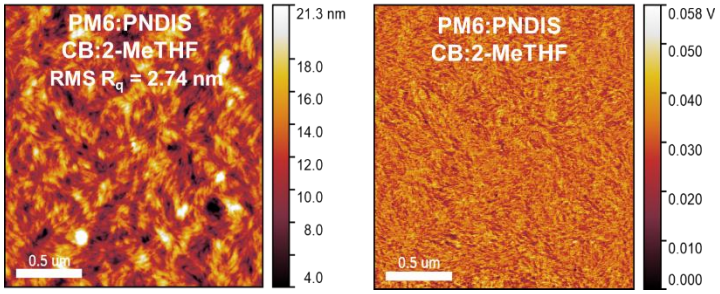

Figure A-5. AFM images (2 μm x 2 μm) of the surfaces of PM6:PNDIS blend films processed from the CB:2-MeTHF co-solvent system. The scale bars are 500 nm.

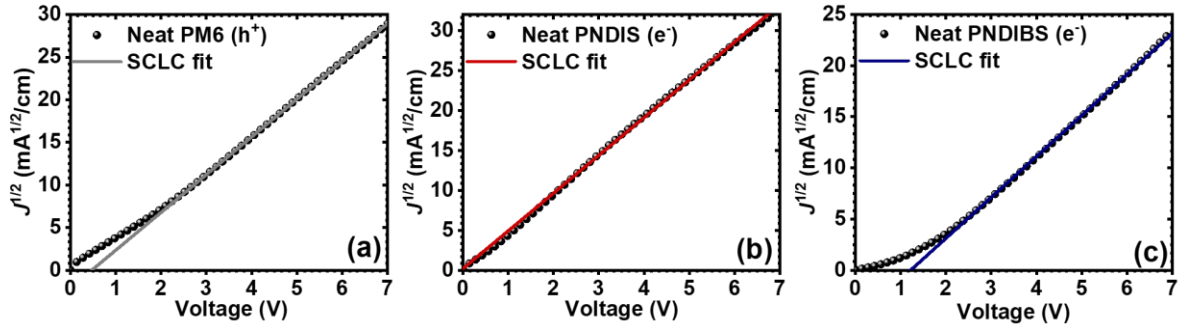

Figure A-6. *J-V* curves measured by the space-charge-limited current (SCLC) method and fitting for neat films of (a) PM6, (b) PNDIS, and (c) PNDIBS.

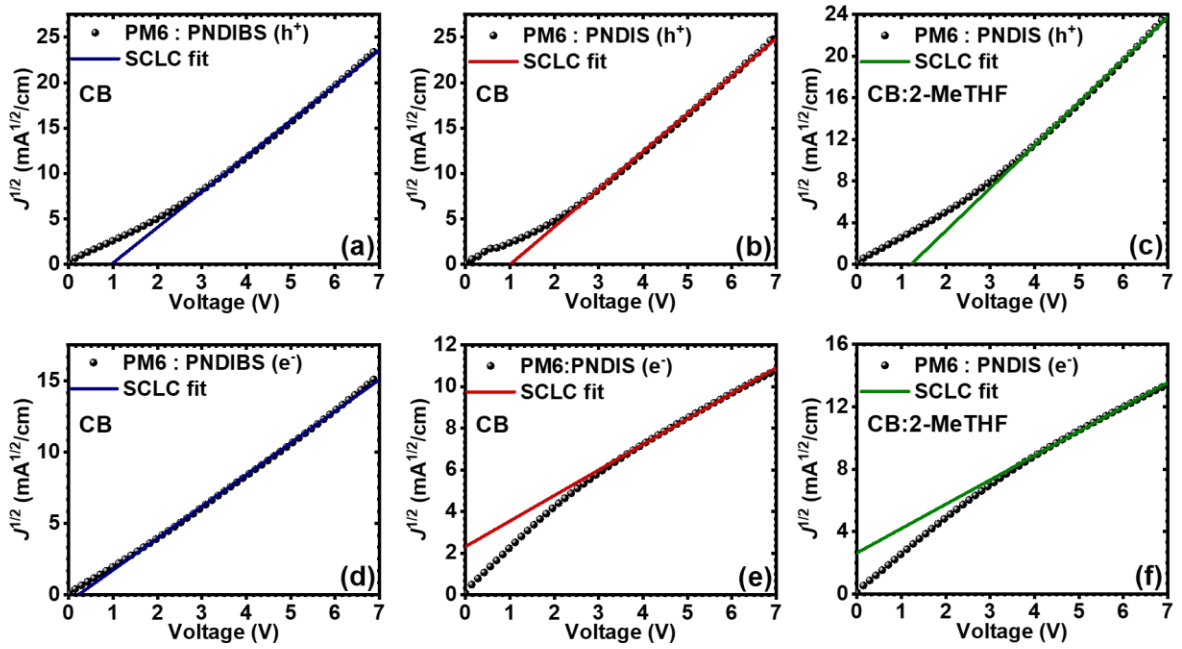

Figure A-7. *J-V* curves measured by the space-charge-limited current (SCLC) method and fitting for PM6:PNDIS and PM6:PNDIBS blend films: hole-only devices (a, b, c) and electron-only devices (d, e, f).

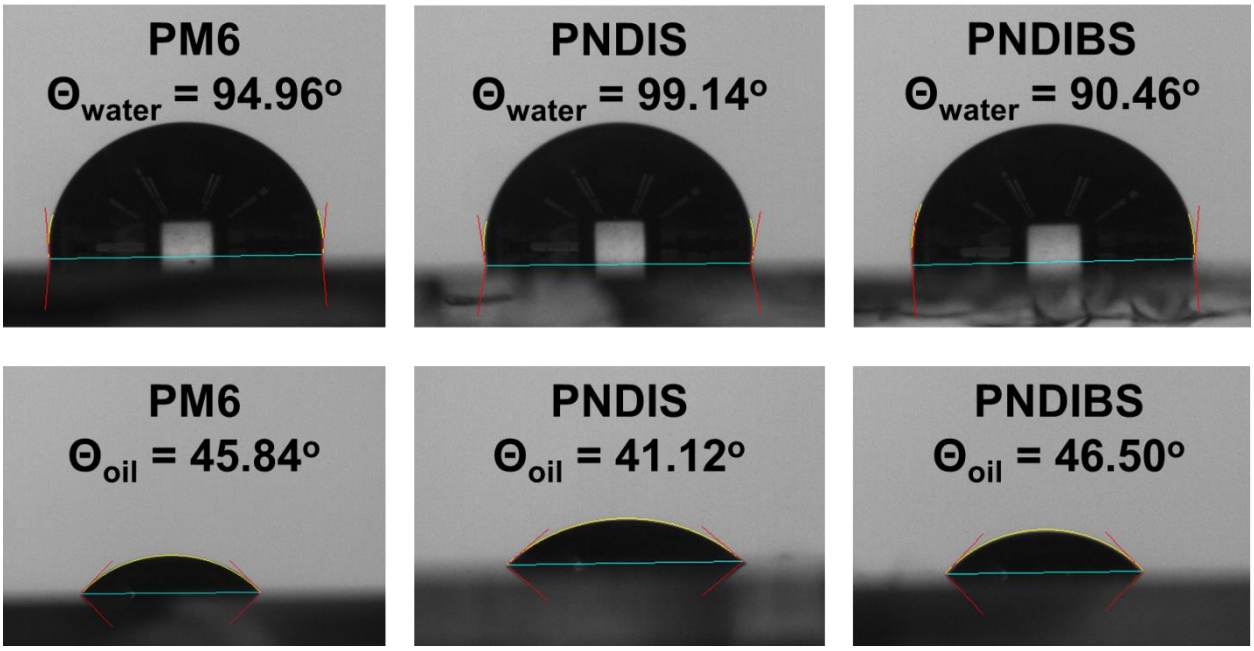

Figure A-8. Contact angle measurements on neat films of PM6, PNDIS, and PNDIBS with deionized water and oil (diiodomethane) as the wetting liquids. All neat films were thermally annealed at 110°C for 10 min.

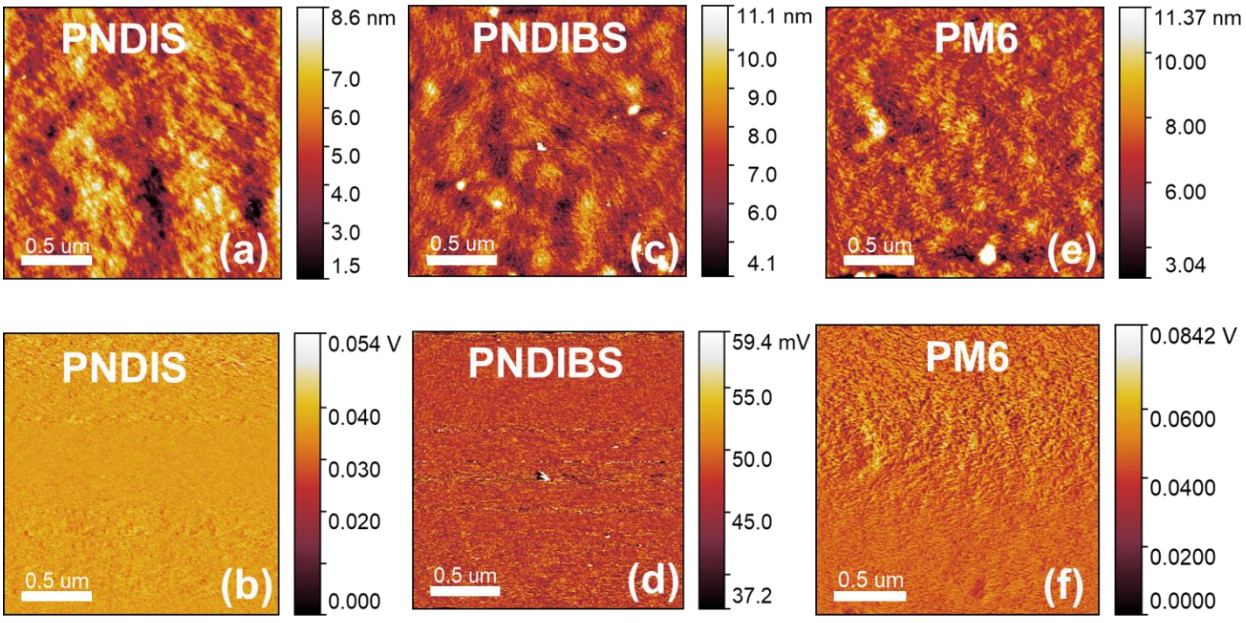

Figure A-9. AFM height (a, c, e) and phase (b, d, f) images (2 μm x 2 μm) of the surfaces of neat films of PNDIS (a, b), PNDIBS (c, d), and PM6 (e, f). The scale bars are 500 nm.

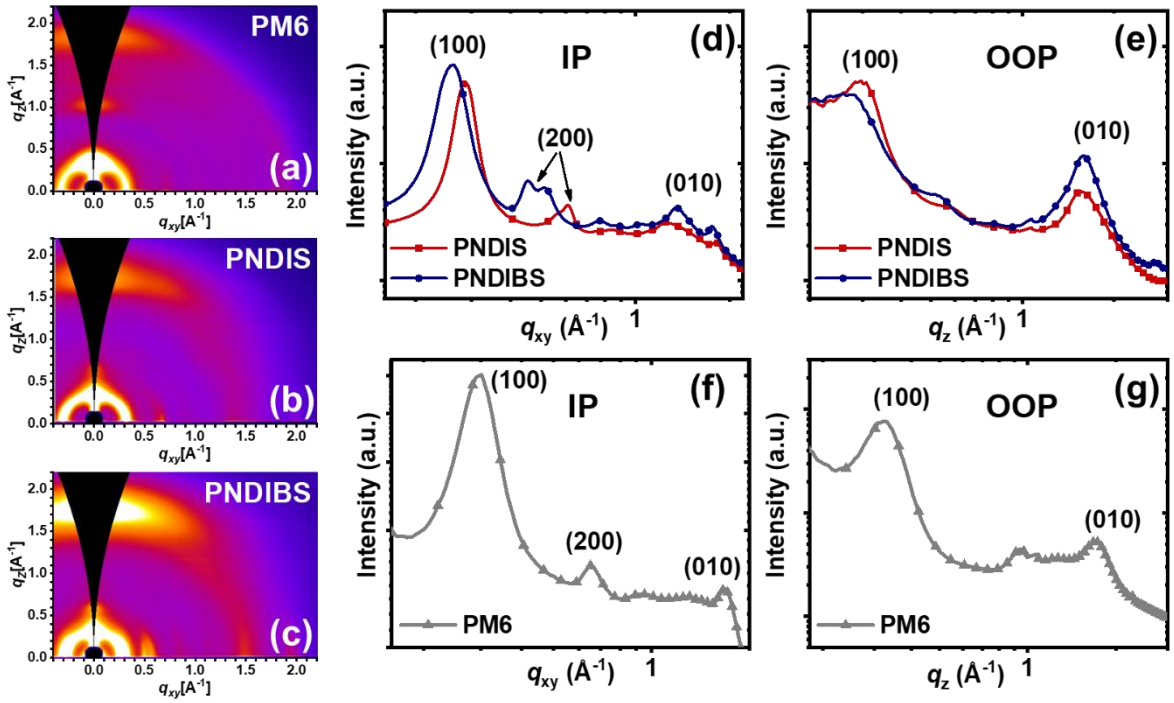

Figure A-10. (a) 2D-GIWAXS images of neat donor (PM6) and acceptor (PNDIS, PNDIBS) films. (b) In-plane (IP) line cut of neat PNDIS and PNDIBS films. (c) Out-of-plane (OOP) line cut of neat PNDIS and PNDIBS films. (d) In-plane line cut of neat PM6 films. (e) Out-of-plane line cut of neat PM6 films.

Table A-1. Photovoltaic Properties of PBDB-T:PNDIS and PBDB-T:PNDIBS Devices Processed at the Same Conditions as those of PM6:PNDIS and PM6:PNDIBS Devices, respectively.

Blend	J_{sc} (mA/cm^2)	V_{oc} (V)	FF	PCE$_{ave}$[(a)] (%)	$J_{sc}^{calc.}$ (mA/cm^2)
PBDB-T:PNDIS	15.00 (14.81±0.48)	0.827 (0.827±0. 003)	0.62 (0.61±0. 03)	7.72 (7.46±0.27)	14.26
PBDB-T:PNDIBS	15.87 (15.60±0.26)	0.851 (0.843±0. 012)	0.58 (0.58±0. 02)	7.90 (7.57±0.29)	15.01

[(a)]Average of over 12 devices.

Table A-2. Detail Device Optimization of PM6:PNDIS Blends Processed from Chlorobenzene (CB).

Variable	Condition	J_{sc} (mA/cm^2)	V_{oc} (V)	FF	PCE$_{ave}$[(a)] (%)
D:A ratio	D:A = 1:0.4	11.96 ± 0.11	0.967 ± 0. 004	0.644 ± 0. 31	7.45 ± 0.40
	D:A = 1:0.6	11.89 ± 0.15	0.962 ± 0. 003	0.661 ± 0. 020	7.55 ± 0.25
	D:A = 1:0.8	11.75 ± 0.07	0.960 ± 0. 003	0.645 ± 0. 036	7.28 ± 0.46
	D:A = 1:1	11.21 ± 0.06	0.953 ± 0. 005	0.619 ± 0. 047	6.61 ± 0.52
Processing solvent additives	0.5% DIO	12.18 ± 0.28	0.969 ± 0. 006	0.680 ± 0. 028	8.03 ± 0.54
	0.5% DPE	12.37 ± 0.16	0.969 ± 0. 004	0.609 ± 0. 004	7.30 ± 0.02
	0.5% CN	10.78 ± 0.36	0.968 ± 0. 005	0.651 ± 0. 029	6.81 ± 0.52
	0.5% ODT	12.46 ± 0.30	0.966 ± 0. 010	0.636 ± 0. 056	7.68 ± 0.86
	1.0% DIO	12.55 ± 0.39	0.978 ± 0. 004	0.669 ± 0. 025	8.22 ± 0.42
	1.0% ODT	12.79 ± 0.27	0.974 ± 0. 008	0.617 ± 0. 052	7.71 ± 0.87
	0.5% DIO + 0.5% ODT	12.72 ± 0.27	0.962 ± 0. 010	0.608 ± 0. 039	7.43 ± 0.29
	0.25% DIO + 0.25% ODT	12.99 ± 0.08	0.970 ± 0. 005	0.661 ± 0. 035	8.33 ± 0.45

(a) Average PCE of 4 devices.

Table A-3. Detail Device Optimization of PM6:PNDIBS Blends Processed from CB.

Variable	Condition	J_{sc} (mA/cm^2)	V_{oc} (V)	FF	PCE$_{ave}$[(a)] (%)
D:A ratio	D:A = 1:0.4	6.93 ± 0.05	0.939 ± 0. 003	0.490 ± 0. 006	3.19 ± 0.04
	D:A = 1:0.6	6.31 ± 0.09	0.930 ± 0. 003	0.510 ± 0. 004	2.97 ± 0.00
	D:A = 1:0.8	5.31 ± 0.14	0.914 ± 0. 003	0.508 ± 0. 005	2.46 ± 0.04
	D:A = 1:1	4.60 ± 0.07	0.907 ± 0. 003	0.510 ± 0. 004	2.12 ± 0.02
Annealing temperature	110^{o}C – 10min	6.99 ± 0.07	0.940 ± 0. 001	0.483 ± 0. 005	3.18 ± 0.06
	130^{o}C – 10min	6.95 ± 0.11	0.926 ± 0. 001	0.485 ± 0. 012	3.17 ± 0.07
	150^{o}C – 10min	7.07 ± 0.31	0.934 ± 0. 002	0.488 ± 0. 015	3.17 ± 0.13
	175^{o}C – 10min	6.03 ± 0.24	0.915 ± 0. 004	0.478 ± 0. 026	2.64 ± 0.23
Processing solvent additives	0.5% DPE	7.08 ± 0.03	0.929 ± 0. 002	0.528 ± 0. 012	3.47 ± 0.07
	0.5% DIO	7.13 ± 0.01	0.921 ± 0. 007	0.512 ± 0. 009	3.36 ± 0.08
	0.5% CN	5.77 ± 0.16	0.933 ± 0. 007	0.502 ± 0. 018	2.70 ± 0.06
	0.5% ODT	6.66 ± 0.42	0.883 ± 0. 033	0.425 ± 0. 055	2.53 ± 0.50
	0.5% DIO + 0.5% ODT	6.44 ± 0.12	0.929 ± 0. 004	0.528 ± 0. 005	3.16 ± 0.07

(a) Average PCE of 4 devices.

Table A-4. Detail Device Optimization of PM6:PNDIS Blends Processed from CB:2-MeTHF Co-Solvent.

Variable	Condition	J_{sc} (mA/cm^2)	V_{oc} (V)	FF	PCE$_{ave}$[(a)] (%)
CB:2-MeTHF (v:v) ratio	90:10	12.60 ± 0.27	0.968 ± 0. 002	0.659 ± 0. 005	8.04 ± 0.13
	80:20	12.87 ± 0.14	0.968 ± 0. 002	0.643 ± 0. 008	8.00 ± 0.01
	70:30	13.26 ± 0.21	0.963 ± 0. 002	0.649 ± 0. 004	8.29 ± 0.09
	60:40	13.61 ± 0.18	0.966 ± 0. 003	0.612 ± 0. 001	8.04 ± 0.13
Processing solvent additives	As-cast	13.41 ± 0.22	0.976 ± 0. 001	0.590 ± 0. 007	7.72 ± 0.08
	90^{o}C – 10min	14.39 ± 0.61	0.968 ± 0. 003	0.594 ± 0. 025	8.26 ± 0.11
	110^{o}C – 10min	14.75 ± 0.22	0.963 ± 0. 001	0.603 ± 0. 010	8.57± 0.10
	130^{o}C – 10min	14.58 ± 0.16	0.959 ± 0. 002	0.608 ± 0. 003	8.50 ± 0.13

(a) Average PCE of 4 devices.

Table A-5. Contact Angle and Surface Energy Analysis of the Neat Polymers and the Flory-Huggins Interaction Parameters for Blends.

Polymer	θ_{water} (^{o})	θ_{oil} (^{o})[(a)]	$\gamma_{dispersion}$ (mN/m)	γ_{polar} (mN/m)	γ (mN/m)	$\chi_{donor,\ acceptor}$[(b)]
PM6	94.96	45.84	36.56	0.49	37.05	-
PNDIS	99.14	41.12	39.04	0.04	39.08	0.0271K
PNDIBS	90.46	46.50	36.20	1.26	37.46	0.00113K

(a) θ_{oil} is the contact angle measured using diiodomethane as the wetting liquid. (b) The estimated Flory-Huggins interaction parameter ($\chi_{donor,\ acceptor}$) derived from the empirical relation $\chi_{donor,acceptor} = K\left(\sqrt{\gamma_{donor}} - \sqrt{\gamma_{acceptor}}\right)^2$, where K is a constant.

Table A-6. Summary of (100) and (010) Peaks in Both In-Plane (IP) and Out-of-Plane (OOP) Directions in Neat Component and Blend Polymer Thin Films.

Polymer	$q_{xy,\,(100)\,IP}$ ($Å^{-1}$)	$d_{(100)\,IP}$ (Å)	$L_{c,\,(100)\,IP}$ (nm)	$q_{z,\,(100)\,OOP}$ ($Å^{-1}$)	$d_{(100)\,OOP}$ (Å)	$q_{z,\,(010)\,OOP}$ ($Å^{-1}$)	$d_{(010)\,OOP}$ (Å)
PM6	0.30	20.94	7.13	0.33	19.04	1.71	3.67
PNDIS	0.29	21.67	13.6	0.29	21.67	1.57	4.00
PNDIBS	0.26	24.17	11.8	-	-	1.58	3.98
PM6 : PNDIS	0.29	21.67	10.5	0.32	19.64	1.71	3.67
PM6:PNDIBS	0.29	21.67	8.14	0.31	20.27	1.69	3.72

Appendix B

Appendix B presents supplementary information accompanied Chapter 2, Section 2.2: Elucidating Impacts of Molecular Weights on the Morphology, Charge Transport, Photophysics, and Performance of All-Polymer Solar Cells.

B.1. Detailed Synthesis and Characterization of Monomers and PNDIBS Polymers.

Synthesis of 2,2'-biselenophene. In a 100 mL round bottom flask previously burn and purged, add 1g (7.63 mmol. 1eq) of selenophene, 20 mL of ethyl ether and put at 0 °C. Then, add dropwise 3,5 mL of *n*-buthyllithium (2.5M) (7.63 mmol, 1eq) and let stir for 1h while letting it goes back to room temperature. Put the reaction at -78 ^{o}C and add 1.33 g (9.92 mmol, 1.3eq) of $CuCl_2$ portion wise. Let stir at -78 °C for 5 minutes before letting it come back to room temperature and stir for 16h. Add about 10 mL of ethyl ether before filtering over celite. Then, wash with a solution of 1M HCl, 5% $NaHCO_3$ and then water. Dry the organic phase with Na_2SO_4, filter and evaporate to obtain 543 mg (2.088 mmol) of white crystals for a yield of 55%. (If the crystals are yellow, filter it over activated charcoal with ethyl ether). ^{1}H NMR (400 MHz, $CDCl_3$, ppm): δ 7.87(dt, 2H, *J*= 5.6-0.9 Hz); 7.31-7.25 (m, 2H); 7.23(dd, 2H, *J* = 5.5-3.8 Hz) (Figure S1). ^{13}C NMR (126 MHz, $CDCl_3$) δ 144.77; 130.23; 129.68; 129.12; 126.72.

Synthesis of 5,5'-bistrimethylstannyl-2,2'-biselenophene. In a 100 mL round bottom flask previously burn and purged, add 500 mg (1.92 mmol. 1eq) of 2,2'-biselenophene, 27 mL of dry THF and put at -78 °C. Then, add dropwise 1.77 mL of *n*-buthyllithium (2.5M) (4.42 mmol, 2.3eq) and let stir for 2h at -78 °C and then let it goes back to room temperature for another hour. Put the reaction at -78 ^{o}C and add 4.6 mL (4.6mmol, 2.4eq) of Me_3SnCl one shot. Let stir at -78 °C for 5 minutes before letting it come back to room temperature and stir for 16h. Pour the solution on water and extract with ethyl ether. Dry the organic phase with Na_2SO_4, filter and

evaporate. A recrystallization in isopropanol was performed, however this caused the degradation of the monomer and only 47mg (0.08mmol) of yellowish crystals was obtain for a yield of 4%. ^{1}H NMR (400 MHz, $CDCl_3$, ppm): δ 7.40-7.31(m, 6H); 0.31-0.44 (t, 24H, *J*=0.5 Hz). (Figure S2). ^{13}C NMR (126 MHz, $CDCl_3$) δ 138.50; 128.26; 7.90.

DHAP Synthesis of poly[[N,N′-bis(2-octyldodecyl)-naphthalene-1,4,5,8-bis(dicarboximide)-2,6-diyl]-alt-5,5′-biselenophene] (PNDIBS). In a 10 mL oven dry biotage microwave vial with a magnetic stirring bar, 189.4 mg (0.192 mmol, 1 eq) of N,N'-bis(2-octyldodecyl)-2,6-dibromo-1,4,5,8-naphtalenediimide, 50 mg (0.192 mmol, 1eq) of 2,2'-biselenophene, 1.8 mg (0.0019 mmol, 1 %mol) of $Pd_2(dba)_3$, 19.6 mg (0.192 mmol, 1eq) of pivalic acid and 79.7 mg (0.577 mmol, 3eq) of anhydrous potassium carbonate are added. The vial was sealed and purged by vacuum and filled with argon three times. Then, 0.4 mL of degassed dry chlorobenzene was added and the solution stirred at room temperature for 15 min to dissolve the monomers. The vial was placed in a preheated oil bath at 100 °C for 18 hr. The reaction was cooled at 50 °C and 20 mL of chloroform and 5 mL of *o*-dichlorobenzene were added prior to precipitation of the polymer in methanol. The precipitate was filtered and Soxhlet extraction using acetone and followed by hexanes was performed to remove catalyst residues and low molecular weight material. Chloroform was then used to recover the polymer. The solvent was reduced to about 10 mL and precipitated into methanol, filtered through 0.45 μm nylon filter and air-dried to afford the deep blue polymer PNDIBS with a yield of 95%.

Stille Synthesis of poly[[N,N′-bis(2-octyldodecyl)-naphthalene-1,4,5,8-bis(dicarboximide)-2,6-diyl]-alt-5,5′-biselenophene] (PNDIBS). In a 10 mL oven dry biotage microwave vial with a magnetic stirring bar, 75.7 mg (0.077 mmol, 1 eq) of N,N'-bis(2-octyldodecyl)-2,6-dibromo-1,4,5,8-naphtalenediimide, 45 mg (0.077 mmol, 1eq) of 5,5'-bistrimethylstannyl-2,2'-

biselenophene, 2.46 mg (0.0027 mmol, 3.5 %mol) of $Pd_2(dba)_3$ and 4.2 mg (0.0138 mmol, 18 %mol) of tri(*o*-tolyl)phosphine were added. The vial was sealed and purged by vacuum and filled with argon three times. Then, 3.5 mL of degassed dry chlorobenzene was added and the solution stirred at room temperature for 15 min to dissolve the monomers. The vial was placed in a preheated oil bath at 120 °C for 4 days. Then 0.05mL of 2-trimethylstannylthiophene and bromobenzene were added at 8h interval. The reaction was cooled at 50 °C and 4.5 mL of chloroform was added prior to precipitation of the polymer in methanol. The precipitate was filtered and Soxhlet extraction using acetone followed by hexanes was performed to remove catalyst residues and low molecular weight material. Chloroform was then used to recover the polymer. The solvent was reduced to about 10 mL and precipitated into methanol, filtered through 0.45 μm nylon filter and air-dried to afford the deep blue polymer PNDIBS with a yield of 93%.

Characterizations. ^{1}H NMR spectra were recorded using a Varian AS400 in deuterated chloroform at 298 K. Chemicals shifts were reported as δ values (ppm) relative to chloroform value of 7.26 ppm. ^{1}H spectra of the polymers were recorded on a Varian Agilent DD2 500 MHz apparatus in 1,1,2,2-tetrachloroethane-D_2 at 90 °C. Number-average (M_n) and weight-average (M_w) molecular weights were determined by size exclusion chromatography (SEC) using a high temperature Varian Polymer Laboratories GPC220 equipped with an RI detector and a PL BV400 HT Bridge Viscometer. The column set consists of 2 PL gel Mixed C (300 x 7.5 mm) columns and a PL gel Mixed C guard column. The flow rate was fixed at 1mL/min using 1,2,4-trichlorobenzene (TCB) (with 0.0125% BHT w/v) as the eluent. The temperature of the system was set to 110 °C. The samples (2 mg) were dissolved in 2 mL of TCB in a 5 mL chromatography vial then stirred and heated to 110 °C for 1 hour for a complete dissolution.

Then, a filtration through a 0.45 µm cellulose fiber film in a 5 mL chromatography vial lead to a homogenous polymeric solution. Dissolution of the polymers was performed through a loop of 200 µL with a Varian Polymer Laboratories PL-SP 260VC sample preparation system. The calibration method used to generate the reported data was the classical polystyrene method using polystyrene narrow standards Easi-Vials PS-M from Varian Polymer Laboratories which were dissolved in TCB. Thermogravimetric analyses (TGA) of the polymers were performed with a TGA/SDTA 851e from Metler-Toledo. The acquisitions were recorded under argon with a 10 °C/min scan rate from 50 to 800 °C. While the Stille-prepared had a degradation temperature (T_d) of 416°C, the DHAP-prepared polymer of similar molecular weight showed a markedly higher T_d at 440°C. The higher thermal stability of the DHAP-prepared PNDIBS strongly suggests minimal structural defects in the DHAP-prepared polymer compared to the Stille-prepared one. The reported degradation temperatures (DT) correspond to a 5% mass lost. UV vis-NIR absorption spectra were recorded using a Perkin Elmer model Lambda 900 UV-Vis/near IR spectrophotometer. Polymer solutions in chlorobenzene were spin-coated on untreated glass substrate for solid-state absorption spectra measurements. The optical bandgap was calculated from the onset of the absorption band.

Cyclic voltammetry. Cyclic voltammetry (CV) was performed on an EG&G Princeton Applied Research potentiostat/galvanostat model 273A. A three-electrode cell was used where platinum wires were used as both the working and counter electrodes. The reference electrode contained silver/silver ions (Ag in 0.01M $AgNO_3$ solution). The working electrodes were made by coating the platinum wires with PNDIBS solutions and subsequently dried in oven at 65°C overnight. The CV measurements were done in a 0.1M tetrabutylammonium hexafluorophosphate (Bu_4NPF_6) electrolyte solution in acetonitrile, which was purged with N_2 gas before use, at a

scan rate of 50mV/s. Ferrocene was used as an internal standard. The HOMO and LUMO energy levels were determined from the oxidation onset potential and reduction onset potential following the equations: $E_{HOMO} = -(eE_{ox}^{onset} - E_{Fc/Fc+} + 4.8)$ and $E_{LUMO} = -(eE_{red}^{onset} - E_{Fc/Fc+} + 4.8)$, respectively.

Scheme B-1. General polymerization conditions for the preparation of acceptor copolymer PNDIBS by DHAP and Stille coupling methods.

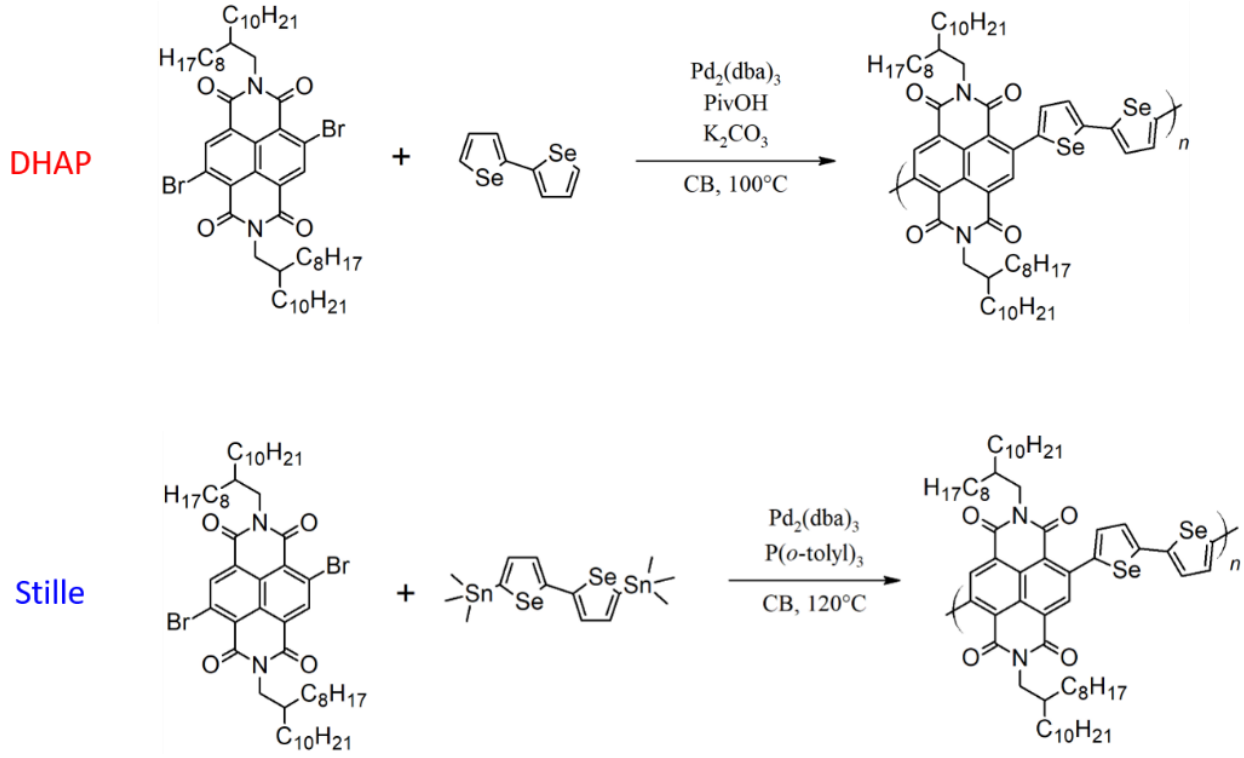

B.2. Supplementary Figures

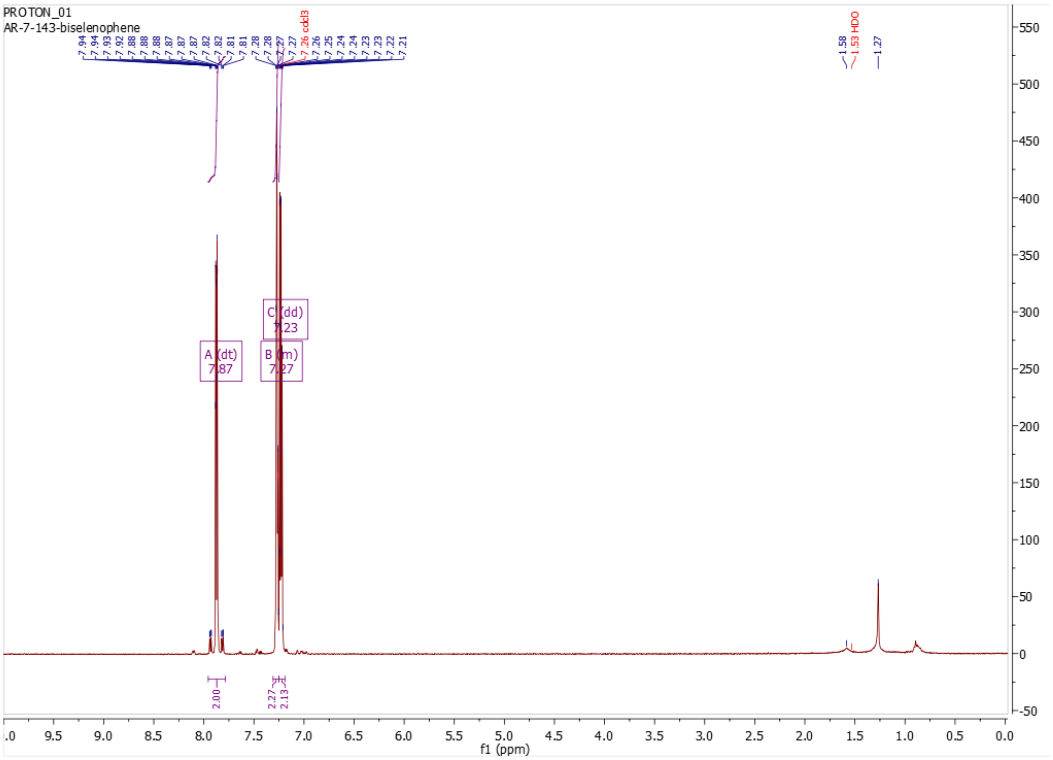

Figure B-1. ^{1}H NMR of 2,2'-biselenophene.

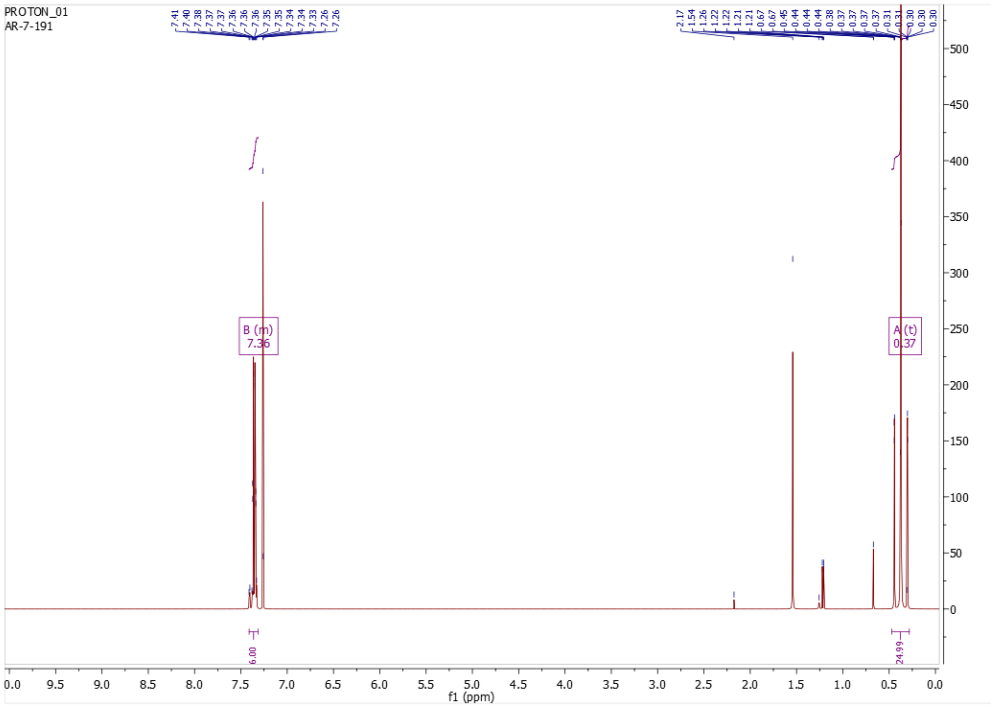

Figure B-2. ^{1}H NMR of 5,5'-triméthyl-2,2'-biselenophene.

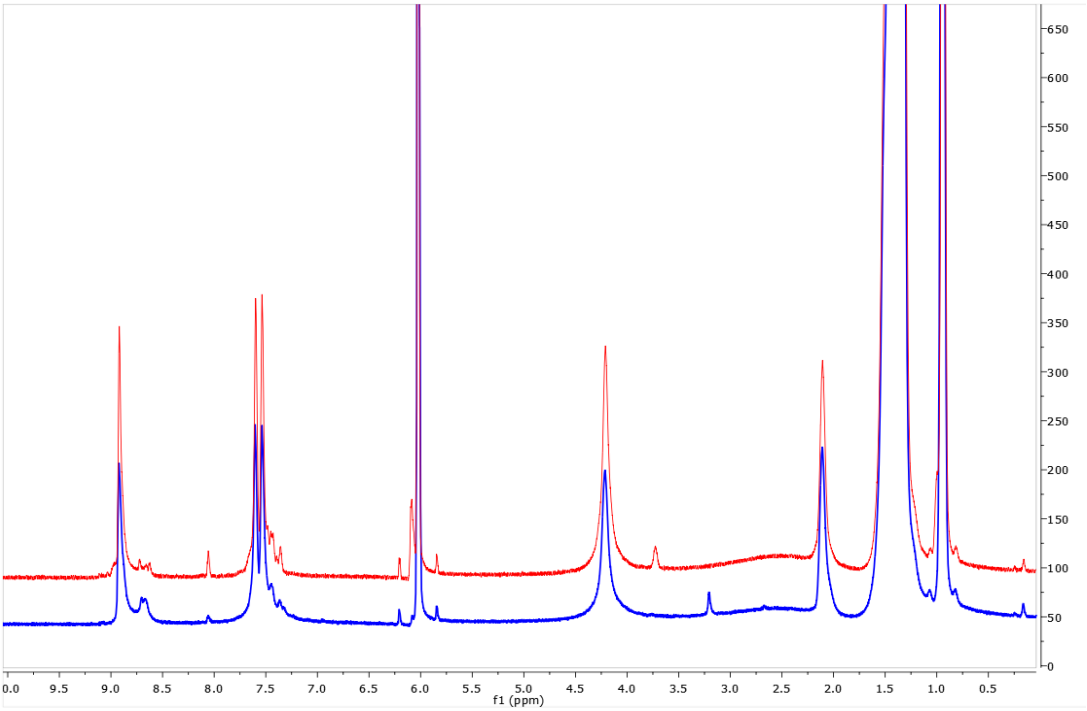

Figure B-3. ^{1}H NMR spectrum of DHAP (red) and Stille (blue) prepared PNDIBS samples.

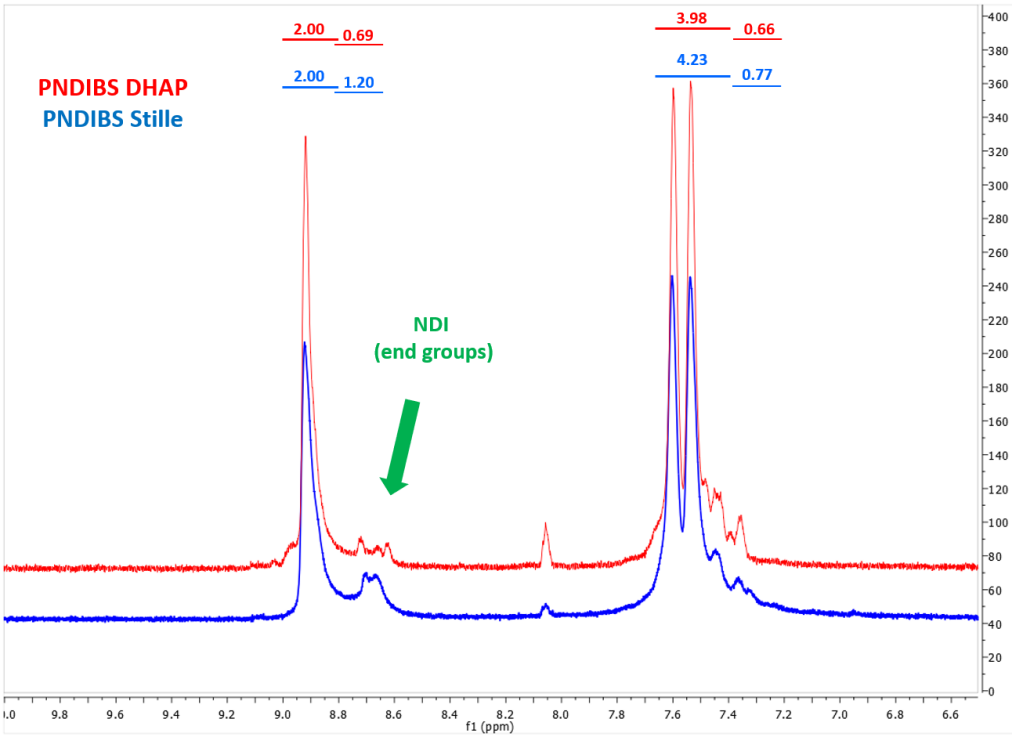

Figure B-4. Aromatic region close-up of the ^{1}H NMR of DHAP-prepared (red) and Stille-prepared (blue) PNDIBS samples.

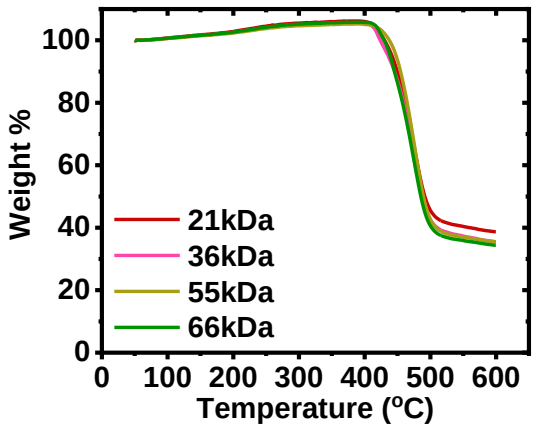

Figure B-5. TGA traces of PNDIBS polymer of different M_n heating at 20°C/min.

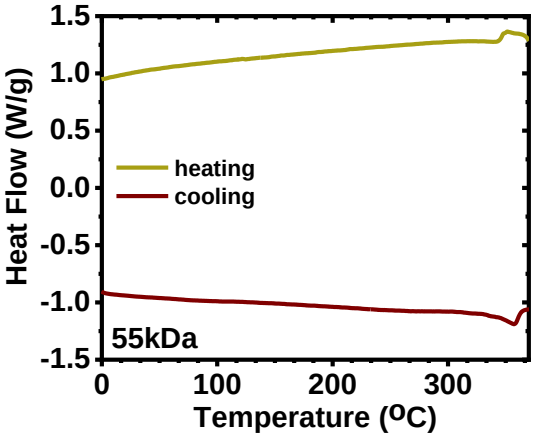

Figure B-6. Second heating and cooling DSC scans of PNDIBS of 55kDa at 10°C/min under N_2 flow.

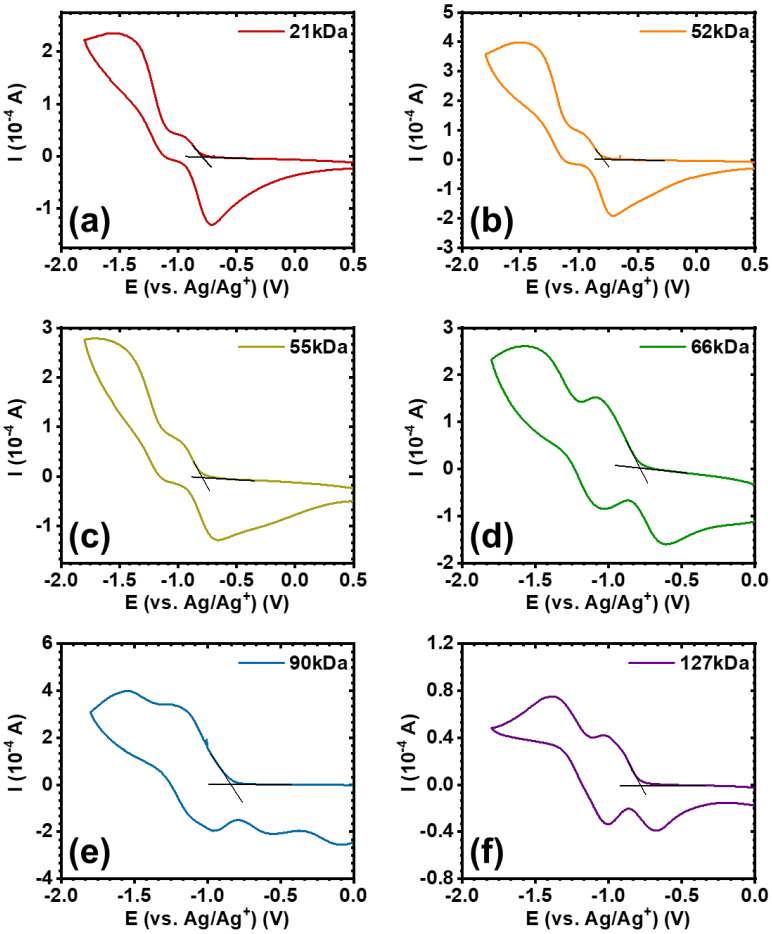

Figure B-7. Cyclic voltammogram for reduction of PNDIBS thin film of different molecular weights in 0.1M tetrabutylammonium hexafluorophosphate (Bu_4NPF_6) solution in acetonitrile at a scan rate of 50 mV/s.

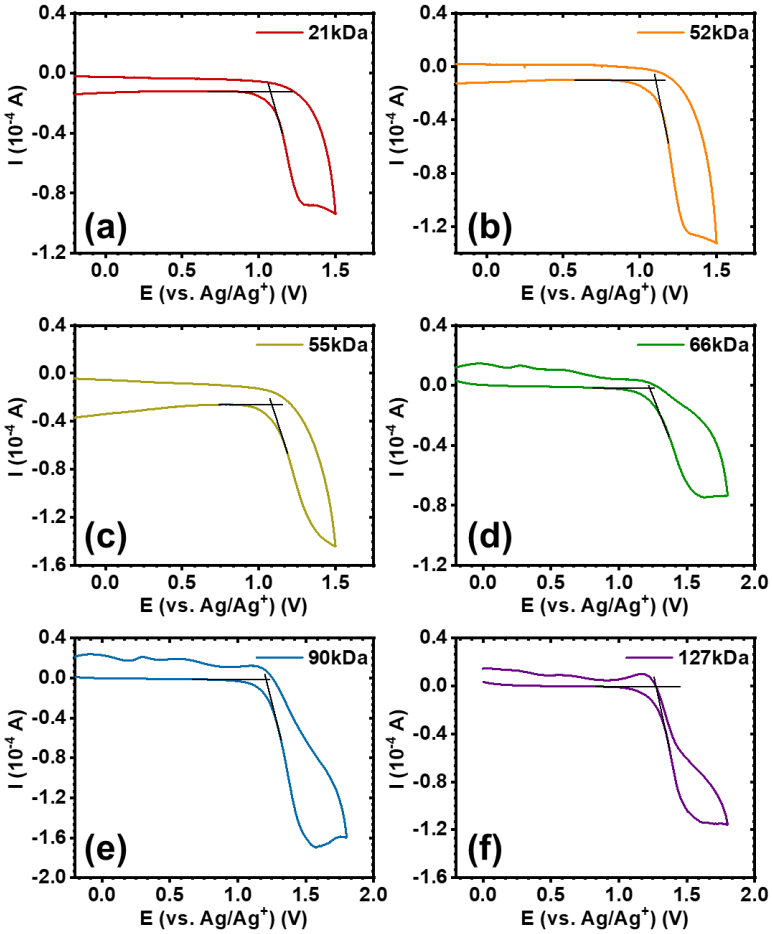

Figure B-8. Cyclic voltammogram for oxidation of PNDIBS thin film of different molecular weights in 0.1M tetrabutylammonium hexafluorophosphate (Bu_4NPF_6) solution in acetonitrile at a scan rate of 50 mV/s.

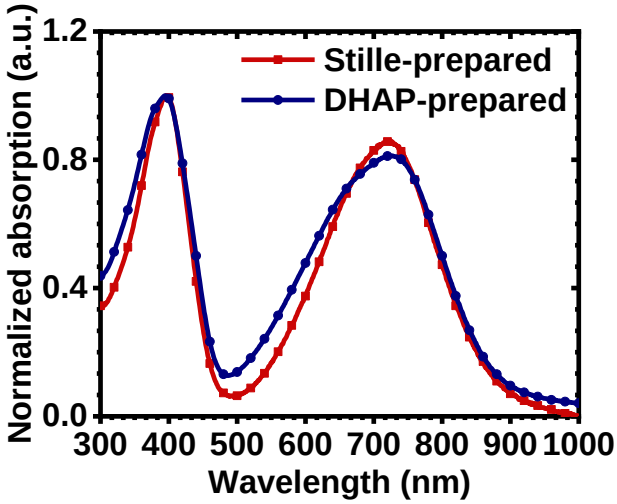

Figure B-9. Thin film UV-Visible spectra of PNDIBS synthesized via DHAP and Stille.

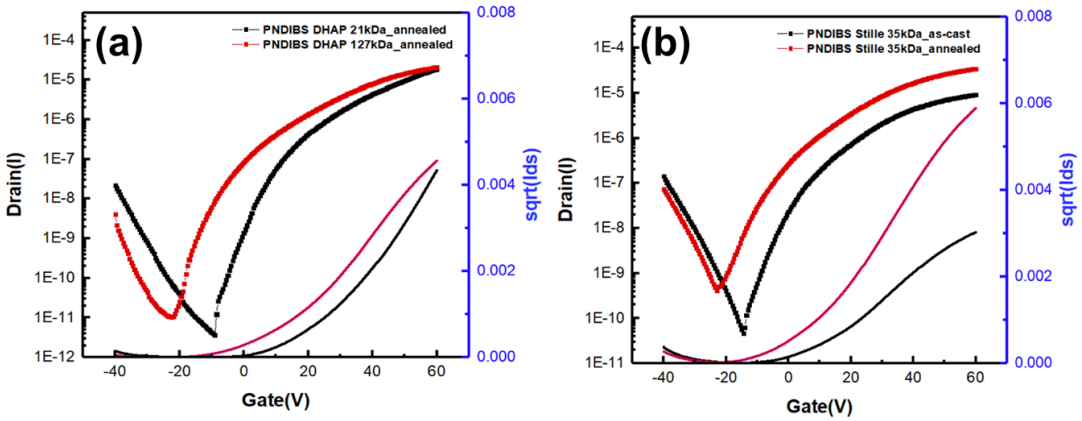

Figure B-10. Representative transfer curves for neat PNDIBS films without annealing and annealed at 170◦C (a) PNDIBS DHAP 21kDa and (b) PNDIBS Stille 35kDa.

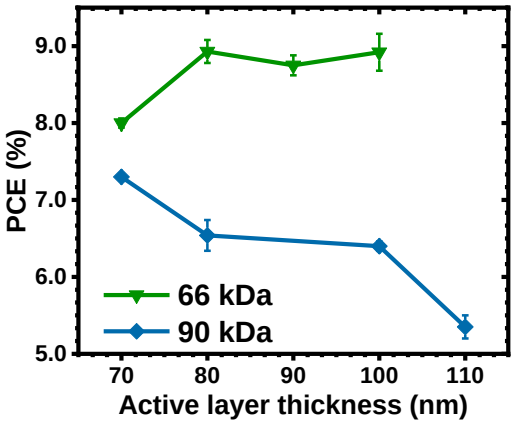

Figure B-11. The relationship of the power conversion efficiency (PCE) of the optimized PBDB-T:PNDIBS devices as a function of the active layer thicknesses for the 66kDa and 90kDa molecular weights. The error bars were generated from 8 devices.

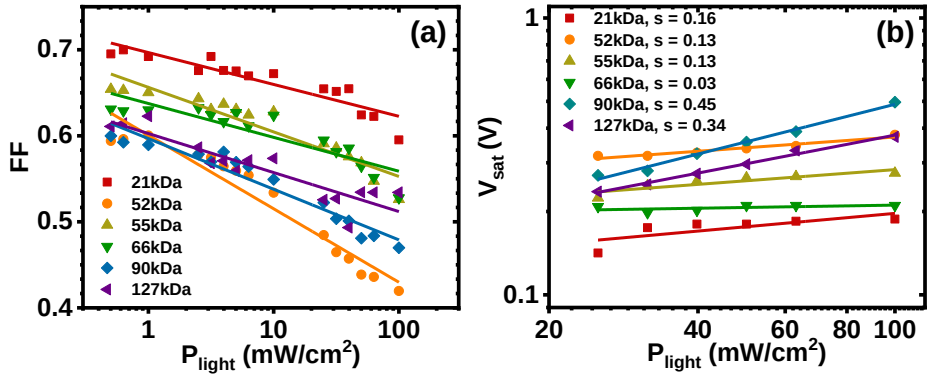

Figure B-12. (a) FF dependency on incident light intensity for the optimized PBDB-T:PNDIBS devices of various acceptor polymer molecular weight. (b) Saturation voltage (V_{sat}) vs. incident

light intensity (P_{light}) for optimized PNDIBS:PBDB-T devices of various acceptor polymer molecular weights.

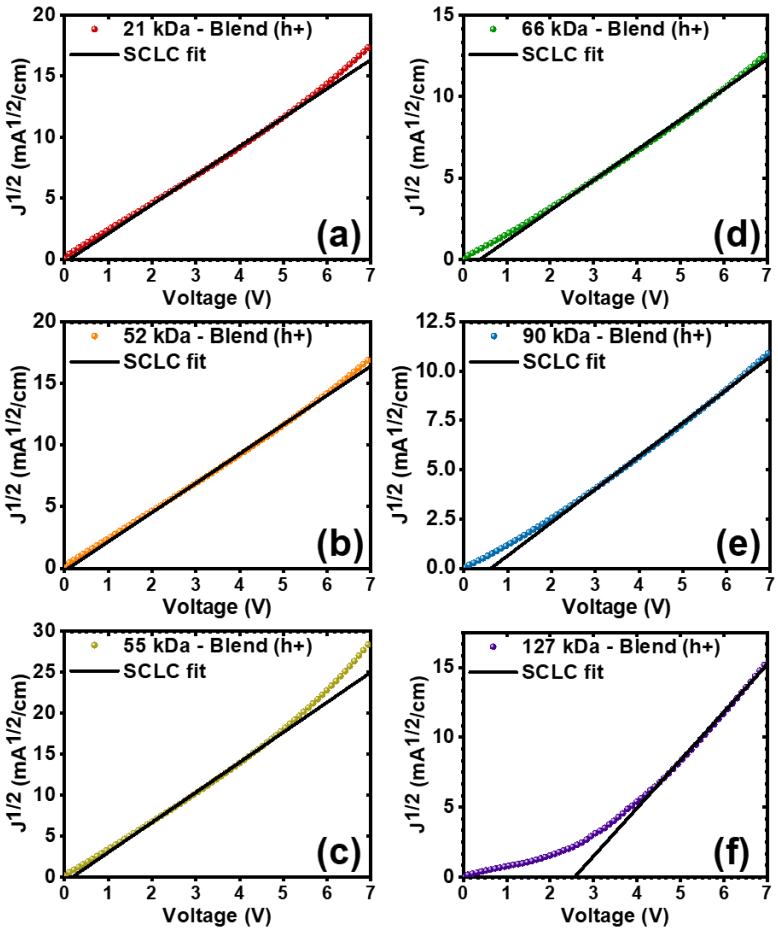

Figure B-13. *J-V* curves measured by the space-charge-limited current (SCLC) method of hole-only devices and fitting for PBDB-T:PNDIBS blend films of various acceptor molecular weights. All active layers were processed at optimal conditions.

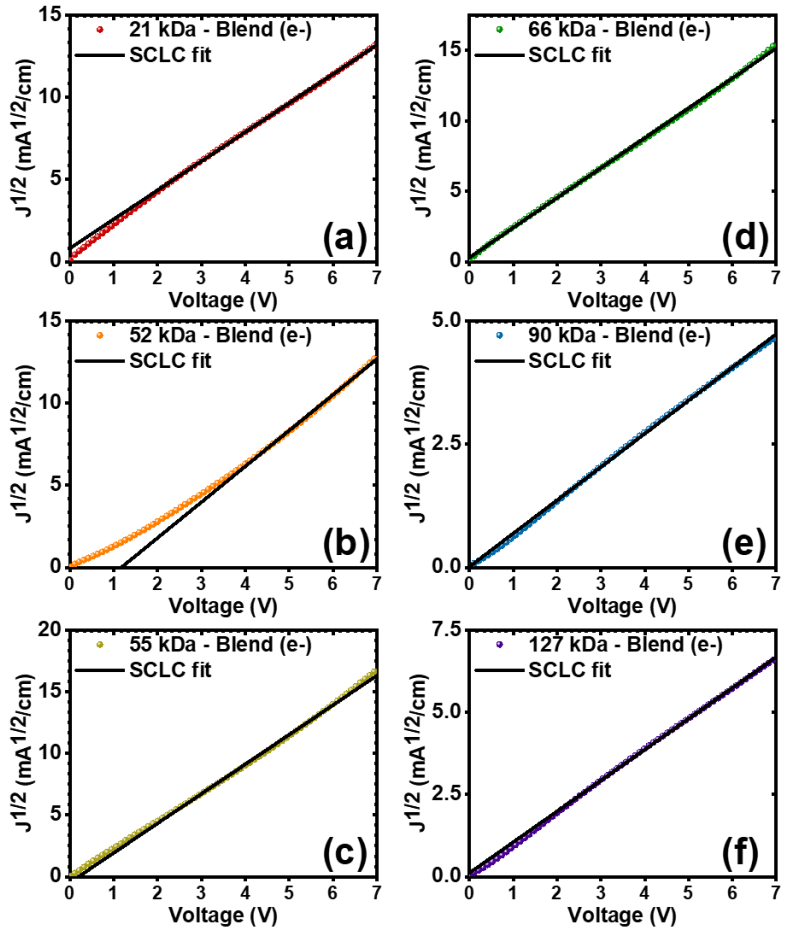

Figure B-14. *J-V* curves measured by the space-charge-limited current (SCLC) method of electron-only devices and fitting for PBDB-T:PNDIBS blend films of various acceptor molecular weights. All active layers were processed at optimal conditions.

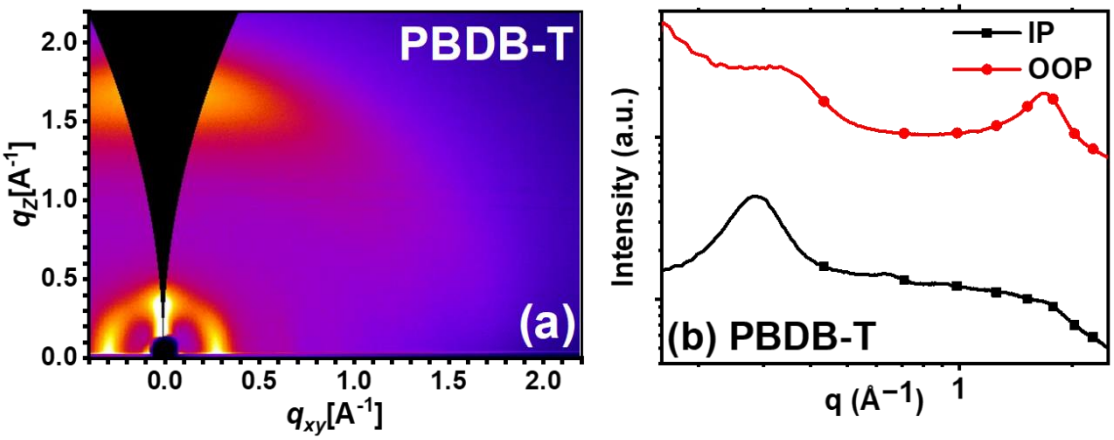

Figure B-15. (a) 2D-GIWAXS patterns and (b) 1D line cut in the in-plane (IP) and out-of-plane (OOP) direction of neat PBDB-T film.

B.3. Supplementary Tables

Table B-1. Direct Hetero(Arylation) Polymerization Conditions for Different Molecular Weight of PNDIBS Acceptor Copolymer.

Polymers	M_n (kDa)	PDI	Polymerization time (hr)
PNDIBS (DHAP) 21 kDa	21	1.7	3
PNDIBS (DHAP) 52 kDa	52	3.3	16
PNDIBS (DHAP) 55 kDa	55	2.4	18
PNDIBS (DHAP) 66 kDa	66	2.6	13
PNDIBS (DHAP) 90 kDa	90	3.0	20
PNDIBS (DHAP) 127 kDa	127	2.3	22

Table B-2. Electron Mobility of PNDIBS Acceptor Polymer Measured via Bottom-Gate Top-Contact OFET Architecture.

Polymer	T_{anneal} (°C)	$\mu_{e,\ ave}^{FET}$ (cm^2/Vs)	I_{on}/I_{off}	$V_{threshold}$ (V)
PNDIBS (DHAP) 21 kDa	170	0.16	4×10^6	26
PNDIBS (Stille) 35kDa	25°C	0.04	2×10^5	26
PNDIBS (Stille) 35kDa	170	0.15	1×10^5	31

Table B-3. Charge Extraction Probability at Short-Circuit Condition and Maximum Charge Photogeneration Rate of the Optimized PBDB-T:PNDIBS All-PSC Devices for Different Acceptor Polymer Molecular Weight.

Blend	P_c *(E,T)* (%)	G_{max} ($m^{-3}s^{-1}$)
PBDB-T:PNDIBS (21kDa)	97.24	1.06×10^{28}
PBDB-T:PNDIBS (52kDa)	97.48	1.14×10^{28}
PBDB-T:PNDIBS (55kDa)	94.08	1.21×10^{28}
PBDB-T:PNDIBS (66kDa)	97.25	1.10×10^{28}
PBDB-T:PNDIBS (90kDa)	89.31	1.09×10^{28}
PBDB-T:PNDIBS (127kDa)	93.69	1.09×10^{28}

Table B-4. Summary of (100) and (010) Peaks in Both In-Plane (IP) and Out-of-Plane (OOP) Directions in Neat Component and Blend Polymer Thin Films.

Polymer	q_{xy} ($Å^{-1}$) (100) IP	q_z ($Å^{-1}$) (010) OOP
PBDB-T	0.29	1.69
PBDB-T:PNDIBS (21kDa)	0.27	1.63
PBDB-T:PNDIBS (52kDa)	0.27	1.66
PBDB-T:PNDIBS (55kDa)	0.27	1.63
PBDB-T:PNDIBS (66kDa)	0.25	1.52
PBDB-T:PNDIBS (90kDa)	0.26	1.63
PBDB-T:PNDIBS (127kDa)	0.25	1.61

Appendix C

Appendix C presents supplementary information accompanied Chapter 3: Unified Understanding of Molecular Weight Dependence of Electron Transport in Naphthalene Diimide-Based n-Type Semiconducting Polymers.

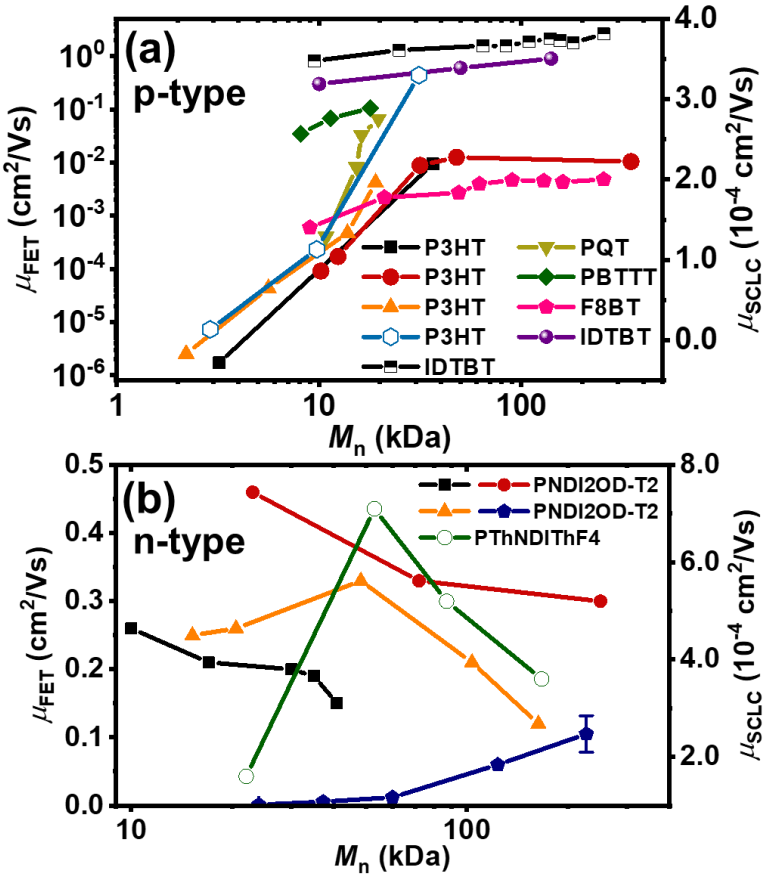

Figure C-1. (a) Dependence of field-effect *hole* mobility (μ_{FET}, filled symbols) and bulk *hole* mobility (μ_{SCLC}, unfilled symbols) on number-average molecular weight (M_n) of *p-type* semiconducting polymers previously reported.[157, 163, 164, 167, 170-172, 270, 271] (b) Dependence of field-effect *electron* mobility (μ_{FET}, filled symbols) and bulk *electron* mobility (μ_{SCLC}, unfilled symbols) on M_n of various *n-type* semiconducting polymers previously reported.[33, 178-181]

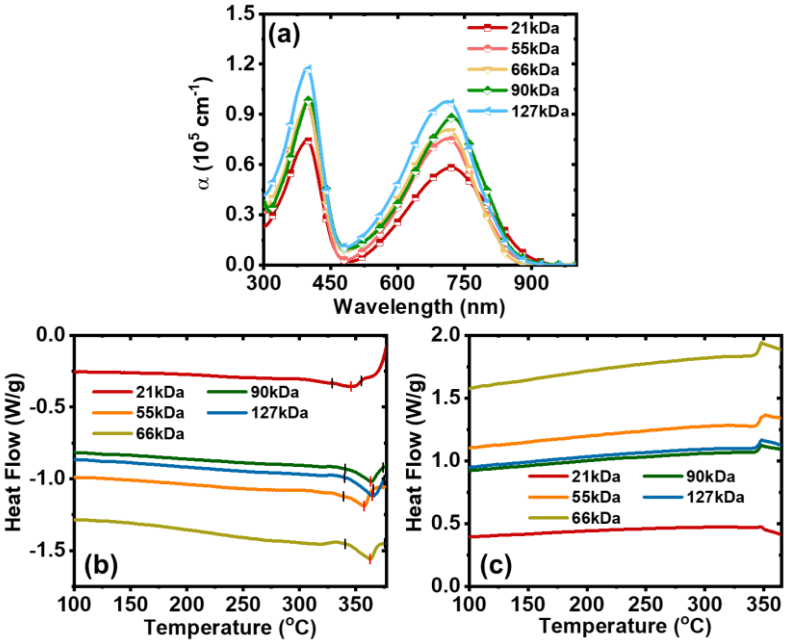

Figure C-2. (a) Thin-film optical absorption spectra of PNDIBS polymer of different number-average molecular weight (M_n). Reproduced from Ref.[69] with permission from the Royal Society of Chemistry. (b) DSC heating scans of PNDIBS polymers of different M_n at a heating rate of 10°C/min under N_2 gas flow, and (c) DSC cooling scans of PNDIBS polymers of different M_n at a cooling rate of 10°C/min under N_2 gas flow.

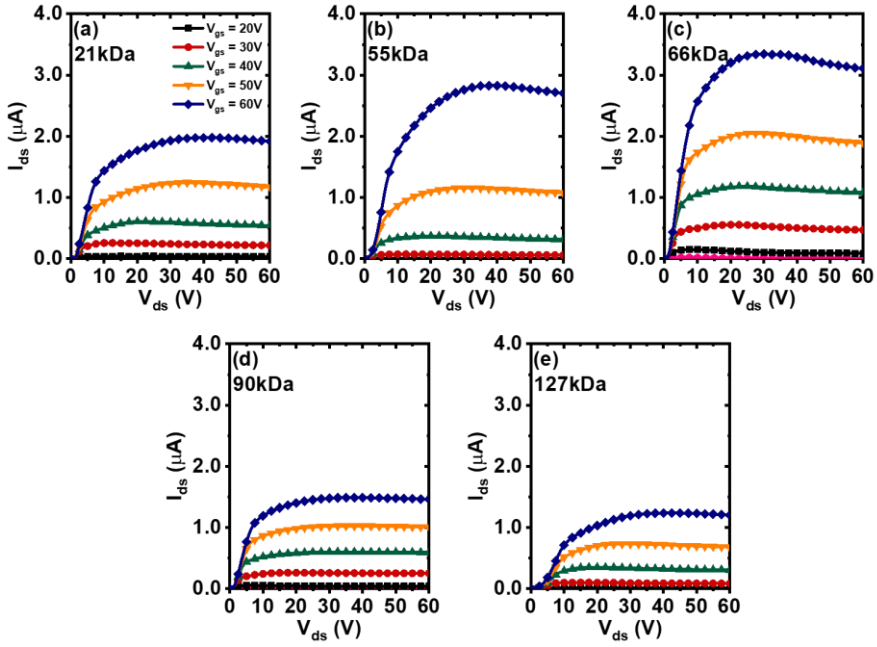

Figure C-3. Output curves of n-channel bottom-gate top-contact field-effect transistors based on PNDIBS semiconducting polymer of different number-average molecular weight (M_n) values: (a)

21kDa, (b) 55kDa, (c) 66kDa, (d) 90kDa, and (e) 127kDa. These devices were fabricated and characterized at TAIWAN TECH.

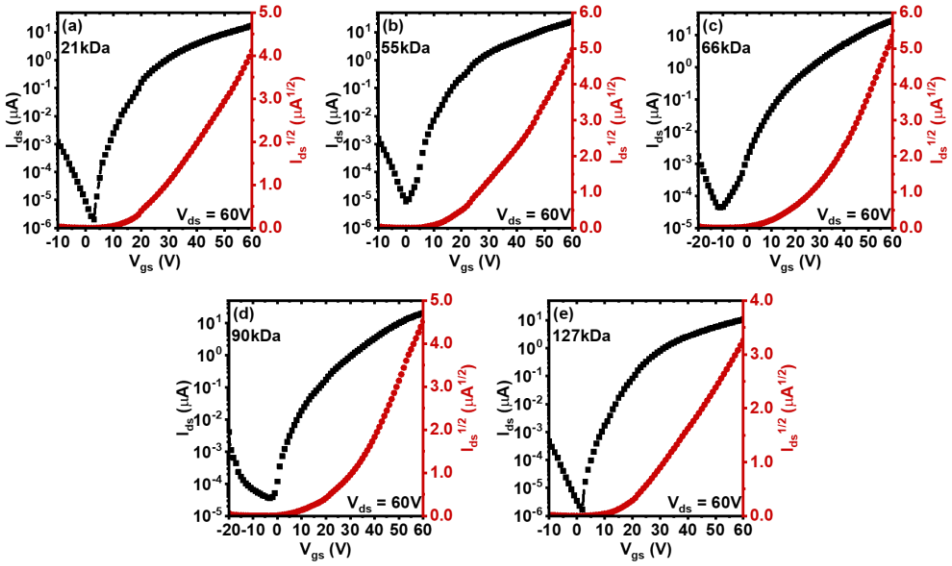

Figure C-4. Transfer curves of n-channel bottom-gate top-contact field-effect transistors based on PNDIBS semiconducting polymer of different number-average molecular weight (M_n) values: (a) 21kDa, (b) 55kDa, (c) 66kDa, (d) 90kDa, and (e) 127kDa. These devices were fabricated and characterized at TAIWAN TECH.

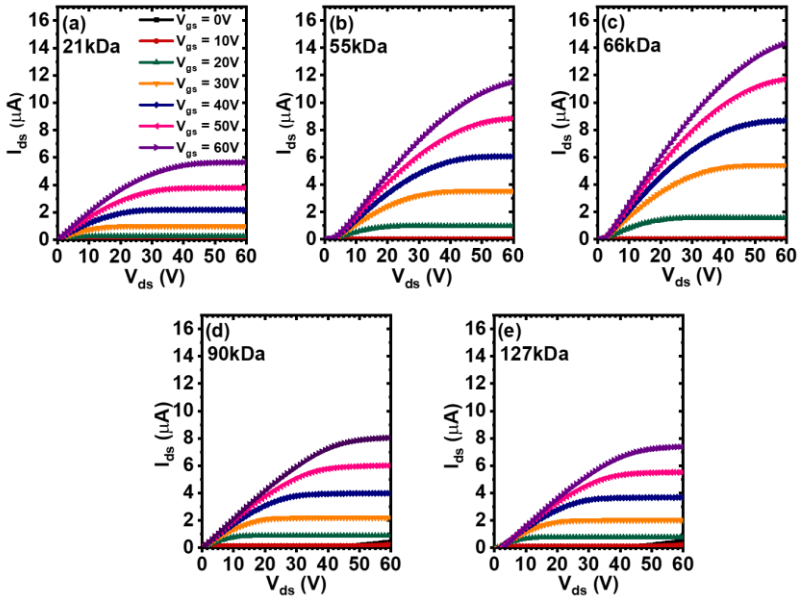

Figure C-5. Output curves of n-channel bottom-gate top-contact field-effect transistors based on PNDIBS semiconducting polymer of different number-average molecular weight (M_n) values: (a) 21kDa, (b) 55kDa, (c) 66kDa, (d) 90kDa, and (e) 127kDa. These devices were fabricated and characterized at the University of Washington.

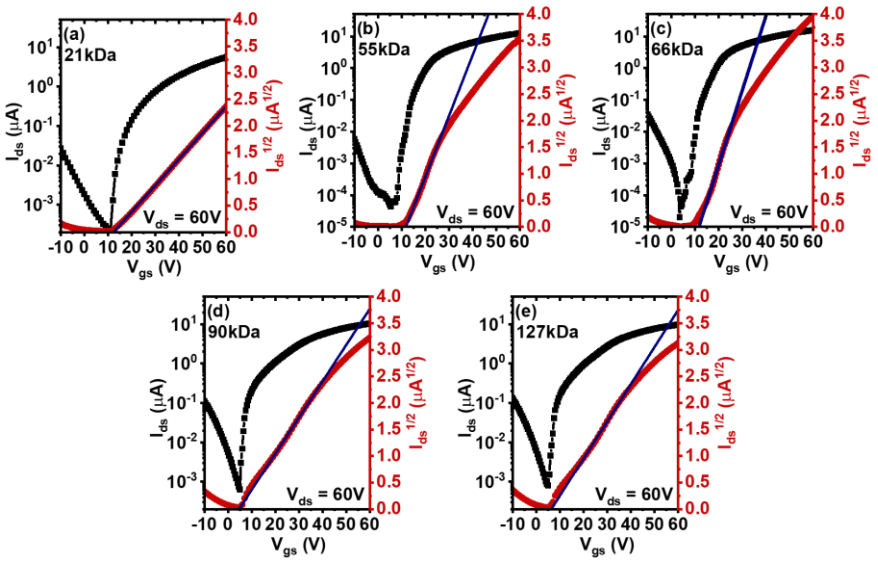

Figure C-6. Transfer curves of n-channel bottom-gate top-contact field-effect transistors based on PNDIBS semiconducting polymer of different number-average molecular weight (M_n) values: (a) 21kDa, (b) 55kDa, (c) 66kDa, (d) 90kDa, and (e) 127kDa. These devices were fabricated and characterized at the University of Washington.

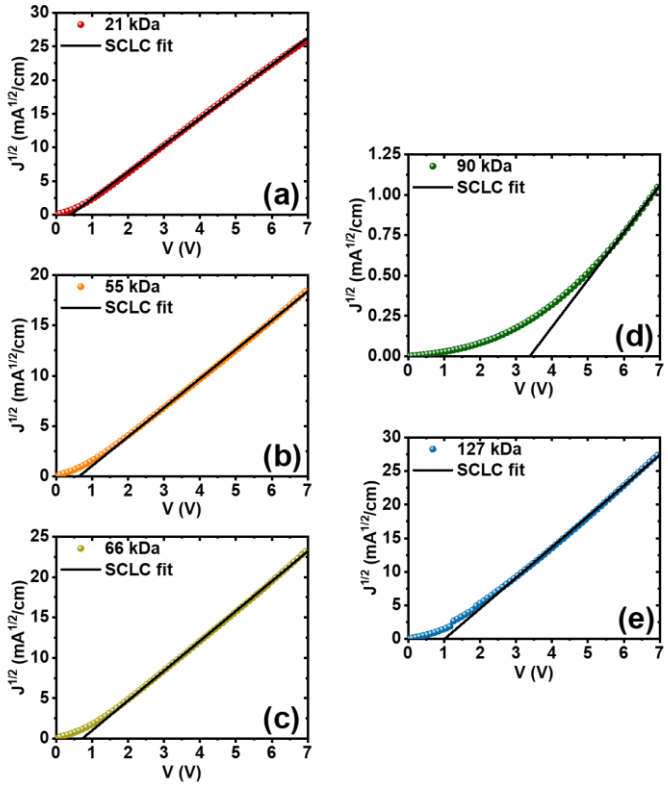

Figure C-7. $J^{1/2}$-V curves measured by space-charge-limited current (SCLC) technique and Mott-Gurney equation fitting for PNDIBS polymer at different number-average molecular weight (M_n) values. (a) 21kDa, (b) 55kDa, (c) 66kDa, (d) 90kDa, and (e) 127kDa.

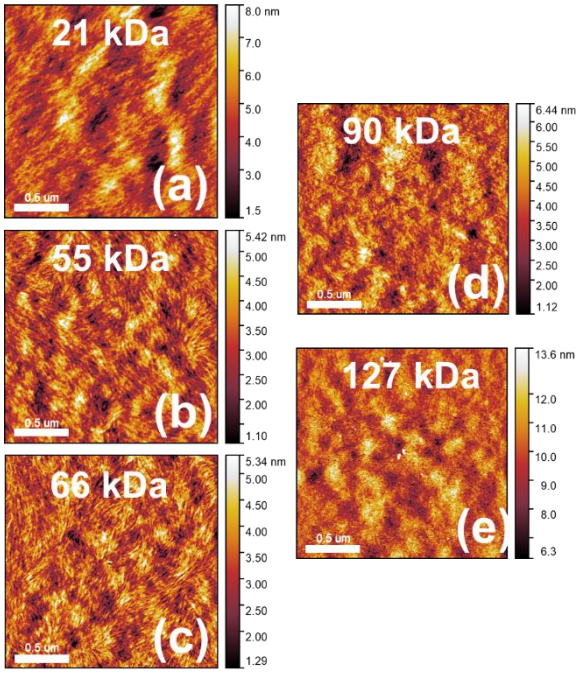

Figure C-8. AFM height images (2 μm x 2 μm) of PNDIBS thin films of different number-average molecular weight (M_n) values and estimated root-mean-square surface roughness (R_q): (a) 21kDa (R_q = 0.97 nm), (b) 55kDa (R_q = 0.72 nm), (c) 66kDa (R_q = 0.68 nm), (d) 90kDa (R_q = 0.86 nm), and (e) 127kDa (R_q = 1.09 nm).

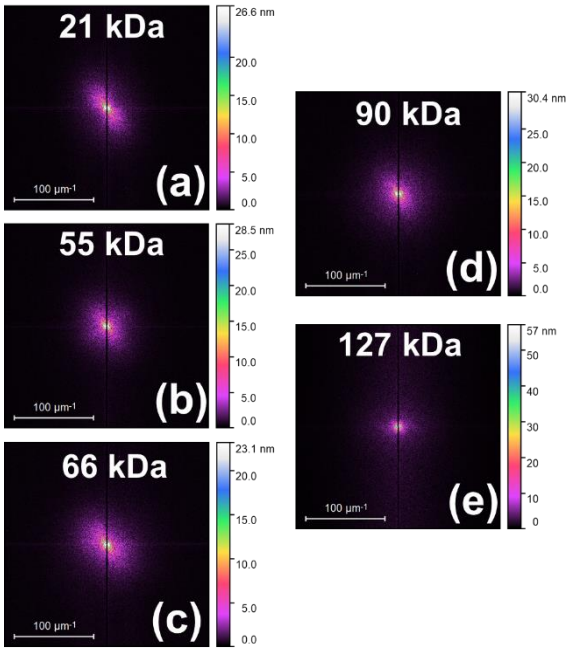

Figure C-9. Two-dimensional Fast Fourier-transformed (2D-FFT) images obtained from the AFM height images of the PNDIBS thin films at different number-average molecular weights. (a) 21kDa, (b) 55kDa, (c) 66kDa, (d) 90kDa, and (e) 127kDa.

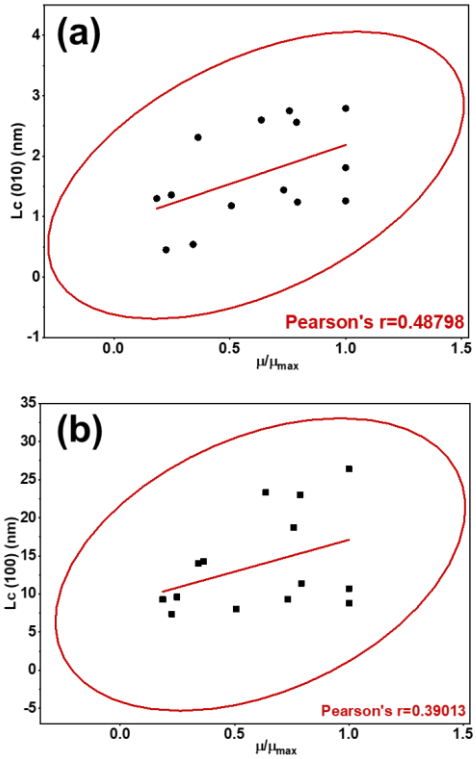

Figure C-10. Correlation between crystalline coherence length (L_c) and normalized mobility (μ/μ_{max}) of different naphthalene diimide (NDI)-based conjugated polymers.[33, 178-180] (a) L_c (010) vs. μ/μ_{max}, and (b) L_c (100) vs. μ/μ_{max}.

Table C-1. Summary of Diffraction Peak Positions in the In-Plane (IP) and Out-of-Plane (OOP) Directions of PNDIBS Films at Different Number-Average Molecular Weight (M_n) Values.

M_n (kDa)	q_{xy} (Å^{-1}) (100) IP	q_{xy} (Å^{-1}) (200) IP	q_{xy} (Å^{-1}) (300) IP	q_z (Å^{-1}) (010) OOP
21	0.270	-	-	1.64
55	0.255	0.53	0.77	1.59
66	0.255	0.52	0.76	1.59
90	0.248	0.51	0.74	1.55
127	0.255	0.51	0.76	1.57

Appendix D

Appendix D presents supplementary information accompanied Chapter 4: Chain Length Dependence of Electron Transport in an n-Type Conjugated Polymer with a Rigid-Rod Chain Topology.

D.1. Supplementary Figures.

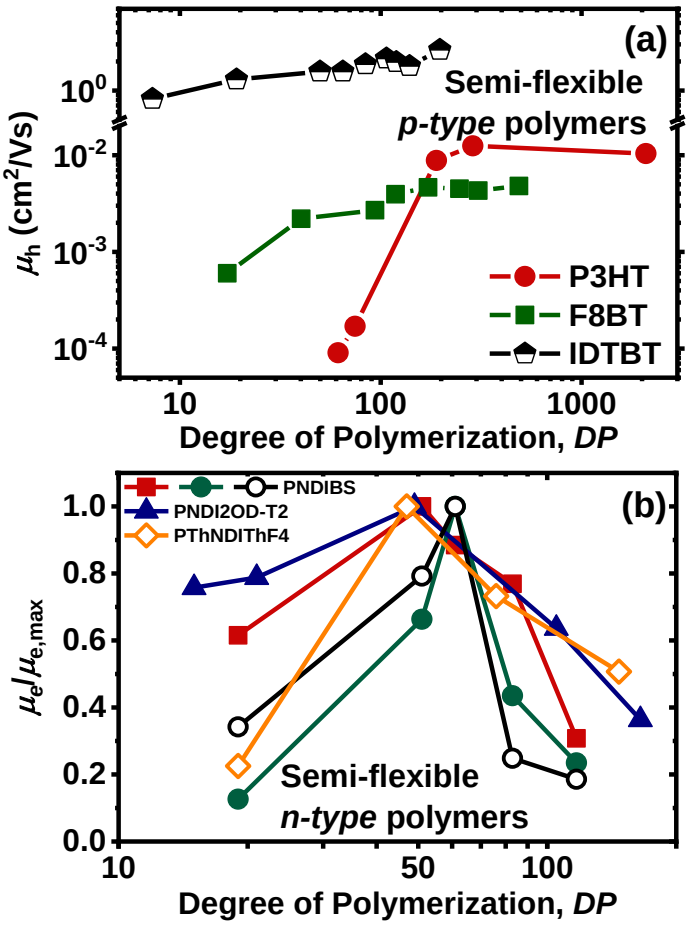

Figure D-1. Dependence of charge carrier mobility on the degree of polymerization (*DP*) in semi-flexible ***p-type*** polymers (a) and semi-flexible ***n-type*** polymers (b).

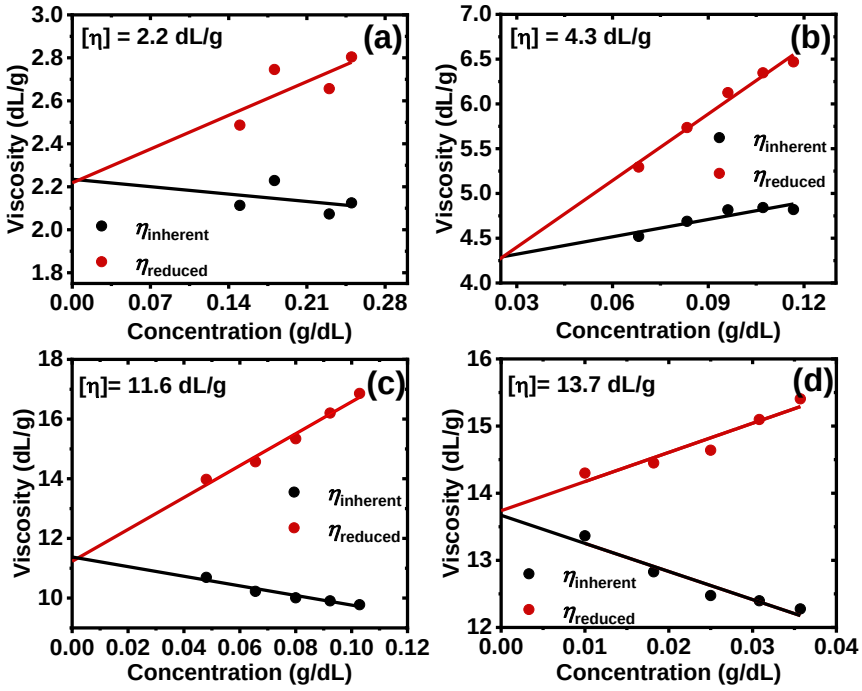

Figure D-2. Dependence of inherent viscosity ($\eta_{inherent}$) and reduced viscosity ($\eta_{reduced}$) on the concentration of BBL polymer solutions. Data were linear fitted according to Equations 4-1 and 4-2 and extrapolated to near zero concentrations to determine the intrinsic viscosity ([η]) of the polymers.

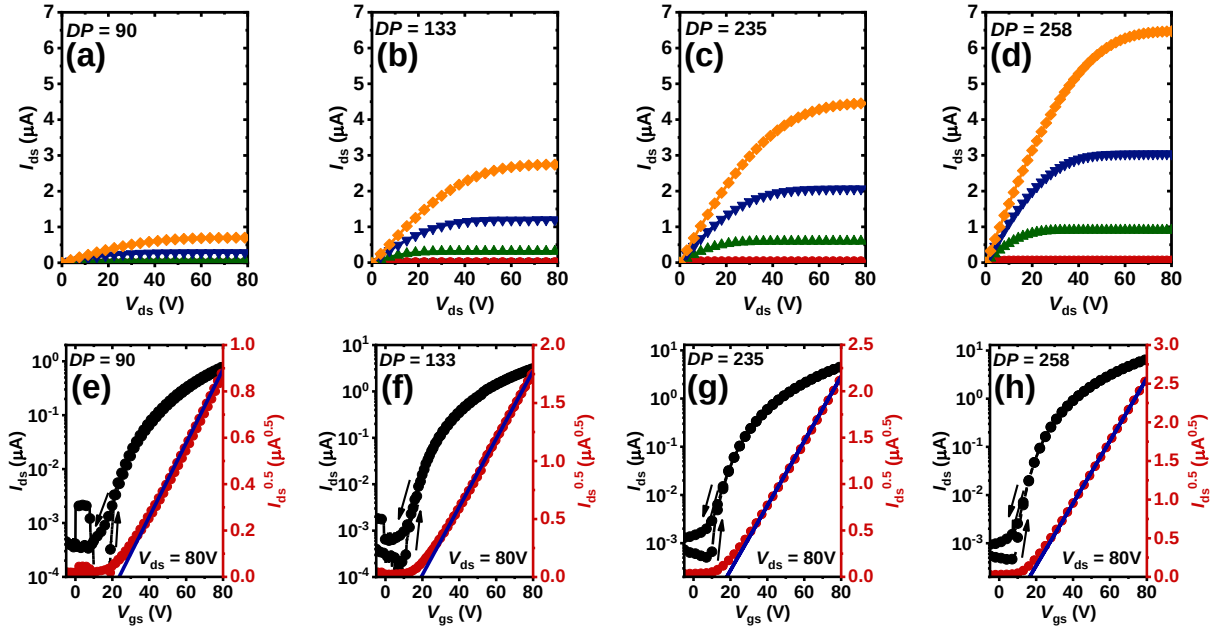

Figure D-3. (a – d) Output curves and (e – h) transfer curves of BBL n-channel organic field-effect transistor devices at different degree of polymerization (*DP*) values: (a, e) *DP* = 90, (b, f) *DP* = 133, (c, g) *DP* = 235, (d, h) *DP* = 258.

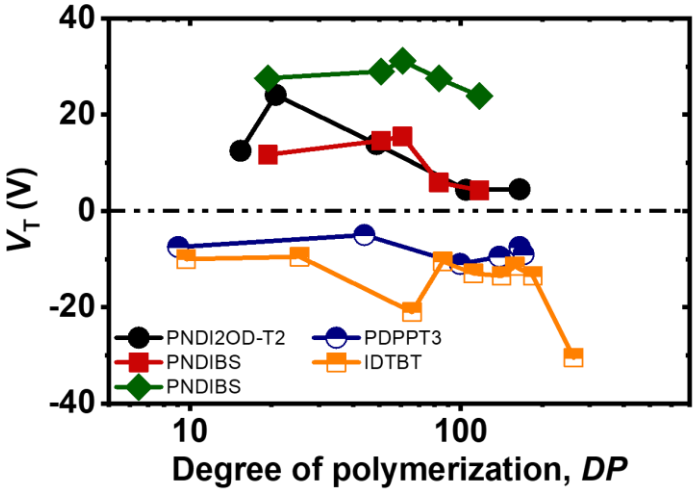

Figure D-4. Dependence of threshold voltage (V_T) on degree of polymerization (DP) of semi-flexible conjugated polymers: n-type polymers (PNDI2OD-T2, PNDIBS) and p-type polymers (PDPPT3, IDTBT).

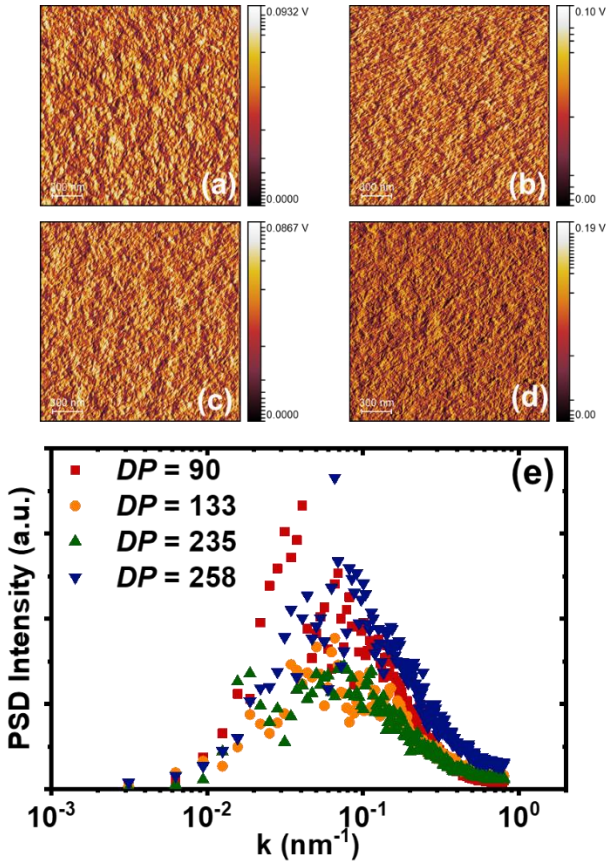

Figure D-5. (a-d) AFM phase images of BBL thin films at different degree of polymerization (*DP*): (a) *DP* = 90, (b) *DP* = 133, (c) *DP* = 235, (d) *DP* = 258; (e) Power spectral density (PSD) profiles of BBL thin films extracted of the phase images.

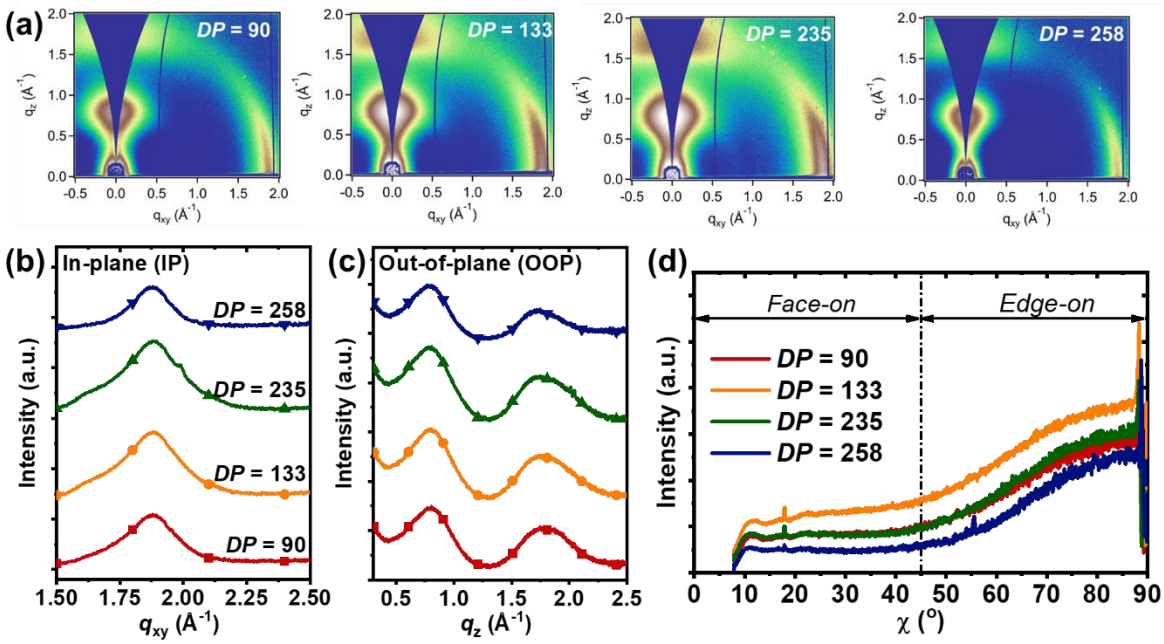

Figure D-6. (a) 2D-GIWAXS diffraction patterns of BBL thin films; (b and c) 1D line cuts of GIWAXS patterns in the in-plane (IP) direction (b) and the out-of-plane (OOP) direction (c); (d) Pole figure of BBL thin films at different degree of polymerization (*DP*) values.

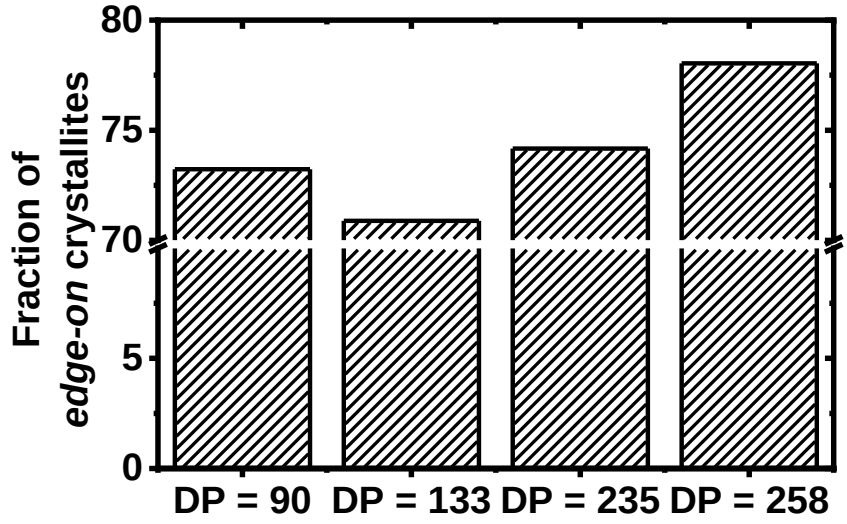

Figure D-7. Dependence of volume fraction of *edge-on* oriented crystallites on the degree of polymerization (*DP*).

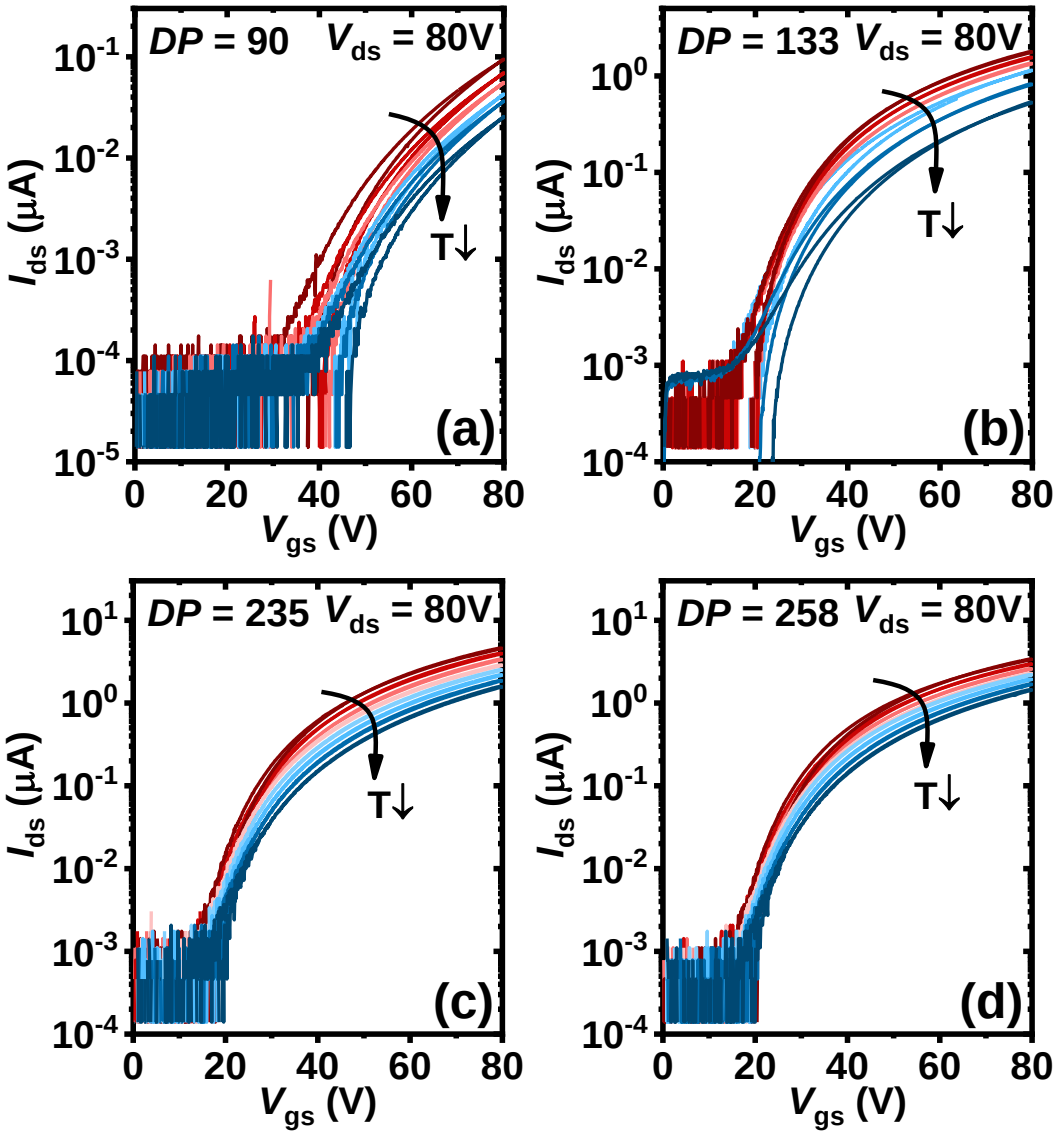

Figure D-8. Temperature dependent transfer curves of BBL transistor devices of different degree of polymerization (*DP*) values: (a) *DP* = 90, (b) *DP* = 133, (c) *DP* = 235, (d) *DP* = 258.

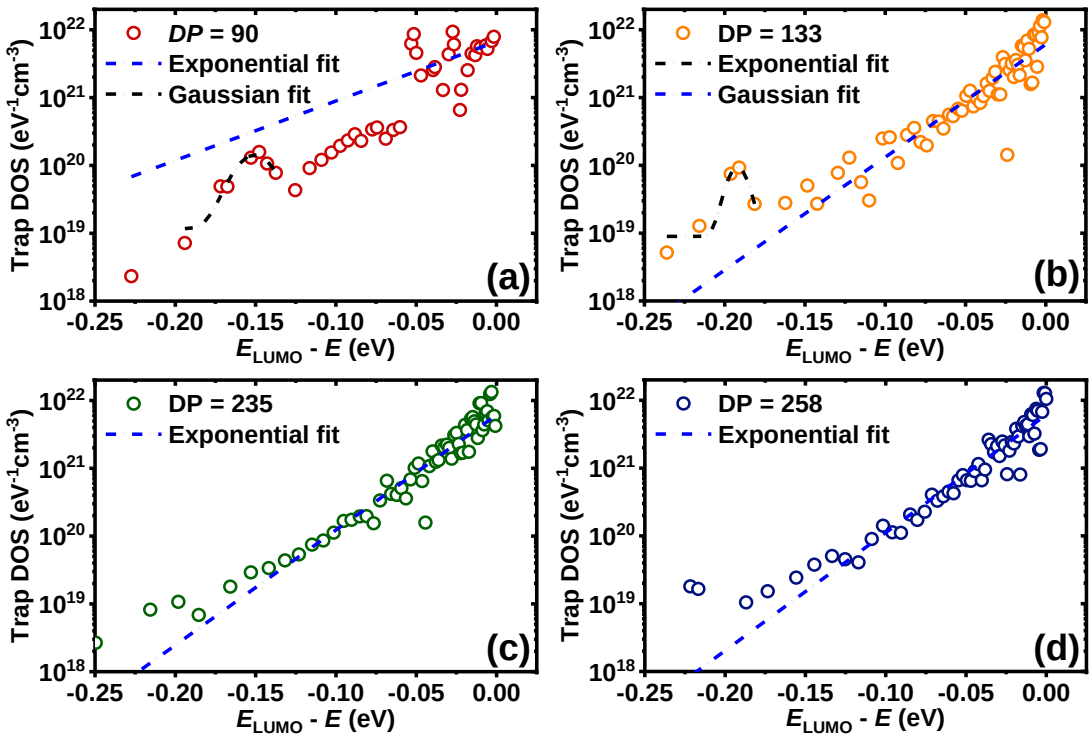

Figure D-9. Density of states (DOS) spectra of BBL devices at different degree of polymerization (*DP*): (a) *DP* = 90, (b) *DP* = 133, (c) *DP* = 235, and (d) *DP* = 258. Data are fitted to an exponential distribution to model shallow traps ($E_{LUMO} - E < -0.1$ eV) and gaussian distribution to model deep traps ($E_{LUMO} - E > -0.1$ eV).

D.3. Supplementary Tables

Table D-1. Summary of Diffraction Peak Positions in the Out-of-Plane (q_z) and In-Plane (q_{xy}) Directions, *d*-Spacings (*d*), Crystalline Coherence Length (L_c), and Paracrystallinity Disorder (*g*) of the (010) Diffraction Peaks for BBL Films at Different Degree of Polymerization (*DP*) Values.

DP	q_z (Å^{-1}) (100) OOP	q_z (Å^{-1}) (010) OOP	q_{xy} (Å^{-1}) (010) IP	*d* (Å) (010) OOP	L_c (nm) (010) OOP	g_π (%) (010) OOP
90	0.79	1.79	1.87	3.50	0.45	33.5
133	0.79	1.78	1.88	3.53	0.52	31.4
235	0.78	1.76	1.88	3.56	0.53	31.1
258	0.78	1.74	1.87	3.61	0.89	24.1

Table D-2. Model Parameters for the Exponential Shallow Trap Distribution $\left(N_{trap} = \frac{N_o}{E_o}\exp\left(\frac{E}{E_o}\right)\right)$ and Gaussian Deep Trap Distribution $\left(N_{trap} = N_1 + N_2\exp\left[-\frac{(E-E_1)^2}{(2\sigma)^2}\right]\right)$ of BBL Transistor Devices at Different Degree of Polymerization (*DP*) Values.

DP	N_o[a] ($eV^{-1}cm^{-3}$)	E_o[b] (meV)	$N_{shallow}$[c] ($states/cm^3$)	N_1[d] ($eV^{-1}cm^{-3}$)	N_2[e] ($eV^{-1}cm^{-3}$)	E_1[f] (meV)	σ[g] (meV)
90	3.32×10^{20}	49.6	2.88×10^{20}	1.16×10^{19}	1.31×10^{20}	150.1	8.1
133	1.59×10^{20}	26.1	1.56×10^{20}	8.94×10^{18}	8.50×10^{19}	192.0	4.3
235	1.57×10^{20}	25.6	1.54×10^{20}	-	-	-	-
258	1.53×10^{20}	25.0	1.51×10^{20}	-	-	-	-

[a]N_o, pre-exponential coefficient; [b]E_o, width of exponential distribution; [c]$N_{shallow}$, total concentration of trap states calculated by analytical integration of the exponential trap distribution from -0.1 eV to 0.0 eV; [d]N_1, offset coefficient of Gaussian distribution; [e]N_2, amplitude of Gaussian distribution; [f]E_1, peak center of Gaussian distribution; [g]σ, width of Gaussian distribution.

Appendix E

Appendix E presents supplementary information accompanied Chapter 5: Probing the Formation of Polarons, Polaron Pairs, and Bipolarons in n-Type Poly(Benzimidazobenzophenanthroline) Based π-Conjugated Redox Polymer.

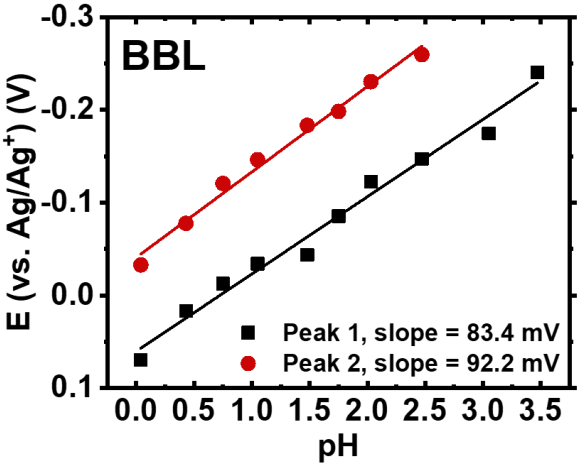

Figure E-1. Representative Pourbaix of BBL thin films in at least 0.1M $KCl_{(aq)}$ electrolyte.

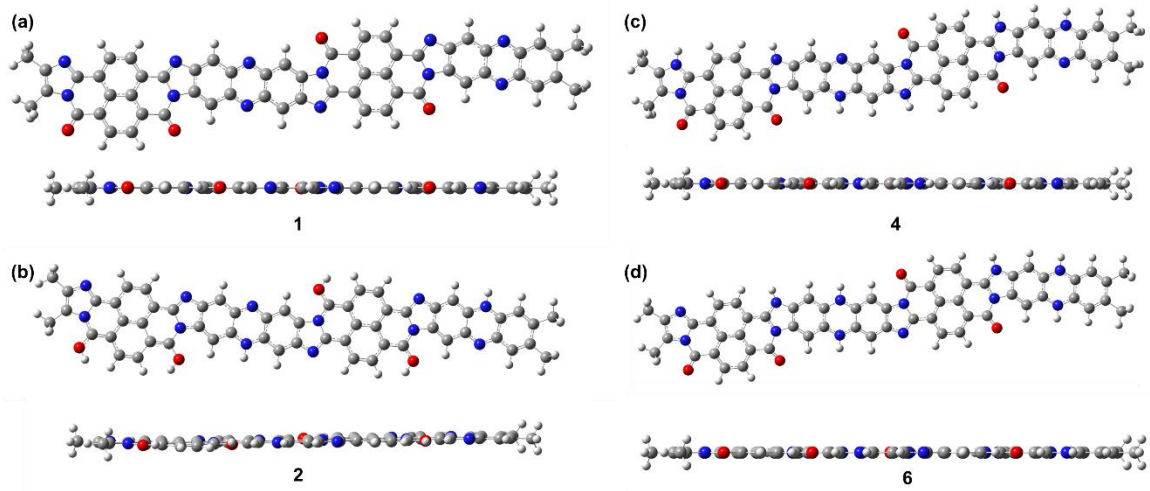

Figure E-2. DFT calculations of the optimized ground-state molecular geometry of different redox states of BBL-P dimers: (a) neutral BBL-P corresponding to structure 1 to Scheme 2, (b) reduced unprotonated BBL-P corresponding to structure 2 in Scheme 2, (c) reduced protonated BBL-P corresponding to structure 4 in Scheme 2, and (d) reduced protonated BBL-P corresponding to structure 6 in Scheme 2. Calculations were performed at the ωB97XD/6-31G(d,p) level of theory.

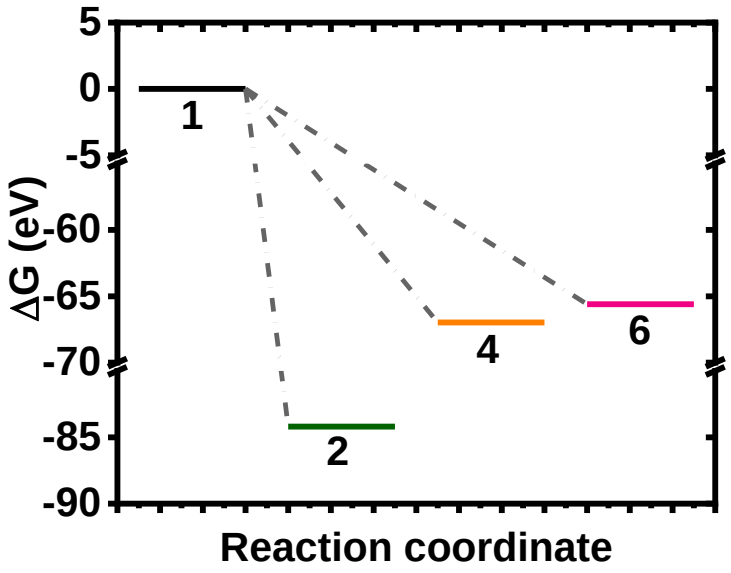

Figure E-3. Gibbs free energy change (Δ*G*) for each acid-base coupled redox reaction of BBL-P.

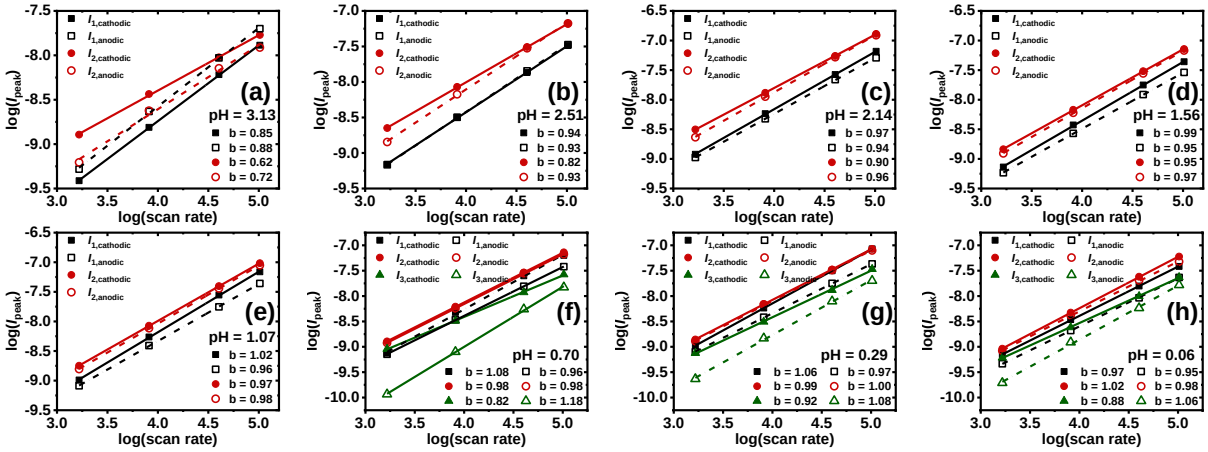

Figure E-4. Relationship between log(*i*) and log (v) for different redox event at various electrolyte pH.

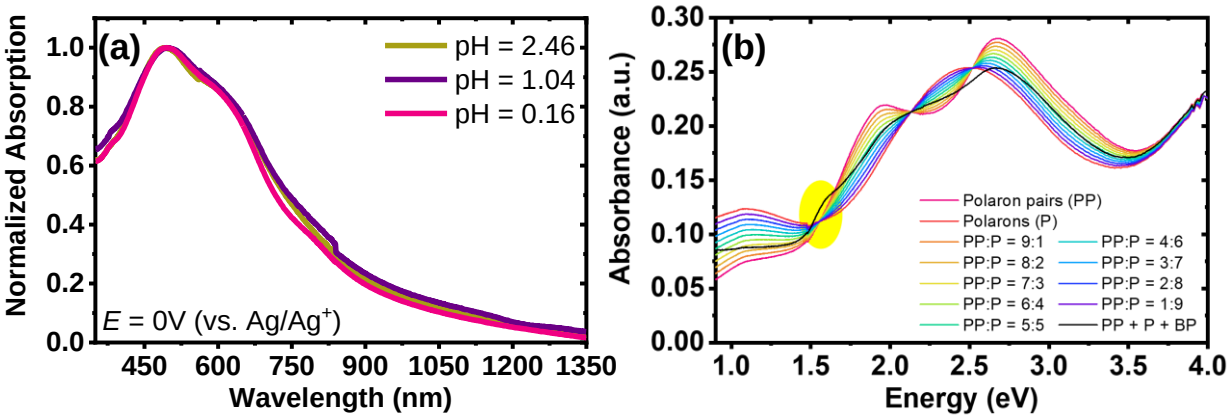

Figure E-5. (a) Thin film optical absorption spectra of BBL-P in 0.1M KCl aqueous electrolyte solution of varying pH 2.46, 1.04, and 0.16; (b) Optical absorption spectra of BBL-P thin films at different varying composition of polaron pairs (PP) and polarons (P).

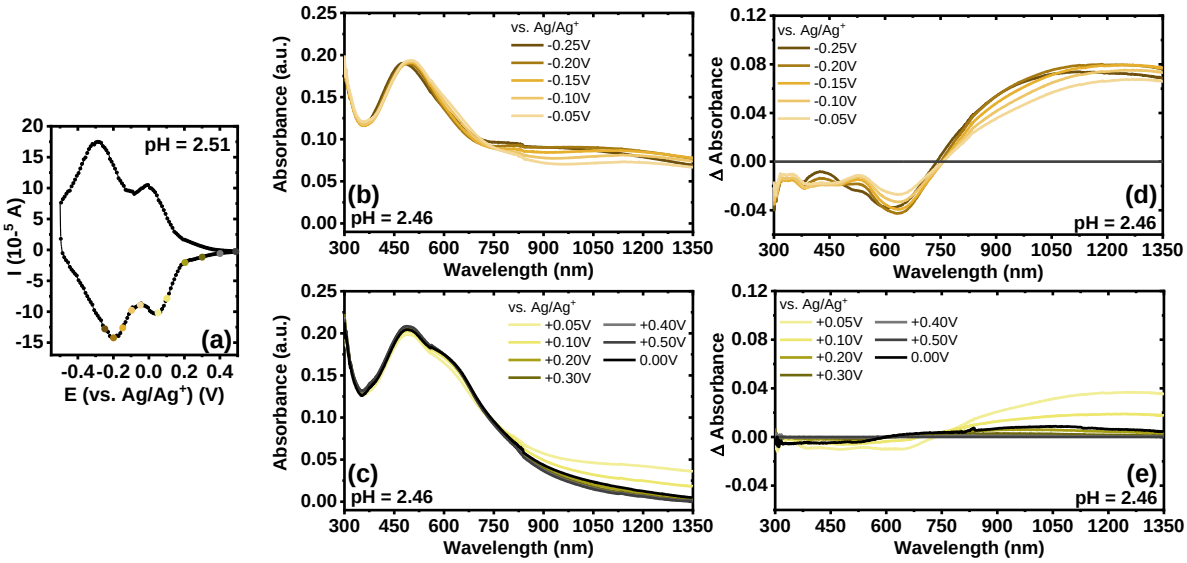

Figure E-6. (a) Cyclic voltammogram of BBL-P thin films in aqueous KCl electrolyte of pH 2.51 collected at a scan rate of 25 mV/s; (b – c) UV-Vis-NIR optical absorption spectra under different potentials of BBL-P thin films in electrolyte of pH ~ 2.5; (d – e) Differential UV-Vis-NIR optical absorption spectra under different potentials of BBL-P thin films. The baseline spectrum was taken at +0.50V to de-dope the films prior to each doping step.

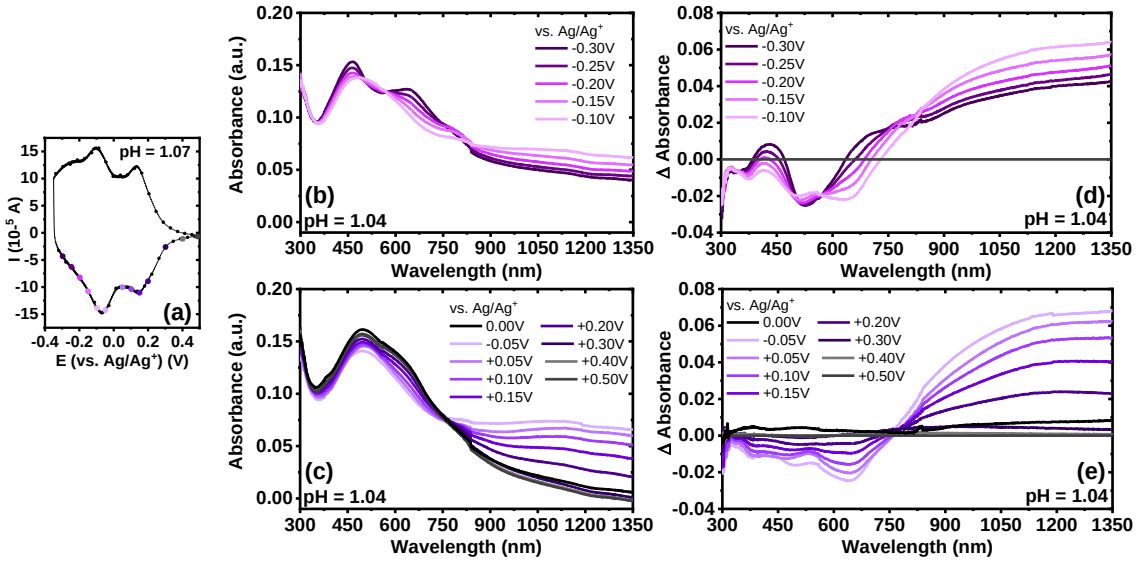

Figure E-7. (a) Cyclic voltammogram of BBL-P thin films in aqueous KCl electrolyte of pH 1.07 collected at a scan rate of 25 mV/s; (b – c) UV-Vis-NIR optical absorption spectra under different potentials of BBL-P thin films in electrolyte of pH = 1.04; (d – e) Differential UV-Vis-NIR optical absorption spectra under different potentials of BBL-P thin films. The baseline spectrum was taken at +0.50V to de-dope the films prior to each doping step.

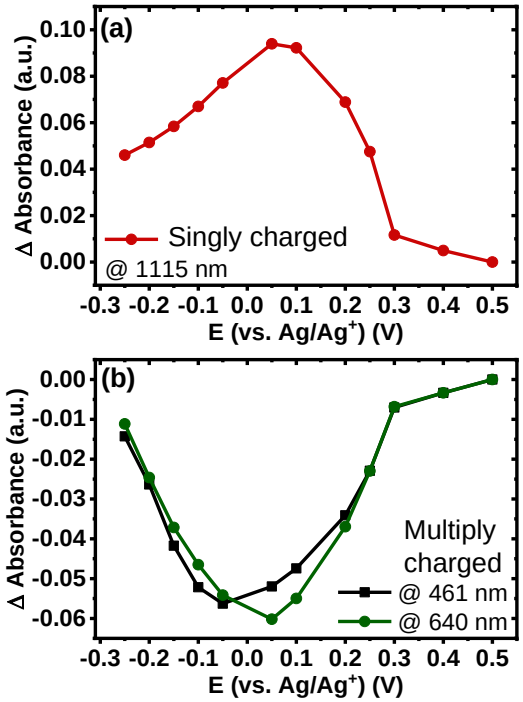

Figure E-8. Dependence of differential absorbance of BBL-P in electrolyte of pH < 1 on doping potential at selected wavelength: (a) 1115 nm and (b) 461 nm and 640 nm.

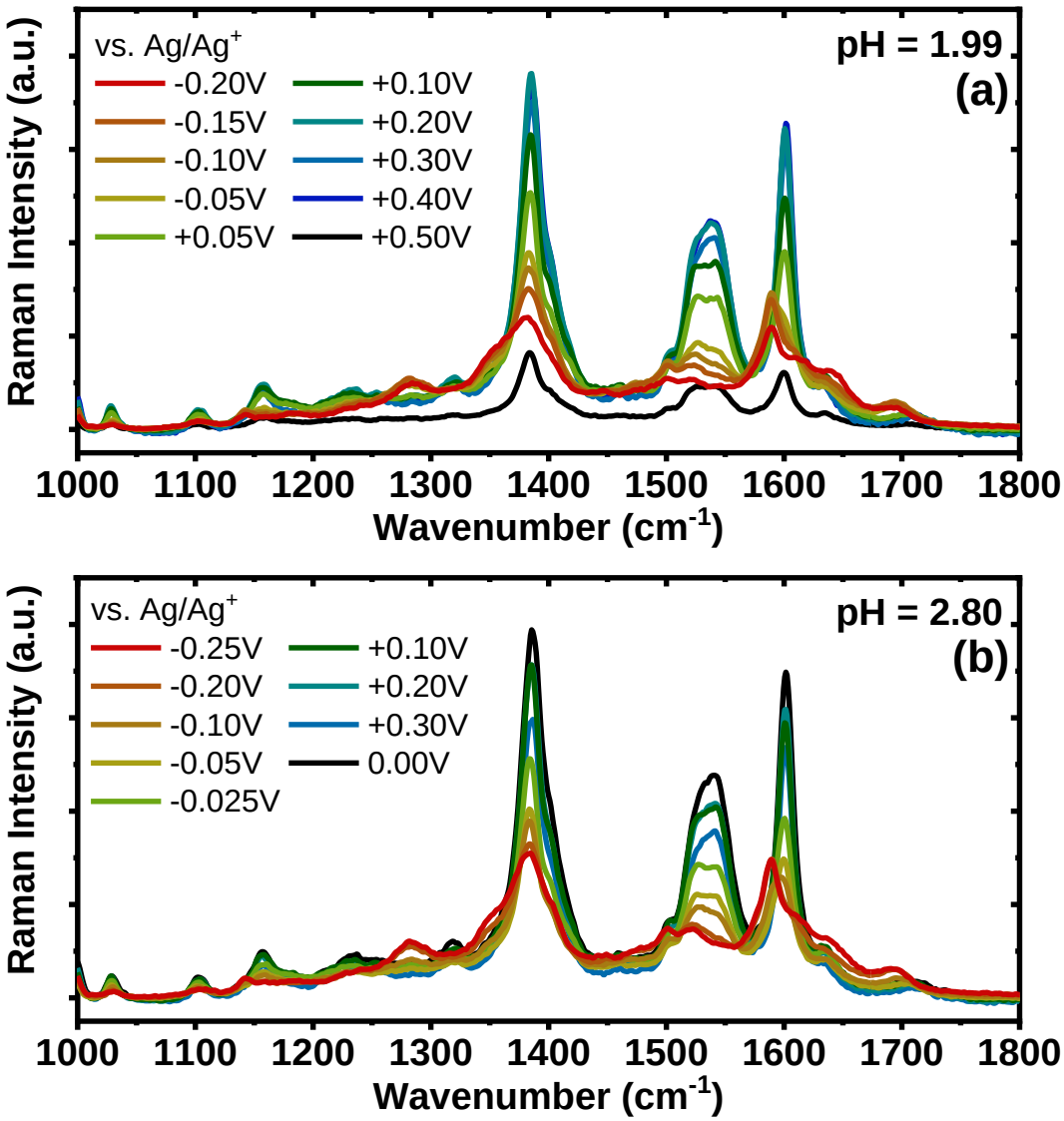

Figure E-9. *In-operando* Raman spectra of BBL-P films collected in 0.1M $KCl_{(aq)}$ electrolyte of varying pH value: (a) pH = 1.99, and (b) pH = 2.80. Raman measurements were collected using 532 nm excitation with BBL-P films coated on gold covered glass substrates as the working electrode, Pt mesh as the counter electrode, Ag/AgCl pellet as reference electrode positioned away from the illuminated area.

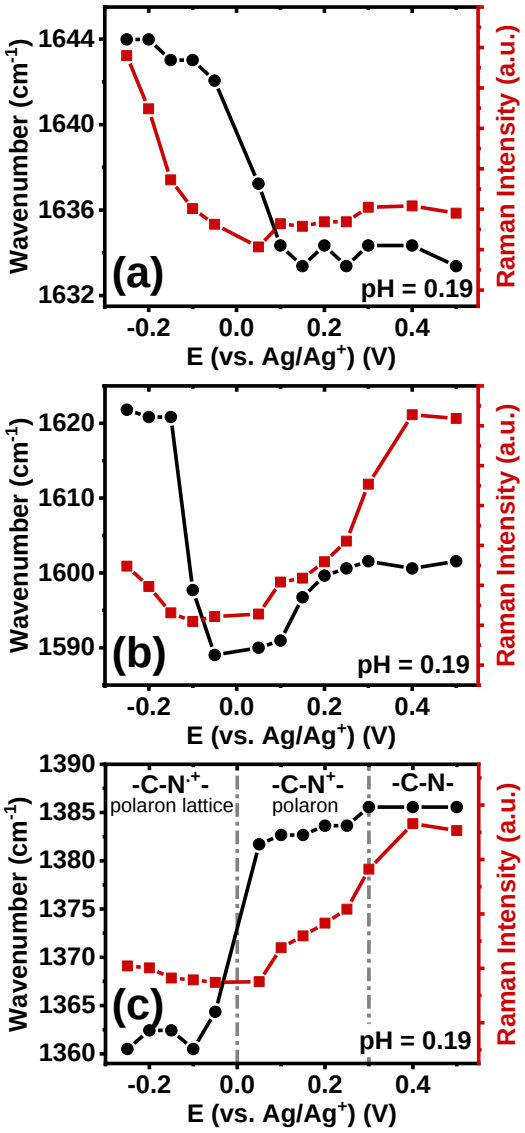

Figure E-10. (a) Evolution of Raman frequency and Raman intensity associated with the C=N vibrational mode as a function of doping potential; (b) Evolution of Raman frequency and Raman intensity associated with the C=C/C-C breathing of the naphthalene ring as a function of doping potential; (c) Raman signatures of singly charged species (polaron) and multiply charged species (coupled polaron pairs).

VITA

Duyen Ky Tran was born and raised in Ho Chi Minh City, Vietnam. She earned an Associate of Arts in Chemistry from Evergreen Valley College in San Jose, California in 2014, and a Bachelor of Science in Chemical Engineering from the University of California, Berkeley in 2016. She then moved to Seattle, Washington to pursue her Ph.D. degree in Chemical Engineering at the University of Washington. She has been conducting research under the guidance of Professor Samson A. Jenekhe to study semiconducting polymers for organic electronic and optoelectronic device applications. During her graduate studies, she earned a Master of Science in Chemical Engineering in 2020 and received the Jane and Joseph McCarthy Award for Excellence in Chemical Engineering Graduate Student Teaching in 2020, the High Impact Publication Award in 2021, the Faculty Lecture Award in 2022, and Barbara Krieger-Brocket Travel Award in 2022 from the Department of Chemical Engineering. She was recognized by the American Chemical Society Polymer Division for Excellence in Graduate Polymer Research in 2021. She placed first at the Electronic and Photonic Materials: Graduate Student Awards Session, Area 08E at the 2022 Annual American Institute of Chemical Engineers (AIChE) Meeting. She was one of the finalists for the 2023 Frank J. Padden Jr. Award for Excellence in Polymer Research by the American Physical Society.

The following is the list of the author's publications:

16. **Tran, D. K.**; Jenekhe, S. A. All-Polymer Solar Cells – A Perspective on Materials and Devices, *in preparation*.

15. **Tran, D. K.**; West, S. M.; Guo, J.; Chen, S. E.; Ginger, D. S.; Jenekhe, S. Probing the Formation of Polarons, Polaron Pairs, and Bipolarons in n-Type Poly(Benzimidazobenzophenanthroline) Based π-Conjugated Redox Polymer **2023**, *in preparation.*

14. **Tran, D. K.**; West, S. M.; Guo, J.; Chen, S. E.; Ginger, D. S.; Jenekhe, S. A. Electron Transport Physics of a Model Rigid-Rod n-Type Semiconducting Polymer: Ladder Poly(Benzimidazobenzophenanthroline) (BBL). **2023**, *to be submitted.*

13. Ding, X.; **Tran, D. K.**; West, S. M.; Nguyen, M.; Kuzuhara, D.; Koganezawa, T.; Kaminsky, W.; Jenekhe, S. A. Ladder Molecule Acceptors for High-Performance Organic Solar Cells: Design, Synthesis, Enhanced Intrinsic Stability and Photovoltaic Properties. **2023**, *to be submitted.*

12. Ding, X; **Tran, D. K.**; West, S. M.; Kuzuhara, D.; Koganezawa, T.; Kaminsky, W.; Jenekhe, S. A. Effects of Side Chains and Halogenation on Ladder Molecule Acceptors. **2023**, *to be submitted.*

11. West, S. M.; **Tran, D. K.**; Guo, J.; Chen, S. E.; Ginger, D. S; Jenekhe, S. p-Type Semiconducting Ladder Poly(pyrrolobenzothiazine)s: Effects of N-Alkyl Side Chains on the Chain Conformation, Electronic Structure, and Charge Transport Properties. *Macromolecules* **2023,** *submitted*.

10. West, S. M.; **Tran, D. K.**; Guo, J.; Chen, S. E.; Ginger, D. S; Jenekhe, S. A. Phenazine-Substituted Poly(benzimidazobenzophenanthrolinedione): Electronic Structure, Thin Film Morphology, Electron Transport, and Mechanical Properties of an n-Type Semiconducting Ladder Polymer. *Macromolecules* **2023**, *56* (5), 2081 – 2091.

9. Guo, J.; Flagg, L. Q.; **Tran, D. K.**; Chen, S. E.; Li, R.; Kolhe, N. B.; Giridharagopal, R.; Jenekhe, S. A.; Richter, L. J.; Ginger, D. S. Hydration of a side-chain-free n-type semiconducting ladder polymer driven by electrochemical dopin. *J. Am. Chem. Soc.* **2023**, *145* (3), 1866-1876.

8. **Tran, D. K.**; Robitaille, A.; Hai, I. J.; Kuzuhara, D.; Koganezama, T.; Chiu, Y-C.; Leclerc, M.; Jenekhe, S. A. Unified Understanding of Molecular Weight Dependence of Electron Transport in Naphthalene Diimide-Based n-Type Semiconducting Polymers. *Chem. Mater.* **2022**, *34* (21), 9644-9655.

7. Li, Z.-L.; **Tran, D. K.**; Nguyen, M.; Jian, T.; Jenekhe, S. A.; Chen, C.-L. Amphiphilic Peptoid-Directed Assembly of Oligoanilines into Highly Crystalline Conducting Nanotubes. *Macromol. Rapid Comm.* **2022**, *43*, 2100639.

6. Lee, E.; **Tran, D. K.**; Park, J.; Ko, W.; Jenekhe, S. A.; Hwang, Y.-J. Benzodithiophene-based Wide Bandgap Small-Molecule Donors for Organic Photovoltaics with Large Open-Circuit Voltages. *Org. Electron.* **2021**, *88*, 105996.

5. **Tran, D. K.**;* Robitaille, A.;* Hai, I. J.; Ding, X.; Kuzuhara, D.; Koganezama, T.; Chiu, Y-C.; Leclerc, M.; Jenekhe, S. A. Elucidating the Impact of Molecular Weight on Morphology, Charge Transport, Photophysics, and Performance of All-Polymer Solar Cells. *J. Mater. Chem. A* **2020**, *8* (40), 21070-27083. (* denotes equal contribution).

4. Ding, X.; **Tran, D. K.**; Kuzuhara, D.; Koganezama, T.; Jenekhe, S. A. Comparative Study of Selenophene- and Thiophene-Containing n-Type Semiconducting Polymers for High Performance All-Polymer Solar Cells. *ACS Appl. Polym. Mater.* **2021**, *3* (1), 49-59.

3. **Tran, D. K.**; Kolhe, N. B.; Hwang, Y.-J..; Kuzuhara, D.; Koganezama, T.; Jenekhe, S. A. Effects of a Fluorinated Donor Polymer on the Morphology, Photophysics, and Performance of All-Polymer Solar Cells Based on Naphthalene Diimide-Arylene Copolymer Acceptors. *ACS Appl. Mater. Interfaces* **2020**, *12* (14), 16490-16502.

2. Kolhe, N. B.; West, S. M.; **Tran, D. K.**; Ding, X.; Kuzuhara, D.; Yoshimoto, N.; Koganezama, T.; Jenekhe, S. A. Designing High Performance Nonfullerene Electron Acceptors with Rylene Imides for Efficient Organic Photovoltaics. *Chem. Mater.* **2020**, *32* (1), 195-204.

1. Kolhe, N. B.; **Tran, D. K.**; Lee H.; Kuzuhara, D.; Yoshimoto, N.; Koganezama, T.; Jenekhe, S. A. New Random Copolymer Acceptors Enable Additive-Free Processing of 10.1% Efficient All-Polymer Solar Cells with Near-Unity Internal Quantum Efficiency. *ACS Energy Lett.* **2019**, *4* (5), 1162-1170.